

ISSN 2074-272X

науково-практичний
журнал 2022/3



EIE електротехніка і електромеханіка

Electrical Engineering

& Electromechanics

Електричні машини та апарати

Електротехнічні комплекси та системи

Промислова електроніка

Електроізоляційна та кабельна техніка

Електричні станції, мережі і системи

Журнал включено до найвищої категорії «А»

Переліку фахових видань України

З 2021 р. журнал індексується у Scopus

**З 2015 р. журнал індексується
у Web of Science Core Collection:
Emerging Sources Citation Index**



Electrical Engineering & Electromechanics

Scientific Journal was founded in 2002

Founder – National Technical University «Kharkiv Polytechnic Institute» (Kharkiv, Ukraine)

EDITORIAL BOARD

Sokol Ye.I.	Editor-in-Chief , Professor, Corresponding member of NAS of Ukraine, Rector of National Technical University «Kharkiv Polytechnic Institute» (NTU «KhPI»), Ukraine
Korytchenko K.V.	Deputy Editor , Professor, NTU «KhPI», Ukraine
Rozov V.Yu.	Deputy Editor , Professor, Corresponding member of NAS of Ukraine, A. Pidhorneyi Institute of Mechanical Engineering Problems of NAS of Ukraine, Kharkiv, Ukraine
Bolyukh V.F.	Deputy Editor , Professor, NTU «KhPI», Ukraine
Abu-Siada A.	Professor, Curtin University, Perth, Australia
Aman M.M.	Professor, NED University of Engineering & Technology, Karachi, Pakistan
Baltag O.	Professor, Grigore T. Popa University Medicine and Pharmacy, Romania
Baranov M.I.	Professor, Research and Design Institute «Molniya» of NTU «KhPI», Ukraine
Batygin Yu.V.	Professor, Kharkiv National Automobile and Highway University, Ukraine
Bíró O.	Professor, Institute for Fundamentals and Theory in Electrical Engineering, Graz, Austria
Bouktir T.	Professor, Ferhat Abbas University, Setif 1, Algeria
Buriakovskiy S.G.	Professor, NTU «KhPI», Ukraine
Butkevych O.F.	Professor, Institute of Electrodynamics of NAS of Ukraine (IED of NASU), Kyiv, Ukraine
Colak I.	Professor, Nisantasi University, Istanbul, Turkey
Cruz S.	Professor, University of Coimbra, Portugal
Doležel I.	Professor, University of West Bohemia, Pilsen, Czech Republic
Féliachi M.	Professor, Technological Institute of Saint-Nazaire, University of Nantes, France
Grinchenko V.S.	PhD, A. Pidhorneyi Institute of Mechanical Engineering Problems of NAS of Ukraine, Kharkiv, Ukraine
Gurrero J.M.	Professor, Aalborg University, Denmark
Gurevich V.I.	PhD, Honorable Professor, Central Electrical Laboratory of Israel Electric Corporation, Haifa, Israel
Hajjar A.A.	Professor, Tishreen University, Latakia, Syrian Arab Republic
Ida N.	Professor, The University of Akron, Ohio, USA
Izykowski J.	Professor, Wroclaw University of Science and Technology, Poland
Kildishev A.V.	Associate Research Professor, Purdue University, USA
Klepikov V.B.	Professor, NTU «KhPI», Ukraine
Korzeniewska E.	Professor, Lodz University of Technology, Poland
Ktena A.	Professor, National and Kapodistrian University of Athens, Greece
Kuznetsov B.I.	Professor, A. Pidhorneyi Institute of Mechanical Engineering Problems of NAS of Ukraine, Kharkiv, Ukraine
Kyrylenko O.V.	Professor, Academician of NAS of Ukraine, IED of NASU, Kyiv, Ukraine
Levin B.M.	Professor, Holon Institute of Technology, Tel Aviv-Yafo, Israel
Malik O.P.	Professor, University Of Calgary, Canada
Maslov V.I.	Professor, National Science Center «Kharkiv Institute of Physics and Technology», Ukraine
Mi Zou	PhD, Chongqing University of Posts and Telecommunications, China
Mikhaylov V.M.	Professor, NTU «KhPI», Ukraine
Miljavec D.	Professor, University of Ljubljana, Slovenia
Milykh V.I.	Professor, NTU «KhPI», Ukraine
Nacke B.	Professor, Gottfried Wilhelm Leibniz Universität, Institute of Electrotechnology, Hannover, Germany
Petrushin V.S.	Professor, Odessa National Polytechnic University, Ukraine
Podoltsev A.D.	Professor, IED of NASU, Kyiv, Ukraine
Reutskiy S.Yu.	PhD, A. Pidhorneyi Institute of Mechanical Engineering Problems of NAS of Ukraine, Kharkiv, Ukraine
Rezinkin O.L.	Professor, NTU «KhPI», Ukraine
Rezinkina M.M.	Professor, NTU «KhPI», Ukraine
Shcherbak Ya.V.	Professor, NTU «KhPI», Ukraine
Sikorski W.	Professor, Poznan University of Technology, Poland
Suemitsu W.	Professor, Universidade Federal Do Rio de Janeiro, Brazil
Trichet D.	Professor, Institut de Recherche en Energie Electrique de Nantes Atlantique, France
Vaskovskiy Yu.M.	Professor, National Technical University of Ukraine «Igor Sikorsky Kyiv Polytechnic Institute», Kyiv, Ukraine
Vazquez N.	Professor, Tecnológico Nacional de México en Celaya, Mexico
Vinnikov D.	Professor, Tallinn University of Technology, Estonia
Yagup V.G.	Professor, O.M. Beketov National University of Urban Economy in Kharkiv, Ukraine
Yatchev I.	Professor, Technical University of Sofia, Bulgaria
Zagirnyak M.V.	Professor, Member of NAES of Ukraine, Kremenchuk M.Ostrohradskiy National University, Ukraine
Zgraja J.	Professor, Lodz University of Technology, Poland
Grechko O.M.	Executive Managing Editor , PhD, NTU «KhPI», Ukraine

From no. 1 2021 Journal «Electrical Engineering & Electromechanics» is indexing in **Scopus** and from no. 1 2015 Journal is indexing in **Web of Science Core Collection: Emerging Sources Citation Index (ESCI)**.

Also included in DOAJ (Directory of Open Access Journals), in EBSCO's database, in ProQuest's databases – Advanced Technologies & Aerospace Database and Materials Science & Engineering Database, in Gale/Cengage Learning databases.

Editorial office address:

National Technical University «Kharkiv Polytechnic Institute», Kyrpychova Str., 2, Kharkiv, 61002, Ukraine

phones: +380 57 7076281, +380 67 3594696, e-mail: a.m.grechko@gmail.com (**Grechko O.M.**)

ISSN (print) 2074-272X

ISSN (online) 2309-3404

© National Technical University «Kharkiv Polytechnic Institute», 2022

Printed 01 June 2022. Format 60 × 90 ¼. Paper – offset. Laser printing. Edition 200 copies.

Printed by Printing house «Madrid Ltd» (18, Gudanova Str., Kharkiv, 61024, Ukraine)



no. 3, 2022

Table of Contents

Electrical Machines and Apparatus

- Avdieieva O.A., Vakhonina L.V., Sadovoy O.S., Stavinskiy R.A., Tsyganov O.M.** Improving the main indicators of transformers with twisted one-piece magnetic cores by changing the technology of circular winding turns formation..... 3
- Malyar V.S., Hamola O.Ye., Maday V.S., Vasylychshyn I.I.** Mathematical modeling of rheostat-reactor start of wound-rotor induction motors 8
- Panchal T.H., Patel A.N., Patel R.M.** Reduction of cogging torque of radial flux permanent magnet brushless DC motor by magnet shifting technique 15

Electrotechnical Complexes and Systems

- Kuznetsov B.I., Nikitina T.B., Bovdai I.V., Voloshko O.V., Kolomiets V.V., Kobylanskyi B.B.** Comparison of the effectiveness of thruple-loop and double-loop systems of active shielding of a magnetic field in a multi-storey old buildings..... 21

Industrial Electronics

- Vasyliv K.M.** Method of dynamic parameters for mathematical modelling of switching processes of valves closing of semiconductor converters..... 28

Electrical Insulation and Cable Engineering

- Bezprozvannykh G.V., Grynshyna M.V.** Effective parameters of dielectric absorption of polymeric insulation with semiconductor coatings of power high voltage cables..... 39

Power Stations, Grids and Systems

- Ali Moussa M., Derrouazin A., Latroch M., Aillerie M.** A hybrid renewable energy production system using a smart controller based on fuzzy logic 46
- Babes B., Hamouda N., Kahla S., Amar H., Ghoneim S.S.M.** Fuzzy model based multivariable predictive control design for rapid and efficient speed-sensorless maximum power extraction of renewable wind generators..... 51
- Chappa H., Thakur T.** A novel load shedding methodology to mitigate voltage instability in power system 63
- Sekhane H., Labed D., Labed M.A.** Modelling and performance testing of a digital over-current relay enhanced designed model 71

O.A. Avdieieva, L.V. Vakhonina, O.S. Sadovoy, R.A. Stavinskiy, O.M. Tsyganov

Improving the main indicators of transformers with twisted one-piece magnetic cores by changing the technology of circular winding turns formation

Introduction. With the adoption of standards to reduce losses in transformers it is necessary to change the design of transformers that remain unchanged. Further energy saving is possible with the use of non-traditional technical solutions for the improvement of transformers. **Problem.** In order to reduce idle losses, the curved magnetic circuits of power transformers are carried out in the form of low-volume circuits. Windings are injected into assembled magnetic conductors by shuttle machines. The shuttle of windings provides technological gaps in winding windows, which results in an increase in size, metal capacity and losses. **Goal.** Rationale for transformer performance improvement by excluding process gaps in winding windows. **Methodology.** The definition of the change in transformer indicators is performed using optimization functions of the dimensionless indicators of the technological level. The adequacy of the functions is confirmed by the calculation of the mass of the electromagnetic system and the losses of the transformer. The figures of the compact analogue are calculated from the named serial analogue. **Results.** The result is a reduction in mass and a loss in the compactness of the transformer. **Originality.** The improvement of the indicators and the simplification of the winding technology are provided by a change in the design of insulating frames of winding coils. Winding on the rods is ensured by rotating the outer part of the composite insulating frame. **Practical significance.** Replacement the design of the windings of transformer with power of 40 kVA of 1000 V voltage class with a spatially twisted, small-dimensional magnetic conductor on a compact analogue leads to a reduction in mass and overall dimensions by 15 % and (17-18) %. Efficiency increases by 0.3 %. References 14, tables 2, figures 4.

Key words: twisted transformer, one-piece magnetic core, insulating frame, coil, winding.

Виконано аналіз конструктивно-технологічних особливостей електромагнітних систем трансформаторів з витими нероз'ємними магнітопроводами і круговими утворюючими контурами стрижнів та обмоткових витків. Запропоновано конструкцію обмоткової котушки з зовнішньою рухомою та внутрішньою нерухомою частинами опорно-ізоляційного каркасу та заміну вмотки витків на технологію намотки. Показано, що використання замість човникової вмотаної конструкції виконання обмотки з зовнішньою частиною ізоляційного каркаса, що обертається, призводить до поліпшення масогабаритних і енергетичного показників трансформатора. Бібл. 14, табл. 2, рис. 4.

Ключові слова: витий трансформатор, нероз'ємний магнітопровід, ізоляційний каркас, обмотка, намотка.

Problem definition. The total power of transmission system transformers exceeds the generation power by 6-7 times, with the main resource costs and the main losses of five to six times the transformation of electricity accounted for transformers I-III dimensions of mass production [1]. Since the beginning of the 21st century, new standards have been adopted in developed countries, regulating a significant reduction in losses of non-operating movement of low and medium power transformers and reducing the load loss of large transformers [1-5]. Block diagrams and designs of electromagnetic systems (EMS) of transformers in production are indispensable for a century, and the reduction of losses is through the use of innovations in materials science and reducing electromagnetic loads [6]. Further growth of energy saving requirements requires the use of new innovative technical solutions to improve transformers [1-6].

Analysis of recent research and publications. In the last century, the production of magnetic cores of transformers based on plate lamination was supplemented by technologies of winding tape (roll) of electrical steel (ES). The twisted magnetic cores of low-power transformers are made dissected. The presence of joints leads to an increase in losses of up to 30 %. Therefore, twisted magnetic conductors used in the production of single-phase and three-phase transformers up to

2000 kVA are made continuous (integral) with circular forming contours of rods and winding coils (Fig. 1, a, b). Winding with circular turns is wound on shuttle machines, which provides a technological increase in the design gap between adjacent winding coils and between the windings and yokes of transformers with rod and armor magnetic cores. Metal capacity, dimensions and losses are increasing, which reduces the efficiency of ES winding technology in the production of single-phase and three-phase transformers.

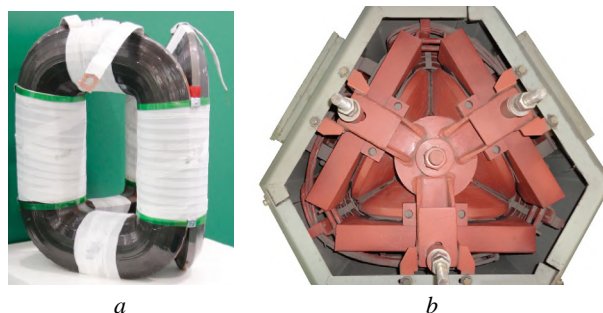


Fig. 1. Twisted three-section magnetic core (a) and top view of the transformer TSM-40-74.OM5 with removed cover (b)

The main modern means of energy efficiency of transformers is the use of tape amorphous ES with minimal losses, but with less operating magnetic flux density and higher cost [1, 7, 8].

Symmetrical spatial twisted axial magnetic conductors (Fig. 1,*a*) made of amorphous ES provide significant opportunities for improving three-phase transformers according to [5]. Thus three-phase transformers, in particular TSZM and TSZMV of sea execution (Fig. 1,*b*) with anisotropic magnetic conductors of a kind (fig. 1,*a*) are mastered in manufacture in 60th years of the 20th century and are manufactured now (Technical description and operating instructions. 140.240, Moscow, InformElectro, 1975, order 1265, 21 p., in Russian).

In addition to the use of tape anisotropic microcrystalline and amorphous ES and three-phase EMS with twisted three-section spatial magnetic cores [5-7] the main innovations are «cable» windings and the use of high-temperature superconductivity windings [1]. There are also opportunities to improve transformers by structural transformations of EMS elements [6]. Known examples of relatively simple structural transformation of twisted magnetic cores are the use of a combination of ES brands in the inner and outer zones and middle layers of ES and the replacement of the outer section of a three-phase three-rod planar magnetic core with two side sections twice as wide [9-11]. However, according to [1, 5] there is a contradiction between the market requirements for cheaper transformer products and the global trend of energy saving based on innovative designs and technologies. In addition, there is the possibility of improving transformers through the use of «residual reserves» of traditional designs and innovative methods of manufacturing EMS elements [6].

Recently, twisted magnetic cores of transformers of limited power are being replaced by analogues with conditionally oblique joints and the technology of forming covering layers by separating and bending sections of the tape of varying length. Special equipment is used to form layers of steel with offset joints («Unicore» – magnetic cores) [1, 12]. However, the use of this technology in the production of EMS with circular forming contours (Fig. 2,*a,b*) of twisted sections (Fig. 3,*a*) with the configuration of the steel scan (Fig. 3,*b*) causes additional difficulties. Also, brittle amorphous steel (glass metal) does not allow small bending radii.

Based on the above, solution of the problem of reducing weight, material consumption and losses, as well as labor costs in the manufacture of transformers with twisted magnetic cores is relevant.

The goal of the paper is to increase the basic indicators of the transformer on the example of electromagnetic systems with wound «shuttle» and wound windings as well as justification of the feasibility of increasing the filling of the winding window by conductors based on changes in winding.

Research methods and results. Increasing the compactness of the EMS by eliminating technological gaps in the winding windows can be considered a reserve for improving transformers with twisted integral magnetic cores. Such an increase is possible by change the

insulation design and change with the simplification of the technology of manufacturing windings by removing the kinematic links of the winding shuttles

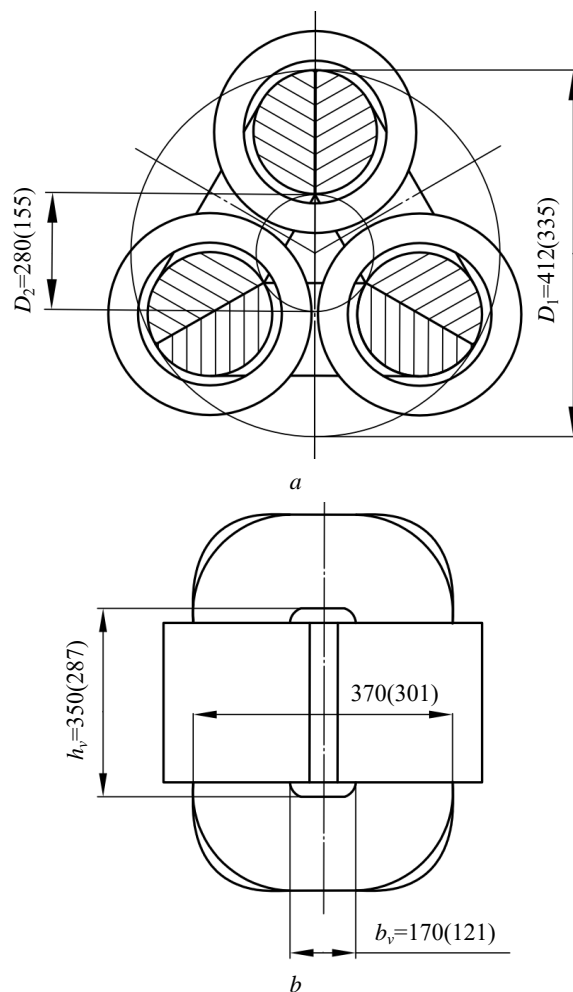


Fig. 2. Geometric parameters of the electromagnetic system of the transformer TSZM-40-74.OM5 with $K_w'' = 0.177$ and its analogue with $K_w'' = 0.3$ in cross section (*a*) and side view (*b*)

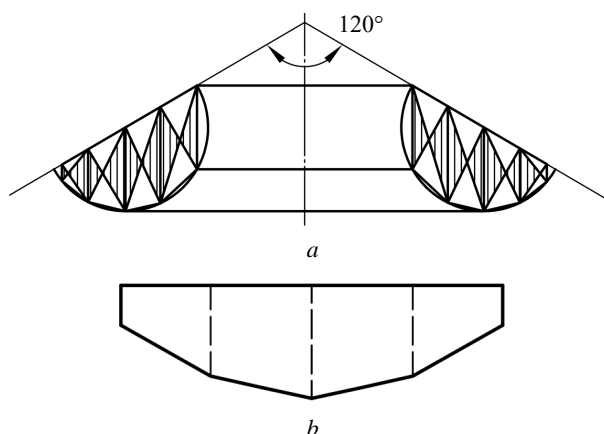


Fig. 3. Schemes of magnetic core section (*a*) and sectional electrical steel strip scan (*b*)

To eliminate technological winding gaps and butt gaps providing the possibility of respectively «shuttle run-in» of the insulating cylinder (layers of turns) and installation of winding coils on the detachable rod part of

the magnetic core, a design with two-layer support-insulating base windings is proposed (Fig. 4,*a*). The inner insulating cylinder of the winding frame, covering the rod, is stationary. The outer layer of the winding frame is a movable cylinder which is connected to the annular insulating elements located above the ends of the winding coils. The surfaces of the zones of the outer diameters of the rings form a kinematic connection with the transmitter of rotational motion from the drive of the winding device (Fig. 4,*b*).

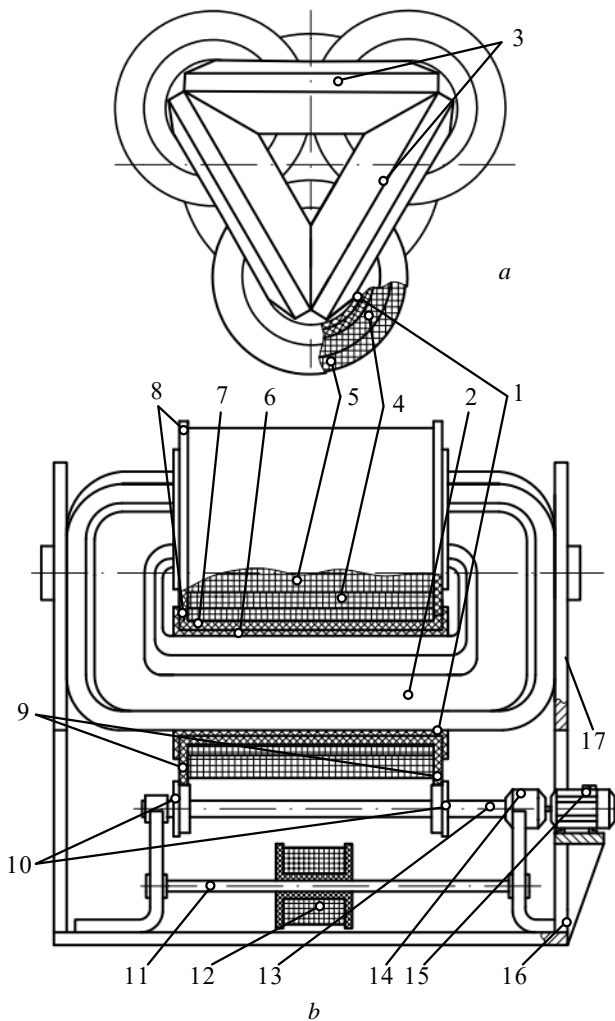


Fig. 4. Top view of the active part (*a*) and the schematic diagram of the winding equipment on the rotating components of the insulating frames (*b*): transformer with twisted one-piece magnetic core: 1 – frame; 2 – rod; 3 – magnetic core; 4, 5 – winding turns of low and high voltages; 6, 7 – fixed and movable insulation layers; 8 – annular insulating element; 9 – kinematic pair; 10 – torque transmitter; 11 – axis; 12 – winding turns coil workpiece; 13 – shaft; 14 – reducer; 15 – drive motor; 16 – base; 17 – support

The winding of the windings on the rods is provided by the rotation of the outer part of the prefabricated winding frame. After winding the phase coils, the outer cylinder is fixed. Concentric winding frames are formed by bonding, in particular gluing, of semi-annular workpieces.

Comparison of EMS variants (Fig. 2) is performed on the basis of the universal method of structural and structural-parametric synthesis of electromechanical devices [6]. The target functions of mass F_m and active power losses F_e with dimensionless optimization components $I_m^*(x_c, y_w)$ and $I_e^*(x_c, y_w, z_e)$ and relative controlled variables [6]:

$$F_m = (I_T)^{3/4} \gamma_{st} I_m^*(x_c, y_w, K_w^{(v)}); \quad (1)$$

$$F_e = (I_T)^{3/4} \gamma_{st} I_e^*(x_c, y_w, z_e, K_w^{(v)}), \quad (2)$$

where I_T is the indicator of output data and electromagnetic loads of the transformer [6]; x_c is the ratio of the diameters D_1 and D_2 of the calculated circles of the magnetic core (Fig. 2,*a*); y_w is the ratio of the height h_v and the width b_v of the winding window (Fig. 2,*b*); $K_w^{(v)}$ is the coefficient of filling of the winding window with copper (voltage class); z_e is the electromagnetic controlled variable; γ_{st} , P_{st} are the density and specific losses of ES, respectively.

Indicators of mass and losses of the mathematical model of the transformer with EMS (Fig. 1,*b* and Fig. 2) are determined by equations [13, 14]:

$$I_m^*(x_c, y_w, K_w^{(v)}) = 2,07 \left\{ \left[K_w^{(v)} K_R K_{st} f(x_c, y_w) \right]^{3/4} \times \left\{ K_w^{(v)} K_R \left[(y_w + 1)(1 - 0,0718x_c)(x_c - 1)^2 + 0,657(x_c - 1)^3 \right] + 3,482 K_w^{(v)} y_w (1 - 0,0718x_c)^2 (1 - 0,0718x_c) \gamma_{cu} / \gamma_{st} \right\} \right\} \quad (3)$$

$$I_e^*(x_c, y_w, z_e, K_w^{(v)}) = 2,07 K_{lst} \left\{ \left[K_w^{(v)} K_R K_{st} f(x_c, y_w) \right]^{3/4} \times \left\{ K_w^{(v)} K_R \left[(y_w + 1)(1 - 0,0718x_c)(x_c - 1)^2 + 0,657(x_c - 1)^3 \right] + 3,482 z_e K_w^{(v)} y_w (1 - 0,0718x_c)^2 (1 - 0,0718x_c) \right\} \right\} \quad (4)$$

$$f(x_c, y_w) = y_w (1 - 0,0718x_c)^2 (x_c - 1)^2,$$

where K_{st} is the filling factor of the ES magnetic core; K_R is the filling factor of the circular forming contour by the cross section of the rod; K_{lst} is the coefficient of additional losses of non-working movement; γ_{cu} is the density of copper.

The calculation substantiation of expediency of change of a design of an insulating framework and a way of laying of a winding in a one-piece magnetic core is executed on an example of the three-phase transformer TSZM-40-74.OM5 (Fig. 1,*b*) and the estimated data of its compact analogue are given in Table 1.

Table 1
Main technical characteristics of the three-phase transformer «TT-40»

Variant	Rated power, kW	Voltage U_1/U_2 , V	Mass of the active part, kg	Efficiency
TSZM-40-74.OM5	40	380/230	182	0.973
Analogue	40	380/230	154.15	0.976

The calculation of the value of losses and efficiency of variants TT-40 (Table 1) is performed at the value of the relative electromagnetic controlled variable [14]

$$z_e = \frac{K_{lcu} \gamma_{cu} P_{cu}^2 J_w^2}{K_{lst} \gamma_{st} P_{st}} = \frac{1,04 \cdot 8900 \cdot 2,4 \cdot 10^{-12} \cdot (2 \cdot 10^6)^2}{1,34 \cdot 76500 \cdot 1,1} = 7,88; \quad (5)$$

where K_{lcu} , P_{cu} , J_w are, respectively, the coefficient of additional short-circuit losses, the indicator of specific losses and the current density of the copper windings of the TT-40 dry variant.

The coefficient K_{lst} is determined by the presence of third harmonics of the sectional magnetic fluxes of the magnetic core. Specific losses P_{st} correspond to the amplitude of the magnetic flux density 1.6 T and ES brand 3407.

The values of geometric and design parameters of the TT-40 variants are presented in Table 2. The calculated values (Table 1) of EMS mass and TSZM losses (Fig. 1,b) practically coincide with the passport data, which confirms the adequacy of the mathematical model [13, 14]. These values are obtained by (3), (4), data and real values of the size of the EMS (Fig. 2).

Table 2
Geometric and design parameters of «TT-40» variants

Variants	Values of controlled variables, p.u.			Efficiency
	x_c	y_w	z_e	
TSZM-40-74.OM5	412/208= =1.98	350/170= =2.06	7.88	0.177
Analogue	335/155= =2.16	287/301= =2.37	7.88	0.3

The calculated values of the indicators (Table 1) of the compact analogue TT-40 are determined at identical for the options (Fig. 2) values of I_T (1), (2). The extreme values x_c , y_w of (3), (4) meet the criterion for optimizing the minimum mass of the EMS.

Increasing the value $K_w'' = 0.177$ to a value corresponding to the voltage class up to 1000 V ($K_w'' = 0.3$), leads to a significant improvement in the technical characteristics of the TT-40.

Conclusions.

Replacement of the wrapped «shuttle» electromagnetic systems design with continuous tape (one-piece) sections of the magnetic core by compact design without technological intercoil gaps leads to improved indicators of transformers with twisted three-section magnetic cores.

The reduction in the mass and dimensions of the electromagnetic systems of voltage class 1000 V at power of 40 kVA is approximately 15 % and (17-18) %. The efficiency increases by about 0.3 %.

Conflict of interest. The authors declare no conflict of interest.

REFERENCES

1. Kostinskiy S.S. The review of the condition of branch of transformer manufacture and tendencies of development of the design of power transformers. *Izvestiya Vysshikh Uchebnykh Zavedenii. Problemy Energetiki*, 2018, vol. 20, no. 1-2, pp. 14-32. (Rus). doi: <https://doi.org/10.30724/1998-9903-2018-20-1-2-14-32>.
2. Targosz R., Topalis F.V. Energy efficiency of distribution transformers in Europe. *2007 9th International Conference on Electrical Power Quality and Utilisation*, 2007, pp. 1-5. doi: <https://doi.org/10.1109/EPQU.2007.4424121>.
3. De Almeida A., Santos B., Martins F. Energy-efficient distribution transformers in Europe: impact of Ecodesign regulation. *Energy Efficiency*, 2016, vol. 9, no. 2, pp. 401-424. doi: <https://doi.org/10.1007/s12053-015-9365-z>.
4. Charalampopoulos C., Psomopoulos C.S., Ioannidis G.Ch., Kaminaris S.D. Implementing the EcoDesign Directive in distribution transformers: First impacts review. *AIMS Energy*, 2017, vol. 5, no. 1, pp. 113-124. doi: <https://doi.org/10.3934/energy.2017.1.113>.
5. *Innovative breakthrough in the power transformer market.* (Rus). Available at: <http://www.elec.ru/articles/innovacionnye-proryv-na-rynke-silovyh-transformatorov> (Accessed 24 March 2021).
6. Stavinskii A.A., Avdeyeva Y.A., Pal'chikov O.O., Stavinskii R.A. The Generalized Method for Structural-Parametric Synthesis of the Electromagnet Systems of Electrical Machines and Induction Apparatuses. Part 1. Results from a Comparative Analysis of Different Versions of Three-Phase Transformer Electromagnet Systems. *Elektrichestvo*, 2017, vol. 4, pp. 39-49. (Rus). doi: <https://doi.org/10.24160/0013-5380-2017-4-39-49>.
7. Almen J., Breitholtz M. *Performance evaluation of amorphous hexa-core for distribution transformers.* Bachelor's Thesis in Electric Power Engineering. Chalmers University of Technology, Gothenburg, Sweden 2012. 50 p. Available at: <https://publications.lib.chalmers.se/records/fulltext/167013.pdf> (Accessed 20 March 2021).
8. Najafi A., Iskender I. Comparison of core loss and magnetic flux distribution in amorphous and silicon steel core transformers. *Electrical Engineering*, 2018, vol. 100, no. 2, pp. 1125-1131. doi: <https://doi.org/10.1007/s00202-017-0574-7>.
9. Kefalas T. Transformers Made of Composite Magnetic Cores: An Innovative Design Approach. *Recent Patents on Electrical Engineering*, 2009, vol. 2, no. 1, pp. 1-12. doi: <https://doi.org/10.2174/1874476110902010001>.
10. Kefalas T.D., Kladas A.G. Development of Distribution Transformers Assembled of Composite Wound Cores. *IEEE Transactions on Magnetics*, 2012, vol. 48, no. 2, pp. 775-778. doi: <https://doi.org/10.1109/TMAG.2011.2172976>.
11. Kefalas T.D., Magdaleno-Adame S. Techno-economic comparative evaluation of mixed and conventional magnetic wound cores for three-phase distribution transformers. *Electric Power Systems Research*, 2018, vol. 155, pp. 331-339. doi: <https://doi.org/10.1016/j.epsr.2017.11.003>.
12. Hernandez I., Olivares-Galvan J.C., Georgilakis P.S., Canedo J.M. A Novel Octagonal Wound Core for Distribution Transformers Validated by Electromagnetic Field Analysis and Comparison With Conventional Wound Core. *IEEE Transactions on Magnetics*, 2010, vol. 46, no. 5, pp. 1251-1258. doi: <https://doi.org/10.1109/TMAG.2010.2040623>.
13. Avdieieva E.A., Stavinskiy R.A. Mass and cost figures for spatial axial three-phase electromagnetic systems with circular and hexagonal forming contours of twisted magnetic core rods. *Electrical Engineering & Electromechanics*, 2014, no. 1, pp. 15-20. doi: <https://doi.org/10.20998/2074-272X.2014.1.02>.

14. Avdieieva E.A., Stavinskiy R.A. Watt loss in three-phase transformers with circular and hexagonal forming contours of twisted spatial magnetic core rods. *Electrical Engineering & Electromechanics*, 2014, no. 2, pp. 14-17. doi: <https://doi.org/10.20998/2074-272X.2014.2.02>.

Received 17.01.2022
Accepted 23.03.2022
Published 01.06.2022

O.A. Avdieieva¹, PhD,
L.V. Vakhonina², PhD, Associate Professor,
O.S. Sadovoy², PhD,
R.A. Stavinskiy¹, PhD, Associate Professor,
O.M. Tsyganov², PhD,

¹ Admiral Makarov National University of Shipbuilding,
9, Avenue Heroes of Ukraine, Mykolaiv, 54020, Ukraine,
e-mail: e.avdeeva@ukr.net

² Mykolayiv National Agrarian University,
9, Georgiya Gongadze Str., Mykolaiv, 54020, Ukraine,
e-mail: sadovuyos@mnau.edu.ua (Corresponding author)

How to cite this article:

Avdieieva O.A., Vakhonina L.V., Sadovoy O.S., Stavinskiy R.A., Tsyganov O.M. Improving the main indicators of transformers with twisted one-piece magnetic cores by changing the technology of circular winding turns formation. *Electrical Engineering & Electromechanics*, 2022, no. 3, pp. 3-7. doi: <https://doi.org/10.20998/2074-272X.2022.3.01>

V.S. Malyar, O.Ye. Hamola, V.S. Maday, I.I. Vasylychshyn

Mathematical modeling of rheostat-reactor start of wound-rotor induction motors

Introduction. Wound-rotor induction motors are less common compared squirrel-cage induction motors. However, they occupy a significant share among electric drives with difficult starting conditions. Their advantage is obtaining a high starting electromagnetic torque at lower values of starting currents. **Problem.** Due to the possibility of including different devices in the rotor circuit, it is possible to shape the starting characteristics according to the needs of the technological process. Due to a narrower range of applications of electric drives based on wound-rotor induction motors, they are less investigated. Selection of parameters of starting and regulating devices, included in the rotor circuit, is carried out by simplified methods, which do not satisfy modern requirements to regulated electric drives. **Goal.** The paper aims to develop mathematical models and methods for calculating the dynamic modes and static characteristics of the wound-rotor induction motor with a reactor in the rotor circuit. **Methodology.** In the developed algorithms, the mathematical model of the motor is presented by the differential equations made for electric circuits in a system of orthogonal coordinates that allows excluding angular coordinate from equations of electric equilibrium. The elements of the Jacobi matrix of equilibrium equations of motor circuits are eigenvalues, and mutual is the differential inductances of electrical circuits, which are determined based on the magnetization characteristics of the main magnetic flux and leakage fluxes of the rotor and stator circuits. **Results.** Mathematical models for the study of starting modes of wound rotor induction motor allow to calculate transients and static characteristics and, on their basis, to carry out design synthesis of starting reactors, which provide the law of change of electromagnetic torque during start-up operating conditions. **Originality.** The mathematical basis of the developed algorithms is the method of solving nonlinear systems of equations by Newton method in combination with the method of continuation by parameter. The developed mathematical models and software made on their basis have high speed that allows to carry out high-reliability calculation of starting modes taking into account saturation of a magnetic circuit of the motor. **Practical value.** The developed algorithms do not require significant computing resources, have high speed, and can be used both for the design synthesis of start-control devices and control of the electric drive in real time and to predict its course. References 25, figures 4.

Key words induction motor, wound rotor, reactor start, mathematical model, static characteristics, transients, magnetic core saturation.

Розроблено математичні моделі, методи і алгоритми аналізу пускових режимів і статичних характеристик асинхронних двигунів з фазним ротором. В розроблених алгоритмах математична модель двигуна подана диференціальними рівняннями, складеними для електричних контурів в системі ортогональних координат. Математичною основою розроблених алгоритмів розрахунку статичних характеристик є розв'язування нелінійних систем скінченних рівнянь електричної рівноваги методом Ньютона в поєднанні з методом продовження по параметру, а пускових режимів – числове інтегрування нелінійних систем диференціальних рівнянь електромеханічної рівноваги. Елементами матриці Якобі в розроблених алгоритмах є власні і взаємні диференціальні індуктивності електричних контурів, які визначаються на основі характеристик намагнічування основним магнітним потоком, а також потоками розсіювання контурів ротора і статора, що дає змогу здійснювати розрахунок з урахуванням насичення магнітопроводу двигуна. Розроблені програми і алгоритми мають високу швидкодію і дають змогу здійснювати проектний синтез пускових активних і реактивних опорів в колі ротора з метою забезпечення закону зміни електромагнітного моменту під час пуску, який відповідає роботі системи електроприводу в заданих технологічних умовах, а також здійснювати мікропроцесорне керування в динамічних режимах. Бібл. 25, рис. 4.

Ключові слова: асинхронний двигун, фазний ротор, реакторний пуск, математична модель, статичні характеристики, перехідні процеси, насичення магнітопроводу.

Introduction. The most common among electric drives in industry, agriculture and household applications are squirrel-cage induction motors (IMs). Their main disadvantages are significant starting currents, which exceed 5-7 and even more times the nominal values, as well as a relatively small driving torque, which is insufficient for many technological processes. In addition, the direct connection of the motor to the network is accompanied by significant pulsations of the electromagnetic torque [1]. The development of start and regulating systems of automated control, as well as frequency converters has significantly expanded the scope of use of squirrel-cage IMs. However, the problem of starting the mechanisms of electric drives with difficult starting conditions needs further development and improvement.

In recent years, there has been a significant increase in interest in wound-rotor induction motors due to the expansion of the range of electric drives based on them, and therefore there is a need to study them, including mathematical modeling methods.

The starting properties of the induction electric drive can be significantly improved by using wound-rotor IMs [2], which, despite the higher cost compared with squirrel-cage rotor IMs, thanks to modern electronic control systems received a new impetus in development and application for lifting and transport mechanisms, conveyors, winches and other mechanisms with difficult starting conditions. Increasing the starting torque is achieved by connecting to the rotor winding of various

devices. Rheostat is most often used for this purpose, the active resistance of which can be changed discretely by switching on or shorting its sections [2]. Due to the increase in the active resistance of the rotor phases, the critical value of the electromagnetic torque does not change, and the critical slip increases with increasing resistance of the rheostat. Therefore, we can achieve the maximum value of the electromagnetic torque when sliding $s = 1.0$. This property is used to start the motor at torque of resistance exceeding the rated value of the starting torque. This reduces the starting current and increases $\cos\varphi$ [1, 2]. However, unsuccessful selection of the value of the additional resistance in the rotor circuit leads to a decrease in the starting electromagnetic torque. By changing the additional resistance in the rotor circuit, we can adjust the speed of rotation of the rotor down from the main one, although this method of regulation is uneconomical.

To ensure smooth acceleration during start, in addition to the active resistance, the inductance of a special design is sometimes included in the rotor circuit [3–8]. The inductive element can be connected both in series to the active one (Fig. 1) and in parallel. The reactor allows to provide smooth acceleration of the electric drive with a small number of sections of the rheostat, i.e. essentially acts as an automatic current regulator in the rotor and under certain conditions can ensure constant torque of the motor during start. As a result, the rotor current decreases more slowly than if there is only active resistance. In the case of a parallel connection between a resistor and an inductive coil at the beginning of the start, when the frequency of the current in the rotor is high, the current is mainly closed through the rheostat, which provides a sufficiently large starting torque. As the frequency decreases, the inductance decreases and the current is shorted through the inductive element.

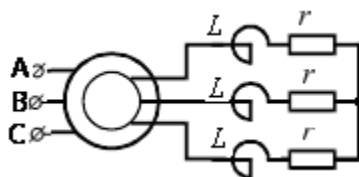


Fig. 1. Diagram of IM with a starting reactor in the wound-rotor circuit

The choice of a rational way to connect the active and inductive elements and their parameters can be made by mathematical modeling, the reliability of the results of which is determined by the adequacy of the mathematical model. In addition, to automate the process of IM start with the help of programmable microcontrollers, it is necessary to have analysis software that has a sufficiently high speed, does not require a significant amount of computation. Therefore, the development of methods and algorithms for calculating the starting processes in wound-rotor IMs is an urgent task.

Analysis of recent research. The task of developing an algorithm for starting equipment operation requires determining the laws of change of starting currents and electromagnetic torque during start. To do this, it is necessary to have appropriate mathematical models for calculating static characteristics, as well as dynamic modes, in particular transients, taking into account the law of change of the torque of loading. They are based on mathematical models of motors which determine the accuracy of the results of mathematical modeling, as well as computational methods that serve as a mathematical basis for obtaining calculation results and on which the speed of developed software depends.

Most methods of analysis of steady and dynamic modes of operation of squirrel-cage IMs are developed using substitution circuits with constant parameters, which are mostly used in known mathematical application codes. This approach is also applied to the development of mathematical models based on wound-rotor IMs [3-14]. Although such motors do not need to take into account the displacement of currents in the rotor winding due to the absence of the skin effect, the influence of scattering fluxes on the course of processes is significant [9]. The analytical method of calculating static characteristics in the phase coordinate basis developed in [13] makes it possible to consider asymmetric and non-sinusoidal processes, but the inductive parameters are assumed to be constant.

The saturation of the magnetic cores of modern motors causes nonlinear dependencies of the flux linkages of circuits on currents, so mathematical models developed on the assumption of linearity of electromagnetic connections do not provide the ability to calculate dynamic modes with the required accuracy. The linearization of electromagnetic connections in the vicinity of the operating point [6] does not solve the problem, because in a real machine the saturation varies widely, and therefore it is a priori impossible to determine.

In recent years, there have been models that take into account the saturation by only the main magnetic flux [11-14]. This significantly increases the accuracy of the calculation, however, these models are not accurate enough for the analysis of dynamic processes [13, 16, 17], because, as noted in [9, 24] studies must take into account the effect of magnetic saturation not only on the main path of the magnetic flux, but also on the paths of scattering fluxes, the influence of which on the course of processes is decisive. In [15] an experimental procedure for determining the parameters of the machine was adopted, but it is too expensive and impossible to do at the design stage.

To form the necessary mechanical characteristics of the wound-rotor IM, programmable microcontroller starting systems are used [3, 23, 24], the programming of which requires appropriate preliminary research by methods of mathematical modeling. Advances in starter

switching, electronic processing, and microprocessor control require robust control algorithms based on appropriate controller software.

Reliable information about the course of processes during start can be obtained only with the help of highly developed mathematical models of IMs, which adequately take into account the saturation of the magnetic core. Since the methods based on the calculation of the magnetic field [20] due to bulkiness are not suitable for controlling the process of IM start in real time, the optimal in terms of accuracy and complexity are circuit methods [18, 21, 23], in which electromagnetic parameters are calculated based on characteristics of magnetization of the motor magnetic core [25]. Software developed on their basis does not require significant computing resources, allows to perform calculations in real time and uses them to automate [24] both starting and other dynamic modes.

The goal of the paper is the development of mathematical models, methods for calculating static characteristics and dynamic modes of wound-rotor induction motors with various parameters of the starting device in the rotor circuit.

Presentation of main material. An important issue in the development of mathematical models of electric drives is their complexity and speed, which is crucial in the case of their use to control the process in real time. Therefore, it is important to choose the coordinate system to describe the electromagnetic connections in the IM, which depends on both the amount of calculations and the accuracy of the calculation results.

Most of the practically important problems of mathematical modeling of processes in IMs can be solved using transformed coordinate systems, which are based on the theory of image vectors [1, 18]. The calculation algorithms described in the paper use a system of orthogonal axes x, y [25], which rotate at arbitrary speed. For symmetrical modes of operation of the IM, it has the lowest amount of calculations and a fairly high accuracy of the calculation results.

Electromagnetic processes in the wound-rotor IM in the x, y axes are described by a system of four differential equations (DEs) of electrical equilibrium

$$\begin{cases} \frac{d\psi_{sx}}{dt} = \omega_0\psi_{sy} - r_s i_{sx} + u_{sx}; \\ \frac{d\psi_{sy}}{dt} = -\omega_0\psi_{sx} - r_s i_{sy} + u_{sy}; \\ \frac{d\psi_{rx}}{dt} = s\omega_0\psi_{ry} - (r_r + r_p) i_{rx}; \\ \frac{d\psi_{ry}}{dt} = -s\omega_0\psi_{rx} - (r_r + r_p) i_{ry}, \end{cases} \quad (1)$$

where $\psi_{sx}, \psi_{sy}, \psi_{rx}, \psi_{ry}, i_{sx}, i_{sy}, i_{rx}, i_{ry}$ are the flux linkages and currents of the converted circuits of the stator (index s) and rotor (index r); r_s, r_r are the active resistances of these circuits; r_p is the resistance of the

rheostat phase in the rotor circuit; ω_0 is the cyclic frequency of the supply voltage; s is the rotor sliding.

In equations (1), the parameters of the rotor winding are reduced to the stator winding according to the generally accepted method [19]. In addition, we will consider the image vector of the stator winding voltage \vec{U} aligned with the x -axis, i.e. we take $u_{sx} = U_m$, and $u_{sy} = 0$.

To calculate the process of the IM start, it is necessary to supplement the DE system (1) with the equation of rotor dynamics:

$$\frac{ds}{dt} = -\frac{p_0}{J\omega_0} \left(\frac{3}{2} p_0 (\psi_{sx} i_{sy} - \psi_{sy} i_{sx}) - M_c(t) \right), \quad (2)$$

where p_0 is the number of pole pairs of the IM; J is the reduced to the motor shaft moment of inertia of the electric drive system; M_c is the torque of loading on the motor shaft.

The DE system (1) together with (2) makes it possible to calculate the transient during the IM start. To do this, it is necessary to integrate it numerically under zero initial conditions, calculating at each step of integration the matrix of differential inductances as elements of the Jacobi matrix and the vector of flux linkages [25].

The flux linkage of each circuit consists of flux linkage with the main magnetic flux and with the scattering fluxes, and the flux linkage of the scattering of the stator circuits and the rotor circuits are mutually independent. Therefore, in order to take into account the inductance of the reactor in the rotor circuit, the equations for flux linkages of the rotor circuits can be represented as

$$\begin{aligned} \psi_{rx} &= \psi_{\delta rx} + (L_{\sigma r} + L_p) \cdot i_{rx}; \\ \psi_{ry} &= \psi_{\delta ry} + (L_{\sigma r} + L_p) \cdot i_{ry}, \end{aligned}$$

where $\psi_{\delta rx}, \psi_{\delta ry}$ are the flux linkages of the respective rotor circuits due to the main magnetic flux; $L_{\sigma r}$ is the scattering inductance of the rotor circuits, which is determined from the magnetization characteristics of the scattering fluxes of the rotor winding, calculated on the basis of the geometry of the motor magnetic core [19]

$$\psi_{\sigma r} = \psi_{\sigma r}(i_r); \quad i_r = \sqrt{i_{rx}^2 + i_{ry}^2}, \quad (3)$$

where L_p is the inductance of the reactor in the rotor circuit, which is determined by the appropriate design formulas.

It is impossible to choose the parameters of the reactor and code the starting and regulating device based on the calculation of the transient. This problem requires the calculation and analysis of static characteristics, which can be calculated using equations (1) of electrical equilibrium. Having chosen on the basis of calculation of static characteristics resistive and inductive parameters of the starting device and the law of their change according to time dependence of the torque of loading $M_c = M_c(t)$, we carry out calculation of time dependencies of

coordinates by numerical integration of nonlinear DE system (1), (2).

Consider the algorithm for calculating static characteristics. In the steady-state mode of IM operation sliding s , the DE system of electromagnetic equilibrium (1) is reduced to a system of nonlinear algebraic equations, which in order to present the algorithm for calculating the steady-state are written in the form of the vector DE

$$\bar{Q}(\bar{Y}(\bar{I}_{xy})) = \Omega_{xy} \bar{\Psi}_{xy} + R_{xy} \bar{I}_{xy} - \bar{U}_{xy}, \quad (4)$$

where $\bar{\Psi}_{xy} = (\psi_{sx}, \psi_{sy}, \psi_{rx}, \psi_{ry})^*$; $\bar{I}_{xy} = (i_{sx}, i_{sy}, i_{rx}, i_{ry})^*$; $\bar{U}_{xy} = (U_m, 0, 0, 0)^*$ are the vectors of flux linkages, circuit currents and voltages applied to them;

$$R_{xy} = \begin{bmatrix} r_s & 0 & 0 & 0 \\ 0 & r_s & 0 & 0 \\ 0 & 0 & r_r + r_p & 0 \\ 0 & 0 & 0 & r_r + r_p \end{bmatrix}$$

is the matrix of active resistances of circuits;

$$\Omega_{xy} = \begin{bmatrix} 0 & -\omega_0 & 0 & 0 \\ \omega_0 & 0 & 0 & 0 \\ 0 & 0 & 0 & -s\omega_0 \\ 0 & 0 & s\omega_0 & 0 \end{bmatrix}$$

is the auxiliary matrix in which ω_0 is the cyclic frequency of supply voltage.

Since the flux linkage vector $\bar{\Psi}_{xy}$ is determined by a set of circuit currents, unknown in the system of finite equations (4) is the current vector \bar{I}_{xy} , which can be used to determine the flux linkage, electromagnetic torque, etc. Since equation (4) includes the coordinates U_m, s, r_p, L_p , we can assume that the vector of currents is a function of these coordinates

$$\bar{I}_{xy} = \bar{I}_{xy}(\bar{U}_{xy}, s, r_p, L_p).$$

Equation (4) makes it possible to investigate the influence of each of these coordinates on the value of the current vector \bar{I}_{xy} , i.e. to calculate the multidimensional static characteristic as the dependence of the current vector components on a given coordinate. To do this, we must change this coordinate within the specified limits as a parameter, leaving the others unchanged. Obviously, here there is a problem of solving nonlinear systems of finite equations, and since system (4) is nonlinear due to the saturation of the magnetic core, it can be solved by one of the numerical methods, in particular, Newton method.

According to Newton iterative method, the $(k+1)$ -th approximation of the vector \bar{Y} is determined by the formula

$$\bar{Y}^{(k+1)} = \bar{Y}^{(k)} + \Delta \bar{Y}^{(k)}, \quad (5)$$

where $\Delta \bar{Y}^{(k)}$ is the increment of the vector $\bar{Y}^{(k)}$, which at each step is determined from a linear system of equations

$$J \Delta \bar{Y}^{(k)} = -\bar{Q}(\bar{Y}^{(k)}), \quad (6)$$

in which $\bar{Q}(\bar{Y}^{(k)})$ is the value of the residual vector \bar{Q} at $\bar{Y} = \bar{Y}^{(k)}$; J is the Jacobi matrix of vector function (4).

Due to the fact that the flux linkages of the IM circuits consist of flux linkages due to the main magnetic flux ψ_δ and scattering flux linkages ψ_σ together with the flux linkage ψ_p of the reactor

$$\begin{cases} \omega_0 \psi_{sx} = \omega_0 \psi_\delta x + x_{\sigma s} i_{sx}; \\ \omega_0 \psi_{sy} = \omega_0 \psi_\delta y + x_{\sigma s} i_{sy}; \\ \omega_0 \psi_{rx} = \omega_0 \psi_\delta x + (x_{\sigma r} + x_p) i_{rx}; \\ \omega_0 \psi_{ry} = \omega_0 \psi_\delta y + (x_{\sigma r} + x_p) i_{ry}; \end{cases} \quad (7)$$

the Jacobi matrix is determined by the formula

$$J = X_\delta + X_\sigma + R_{xy}, \quad (8)$$

where

$$X_\delta = \begin{bmatrix} x_{systx} & x_{systy} & x_{syrtx} & x_{syry} \\ -x_{sxsx} & -x_{sxsy} & -x_{sxrx} & -x_{sxry} \\ sx_{rysx} & sx_{rysy} & sx_{ryrx} & sx_{ryry} \\ -sx_{rysx} & -sx_{ryxy} & -sx_{rxrx} & -sx_{rxry} \end{bmatrix};$$

$$\bar{X}_\sigma = \begin{bmatrix} x_{\sigma s} & 0 & 0 & 0 \\ 0 & -x_{\sigma s} & 0 & 0 \\ 0 & 0 & s(x_{\sigma r} + x_p) & 0 \\ 0 & 0 & 0 & -s(x_{\sigma r} + x_p) \end{bmatrix}.$$

As can be seen from (8), the elements of the Jacobi matrix are the own and mutual differential inductances of the IM circuits. They are determined according to [25]. In addition, to calculate the electromagnetic torque, it is necessary to determine the flux linkage of the circuits in accordance with the selected coordinate system.

Newton iterative method has quadratic convergence, but requires an initial approximation, which lies around attraction. The following algorithm is used to determine it.

Given the value of sliding $s = 1.0$ and the parameters r_p, L_p equal to zero, we increase in 5–10 steps in proportion to the parameter ε ($0 < \varepsilon \leq 0$) from zero to the nominal value of the applied voltage $U = \varepsilon U_m$. This makes it possible to ensure the convergence of the iterative process at every step. The resulting value of the components of the vector \bar{I}_{xy} serves as the initial conditions for calculating the static characteristics. Given a number of sliding values s of the rotor, we can obtain a multidimensional static characteristic in the form of the dependence of the coordinates on the sliding. However, the calculation of any static characteristic can be done by a differential method. To do this, we differentiate equation (4) by one of the coordinates ($\lambda = s, r_p, L_p$) as a

parameter of the required characteristic. As a result, we obtain the DE of the argument λ

$$J \frac{d\vec{I}_{xy}}{d\lambda} = \frac{\partial \vec{Q}}{\partial \lambda}, \quad (9)$$

in which the Jacobi matrix is the same as in (6).

Equation (9) for different independent coordinates of the static characteristic differs only in the vector of the right parts. In particular, for the coordinates s , r_p , x_p they have the form

$$\frac{\partial \vec{Q}}{\partial s} = \begin{bmatrix} 0 \\ 0 \\ \omega_0 \psi_{ry} \\ -\omega_0 \psi_{rx} \end{bmatrix}; \quad \frac{\partial \vec{Q}}{\partial r_p} = \begin{bmatrix} 0 \\ 0 \\ -i_{rx} \\ -i_{ry} \end{bmatrix}; \quad \frac{\partial \vec{Q}}{\partial x_p} = \begin{bmatrix} 0 \\ 0 \\ -i_{rx} \\ -i_{ry} \end{bmatrix}.$$

As a result of integrating the nonlinear DE system (9) by one of the numerical methods on s we obtain a multidimensional characteristic in the form of dependencies of the set of coordinates of the vector \vec{I}_{xy} on the chosen independent coordinate, using which we obtain dependencies of flux linkages, electromagnetic torque and so on.

Figures 2–4 show examples of calculation of the static characteristics of the wound-rotor IM ($P_N = 250$ kW, $U = 380$ V, $I = 263$ A, $n_N = 1000$ rpm).

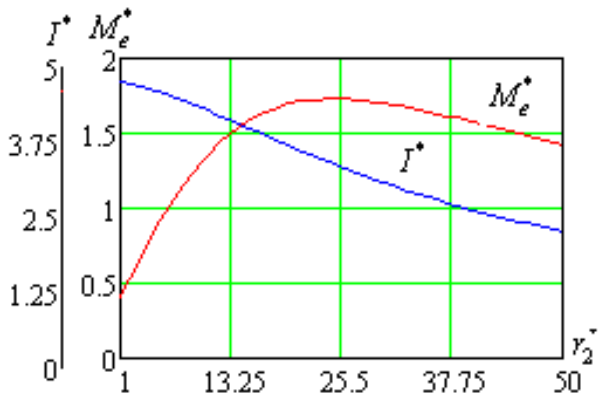


Fig. 2. Dependencies of current (I^*) and electromagnetic torque (M_e^*) in relative units on the active resistance in the rotor circuit when sliding $s = 1.0$

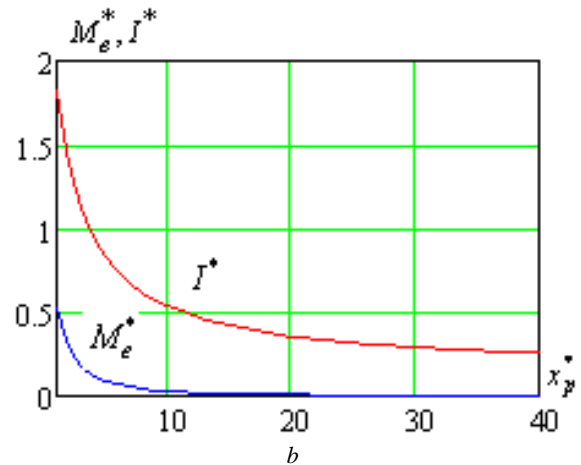
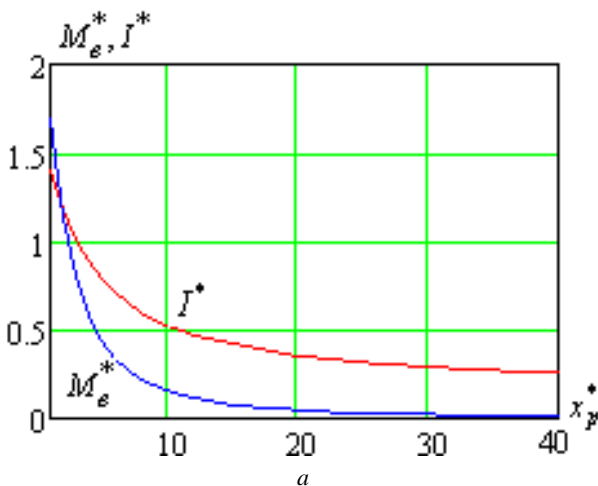


Fig. 3. Dependencies of relative values of current (I^*) and electromagnetic torque (M_e^*) at $s = 1.0$ on relative value $x_p = x_r / x_{2\sigma}'$ of inductance in the rotor circuit and different values of the multiplicity of the active reactance of the reactor: a) – 1.0; b) – 10.0

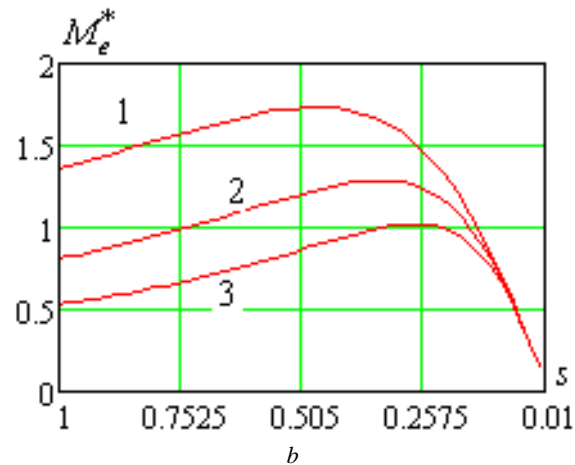
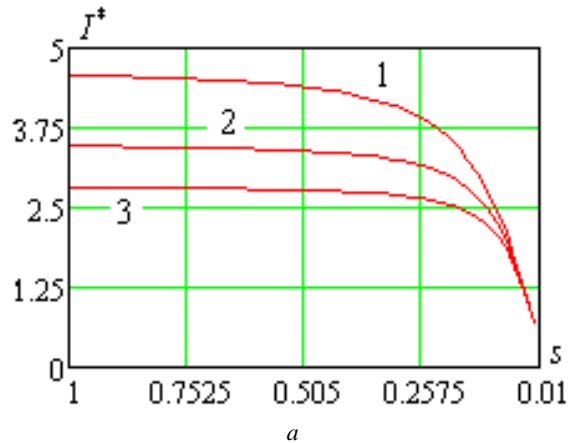


Fig. 4. Static starting characteristics with three values of inductance in the rotor circuit and two relative values of active resistances: a) – 3.9; b) – 11.7

Presented curves serve only as an illustration of the possibility of developed calculation algorithms. It is obvious that, having chosen one of the parameters of the starting and regulating device, it is necessary to calculate

the mechanical characteristic, and each value of active resistance corresponds to its mechanical characteristic, which in turn depends on the inductance of the reactor. Since the resistance of the inductive coil depends on the frequency of the current in the rotor, which is variable during start, its correctly selected parameters have a positive effect on the value of the starting current, automatically reducing its value.

Conclusions.

Unlike squirrel-cage induction motors, less attention is paid to wound-rotor motors in the technical literature, although the wound rotor allows for more diverse mechanical characteristics, which is important for electric drives with difficult starting conditions.

The calculation methods developed in the paper allow utilization of mathematical modeling methods to analyze static starting characteristics and transients of wound-rotor IMs with different laws of regulation of starting device parameters in rotor winding in order to provide the necessary law of electromagnetic torque change.

The calculation code is based on a mathematical model of the IM, which uses the real characteristics of the magnetization by the main magnetic flux and the scattering fluxes of the stator and rotor windings, which allows to adequately take into account the saturation of the magnetic core which ensures the accuracy of the calculation results.

The described methods of calculation of modes and characteristics in orthogonal coordinate axes x , y allow to perform modeling with a minimum amount of calculations and, accordingly, the cost of CPU time, which allows to use them to control the electric drive system in dynamic modes in real time.

Conflict of interest. The authors of the paper state that there is no conflict of interest.

REFERENCES

1. Chorny O.P., Tolochko O.I., Tytiuk V.K., Rodkin D.Y., Chekavskiy H.S. *Matematychni modeli ta osoblyvosti chyselnykh rozrakhunkiv dynamiky elektropryvodiv z asynkhronnyimi dvyhunamy: monohrafiia* [Mathematical models and features of numerical calculations of dynamics of electric drives with induction motors: monograph]. Kremenchuk, PE Shcherbatykh O.V. Publ., 2016. 302 p. (Ukr).
2. Veshenevskiy S.N. *Kharakteristiki dvigatelei v elektroprivode* [Characteristics of motors in the electric drive]. Moscow, Energy Publ., 1977. 432 p. (Rus).
3. Meshcheriakov V.N., Morozov S.V., Telychko L.Ia. Calculation of induction resistance parameters for a wound-rotor induction motor. *Izvestia of the USSR Higher Educational Institutions. Electromechanics*, 1989, no. 3, pp. 50-52. (Rus).
4. Kyrychek H.M. Induction resistances in the rotor circuit of a two-speed induction motor. *Technical Electrodynamics*, 1979, no. 1, pp. 52-56. (Rus).
5. Golovan V.I. Mathematical formulation of the problem of induction motor system synthesis with inductive resistance in the rotor circuit. *Technical Electrodynamics, special issue*, 2002, part 4, pp. 37-42. (Rus).
6. Golovan V.I. *Asynkhronnyi dvigatel' s induktsionnym soprotivleniem v tsepi faznogo rotora: monografiia* [Induction motor with induction resistance in the phase rotor circuit]. Chernivtsi, Prut Publ., 2000. 160 p. (Ukr).
7. Golovan V.I., Golovan I.V. Automated design of induction resistance of an induction motor. *Technical Electrodynamics, special issue*, 2000, part 5, pp. 100-105. (Rus).
8. Golovan V.I., Golovan I.V. Resource-saving aspects in the development of technical solutions for induction motors with induction rheostat in the rotor circuit. *Electrical Engineering & Electromechanics*, 2003, no. 2, pp. 19-23. (Ukr).
9. Hany M. Jabr, Narayan C. Kar. Leakage flux saturation effects on the transient performance of wound-rotor induction motors. *Electric Power Systems Research*, 2008, vol. 78, no. 7, pp. 1280-1289. doi: <https://doi.org/10.1016/j.epsr.2007.11.004>.
10. Hilmi F. Ameen. Computer Simulation and Mathematical Modelling of Static Rotor Resistance Chopper Control of WRIM by Reference Frame Theory. *Procedia Computer Science*, 2011, vol. 3, pp. 1009-1017. doi: <https://doi.org/10.1016/j.procs.2010.12.166>.
11. Joksimovic G. Modelling and analysis of series-connected wound rotor induction motor. *2008 18th International Conference on Electrical Machines*, 2008, pp. 1-5. doi: <https://doi.org/10.1109/ICELMACH.2008.4800247>.
12. Omel'chenko E.Y. Mathematical model of the wound-rotor three-phase induction motor. *Russian Electrical Engineering*, 2007, vol. 78, no. 11, pp. 580-585. doi: <https://doi.org/10.3103/S1068371207110041>.
13. Omelchenko E.Y., Telezhkin O.A., Enin S.S., Tanich V.O. Computer Model of a Synchronized Asynchronous Motor. *Procedia Engineering*, 2015, vol. 129, pp. 629-634. doi: <https://doi.org/10.1016/j.proeng.2015.12.082>.
14. Rozov Yu.M., Tyhunov A.P. *Metodicheskie rekomendatsii po raschetu asynkhronnogo dvigatel'ia s induktsionnym rotornym soprotivleniem* [Methodical recommendations for the calculation of an induction motor with induction rotor resistance]. AS of the USSR. Institute for Problems of Modeling in Power Engineering. Naukova Dumka Publ., Kyiv, 1981. 52 p. (Rus).
15. Vlasov V.G. Experimental studies and methods of calculation of induction motors with induction resistance in the rotor circuit. *Electrical industrial. Series «Electric Drive»*, 1967, no. 293, pp. 3-6. (Rus).
16. Al-Jufout S., Khandakji K. Dynamic simulation of starting and chopper speed control of wound-rotor induction motor. *International Journal of Simulation: Systems, Science & Technology*, 2007, vol. 8, no. 2, pp. 1-7.
17. Yahaya A.E., Adamu M.Z., Paul O.A.-A., Isah A.A. Analysis of power flow and torque of asynchronous induction motor equivalent circuits. *International Journal of Advanced Scientific and Technical Research*, 2013, vol. 3, no. 6, pp. 713-732.
18. Tytiuk V., Baranovska M., Rozhnenko Z., Chorny O., Burdilna E., Kobylanskyi B. Application of the generalized electromechanical converter theory to analysis of the static characteristics of an induction motor. *Electromechanical and Energy Saving Systems*, 2020, vol. 2, no. 50, pp. 16-24. (Rus). doi: <https://doi.org/10.30929/2072-2052.2020.2.50.16-24>.
19. Kopylov I.P., Goryainov F.A., Klokov B.K. *Proektirovanie elektricheskikh mashin* [Electrical machines designing]. Moscow, Energy Publ., 1980. 496 p. (Rus).
20. Milykh I.I., Polyakova N.V. Determination of electromagnetic parameters of electric machines based on numerical calculations of magnetic fields. *Electrical Engineering & Electromechanics*, 2006, no. 2, pp. 40-46.

21. Malyar V., Hamola O., Maday V., Vasylchyshyn I. Mathematical modeling start-up and steady state modes of asynchronous motors operation with capacitive compensation of reactive power. *Przeglad Elektrotechniczny*, 2020, vol. 96, no. 11, pp. 109-114. doi: <https://doi.org/10.15199/48.2020.11.22>.
22. Mengoni M., Rizzoli G., Zarri L., Tani A., Amerise A., Serra G. Control of a Three-Phase Wound-Rotor Induction Motor Drive for Automation Applications. *2019 IEEE International Electric Machines & Drives Conference (IEMDC)*, 2019, pp. 1267-1272. doi: <https://doi.org/10.1109/IEMDC.2019.8785281>.
23. Meshcheryakov V.N., Muravyev A.A., Boikov A.I., Pikalov V.V. The Soft Starting System for an Induction Motor with an Induction Resistance in the Wound Rotor Circuit. *2019 International Multi-Conference on Industrial Engineering and Modern Technologies (FarEastCon)*, 2019, pp. 1-5. doi: <https://doi.org/10.1109/FarEastCon.2019.8934280>.
24. Telezhkin O.A. *Razrabotka avtomatizirovannogo elektroprivoda blochnogo stana grubogo volocheniia na osnove sinkhronizirovannogo asinkhronnogo dvigatel'ia: avtoref. dis.* [Development of automated electric drive for block coarse-drawing mill based on synchronized induction motor. Cand. tech. sci. diss.]. Magnitogorsk, MSTU Publ., 2018. 20 p. (Rus).
25. Fil'ts R.V. *Matematicheskie osnovy teorii elektromekhanicheskikh preobrazovatelei* [Mathematical foundations of the theory of electromechanical transducers]. Kyiv, Naukova dumka Publ., 1979. 208 p. (Rus).

Received 10.01.2022

Accepted 09.03.2022

Published 01.06.2022

V.S. Malyar¹, Doctor of Technical Science, Professor,
 O.Ye. Hamola¹, PhD, Associate Professor,
 V.S. Maday¹, PhD, Associate Professor,
 I.I. Vasylchyshyn¹, PhD, Associate Professor,
¹ Lviv Polytechnic National University,
 12, Bandera Str., Lviv, 79013, Ukraine,
 e-mail: vasyi.s.maliar@lpnu.ua,
 orest.y.hamola@lpnu.ua (Corresponding author),
 volodymyr.s.madai@lpnu.ua,
 ivanna.i.vasylchyshyn@lpnu.ua

How to cite this article:

Malyar V.S., Hamola O.Ye., Maday V.S., Vasylchyshyn I.I. Mathematical modeling of rheostat-reactor start of wound-rotor induction motors. *Electrical Engineering & Electromechanics*, 2022, no. 3, pp. 8-14. doi: <https://doi.org/10.20998/2074-272X.2022.3.02>

T.H. Panchal, A.N. Patel, R.M. Patel

Reduction of cogging torque of radial flux permanent magnet brushless DC motor by magnet shifting technique

Introduction. In spite of many advantages of radial flux permanent magnet brushless DC motors it suffers from the distinct disadvantage of high cogging torque. The designer must emphasize to reduce the cogging torque during the design stage. This paper introduces magnet shifting technique to mitigate cogging torque of surface mounted radial flux brushless DC motor. **Methodology.** Initially 200 W, 1000 rpm surface mounted radial flux permanent magnet brushless DC motor is designed with symmetrical placement of permanent magnets with respect to each other on rotor core. Cogging torque profile of this initial motor is obtained by performing finite element modelling and analysis. **Originality.** This design has been improved by shifting the position of permanent magnets with respect to adjacent permanent magnets. The effect of magnet shifting on cogging torque has been analyzed by performing finite element analysis. **Results.** It has been examined that the peak to peak cogging torque is decreased from 1.1 N-m to 0.6 N-m with shifting of permanent magnets respectively. References 19, tables 2, figures 11.

Key words: cogging torque, finite element analysis, magnet shifting, permanent magnet brushless DC motor.

Вступ. Незважаючи на багато переваг безщіткових двигунів постійного струму з радіальним магнітним потоком, вони мають явний недолік, що полягає у високому крутному моменті зубчатої передачі. Проективальник повинен зосередитись на зниженні крутного моменту зубчатої передачі на етапі проектування. У цій статті представлена методика зсуву магніту для зменшення крутного моменту зубчатої передачі безщіткового двигуна постійного струму з радіальним потоком, встановленого на поверхні. **Методологія.** Спочатку безщітковий двигун постійного струму з радіальним магнітним потоком потужністю 200 Вт, 1000 об/хв спроектований із симетричним розміщенням постійних магнітів відносно один одного на сердечнику ротора. Розподіл крутного моменту зубчатої передачі цього початкового двигуна отриманий шляхом аналізу методом скінчених елементів (МСЕ). **Оригінальність.** Ця конструкція була вдосконалена за рахунок зсуву положення постійних магнітів по відношенню до сусідніх постійних магнітів. Вплив зсуву магніту на крутний момент зубчатої передачі було проаналізовано за допомогою аналізу МСЕ. **Результати.** Досліджено, що піковий крутний момент зубчатої передачі зменшився з 1,1 Н-м до 0,6 Н-м, відповідно, при зсуві постійних магнітів. Бібл. 19, табл. 2, рис. 11.

Ключові слова: крутний момент зубчатої передачі, аналіз методом скінчених елементів, зсув магніту, безщітковий двигун постійного струму з постійними магнітами.

Introduction. Permanent magnet brushless DC (PMBLDC) motors exhibit superior performance in comparison to conventional motors. They are inherently efficient, compact and having wide speed range and fast dynamic response [1, 2]. Because of the advancement in permanent magnet (PM) materials and semiconductor technology, PMBLDC motors have found various applications demanding precise speed and position control. This type of motors has potential to become workhorse of many industrial applications due to its attractive features. Noticeable torque ripple is one of the important limitations of PMBLDC motor. Vibration and acoustic noise is introduced by the torque ripple in the drive system which deteriorates overall performance. Torque ripple is high due to cogging torque and non-ideal commutation of exciting currents. Torque ripple can be reduced with decrease in cogging torque and modification in excitation pattern. Any modification in excitation pattern usually results into a reduction in efficiency. It is highly desirable to reduce cogging torque of permanent magnet motor during design to reduce torque ripple. Cogging torque is innate in PM motors due to presence of permanent magnets and slotted stator. Interaction between rotor PM magnetomotive force and slot reluctance originates cogging torque. Due to this interaction, the PMs constantly seek a position with low reluctance. The cogging torque does not depend on stator current which means that it occurs even though the stator winding is unexcited.

Reduction of cogging torque is of utmost importance as it improves the torque quality. Improvement in torque quality makes them suitable in various torque sensitive

applications. Various methods are proposed in literature for cogging torque reduction of radial flux PMBLDC motor viz. skewing of either stator or rotor, magnet pole arc variation, shifting of slot opening, teeth notching, unequal teeth width, magnet shaping and sizing, pole arc to pole pitch ratio, fractional pole pairs, number of slots/pole, addition of dummy slots, variation in air-gap length, magnet pole shaping, lowering magnet flux density, choosing proper thickness of stator teeth tips, variation in width of slot opening, etc. [3-18]. Skewing of either stator or rotor results in undesirable axial thrust. Skewing of stator slot increases length of conductors thus increases copper losses. Also winding becomes difficult to wind. Skewing of PMs and/or stator slots increases manufacturing complexity and production cost. Step skew of PMs also increases manufacturing complexity. To eradicate the cogging torque by skewing, the skewing angle should be one slot pitch. The cogging torque can be decreased by varying the magnet pole arc width. It is found that PM covers almost « m » times that of slot pitch chosen, where « m » is an integer. Generally, the pole pitch of $(m + 0.17)$ or $(m + 0.14)$ produces minimum cogging torque. A small variation in pole arc width results in considerable reduction in cogging torque. The cogging torque harmonic components can be diminished by notching the stator teeth i.e. incorporation of dummy slots in stator teeth. Addition of dummy slot increases the frequency of interaction between slot and salient poles. This reduces the magnitude of cogging torque. However, introduction of notches removes some material from

© T.H. Panchal, A.N. Patel, R.M. Patel

stator teeth and gives rise to saturation. Hence, this technique is not appropriate for minimization of cogging torque. The cogging period is given by one complete mechanical revolution divided by least common multiple of stator slots number N_s and rotor poles number N_p . The peak amplitude of cogging torque reduces as the frequency of cogging cycles increases. The cogging torque decreases considerably as number of stator slots increases minutely thus resulting in fractional slot pitch. The distance between stator slot and PM denotes to length of air-gap. The length of air-gap is different as the size of the motor changes. The recommended length of air-gap range for very small size motor is 0.12 – 0.25 mm, medium size motor is 0.38 – 0.5 mm, and large motor is, 0.63 – 0.88 mm. The cogging torque can be decreased by increasing length of air-gap thus reducing $dR/d\theta$. However, increase in air-gap length decreases the air-gap flux Φ_g thus lowering the magnitude of cogging torque further. To keep Φ_g constant, the width of magnet pole arc is required to be increased. The rate of change of flux density at magnet edges affects the cogging torque. Thus, shaping the magnet edges lowers the magnitude of cogging torque. The cogging torque can be decreased by reducing the air gap flux density. This can be done by changing the grades of PM material. The width of stator teeth influences the cogging torque. If the stator teeth tips are too thin, saturation is established in it which increases cogging torque. The width of slot opening and thickness of stator teeth tips should be equal. Cogging torque is also affected by the slot opening width. If the width of slot opening is decreased, the rate of change of permeance between PM and stator teeth is reduced. This lowers magnitude of cogging torque.

The aim of this paper is to present a magnet shifting technique which reduces cogging torque of surface mounted radial flux permanent magnet brushless DC motors.

Magnet shifting technique is relatively easy to implement hence it has better feature as far as manufacturability is concerned. There is no adverse implication on initial cost of motor as cost of PM remains unchanged. Lower order harmonics have been suppressed on account of shifting of magnets from its original position. Magnets are placed accordingly with an objective of harmonic suppression of cogging torque. Initially, the basics of cogging torque and reference design of radial flux PMBLDC motor is discussed. Thereafter, the magnet shifting technique used to decrease cogging torque of initially designed motor is explained. Thereafter, Improved design of PMBLDC motor incorporating magnet shifting technique, simulation results and analysis have been presented. At the end, Conclusion of this paper is presented

Basics of cogging torque. Following equation expresses the cogging torque and factors affecting it

$$T_{cog} = -\frac{1}{2} \cdot \Phi_g^2 \cdot \frac{dR}{d\theta_m}, \quad (1)$$

where Φ_g is the flux crossing air-gap; R is the reluctance of gap; θ_m is the angular displacement of rotor.

The cogging torque has zero average value and generated by propensity of PMs to align with stator teeth. There is periodical variation of air gap reluctance which makes cogging torque to vary periodically. Fourier series expresses cogging torque as under,

$$T_{cog} = \sum_{i=1}^{\infty} T_{jk} \cdot \sin(j \cdot k \cdot \theta), \quad (2)$$

where j is the least common multiple of number of slots (N_s) and poles (N_p); $i = 1, 2, 3, \dots$; T_{jk} is the coefficient of Fourier series.

In one mechanical revolution of rotor, cogging torque has j periods and N_s and N_p are directly related with it [19].

Equation (1) depicts that elimination of cogging torque can be achieved either by forming Φ_g zero or by forcing $dR/d\theta_m$ zero. It is not practical to reduce magnetic flux since it affects the torque productivity which is required to drive the motor. Hence, cogging torque can be reduced adequately with design modification because of air-gap reluctance variation. It is practically impossible to completely eliminate cogging torque.

Equation (2) shows that the cogging torque can be characterized as a Fourier series and is superposition of all sinusoidal harmonic components. In PM motors without any cogging torque reduction techniques, each magnet pole's cogging torque is added. This happens because each magnet pole is symmetrically placed with respect to the stator slots. The torque due to each PM is cophasel torque due to adjacent PM. Because of this, there is summation of each magnet pole's harmonic components. If the PM motor is designed such that cogging torque of magnet poles are out of phase with respect to others, some of the harmonic components of (2) are cancelled out. This results in to decrement of cogging torque of PM motors.

Reference design of radial flux PMBLDC motor.

The surface mounted PMBLDC motor of 200 W, 1000 rpm is analytically designed and is considered as reference motor for the analysis. The sizing of reference PMBLDC motor is carried out by assuming various design variables i.e. specific magnetic and electric loadings, stator current density, flux densities of stator and rotor cores, space factor, stacking factor, winding factor etc. Design variables are assumed considering performance requirements and availability of materials.

Cross sectional view of reference PMBLDC motor is shown in Fig. 1,a. The rotor poles are made of high energy NdFeB permanent magnet material of grade N42. Figure 1,b shows the design of surface mounted four pole rotor reference design. The design information of reference motor has been presented in Table 1.

Finite element (FE) analysis has been performed to attain cogging torque versus rotor angle characteristic of reference motor. The model of reference motor is prepared using FE software according to the calculated dimensions and appropriate materials are assigned to different sections of the motor. The waveform is obtained by rotating the rotor for discrete positions of 1° mechanical each and cogging torque values are obtained up to 15° . Figure 2 shows the cogging torque profile of reference motor. It is observed that reference PMBLDC motor has cogging torque (peak-to-peak, p-p) of 1.1 N-m.

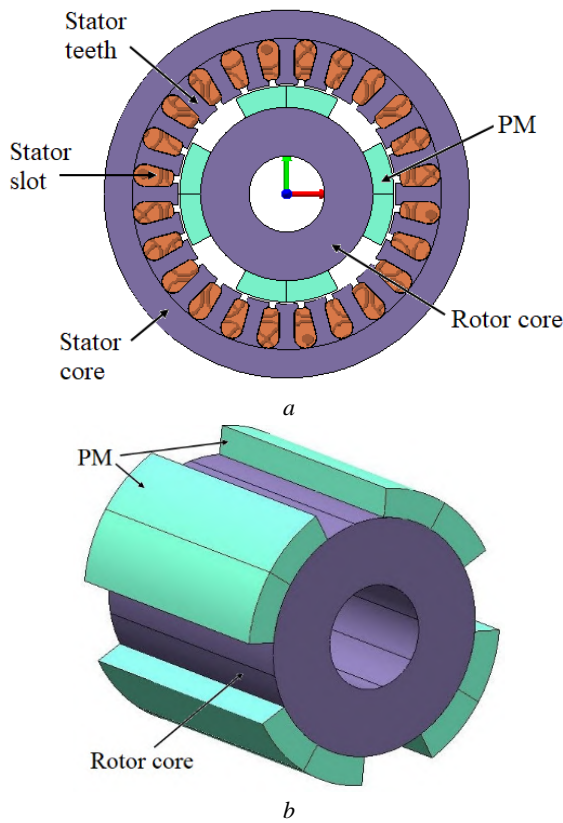


Fig. 1. Reference radial flux PMBLDC motor: a – cross sectional view; b – 3-D view of rotor

Table 1
Design information of radial flux PMBLDC motor

Design parameter	Value
Outer diameter of stator, mm	87
Outer diameter of rotor, mm	51
Axial length, mm	50
Inner diameter of stator, mm	52
No. of stator slots	24
No. of phases	3
No. of rotor poles	4
No. of slots/pole/phase	2
PM thickness, mm	5
Air-gap length, mm	0.5
Type of PM	NdFeB
Stator core material	M19
Rotor core material	M19

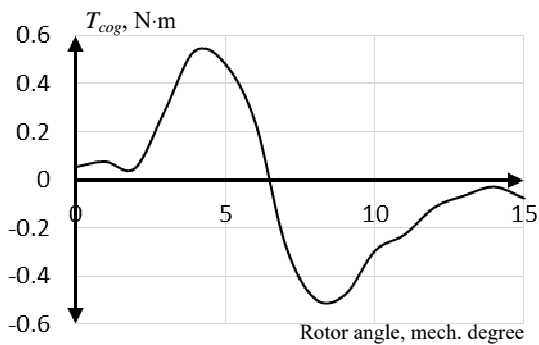


Fig. 2. Cogging torque versus rotor angle characteristic of reference PMBLDC motor

The average torque developed by the motor has been determined with 2-D FE analysis. Series of

2-D transient simulations have been performed. In this analysis, the rotor is rotated at rated speed of 1000 rpm and the stator winding is energized by appropriate switching of inverter switches. The value of electromagnetic torque at discrete rotor positions are obtained and plotted against these rotor positions. Figure 3 shows torque profile of reference motor. The average torque obtained using FE analysis is 1.91 N·m.

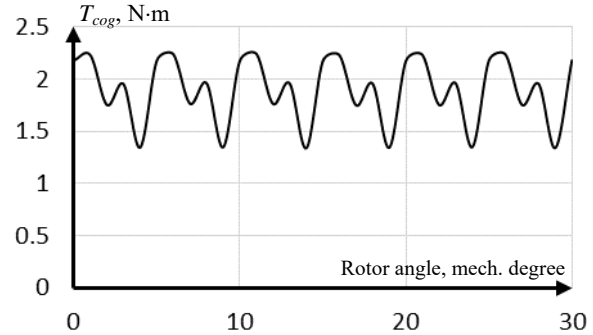


Fig. 3. Average torque profile of reference PMBLDC motor

Magnet shifting technique. The cogging torques due to each magnet pole are in phase in PM motor and thus all of them are added. This results into substantial cogging torque effect. To reduce this summative effect, placement of PMs can be shifted in comparison to adjacent PM so that cogging torque of adjacent magnets is out of phase with each other. Figure 4 shows surface magnet rotor with PM shifted by θ_0 .

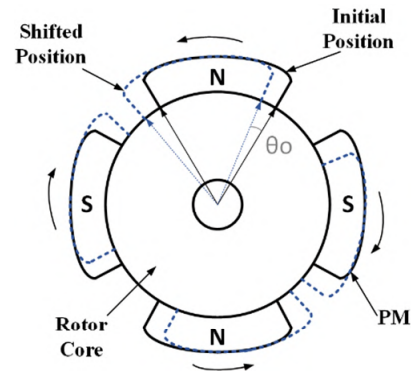


Fig. 4. Shifting of PM in surface mounted radial flux PMBLDC motor

The cogging torque influence of each PM is given by

$$T_{cog} = \sum_{i=1}^{\infty} T_{PN_i} \cdot \sin(N_s \cdot i \cdot \theta), \quad (3)$$

where T_{PN_i} is the per magnet coefficient;

$$T_{cog} = N_p \cdot \sum_{i=1}^{\infty} T_{PN_i} \cdot \sin(N_s \cdot i \cdot \theta), \quad (4)$$

which is equivalent to that given by (2) and rewritten as

$$T_{cog} = \sum_{i=1}^{\infty} T_{N_i} \cdot \sin(N_s \cdot i \cdot \theta). \quad (5)$$

Cogging torque produced by each magnet is in phase with the adjacent magnet hence it is imperative that each magnet's position can be shifted with respect to the adjacent one. The sum of all cogging torques from each magnet gives net cogging torque in the motor and is given by

$$T_{cog} = \sum_{k=0}^{N_p-1} \sum_{i=1}^{\infty} T_{PN_{si}} \cdot \sin(N_s \cdot i \cdot (\theta - k \cdot \theta_o)), \quad (6)$$

where θ_o is the angle through which each PM is shifted in comparison to adjacent PM.

The net cogging torque is reduced to

$$T_{cog} = \sum_{i=1}^{\infty} T_{N_s N_p i} \cdot \sin(N_s \cdot N_p \cdot i \cdot \theta). \quad (7)$$

Harmonics other than multiples of N_p^{th} are cancelled, hence reducing the cogging torque.

Improved design using magnet shifting technique. The design is improved with application of magnet shifting technique to 200 W, 1000 rpm PMBLDC motor. The rotor of initial design is shown in Fig. 5,a and rotor of improved design with magnet shifting technique is shown in Fig. 5,b. Series of simulation exercise have been performed with FE technique to obtain cogging torque profile with relative magnet shifting from 1° to 3°.

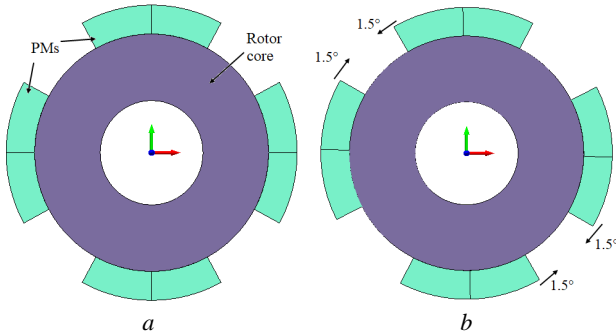


Fig. 5. Sectional view of rotor (a) reference design with regular PMs (b) improved design with shifted PMs

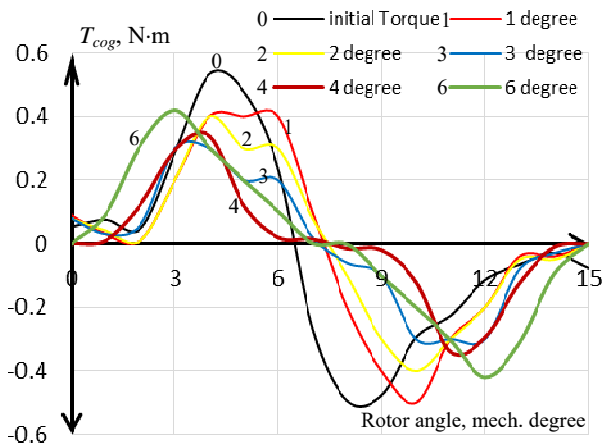


Fig. 6. Comparison between cogging torque profiles of reference design and improved design

The reference design of PMBLDC motor has cogging torque (p-p) of 1.1 N-m. With an objective of cogging torque reduction, magnet shifting is performed from 1° to 6° in the step of 1°. Figure 6 shows simulation results of cogging torque response on account of magnet shifting and its comparison with cogging torque profile of reference motor. It is observed that the improved design having magnet shifting of 3° has the minimum cogging torque (p-p) of 0.6 N-m. Cogging torque (p-p) has been reduced from 1.1 N-m to 0.6 N-m. Table 2 shows variation of cogging torque with variation in magnet shift

angle. It is observed that cogging torque has been reduced significantly as magnet shifting angle is increased up to 3°. The cogging torque is increased for magnet shift angle of 4° and 6°. The reduction in average torque is marginal in improved designs.

Table 2
Comparison between initial and improved designs of radial flux PMBLDC motor

Sr. no.	Design details	Cogging torque peak to peak (N-m)	Average torque (N-m)
1	Initial design	1.10	1.91
2	Improved design	Magnet shift 1°	1.89
3		Magnet shift 2°	1.89
4		Magnet shift 3°	1.89
5		Magnet shift 4°	1.88
6		Magnet shift 6°	1.87

Comparison between average torque of reference design and improved design with magnet shift angle of 3° is shown in Fig. 7. It is seen that the torque ripple is also decreased in improved design incorporating magnet shifting technique.

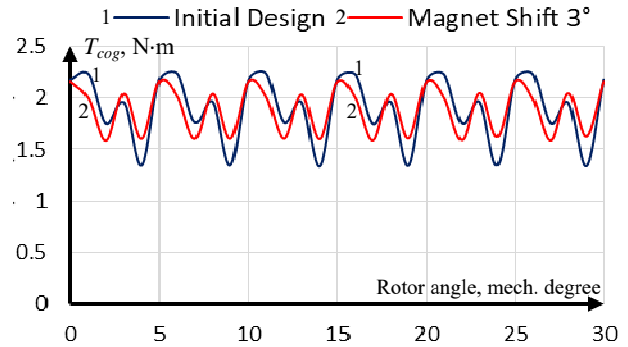


Fig. 7. Comparison between average torque profile of reference design and improved design

The back electromotive force (EMF) profiles of initial design and improved design are shown in Fig. 8. It is observed that the back EMF waveform is slightly improved when magnet shifting technique is applied. The value of back EMF remains nearly equal in both the designs. The harmonic spectrum of back EMF of initial design and improved design is shown in Fig. 9. It is observed that Total Harmonic Distortion (THD) is reduced from 8.03 % to 6.54 %.

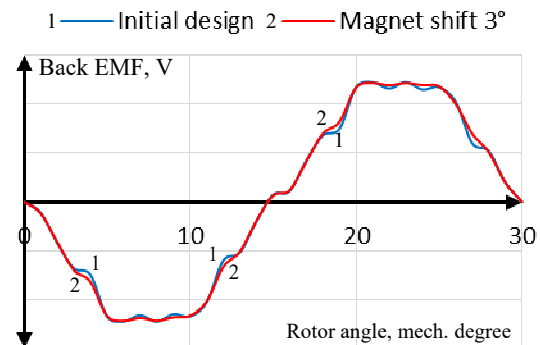


Fig. 8. Comparison between back EMF profile of initial design and improved design

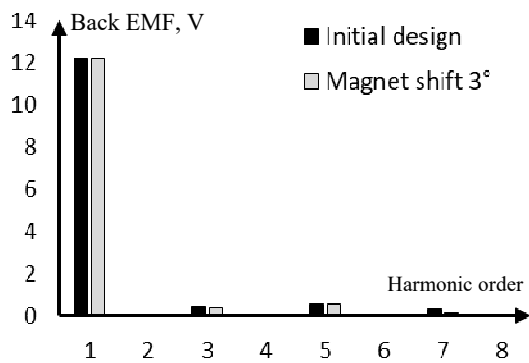


Fig. 9. Comparison of fast Fourier transform (FFT) analysis of back EMF

It is highly desirable to compare actual flux densities set up in various parts of motor with assumed flux densities in respective sections. Electromagnetic field analysis with FE software is carried out, on initially

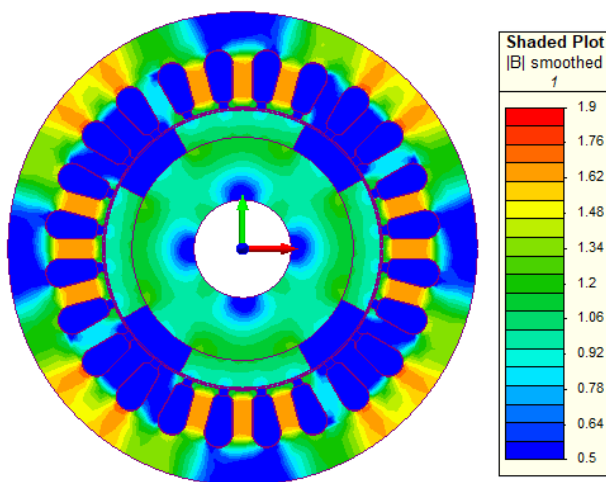


Fig. 10. Flux density distribution of reference design

designed reference motor and improved designed motor with magnet shifting technique, to evaluate flux densities in various portions of the motor.

A numerical technique, FE method is flexible, reliable and effective method in the analysis of power-frequency electromagnetic devices. FE analysis software uses this technique to perform electromagnetic field analysis in electromagnetic devices. The motor model is divided into FEs using self adaptive meshing. The Maxwell equations are used to evaluate flux densities and field intensities in each FE. The results obtained for each FE is integrated to obtain the flux density in various parts of the motor.

Shaded field plot of reference design and improved design have been shown in Fig. 10, 11 respectively. Actual flux densities in different parts of the motor are close to assumed flux densities of reference and improved designs. Hence, both designs are validated.

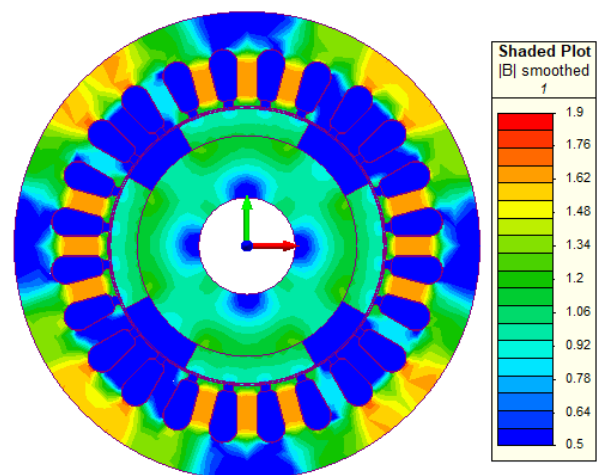


Fig. 11. Flux density distribution of improved design

Conclusions.

The magnet shifting technique is introduced in this paper to analyze its effect on cogging torque of permanent magnet brushless DC motor. The surface mounted permanent magnet brushless DC motor of 200 W, 1000 rpm is designed initially by mounting four permanent magnets symmetrically with respect to each other and considered as a reference design for the analysis. Design is improved by shifting position of permanent magnets by 1°, 2°, 3°, 4° and 6° mechanical degree with respect to each other. Finite element analysis is carried out to find cogging torque of both reference design and improved design. As the magnet shift angle increases, the cogging torque reduces. It has been analyzed that cogging torque (p-p) is reduced to 54.5 % for magnet shift angle of 3° with marginal reduction in average torque. Thus, it is examined that magnet shifting technique is an effective technique to reduce cogging torque of radial flux permanent magnet brushless DC motor.

Conflict of interest. The authors declare that they have no conflicts of interest.

REFERENCES

1. D. C. Hanselman, *Brushless Permanent Magnet Motor Design*, New York, McGraw- Hill, 1994.
2. Akkouchi K., Rahmani L., Lebied R. New application of artificial neural network-based direct power control for

- permanent magnet synchronous generator. *Electrical Engineering & Electromechanics*, 2021, no. 6, pp. 18-24. doi: <https://doi.org/10.20998/2074-272X.2021.6.03>.
3. Liu Ronghui, Wang Rumei, Li Jiebao. Reduction of cogging torque in surface-mounted permanent magnet brushless motor based on Motorsolve. *IEEE PES Innovative Smart Grid Technologies*, 2012, pp. 1-4. doi: <https://doi.org/10.1109/ISGT-Asia.2012.6303245>.
4. Liu T., Huang S., Gao J., Lu K. Cogging Torque Reduction by Slot-Opening Shift for Permanent Magnet Machines. *IEEE Transactions on Magnetics*, 2013, vol. 49, no. 7, pp. 4028-4031. doi: <https://doi.org/10.1109/TMAG.2013.2239977>.
5. Seo J.-D., Yoo J.-H., Jung T.-U. Design on notch structure of stator tooth to reduce of cogging torque of single-phase BLDC motor. *2015 18th International Conference on Electrical Machines and Systems (ICEMS)*, 2015, pp. 1475-1478. doi: <https://doi.org/10.1109/ICEMS.2015.7385273>.
6. Chabchoub M., Ben Salah I., Krebs G., Neji R., Marchand C. PMSM cogging torque reduction: Comparison between different shapes of magnet. *2012 First International Conference on Renewable Energies and Vehicular Technology*, 2012, pp. 206-211. doi: <https://doi.org/10.1109/REVET.2012.6195272>.
7. Islam M.S., Mir S., Sebastian T. Issues in reducing the cogging torque of mass-produced permanent magnet brushless DC motor. *38th IAS Annual Meeting on Conference Record of the Industry Applications Conference*, 2003, vol. 1, pp. 393-400. doi: <https://doi.org/10.1109/IAS.2003.1257531>.
8. Yu H.-C., Yu B.-S., Yu J., Lin C.-K. A Dual Notched Design of Radial-Flux Permanent Magnet Motors with Low

- Cogging Torque and Rare Earth Material. *IEEE Transactions on Magnetics*, 2014, vol. 50, no. 11, pp. 1-4. doi: <https://doi.org/10.1109/TMAG.2014.2329139>.
9. Srisiriwanna T., Konghirun M. A study of cogging torque reduction methods in brushless dc motor. *2012 9th International Conference on Electrical Engineering/Electronics, Computer, Telecommunications and Information Technology*, 2012, pp. 1-4. doi: <https://doi.org/10.1109/ECTICon.2012.6254191>.
10. Zhang B., Wang X., Zhang R., Mou X. Cogging torque reduction by combining teeth notching and rotor magnets skewing in PM BLDC with concentrated windings. *2008 International Conference on Electrical Machines and Systems*, 2008, pp. 3189-3192.
11. Setiabudy R., Wahab H., Putra Y.S. Reduction of cogging torque on brushless direct current motor with segmentation of magnet permanent. *2017 4th International Conference on Information Technology, Computer, and Electrical Engineering (ICITACEE)*, 2017, pp. 81-86. doi: <https://doi.org/10.1109/ICITACEE.2017.8257680>.
12. Karnavas Y.L., Chasiotis I.D., Gkiokas A.D. An Investigation Study Considering the Effect of Magnet Type, Slot Type and Pole-Arc to Pole-Pitch Ratio Variation on PM Brushless DC Motor Design. *2018 5th International Conference on Mathematics and Computers in Sciences and Industry (MCSI)*, 2018, pp. 7-13. doi: <https://doi.org/10.1109/MCSI.2018.00010>.
13. Ki-Jin Han, Han-Sam Cho, Dong-Hyeok Cho, Hyun-Kyo Jung. Optimal core shape design for cogging torque reduction of brushless DC motor using genetic algorithm. *IEEE Transactions on Magnetics*, 2000, vol. 36, no. 4, pp. 1927-1931. doi: <https://doi.org/10.1109/20.877824>.
14. Wang A., Ma D., Shu S. Influence of magnet pole shifting on cogging torque for PMSG application. *2014 17th International Conference on Electrical Machines and Systems (ICEMS)*, 2014, pp. 495-499. doi: <https://doi.org/10.1109/ICEMS.2014.7013521>.
15. Islam R., Husain I., Fardoun A., McLaughlin K. Permanent Magnet Synchronous Motor Magnet Designs with Skewing for Torque Ripple and Cogging Torque Reduction. *2007 IEEE Industry Applications Annual Meeting*, 2007, pp. 1552-1559. doi: <https://doi.org/10.1109/07IAS.2007.240>.
16. Boukais B., Zeroug H. Magnet Segmentation for Commutation Torque Ripple Reduction in a Brushless DC Motor Drive. *IEEE Transactions on Magnetics*, 2010, vol. 46, no. 11, pp. 3909-3919. doi: <https://doi.org/10.1109/TMAG.2010.2057439>.
17. Nur T., Haroon Y. Investigation the influence of magnet slots with fixed slot opening width on the cogging torque of Inset-PMSM. *The 2nd IEEE Conference on Power Engineering and Renewable Energy (ICPERE) 2014*, pp. 195-197. doi: <https://doi.org/10.1109/ICPERE.2014.7067211>.
18. Petrov I., Ponomarev P., Alexandrova Y., Pyrhonen J. Unequal Teeth Widths for Torque Ripple Reduction in Permanent Magnet Synchronous Machines With Fractional-Slot Non-Overlapping Windings. *IEEE Transactions on Magnetics*, 2015, vol. 51, no. 2, pp. 1-9. doi: <https://doi.org/10.1109/TMAG.2014.2355178>.
19. Dosiek L., Pillay P. (). Cogging Torque Reduction in Permanent Magnet Machines. *IEEE Transactions on Industry Applications*, 2007, vol. 43, no. 6, pp. 1565-1571. doi: <https://doi.org/10.1109/TIA.2007.908160>.

Received 26.01.2022

Accepted 25.04.2022

Published 01.06.2022

Tejas H. Panchal¹, Assistant Professor,
 Amit N. Patel¹, PhD, Assistant Professor,
 Rajesh M. Patel², PhD, Professor,
¹Department of Electrical Engineering,
 Institute of Technology, Nirma University,
 Ahmedabad, Gujarat, India,
 e-mail: tejas.panchal@nirmauni.ac.in (Corresponding author),
 amit.patel@nirmauni.ac.in,
²Department of Electrical Engineering,
 MEFGI's Faculty of PG Studies,
 Rajkot, Gujarat, India,
 e-mail: r_mpatel77@hotmail.com

How to cite this article:

Panchal T.H., Patel A.N., Patel R.M. Reduction of cogging torque of radial flux permanent magnet brushless DC motor by magnet shifting technique. *Electrical Engineering & Electromechanics*, 2022, no. 3, pp. 15-20. doi: <https://doi.org/10.20998/2074-272X.2022.3.03>

B.I. Kuznetsov, T.B. Nikitina, I.V. Bovdvi, O.V. Voloshko, V.V. Kolomiets, B.B. Kobylianskyi

Comparison of the effectiveness of thriple-loop and double-loop systems of active shielding of a magnetic field in a multi-storey old buildings

Aim. The issues of comparing the effectiveness of reducing the level of the magnetic field in a five-storey old buildings generated by a single-circuit overhead power transmission lines with a triangular suspension of wires using a thriple-loop and double-loop systems of active screening, which respectively contain three or two compensating windings are considered. **Methodology.** Spatial location coordinates of the compensating windings and the currents in the shielding windings were determined during the design of systems of active screening based on solution of the maximin vector optimization problem, in which the vector of objective function is calculated based on Biot-Savart's law. The solution of this problem is calculated based on algorithms of multi-swarm multi-agent optimization. **Results.** The results of theoretical and experimental comparing the effectiveness of reducing the level of the magnetic field in a five-storey old generated by a single-circuit overhead power transmission lines with a triangular suspension of wires using a thriple-loop and double-loop systems of active screening, which respectively contain three or two compensating windings are presented. **Originality.** For the first time, the comparison the effectiveness of reducing the level of the magnetic field in a five-storey old using a thriple-loop and double-loop systems of active screening are considered. **Practical value.** From the point of view of the practical implementation it is shown the possibility to reduce the level of magnetic field induction in a five-storey old buildings to the sanitary standards of Ukraine for real overhead power transmission lines currents with the help of a synthesized double-loop systems of active screening. A double-loop active screening system is simpler in comparison with a thriple-loop active screening system when implementing. References 48, figures 7.

Key words: overhead power line, magnetic field, system of active screening, computer simulation, experimental research.

Мета. Розглянуто питання порівняння ефективності зниження рівня магнітного поля в п'ятиповерховому домі старої забудови, генеруемого одноконтурною повітряною лінією електропередачі з трикутним підвісом проводів з використанням трьохконтурної та двоконтурної систем активного екранування, які відповідно містять три або дві компенсаційні обмотки. **Методика.** При проектуванні системи активного екранування визначалися координати просторового розташування екрануючих обмоток і струми в екрануючих обмотках на основі рішення задачі максиміної векторної оптимізації, в якій вектор цільової функції розраховується за законом Біо-Савара. Рішення цієї задачі розраховано на основі алгоритмів багаторойової багатоагентної оптимізації. **Результати.** Наведені результати теоретичного та експериментального порівняння ефективності зниження рівня магнітного поля в п'ятиповерховому домі старої забудови, генеруемого одноконтурною повітряною лінією електропередачі з трикутним підвісом проводів з використанням трьохконтурної та двоконтурної систем активного екранування, які містять відповідно три або дві компенсаційні обмотки. **Оригінальність.** Вперше розглянуто порівняння ефективності зниження рівня магнітного поля в п'ятиповерховому домі старої забудови, за допомогою трьохконтурної та двоконтурної систем активного екранування. **Практична цінність.** З точки зору практичної реалізації показано можливість зниження рівня індукції магнітного поля в п'ятиповерховому домі старої забудови до санітарних норм України для реальних струмів повітряної лінії електропередачі за допомогою синтезованої двоконтурної системи активного екранування. Двоконтурна система активного екранування в порівнянні з трьохконтурною системою активного екранування при впровадженні простіша. Бібл. 48, рис. 7.

Ключові слова: повітряна лінія електропередачі, магнітне поле, система активного екранування, комп'ютерне моделювання, експериментальні дослідження.

Introduction. Many existing overhead power transmission lines in Ukraine run near the zones of old residential buildings. Often old residential buildings are located in the immediate vicinity of residential buildings, as shown in Fig. 1. Naturally, in such residential buildings the level of magnetic field (MF) induction exceeds the sanitary standards of Ukraine by two or three times [1–4]. For the safe operation of many old residential buildings, it is economically expedient to reduce the induction level of the initial MF to the level of sanitary standards of Ukraine by means of active shielding [5–18].

These lines generate a magnetic field with a circular space-time characteristic [6] to compensate for which by means of active shielding at least two compensation windings are required [14].

To compensate for this magnetic field in a multi-storey old building, three or more compensation windings may be needed [16–18]. In [19], the issues of reducing the level of the magnetic field generated by a single-circuit power transmission line with a triangular arrangement of wires in a five-storey building of an old building are considered. With the help of such a system of active

shielding, it is possible to reduce the level of the initial magnetic field by 8 times from the induction level of the initial magnetic field of 4 μT to the level of sanitary standards of Ukraine of 0.5 μT . At the same time, sanitary standards are met throughout the entire space of the five-storey building.



Fig. 1. Location of a residential building near overhead power transmission lines

This active screening system has been synthesized for the rated current of the transmission line. However, the real currents in the power transmission lines of Ukraine are two to three times less than the rated currents. In this regard, it is advisable to synthesize an active screening system, with the help of which it is possible to reduce the level of magnetic field induction in old buildings to the sanitary standards of Ukraine at real power transmission line currents.

From the point of view of practical implementation, in comparison with a three-circuit active screening system, a two-circuit active screening system is simpler. When implementing a two-circuit system, firstly, fewer supports are needed to suspend only two rather than three compensating windings. Secondly, to supply the compensating windings of the windings, only two power amplifiers are needed instead of three, and a smaller number of sensors are needed to measure the magnetic flux density of the of magnetic field.

The objective of the work is to synthesize and to compare the effectiveness of triple-loop and double-loop systems of active shielding of the magnetic field generated by single-circuit overhead power lines with a triangular suspension of wires in a multi-story old building.

Problem statement. To reduce the level of the magnetic field around the world, systems of active shielding of the magnetic field are used with the help of a system of special controlled magnetic field sources – windings with adjustable current, installed in the area where it is necessary to maintain internal magnetic field parameters [11–14].

For a given shielding space, in particular an old multi-storey residential building located in the immediate vicinity of an overhead power line, it is necessary to create a magnetic field by means of active shielding, which would compensate for the original magnetic field.

Consider a system of active shielding of magnetic field using a system of special controlled sources of magnetic field – windings with adjustable current, installed in the area where it is necessary to maintain the parameters of the internal magnetic field within specified limits. The man-caused magnetic field is created by a three-phase high-voltage power line.

We introduce the vector of the required parameters of systems of active shielding, the components of which are vector of coordinates of the spatial location of the compensation windings and regulators parameters [20–24]. Also we introduce vector of the parameter of uncertainty of external magnetic field model [23, 24]. Then the problem of synthesis of systems of active shielding is associated with computation of such vector of the required parameters of systems of active shielding which assumes a minimum value from maximum value of the magnetic flux density at selected points of the shielding space [25–29]. However, in this case, it is necessary to simultaneously determine such a value of vector of the parameter uncertainty, at which the maximum value of the same magnetic flux density is maximum. This is the worst-case approach when robust systems synthesis [30–33].

Method of synthesis. This problem is the multi-criteria two-player zero-sum antagonistic game [40, 41].

The vector payoffs are the magnetic flux density in points of the shielding space. The vector payoff is the vector nonlinear functions of vector of the required parameters of systems of active shielding and vector of the parameter of uncertainty of external magnetic field model and calculated based on Biot-Savart's law [1]. In this game the first player is the parameters of systems of active shielding and its strategy is the minimization of vector payoff. The second player is the vector of parameter uncertainty and its strategy is maximization of the same vector payoff. The decision of this game is calculated on based of multi-swarm stochastic multi-agent optimization algorithm [42–48]. This decision is choose from systems of Pareto-optimal decisions [42].

Computer simulation. Let us consider the result of synthesis of triple-loop and double-loop systems of active shielding of the magnetic field generated by single-circuit overhead power lines with a triangular suspension of wires in a multi-story old building. In Fig. 2 are shown the layout of the power transmission line, a five-story building, in which it is necessary to reduce the level of the magnetic field, and the location of three (a) and two (b) compensating windings of systems of active screening.

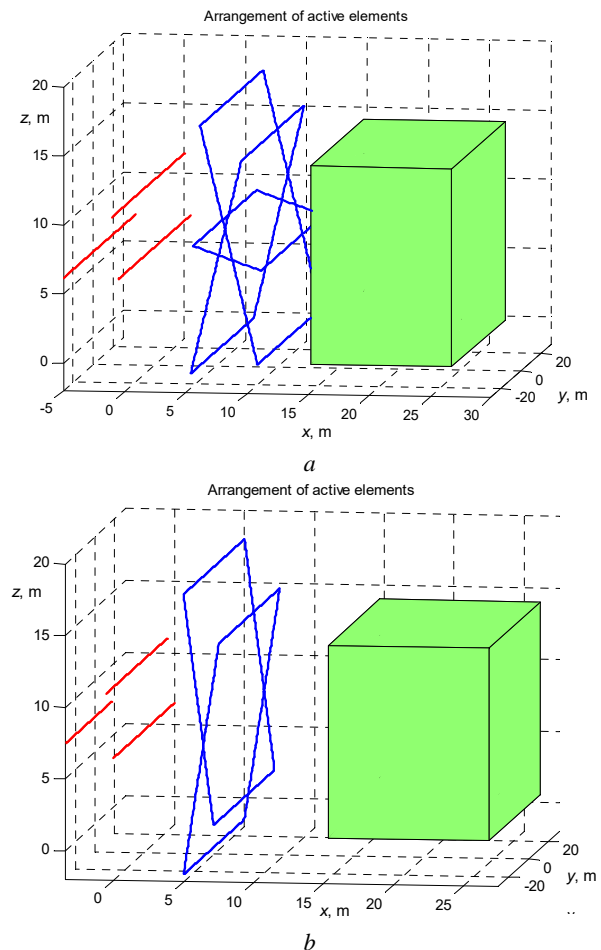


Fig. 2. Layout of the power transmission line, a five-story building, in which it is necessary to reduce the level of the magnetic field, and the location of three (a) and two (b) compensating windings of systems of active screening

The coordinates of the spatial position of the compensation windings, the parameters of the regulators and the currents in the compensation windings are calculated as a

result of solving the problem of vector optimization in the synthesis of the systems of active shielding.

In Fig. 3 are shown the distributions of the resulting magnetic field for triple-loop (a) and double-loop (b) systems. When operating a triple-loop system, as follows from Fig. 3,a, using the systems of active screening, the induction level of the resulting magnetic field in the entire space of a five-story building does not exceed the level of $0.5 \mu\text{T}$, which corresponds to the sanitary standards of Ukraine. However, when operating a double-loop system, as shown in Fig. 3,b, the level of induction of the resulting magnetic field at the border of a five-storey building exceeds the level of sanitary standards of Ukraine in $0.5 \mu\text{T}$. In general, the implementation of sanitary standards is carried out on 90 % of the area of five-story old building.

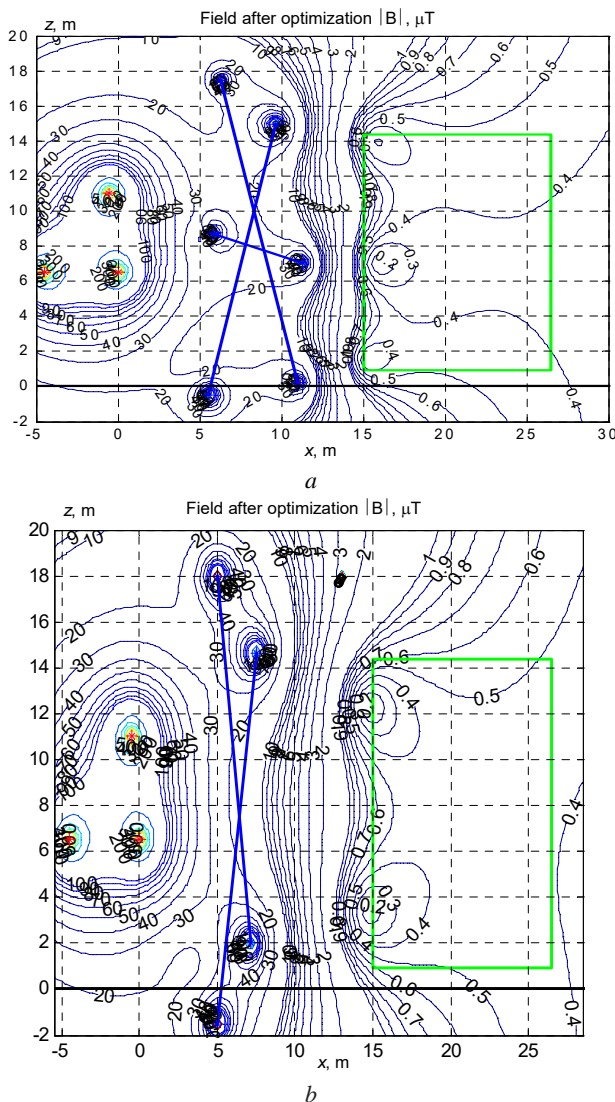


Fig. 3. Distributions of the resulting magnetic field for triple-loop (a) and double-loop (b) systems

In Fig. 4 are shown the dependences of the induction level of the initial MF and the resulting magnetic field as a function of the distance from the power transmission line. When operating a triple-loop systems of active screening, as follows from Fig. 3,a, the induction level in the entire space of a five-story building does not exceed $0.5 \mu\text{T}$. However, during the operation of a two-circuit

systems of active screening, the level of induction is slightly higher than the level of $0.5 \mu\text{T}$ inside a five-story building near a power transmission line, as it shown in Fig. 3,b.

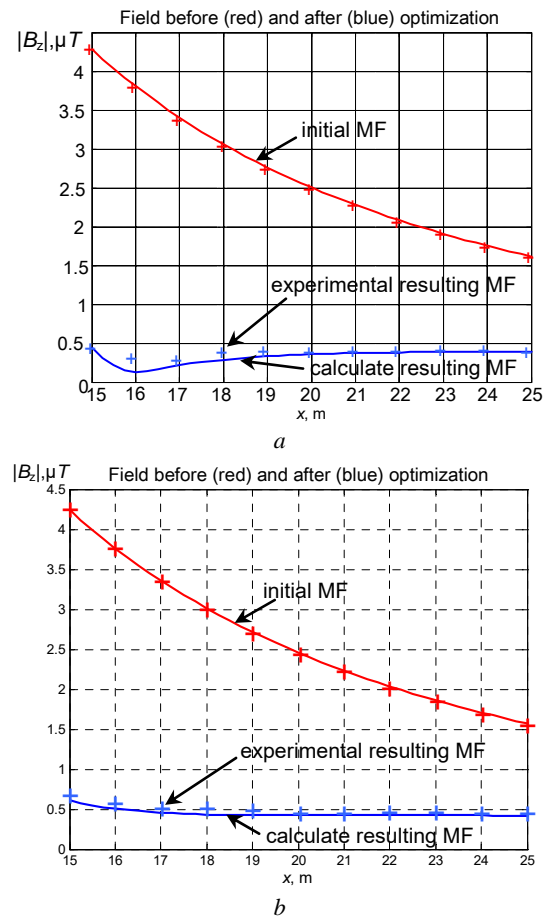


Fig. 4. Dependences of the induction level of the initial MF and the resulting magnetic field as a function of the distance from the power transmission line

In Fig. 5 are shown the spatio-temporal characteristics of the initial magnetic field (1), the magnetic field generated by the compensation windings (2) and the resulting magnetic field (3), respectively, for three-circuit (a) and two-loop (b) active screening systems. As follows from Fig. 5,a, during the operation of a three-loop active screening system, the initial magnetic field is almost completely compensated by the screening windings so that the spatio-temporal characteristic of the resulting magnetic field remaining after the operation of the three-loop active screening system is a point.

This results in a high shielding factor of more than 20 units in a limited area of the shielding space under consideration. However, when a two-loop active screening system operates in this limited area of the screening space, the screening factor is about 6 units. Therefore, the spatio-temporal characteristic of the resulting magnetic field remaining after the operation of the two-loop active screening system is a line.

Experimental results. For experimental research, models of three-loop and two-loop active shielding systems were developed, as well as a model of a single-loop overhead power line with a triangular suspension of wires.

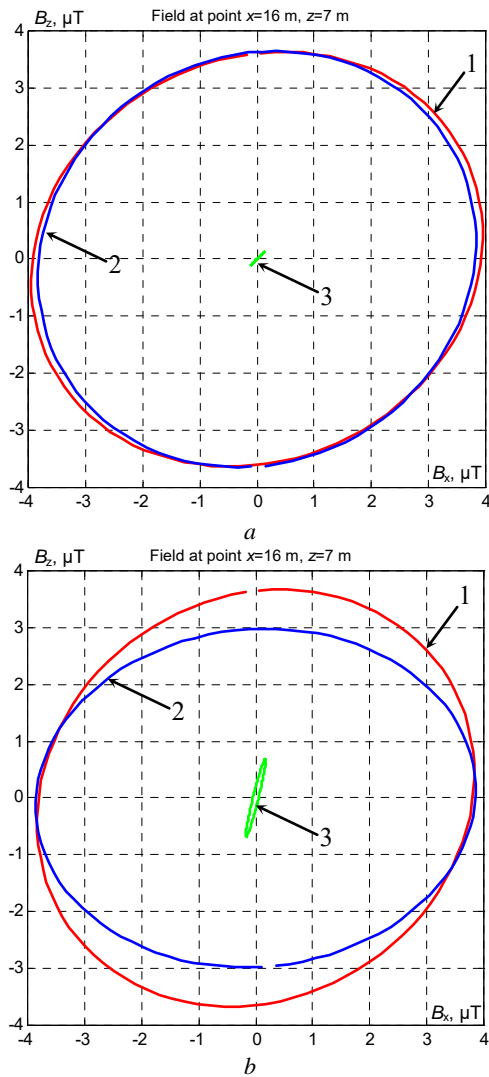


Fig. 5. The spatio-temporal characteristics of the initial magnetic field (1), the magnetic field generated by the compensation windings (2) and the resulting magnetic field (3), respectively, for three-circuit (a) and two-loop (b) active screening systems

Let us consider the field experimental model of systems of active screening. In Fig. 6 are shown three compensation windings (a) a triple-loop active screening system and two compensation windings (b) a double-loop active screening system.

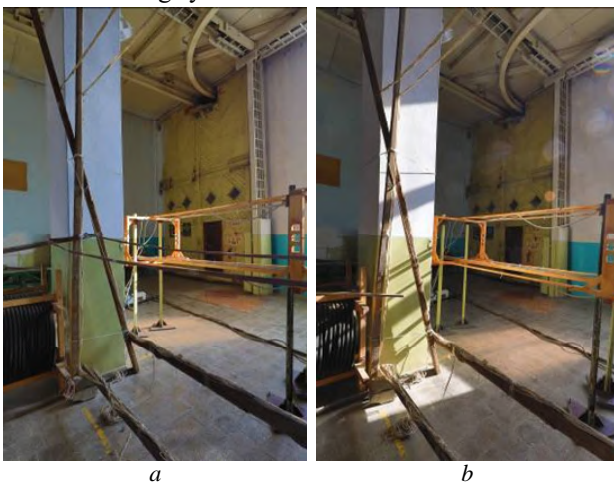


Fig. 6. Three compensation windings (a) for triple-loop active screening system and two compensation windings (b) for double-loop system of active screening

The special measuring system for experimental measurement of space-time characteristics was developed. This measuring system includes two measuring windings, the axes of which are perpendicular to each other. An important issue in tuning this measuring system is the precise setting of the gains and phase shifts of the individual measurement channels. In Fig. 7 are shown experimental measurement space-time characteristics of magnetic field.

In Fig. 7,a is shown experimental measurement space-time characteristics of initial magnetic field. The shape of this characteristic is close to a circle, which corresponds to the calculated space-time characteristics of initial magnetic field characteristic, which are shown in Fig. 5.

In Fig. 7,b is shown experimental measurement space-time characteristics of resulting magnetic field with double-loop system of active shielding is on. The shape of this characteristic is close to to the calculated space-time characteristics of resulting magnetic field with double-loop system of active shielding is on, which is shown in Fig. 5,b.

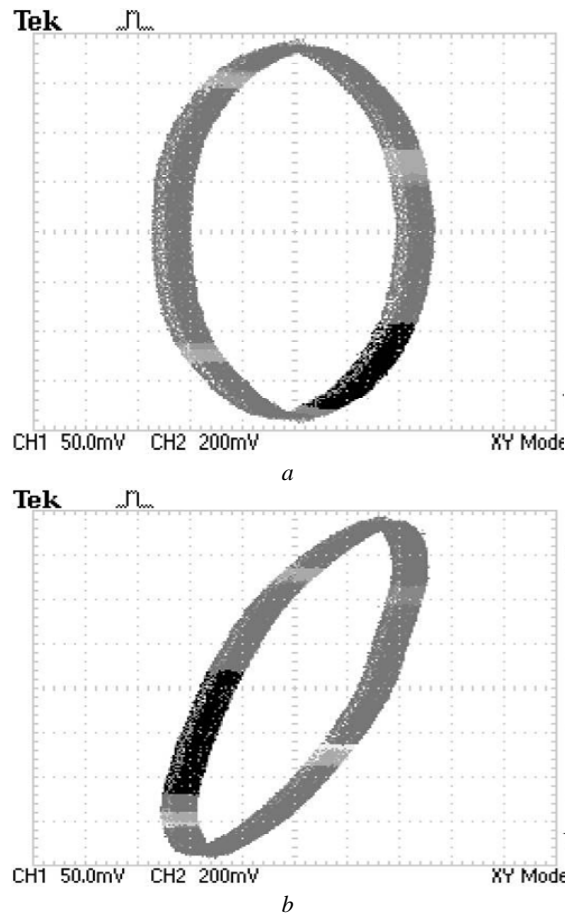


Fig. 7. The experimental measurement space-time characteristics of initial magnetic field (a) and resulting magnetic field (b) with double-loop system of active shielding is on

Note that experimental measurement space-time characteristics of resulting magnetic field with triple-loop system of active shielding is on quite small compared to experimental measurement space-time characteristics of initial magnetic field. The shape of this characteristic is close to a dot, which corresponds to the calculated space-time characteristics of resulting magnetic field with triple-loop system of active shielding is on, which are shown in Fig. 5,a.

In Fig. 4 also are shown the level of induction of magnetic field calculated (solid line) and measured with and without systems of active screening.

The difference of magnetic flux density found by measurements and simulations in the shielding zone does not exceed 20 %. The experimental shielding factor of systems of active screening is more than 8.

Note that real power transmission line currents are two to three times less than the rated currents. That's why from the point of view of the practical implementation it is shown the possibility to reduce the level of magnetic field induction in a five-storey old buildings to the sanitary standards of Ukraine for real overhead power transmission lines currents with the help of a synthesized double-loop systems of active screening. A double-loop system of active screening is simpler in comparison with a triple-loop active screening system when implementing.

Discussion. Note that during the operation of a three-circuit systems of active screening in the distribution of the induction of the resulting magnetic field there is a minimum with an induction value of 0.2 μT at the point with coordinates (16.0, 7.0), for which the screening factor is 20 units. In addition to this global minimum, there are two more local minima with an induction value of 0.4 μT at points with coordinates (16.0, 1.5) and (16.0, 14.0), the screening factor of which is 10 units.

During the operation of a two-circuit systems of active screening in the distribution of the induction of the resulting magnetic field, there are also two local minima with an induction value of 0.2 μT at points with coordinates (15.0, 3.5) and (15.5, 12.5) on the border of a five-storey building, of which the screening factor is 20 units.

The presence of such local minima in the magnetic field induction distribution imposes specific requirements on the algorithms used for solving optimization problems. In particular, in the synthesis of the systems of active screening under consideration, stochastic multi-swarm multi-agent optimization algorithms were used.

Conclusions.

1. The synthesis of triple-loop and double-loop systems of active shielding of the magnetic field generated by 110 kV single-circuit overhead power lines with a triangular suspension of wires in a five-storey old building has been performed. As a result of the synthesis, the coordinates of the location of three and two compensation windings, respectively, were determined, as well as the currents and phases in these compensation windings.

2. To synthesize robust systems of active screening, solutions to minimax vector optimization problems were calculated based on stochastic multi-agent optimization algorithms. The calculation of vector objective functions and constraints was carried out on the basis of the Bio-Savart's law.

3. The study of the efficiency of the synthesized triple-loop and double-loop systems of active screening of the magnetic field in a five-storey old building has been carried out. It is shown that with the help of a triple-loop system, the level of the initial magnetic field is reduced to the sanitary standards of Ukraine in the entire all space of a five-storey building. The screening factor is more than 8 units.

4. It is shown, that for rated currents of 110 kV power transmission line with the help of a double-loop system

the implementation of sanitary standards is carried out only on 90 % of the area of five-storey old building.

5. For real currents of 110 kV power transmission line, which are two to three times less than the rated currents, with the help of a synthesized double-loop systems of active screening, it is possible to reduce the level of induction of magnetic field in the entire all space of a five-storey old building to the sanitary standards of Ukraine.

Conflict of interest. The authors declare that they have no conflicts of interest.

REFERENCES

1. Rozov V.Y., Zavalnyi A.V., Zolotov S.M., Gretsikh S.V. The normalization methods of the static geomagnetic field inside houses. *Electrical Engineering & Electromechanics*, 2015, no. 2, pp. 35-40. doi: <https://doi.org/10.20998/2074-272x.2015.2.07>.
2. Rozov V.Yu., Grinchenko V.S., Yerisov A.V., Dobrodeyev P.N. Efficient shielding of three-phase cable line magnetic field by passive loop under limited thermal effect on power cables. *Electrical Engineering & Electromechanics*, 2019, no. 6, pp. 50-54. doi: <https://doi.org/10.20998/2074-272x.2019.6.07>.
3. Rozov V., Grinchenko V. Simulation and analysis of power frequency electromagnetic field in buildings closed to overhead lines. *2017 IEEE First Ukraine Conference on Electrical and Computer Engineering (UKRCON)*, Kyiv, Ukraine, 2017, pp. 500-503. doi: <https://doi.org/10.1109/ukrcon.2017.8100538>.
4. Rozov V.Yu., Kundius K.D., Pelevin D.Ye. Active shielding of external magnetic field of built-in transformer substations. *Electrical Engineering & Electromechanics*, 2020, no. 3, pp. 24-30. doi: <https://doi.org/10.20998/2074-272x.2020.3.04>.
5. Salceanu A., Paulet M., Alistar B.D., Asimincesei O. Upon the contribution of image currents on the magnetic fields generated by overhead power lines. *2019 International Conference on Electromechanical and Energy Systems (SIEMEN)*. 2019. doi: <https://doi.org/10.1109/sielmen.2019.8905880>.
6. Del Pino Lopez J.C., Romero P.C. Influence of different types of magnetic shields on the thermal behavior and ampacity of underground power cables. *IEEE Transactions on Power Delivery*, Oct. 2011, vol. 26, no. 4, pp. 2659-2667. doi: <https://doi.org/10.1109/tpwr.2011.2158593>.
7. Ippolito L., Siano P. Using multi-objective optimal power flow for reducing magnetic fields from power lines. *Electric Power Systems Research*, Feb. 2004, vol. 68, no. 2, pp. 93-101. doi: [https://doi.org/10.1016/s0378-7796\(03\)00151-2](https://doi.org/10.1016/s0378-7796(03)00151-2).
8. Barsali S., Giglioli R., Poli D. Active shielding of overhead line magnetic field: Design and applications. *Electric Power Systems Research*, May 2014, vol. 110, pp. 55-63. doi: <https://doi.org/10.1016/j.epr.2014.01.005>.
9. Bavastro D., Canova A., Freschi F., Giaccone L., Manca M. Magnetic field mitigation at power frequency: design principles and case studies. *IEEE Transactions on Industry Applications*, May 2015, vol. 51, no. 3, pp. 2009-2016. doi: <https://doi.org/10.1109/tia.2014.2369813>.
10. Beltran H., Fuster V., Garcia M. Magnetic field reduction screening system for a magnetic field source used in industrial applications. *9 Congreso Hispano Luso de Ingeniería Eléctrica (9 CHLIE)*, Marbella (Málaga, Spain), 2005, pp. 84-99. Available at: https://www.researchgate.net/publication/229020921_Magnetic_field_reduction_screening_system_for_a_magnetic_field_source_used_in_industrial_applications (Accessed 22.06.2021).
11. Bravo-Rodríguez J., Del-Pino-López J., Cruz-Romero P. A Survey on Optimization Techniques Applied to Magnetic Field Mitigation in Power Systems. *Energies*, 2019, vol. 12, no. 7, p. 1332. doi: <https://doi.org/10.3390/en12071332>.

12. Canova A., del-Pino-López J.C., Giaccone L., Manca M. Active Shielding System for ELF Magnetic Fields. *IEEE Transactions on Magnetics*, March 2015, vol. 51, no. 3, pp. 1-4. doi: <https://doi.org/10.1109/tmag.2014.2354515>.
13. Canova A., Giaccone L. Real-time optimization of active loops for the magnetic field minimization. *International Journal of Applied Electromagnetics and Mechanics*, Feb. 2018, vol. 56, pp. 97-106. doi: <https://doi.org/10.3233/jae-172286>.
14. Canova A., Giaccone L., Cirimele V. Active and passive shield for aerial power lines. *Proc. of the 25th International Conference on Electricity Distribution (CIRED 2019)*, 3-6 June 2019, Madrid, Spain. Paper no. 1096. Available at: <https://www.cired-repository.org/handle/20.500.12455/290> (Accessed 28.10.2020).
15. Canova A., Giaccone L. High-performance magnetic shielding solution for extremely low frequency (ELF) sources. *CIRED - Open Access Proceedings Journal*, Oct. 2017, vol. 2017, no. 1, pp. 686-690. doi: <https://doi.org/10.1049/oap-cired.2017.1029>.
16. Celozzi S. Active compensation and partial shields for the power-frequency magnetic field reduction. *2002 IEEE International Symposium on Electromagnetic Compatibility*, Minneapolis, MN, USA, 2002, vol. 1, pp. 222-226. doi: <https://doi.org/10.1109/isemc.2002.1032478>.
17. Celozzi S., Garzia F. Active shielding for power-frequency magnetic field reduction using genetic algorithms optimization. *IEE Proceedings - Science, Measurement and Technology*, 2004, vol. 151, no. 1, pp. 2-7. doi: <https://doi.org/10.1049/ip-smt:20040002>.
18. Celozzi S., Garzia F. Magnetic field reduction by means of active shielding techniques. *WIT Transactions on Biomedicine and Health*, 2003, vol. 7, pp. 79-89. doi: <https://doi.org/10.2495/ehr030091>.
19. Kuznetsov B.I., Nikitina T.B., Bovdui I.V., Kolomiets V.V., Kobylanskiy B.B. Overhead power lines magnetic field reducing in multi-story building by active shielding means. *Electrical Engineering & Electromechanics*, 2021, no. 2, pp. 23-29. doi: <https://doi.org/10.20998/2074-272X.2021.2.04>.
20. Martynenko G. Practical application of the analytical method of electromagnetic circuit analysis for determining magnetic forces in active magnetic bearings. *2020 IEEE Problems of Automated Electrodrive. Theory and Practice (PAEP)*, 2020, pp. 1-4, doi: <https://doi.org/10.1109/paep49887.2020.9240774>.
21. Martynenko G., Martynenko V. Modeling of the dynamics of rotors of an energy gas turbine installation using an analytical method for analyzing active magnetic bearing circuits. *2020 IEEE KhPI Week on Advanced Technology (KhPIWeek)*, 2020, pp. 92-97. doi: <https://doi.org/10.1109/KhPIWeek51551.2020.9250156>.
22. Buriakovskiy S.G., Maslii A.S., Pasko O.V., Smirnov V.V. Mathematical modelling of transients in the electric drive of the switch – the main executive element of railway automation. *Electrical Engineering & Electromechanics*, 2020, no. 4, pp. 17-23. doi: <https://doi.org/10.20998/2074-272X.2020.4.03>.
23. Ostroverkhov M., Chumack V., Monakhov E., Ponomarev A. Hybrid Excited Synchronous Generator for Microhydropower Unit. *2019 IEEE 6th International Conference on Energy Smart Systems (ESS)*, Kyiv, Ukraine, 2019, pp. 219-222. doi: <https://doi.org/10.1109/ess.2019.8764202>.
24. Ostroverkhov M., Chumack V., Monakhov E. Output Voltage Stabilization Process Simulation in Generator with Hybrid Excitation at Variable Drive Speed. *2019 IEEE 2nd Ukraine Conference on Electrical and Computer Engineering (UKRCON)*, Lviv, Ukraine, 2019, pp. 310-313. doi: <https://doi.org/10.1109/ukrcon.2019.8879781>.
25. Tytiuk V., Chorny O., Baranovskaya M., Serhienko S., Zachepa I., Tsvirkun L., Kuznetsov V., Tryputen N. Synthesis of a fractional-order $PI^{\alpha}D^{\beta}$ -controller for a closed system of switched reluctance motor control. *Eastern-European Journal of Enterprise Technologies*, 2019, no. 2 (98), pp. 35-42. doi: <https://doi.org/10.15587/1729-4061.2019.160946>.
26. Zagirnyak M., Chorny O., Zachepa I. The autonomous sources of energy supply for the liquidation of technogenic accidents. *Przegląd Elektrotechniczny*, 2019, no. 5, pp. 47-50. doi: <https://doi.org/10.15199/48.2019.05.12>.
27. Chorny O., Serhienko S. A virtual complex with the parametric adjustment to electromechanical system parameters. *Technical Electrodynamics*, 2019, pp. 38-41. doi: <https://doi.org/10.15407/techned2019.01.038>.
28. Shchur I., Kasha L., Bukavyn M. Efficiency Evaluation of Single and Modular Cascade Machines Operation in Electric Vehicle. *2020 IEEE 15th International Conference on Advanced Trends in Radioelectronics, Telecommunications and Computer Engineering (TCSET)*, Lviv-Slavske, Ukraine, 2020, pp. 156-161. doi: <https://doi.org/10.1109/tcset49122.2020.235413>.
29. Shchur I., Turkovskiy V. Comparative Study of Brushless DC Motor Drives with Different Configurations of Modular Multilevel Cascaded Converters. *2020 IEEE 15th International Conference on Advanced Trends in Radioelectronics, Telecommunications and Computer Engineering (TCSET)*, Lviv-Slavske, Ukraine, 2020, pp. 447-451. doi: <https://doi.org/10.1109/tcset49122.2020.235473>.
30. Ostroumov I., Kuzmenko N., Sushchenko O., Pavlikov V., Zhyla S., Solomentsev O., Zaliskyi M., Averyanova Y., Tserne E., Popov A., Volosyuk V., Ruzhentsev N., Dergachov K., Havrylenko O., Kuznetsov B., Nikitina T., Shmatko O. Modelling and simulation of DME navigation global service volume. *Advances in Space Research*, 2021, vol. 68, no. 8, pp. 3495-3507. doi: <https://doi.org/10.1016/j.asr.2021.06.027>.
31. Averyanova Y., Sushchenko O., Ostroumov I., Kuzmenko N., Zaliskyi M., Solomentsev O., Kuznetsov B., Nikitina T., Havrylenko O., Popov A., Volosyuk V., Shmatko O., Ruzhentsev N., Zhyla S., Pavlikov V., Dergachov K., Tserne E. UAS cyber security hazards analysis and approach to qualitative assessment. In: Shukla S., Unal A., Varghese Kureethara J., Mishra D.K., Han D.S. (eds) *Data Science and Security. Lecture Notes in Networks and Systems*, 2021, vol. 290, pp. 258-265. Springer, Singapore. doi: https://doi.org/10.1007/978-981-16-4486-3_28.
32. Zaliskyi M., Solomentsev O., Shcherbyna O., Ostroumov I., Sushchenko O., Averyanova Y., Kuzmenko N., Shmatko O., Ruzhentsev N., Popov A., Zhyla S., Volosyuk V., Havrylenko O., Pavlikov V., Dergachov K., Tserne E., Nikitina T., Kuznetsov B. Heteroskedasticity analysis during operational data processing of radio electronic systems. In: Shukla S., Unal A., Varghese Kureethara J., Mishra D.K., Han D.S. (eds) *Data Science and Security. Lecture Notes in Networks and Systems*, 2021, vol. 290, pp. 168-175. Springer, Singapore. doi: https://doi.org/10.1007/978-981-16-4486-3_18.
33. Sushchenko O.A. Robust control of angular motion of platform with payload based on H_{∞} -synthesis. *Journal of Automation and Information Sciences*, 2016, vol. 48, no. 12, pp. 13-26. doi: <https://doi.org/10.1615/jautomatinfscien.v48.i12.20>.
34. Chikovani V., Sushchenko O. Self-compensation for disturbances in differential vibratory gyroscope for space navigation. *International Journal of Aerospace Engineering*, 2019, vol. 2019, Article ID 5234061, 9 p. doi: <https://doi.org/10.1155/2019/5234061>.
35. Gal'chenko V.Y., Vorob'ev M.A. Structural synthesis of attachable eddy-current probes with a given distribution of the probing field in the test zone. *Russian Journal of Nondestructive Testing*, Jan. 2005, vol. 41, no. 1, pp. 29-33. doi: <https://doi.org/10.1007/s11181-005-0124-7>.
36. Halchenko V.Y., Ostapushchenko D.L., Vorobyov M.A. Mathematical simulation of magnetization processes of arbitrarily shaped ferromagnetic test objects in fields of given spatial configurations. *Russian Journal of Nondestructive Testing*, Sep. 2008, vol. 44, no. 9, pp. 589-600. doi: <https://doi.org/10.1134/S1061830908090015>.

37. Ostroumov I., Kuzmenko N., Sushchenko O., Zaliskyi M., Solomentsev O., Averyanova Y., Zhyla S., Pavlikov V., Tserne E., Volosyuk V., Dergachov K., Havrylenko O., Shmatko O., Popov A., Ruzhentshev N., Kuznetsov B., Nikitina T. A probability estimation of aircraft departures and arrivals delays. In: Gervasi O. et al. (eds) *Computational Science and Its Applications – ICCSA 2021. ICCSA 2021. Lecture Notes in Computer Science*, vol. 12950, pp. 363-377. Springer, Cham. doi: https://doi.org/10.1007/978-3-030-86960-1_26.
38. Chystiakov P., Chornyi O., Zhautikov B., Sivyakova G. Remote control of electromechanical systems based on computer simulators. *2017 International Conference on Modern Electrical and Energy Systems (MEES)*, Kremenchuk, Ukraine, 2017, pp. 364-367. doi: <https://doi.org/10.1109/mees.2017.8248934>.
39. Zagirnyak M., Bisikalo O., Chorna O., Chornyi O. A Model of the Assessment of an Induction Motor Condition and Operation Life, Based on the Measurement of the External Magnetic Field. *2018 IEEE 3rd International Conference on Intelligent Energy and Power Systems (IEPS)*, Kharkiv, 2018, pp. 316-321. doi: <https://doi.org/10.1109/ieps.2018.8559564>.
40. Ummels M. *Stochastic Multiplayer Games Theory and Algorithms*. Amsterdam University Press, 2010. 174 p.
41. Shoham Y., Leyton-Brown K. *Multiagent Systems: Algorithmic, Game-Theoretic, and Logical Foundations*. Cambridge University Press, 2009. 504 p.
42. Ray T., Liew K.M. A Swarm Metaphor for Multiobjective Design Optimization. *Engineering Optimization*, 2002, vol. 34, no. 2, pp. 141-153. doi: <https://doi.org/10.1080/03052150210915>.
43. Zilzter Eckart. *Evolutionary algorithms for multiobjective optimizations: methods and applications*. PhD Thesis Swiss Federal Institute of Technology, Zurich, 1999. 114 p.
44. Xiaohui Hu, Eberhart R.C., Yuhui Shi. Particle swarm with extended memory for multiobjective optimization. *Proceedings of the 2003 IEEE Swarm Intelligence Symposium. SIS'03* (Cat. No.03EX706), Indianapolis, IN, USA, 2003, pp. 193-197. doi: <https://doi.org/10.1109/sis.2003.1202267>.
45. Pulido G.T., Coello C.A.C. A constraint-handling mechanism for particle swarm optimization. *Proceedings of the 2004 Congress on Evolutionary Computation* (IEEE Cat. No.04TH8753), Portland, OR, USA, 2004, vol. 2, pp. 1396-1403. doi: <https://doi.org/10.1109/cec.2004.1331060>.
46. Michalewicz Z., Schoenauer M. Evolutionary Algorithms for Constrained Parameter Optimization Problems. *Evolutionary Computation*, 1996, vol. 4, no. 1, pp. 1-32. doi: <https://doi.org/10.1162/evco.1996.4.1.1>.
47. Parsopoulos K.E., Vrahatis M.N. Particle swarm optimization method for constrained optimization problems. *Proceedings of the Euro-International Symposium on Computational Intelligence*, 2002, pp. 174-181.
48. Xin-She Yang, Zhihua Cui, Renbin Xiao, Amir Hossein Gandomi, Mehmet Karamanoglu. *Swarm Intelligence and Bio-Inspired Computation: Theory and Applications*, Elsevier Inc., 2013. 450 p.

Received 25.02.2022

Accepted 27.03.2022

Published 01.06.2022

B.I. Kuznetsov¹, Doctor of Technical Science, Professor,
 T.B. Nikitina², Doctor of Technical Science, Professor,
 I.V. Bovdii¹, PhD, Senior Research Scientist,
 O.V. Voloshko¹, PhD, Junior Research Scientist,
 V.V. Kolomiets², PhD, Associate Professor,
 B.B. Kobylianskyi², PhD, Associate Professor,
¹A. Pidhornyi Institute of Mechanical Engineering Problems of
 the National Academy of Sciences of Ukraine,
 2/10, Pozharskogo Str., Kharkiv, 61046, Ukraine,
 e-mail: kuznetsov.boris.i@gmail.com (Corresponding author)
²Educational scientific professional pedagogical Institute
 of Ukrainian Engineering Pedagogical Academy,
 9a, Nosakov Str., Bakhmut, Donetsk Region, 84511, Ukraine,
 e-mail: tatjana5555@gmail.com; nnpuiupa@ukr.net

How to cite this article:

Kuznetsov B.I., Nikitina T.B., Bovdii I.V., Voloshko O.V., Kolomiets V.V., Kobylianskyi B.B. Comparison of the effectiveness of triple-loop and double-loop systems of active shielding of a magnetic field in a multi-storey old buildings. *Electrical Engineering & Electromechanics*, 2022, no. 3, pp. 21-27. doi: <https://doi.org/10.20998/2074-272X.2022.3.04>

K.M. Vasylyv

Method of dynamic parameters for mathematical modelling of switching processes of valves closing of semiconductor converters

A method has been developed for mathematical modeling of valve frequency converters (VFC) based on an analysis of the nature of the occurrence and patterns of the flow of inverse current of valves when they are locked using the dynamic parameters of valves, which are series-connected inductance and active resistance, changing in accordance with the pattern of concentration dynamics charges in semiconductor structures (bases, emitters and p-n junctions. Taking into account the presence of the inverse current of semiconductor valves significantly increases the level of adequacy of mathematical modeling of VFCs of arbitrary structure and purpose and in arbitrary modes of their operation, including asymmetric and emergency transient electromagnetic processes of electrotechnical complexes with VFCs, not only during the time interval of switching (closing) of valves, but throughout the entire time modeling. References 21, figures 9.

Key words: valve, switching, inverse current, adequacy level, mathematical model, software code.

Розроблено метод математичного моделювання вентильних перетворювачів частоти (ВПЧ) на підставі аналізу природи виникнення і закономірностей протікання інверсного струму вентилів під час їх запирання застосуванням динамічних параметрів вентилів, якими слугують послідовно з'єднані індуктивність та активний опір, що змінюються відповідно до закономірності динаміки концентрації носіїв електричних зарядів в структурах напівпровідників (базах, емітерах та р-п переходах). Врахування наявності інверсного струму напівпровідникових вентилів істотно підвищує рівень адекватності математичного моделювання ВПЧ довільної структури і призначення та в довільних режимах їх роботи включно з несиметричними та аварійними перехідними електромагнітними процесами електротехнічних комплексів з ВПЧ не лише на проміжку часу комутації (запирання) вентилів, але й в продовж всього часу моделювання. Бібл. 21, рис. 9.

Ключові слова: вентиль, комутація, інверсний струм, рівень адекватності, математична модель, програмний код.

Introduction. One of the research and practical directions of development of Electrical Engineering, called «Electronics», allowed to develop a number of electronic semiconductor devices, based on which a long list of various valve frequency converters (VFCs), which serve as switches for regulated electric drives based on electric [1], alternators [2], autonomous power supply systems [3] and even in multi-winding transformers for simultaneous connection of its secondary windings in the power supply circuit [4]. VFCs are also used in electrical equipment of many other types, for example, in discharge-pulse systems of special technological processes, in particular, the treatment of granular conductive media [5] and so on. The use of VFC as part of electrical equipment has made it possible to fundamentally increase its functionality.

The creation and improvement of valve converter technology is characterized by three main areas: the development of circuit solutions, the definition of static and dynamic characteristics and the study of basic energy relationships. The first direction is characterized by the development of hypothetical models, which are created on the basis of analytical methods using switching functions. A clear expression of this stage are the works [6, 7], which relate to direct frequency converters, but this also applies to other converters (rectifiers, inverters, frequency converters with a DC link, etc.).

Simultaneously with the development and implementation of VFCs, there is a need for mathematical modelling of electromagnetic processes occurring in these converters in order to improve both the systems they belong to and VFCs itself. It is fundamentally important

to note that hypothetical models such as [6, 7] do not allow to model VFC processes.

Judging by the large number of research works aimed at solving the problem of mathematical modelling of VFCs, it turned out to be so complex that the problem of its solution remains relevant today, despite the fact that significant positive results have been clearly achieved.

Today, two approaches are used in the practice of mathematical modelling of VFCs. The first one involves the use of «ready-made» complexes and simulation environments. The MATLAB/Simulink software package has become so widely used, as evidenced by its use are in [8-11]. The same approach should include the use of special boards, for example, in [12] a developing board EPC9035 is used, which is a module of the half-bridge converter, and it was developed by Power Conversion. It is logical to include the software package MotorSolve [13]. It is important to note that in [13] it is emphasized that the models and algorithms embedded in the MotorSolve software are closed to the user, which significantly limits the ability to assess the level of adequacy of models. The same circumstance is typical for other software packages and simulation boards, including MATLAB/Simulink in the context of unavailability of comprehensive information on the used basic mathematical, electrical and other modelling methods, which confirms the need to develop methods and mathematical models of higher adequacy than in the available for modelling of electrical systems that contain VFCs, taking into account all the most important factors influencing the course of processes, among which is the switching of valves. Particular attention should be paid to

© K.M. Vasylyv

insufficiently correct modelling in MATLAB/Simulink of valve locking, which does not take into account the occurrence and flow of inverse currents (currents of opposite direction, sign) during the recovery of valve properties for their closed state, and valves lock (in case of natural switching) immediately at the time of decay of their currents to zero.

The above-mentioned means of mathematical modelling of VFCs, including MATLAB/Simulink, are characterized by a high level of excellence in terms of their practical use. Because here the simulation is performed in the design mode by selecting and combining individual structural and functional elements into a single system, the formation of which automatically creates the appropriate program code (machine algorithm), which is also automatically generated using mathematical, electrical, mechanical or any other methods. Therefore, such modelling tools are often perceived by users as the absolute of perfection, which a priori eliminates the need to critically analyze and assess the level of adequacy of the results.

The second approach is characterized by personal development by researchers of mathematical models and even mathematical and electrical methods and on their basis algorithms and program codes. This requires a thorough knowledge of the whole spectrum from mathematical methods to physics of processes and programming and allows to understand the essence of modelling at the deepest level, and thus have information about the initial assumptions and opportunities to more accurately assess the adequacy of modelling. The position of the author of this article coincides with the second approach.

Based on the above, to substantiate the relevance of the problem to be solved by the article, and to formulate the task set in the article, we perform a brief analysis of the literature to determine the adequacy of mathematical modelling of VFCs in terms of abilities of mathematical and electrical methods used, including initial assumptions made during the development of mathematical models.

Literature analysis. From the point of view of modeling of VFC as a structural element of an arbitrary electrical (electrical power or electromechanical) system, the most effective are methods of two directions, the first of which describes electromagnetic processes by differential equations of electrical state with variable structure and constant parameters [14], and the second one is description of electromagnetic processes by differential equations of electrical state with constant structure and variable parameters.

The first group includes methods in which valves are modelled with ideal keys (S-models) [14]. A convincing advantage of S-models is that they do not need to operate with the parameters of the valves for the locked state, the value of which differs from the parameters for the conductivity state by 6-8 orders of magnitude. This avoids the scatter of parameters and, as a consequence, the rigidity of the system of differential equations and the difficulty of obtaining results in general. However, these

methods have other significant drawbacks that limit the use of S-models of valves in the practice of VFC modelling. Thus, S-models provide a rupture of the valve branches for the closed state of the valves, which a priori means a change in the power circuit of the VFC, and therefore each specific state of the valves must correspond to its circuit power circuit and its corresponding differential equations system (DES). And here there are three problems. The first one is the need to form a large number of DES of electrical state (according to the full combination of all possible circuits of the VFC power circuit, based on each specific state of the valves). This problem entails a second complex problem, which is the need to form conversion functions that establish the connection of two adjacent in time limits of currents and voltages of reactive elements of the valve at the time of switching, i.e. the transition from the previous in time power circuit of the VFC to next one [14]. The process of formation of such functions is a separate task, which not only significantly complicates the mathematical model of the VFC, but also a priori reduces the level of its adequacy. The third problem is to correctly determine the timing of switching valves, because not for all VFCs, and the main for their modes of operation it is possible, for example, for dynamic and asymmetric ones.

Solving the first problem requires significant costs even for VFCs with a simple electrical circuit and it is very difficult to solve this problem when we discuss modelling of transient electromagnetic processes, especially the modelling of asymmetric emergency modes, for which it is almost impossible to correctly predict all valve states. The third problem is solved by determining in advance the state of the valves, which is correct only in the case of artificial switching and only for symmetrical steady state.

Negative on the level of adequacy of key S-models of valves are also affected by ignoring the presence of reverse currents, because the concept of key models a priori excludes the presence of the electric branch of the valve in its closed state, and in terms of physics of process in semiconductor electronic devices such currents (reverse ones) are available.

Known mathematical models, which are based on the formation of a system of differential equations of the electrical state with a constant structure and variable parameters, allow to avoid defects of key models at fundamentally important points [15, 16].

Careful analysis of research literature sources, as well as practical experience in the field of mathematical modelling of VFCs indicates that significant theoretical and practical results in the context of mathematical modeling of electrical systems (ES) with valve frequency converters (according to the concept of their modelling using DES with constant structure and variable parameters) is achieved by combining the idea of modelling valves by separate active-inductive branches [16] with the modular principle of modelling of electrical-machine-valve systems (EMVS) [15] and inversion of DES [17]. This combination made it possible to describe

the electromagnetic and electromechanical processes of arbitrary ES (with VFC of arbitrary structure and with arbitrary control system) by a single DES of electrical and mechanical equilibrium regardless of the state of the valves, which, in turn, allows to take into account mutual influences of EMVS structural elements as well as valve switching and operation of the automatic control system for arbitrary modes of operation of the EMVS (steady and dynamic ones, including symmetrical and asymmetrical, normal and emergency modes).

Let us analyze in more detail the mathematical model of the valve, in which the valve is represented by an active-inductive electric branch [15-17]. Therefore, the mathematical model of the valve as a basic structural element of VFC is developed on the basis of the following initial assumptions:

1) in the conductive state the valve is modelled by an active-inductive branch with small and as close as possible to the real values of inductance and active resistance for the conductive state of the valve;

2) in the locked state the valve is modelled by an active-inductive electric branch with high inductance and active resistance, which correspond as closely as possible to the locked state of the real valve;

3) the valves are switched instantly (the valve is opened according to the results of solving logical equations that describe the operation of the VFC control system), and the valves are closed at the time of transition through zero current of the switching valve (in case of natural switching).

The choice of the values of active resistance and inductance, which are modelled valves, in a sense is arbitrary, and the selection criterion is the highest possible level of adequacy of the model. Based on this, in the practice of VFC modeling for the conductive state we choose such small values of inductance L ($L=0.1 \cdot 10^{-4}$) H and active resistance R ($R=0.1 \cdot 10^{-3}$) Ω , which most closely correspond to the real the value of real valves in the conducting state, and for the closed state the values of inductance and active resistance of the valve branch are taken as those that most accurately correspond to the actual inductance and active resistance for the closed state of the valve $L=0.1 \cdot 10^3$ H and $R=0.1 \cdot 10^4$ Ω . It is critical to note that the L/R ratio (which determines the time constant) for both the conductive and closed states of the valve branch should be such that it is approximately 50 times greater than the integration step and at the same time not less than the minimum time constant of other sections of the electric circuit, the structural element of which is VFC [17].

At the time of transition of the valve to the locked state together with active resistance, also inductance increases by jump by 6-8 orders of magnitude. The consequence of such a change in inductance is the appearance of a rupture of the first current derivative due to a sudden (break type) strong change in the numerical value of the coefficient L at the current derivative in the equation of the electrical state of the valve written according to Kirchhoff second law

$$L \cdot p i + R \cdot i + U = 0, \quad (1)$$

where L , i , R , U are the inductance, current, active resistance and voltage of the valve branch, respectively; $p = d/dt$ is the differentiation operator in time t .

However, after switching the valves, the integral curves are smooth because the first derivative after switching is continuous, which eliminates one of the significant disadvantages of modelling valves with purely active resistance. Maintaining the time constant for the conductive and locked state of the valves constant ensures the stability of the numerical integration of the DES. Due to the sudden and large-scale change of parameters, the currents of closed valves are significantly distorted, but the values of these currents are small enough that at a certain stage of development of the theory of mathematical modeling of VFC, was considered correct to ignore them [15, 17].

Thus, the critical advantage of mathematical modelling of the valve by an active-inductive branch compared to the modelling by purely active resistance is the invariance of the valve time constant for the conducting and locked state [15-17], which provides numerical stability of DES integration that, in turn, is very important in the case of integration of long-term processes.

The necessary task of determining the time of transition of the valve current, which is locked, through zero at the switching step (moment of valve locking time) is determined by a simple procedure of DES inversion, which describes the processes (electromagnetic, electromechanical, mechanical and others) occurring in EMVS containing VFCs [17]. The essence of inversion is to integrate the entire DES at the switching step of the valve, according to its current, which becomes an independent variable, and the numerical value of the integration step is equal to the value of the switching current at the beginning of the switching step. The integration time here becomes an integral variable that is unknown and is the result of the solution of the DES. Therefore, the closing time of the valve is determined by only one step of integration during the inversion of the DES.

It should be noted that the inversion procedure is an indispensable tool for bypassing special points of integral variables, which are characterized by the presence of vertical sections of integral curves, in which the derivative is equal to infinity [17].

Despite the presence of the above rather effective methods of mathematical modelling of VFC, the method in which valves are modelled by active resistances is still used [18].

In the context of the analysis of research literature sources in general it should be noted that other known methods are still used, such as the method of adjustment [19] and the method of fundamental harmonics [20], characterized for which is the adoption of too simplistic (rough) initial assumptions with a focus on their use to calculate symmetric steady-state currents, which a priori does not allow to adequately model the course of

electromagnetic processes occurring in ES with VFC in dynamic and asymmetric modes.

Problem definition. Many years of practice of mathematical modeling of EMVS on the basis of the theory described above [15-17] allowed to obtain results of a fairly high level of adequacy. But a careful analysis of the initial assumptions indicates that there is still a margin in terms of improving the adequacy of VFC mathematical models.

In real operating conditions of semiconductor frequency converters, the state of their valves (in particular, thyristors) and the course of electrical processes occurring in these valves is determined by the concentrations and gradients of positive (holes) and negative (electrons) charges in individual valve structures – emitters, collectors and p-n junctions. It is the concentration and gradients of charge carriers that change over time (restoring the properties of the thyristor for the locked state), ultimately cause a dynamic change in the resistance of the valves during their switching (e.g., locking), and hence the state of each valve.

To restore the properties of the thyristor for the locked state, it is necessary that after the passage of direct current part of the excess charges accumulated in the bases pass through the outer circuit by changing the polarity of the voltage (forward and reverse) at the thyristor electrodes under the action of which there is an inverse (reverse) current which speeds up the process of acquiring a thyristor locked state. Therefore, the state of the valve during the transition from conductive to closed ones changes under the action of reverse voltage and inverse current over a period of time, which is characterized by the presence of appropriate stages of charge concentration in the deep layers of emitters, bases and around *p-n* junctions which means that the valve current during its switching (inverse current) also changes over time according to the change in the concentration of charge carriers.

Based on this, it is obvious that the accepted initial assumption that the valve is locked at the time of transition of the current valve, which switches, to zero (instantaneous switching), is not correct enough.

The process of changing the concentration of charges in the thyristor layers during its locking, if we consider the thyristor as an element of an electric circuit according to the theory of electric circuits, manifests itself in changing (increasing) its resistance to a value equivalent to the resistance of the insulator.

The time of decline of the reverse current in the outer circuit to a certain fixed value does not mean complete restoration of the locked state of the thyristor, because in the deep layers of bases (mainly thick base) there are still excess electrons and holes, which continue to recombine. After the reverse current drops to a steady state, some more pause is required for the excess charges to disappear in the deep layers of the thick base. The total recovery time of the thyristor properties for the locked state t_V which starts from the moment of direct voltage

drop across the thyristor to zero until the thyristor fully acquires the properties for the locked state, is equal to

$$t_V = t_S + t_P, \quad (2)$$

where t_S is the time of decline of the inverse current to a fixed value; t_P is the time of disappearance of excess charges (pauses) in the deep layers of the thick base.

The pause time depends on the geometric dimensions of the thyristor layers, the lifetime of the charge carriers, as well as the rate of decline of the reverse voltage and the rate of increase of the next direct voltage applied to the thyristor. Recovery time t_V is one of the main catalog parameters of the thyristor, because of it its frequency properties depend. It is considered known.

Based on the above, **the goal of the article** is to develop a method of mathematical modelling of electrical processes occurring in valves during their locking, taking into account the restoration of their properties for the closed state, as well as the origin and regularity of inverse current in valves. The development of mathematical models of VFC based on this method will significantly increase the adequacy of mathematical models of both VFC and EMVS, which include VFC.

Substantive provisions. The above analysis of the processes occurring in the thyristor shows that when the valve is closed, first under the action of negative voltage there is an inverse current, and then due to changes in charge concentration in the bases this current decreases, which gives reason to interpret this as an equivalent increase in thyristor resistance if we consider the processes in the thyristor in terms of their external manifestations at the level of the anode-cathode electrical circuit part according to the laws of classical theory of electrical circuits. Based on the latter thesis, it seems logical and correct to consider and, accordingly, to model the switching process that occurs in the thyristor during its locking, based on the following provisions:

1) inductance and active resistance, which simulate the valve branch, dynamically increase according to a certain law, such as linear, parabolic or some other, which provides more accurate than in [16] determination of inverse valve current due to smooth change of inductance and active resistance of the valve and therefore smooth change of the first current derivative in contrast to the rapid one, as in the basic method [16];

2) as the time of the beginning of the dynamic increase of inductance and active resistance of the valve branch we take the moment at which the current of the switching valve is zero (it passes from plus to minus through zero, i.e. there is an inverse current);

3) the DES inversion procedure is performed only to determine the point in time that corresponds to the reference point of the thyristor switching process (occurrence of inverse current), and not for complete locking of the valve;

4) the time of complete recovery of the thyristor for the locked state is considered known and regulated by the technical data of the thyristor;

5) assignment of inductance and active resistance of the valve branch to a value corresponding to the locked state of the thyristor (its final locking) is performed at the time of completion of the process of restoring the properties of the valve for the locked state.

These provisions, together with those adopted in [15-17] in parts 1) and 2) and partly 3) regarding instantaneous valve opening and given above, form the theoretical basis of the method of dynamic parameters of mathematical modelling of valve frequency converters proposed here.

The need to take into account the time of locking valves is obvious not only in terms of patterns of electrophysical processes occurring in valves, but also based on the possibility of operation of a fundamentally certain type of electrical equipment based on VFC which is emphasized in the literature, in particular in [4, 10].

In one of variants, the idea proposed here was implemented in [21] during mathematical modelling of electromagnetic processes occurring in an autonomous power supply system based on an asynchronous generator with a contactless cascade modulator exciter without describing the basic theoretical positions set forth here.

The practical verification of the proposed method is performed on the example of mathematical modelling of N_F -phase AC rectification system (ACRS), a generalized diagram of the power electric circuit of which is shown in Fig. 1, where the letters A, K denote the anode and cathode N_F -phase thyristor groups; the letter M – N_F -phase of the AC network; the letters H, D – the load (rectified current link) and diode, respectively, which serve as structural elements of the ACRS. Other designations are as follows: E, i, R, L, φ – electromotive force, current, active resistance, inductance and electrical potentials of nodes. The letters A, K, M, H, D in the lower indices indicate that the coordinates belong to the structural elements corresponding to the accepted designation, and the letter T – to the thyristors. The numbers in the lower indices indicate the ordinal numbers of the coordinates within the structural elements, and the numbers in the lower indices at the potentials φ – the ordinal numbers of the potentials of the electrical circuit; N_F – the number of phases, the maximum value of which in the program code is limited to 24 ($N_F = 24$).

It is important to note that in the diagram of Fig. 1 (in both the mathematical model and the corresponding program code) provides a choice of either a bridge circuit (when both valve groups are operating and the diode is closed), or a star connection circuit (when the anode group is closed and the diode is constantly in conductive state). Permanently closed diode or valves of the anode group functionally means the rupture of their electrical branches, which changes the generalized circuit to the selected one. The choice of one of these variants of the circuit is performed only during the operation of the program code at the level of numerical values of the state indicators of the thyristors and the diode vector (24).

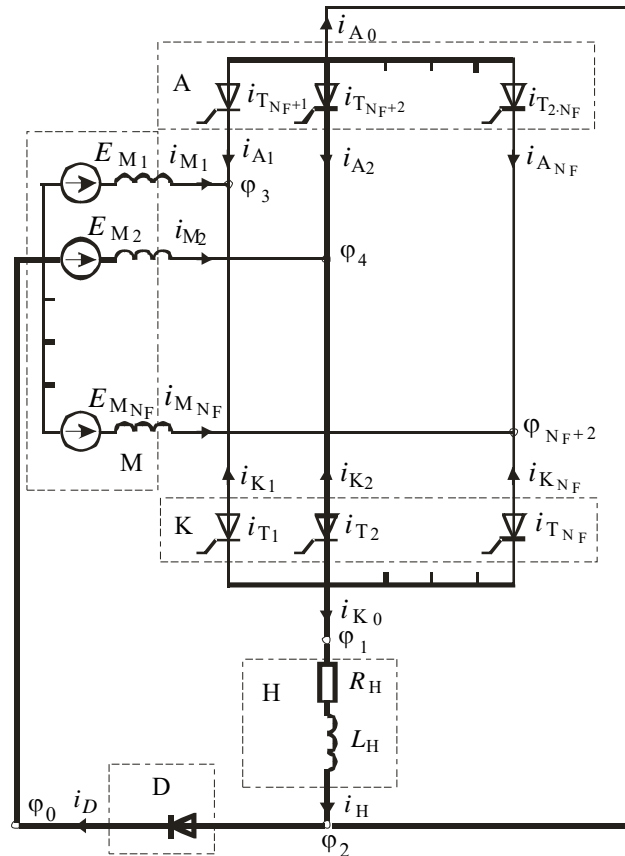


Fig. 1. Diagram of power electric circuit of the N_F -phase AC rectification system

The mathematical model of the N_F -phase ACRS is the DES of the electrical state and the system of logical equations, which simulates the operation of the rectifier control system.

The mathematical model of the N_F -phase system of rectification of electric currents will be developed on the basis of the theory of mathematical modelling of electrical-machine-valve systems [15], according to which mathematical models of arbitrary EMVS are developed on a modular basis, i.e. they are built from «ready» mathematical models of separate structural elements of the diagram of a power electric circuit. As can be seen from Fig. 1, here the following structural elements are: N_F -phase electrical network, N_F -phase cathode and anode thyristor groups, as well as active-inductive load and diode. Consider the mathematical models of each of the structural elements.

Mathematical model of N_F -phase electrical network. We represent the electric network with a $2 \cdot N_F$ -polar, and we describe the electric equilibrium by the vector equation of the outer branches, which has the following form:

$$P i_M + G_M \cdot \varphi_M + T_M = 0, \quad (3)$$

where the vector of currents of external branches:

$$i_M = (i_{M1}, \dots, i_{M_{N_F}}, -i_{M1}, \dots, -i_{M_{N_F}}); \quad (4)$$

coefficient matrix:

$$G_M = \begin{bmatrix} G_e & -G_e \\ -G_e & G_e \end{bmatrix}, \quad (5)$$

in which the diagonal matrix of inverse inductances of the phases of the network:

$$G_e = \text{diag}\left(\frac{1}{L_{M_1}}, \dots, \frac{1}{L_{M_{N_F}}}\right); \quad (6)$$

vector of potentials of external network nodes in which $\varphi_{0_j} = \varphi_0 = 0$ ($j = 1, \dots, N_F$):

$$\varphi_M = (\varphi_3, \varphi_4, \dots, \varphi_{N_F+2}, \varphi_{0_1}, \dots, \varphi_{0_{N_F}}); \quad (7)$$

vector of free terms:

$$T_M = (T_e, -T_e), \quad (8)$$

in which

$$T_e = \left(\frac{i_{M_1} \cdot R_{M_1} - e_{M_1}}{L_{M_1}}, \dots, \frac{i_{M_{N_F}} \cdot R_{M_{N_F}} - e_{M_{N_F}}}{L_{M_{N_F}}} \right). \quad (9)$$

In (6), (9) we indicate L_{M_j} , R_{M_j} , i_{M_j} , e_{M_j} are the inductance, active resistance and instantaneous values of current and electromotive force of the j -th phase of the network.

Mathematical model of N_F -phase cathode thyristor group. The cathode thyristor group is represented by the N_F+1 -polar, and the electrical equilibrium is described by the vector equation of the outer branches, which, according to [15] and the proposed method, has the following form:

$$p i_K + G_K \cdot \varphi_K + T_K = 0, \quad (10)$$

where the vector of currents of external branches:

$$i_K = (i_{K_1}, i_{K_2}, \dots, i_{K_{N_F}}, i_{K_0}) = (-i_{T_1}, -i_{T_2}, \dots, -i_{T_{N_F}}, i_{K_0}), \quad (11)$$

in which

$$i_{K_0} = i_H = \sum_{j=1}^{N_F} i_{T_j}, \quad (12)$$

where i_{T_j} is the current of the j -th thyristor ($j = 1, \dots, N_F$);

where the coefficient matrix:

$$G_K = \begin{bmatrix} G_{T_1} & 0 & \dots & 0 & -G_{T_1} \\ 0 & G_{T_2} & \dots & 0 & -G_{T_2} \\ \vdots & \vdots & \ddots & \vdots & \vdots \\ 0 & 0 & \dots & G_{T_{N_F}} & -G_{T_{N_F}} \\ -G_{T_1} & -G_{T_2} & \dots & -G_{T_{N_F}} & \sum_{j=1}^{N_F} G_{T_j} \end{bmatrix}; \quad (13)$$

vector of external potentials (poles) of the cathode thyristor group:

$$\varphi_K = (\varphi_3, \varphi_4, \dots, \varphi_{2+N_F}, \varphi_1); \quad (14)$$

vector of free terms:

$$T_K = \begin{bmatrix} G_{T_1} \cdot R_{T_1} \cdot i_{T_1} \\ G_{T_2} \cdot R_{T_2} \cdot i_{T_2} \\ \vdots \\ G_{T_{N_F}} \cdot R_{T_{N_F}} \cdot i_{T_{N_F}} \\ -\sum_{j=1}^{N_F} G_{T_0} \cdot R_{T_0} \cdot i_{T_0} \end{bmatrix}. \quad (15)$$

The components of the matrix of coefficients G_K and the vector of free terms T_K are: inverse inductance

$$G_{T_j} = 1/L_{T_j}; \quad (16)$$

where L_{T_j} is the inductance of the j -th thyristor;

R_{T_j}, i_{T_j} are the active resistance and current of the j -th thyristor branch of the cathode valve group.

Mathematical model of N_F -phase anode thyristor group. The electrical equilibrium equation of the anode thyristor group is written based on similar considerations as for the cathode.

Mathematical model of the diode. The diode model is represented by a bipolar, and the electrical equilibrium equations are written on the basis of similar considerations as for thyristor groups.

Mathematical model of active-inductive loading. The static load is represented by a bipolar, and the electric equilibrium is described by the vector equation of the outer branches, which is obtained similarly to the equations of the electric network.

Nodal system of equations of electrical state of N_F -phase current rectification system. The nodal system of equations of electric state is written in the basis of electric potentials of independent nodes of the diagram of a power electric circuit (Fig. 1) and has the following form:

$$A \cdot \varphi + B = 0, \quad (17)$$

where the coefficient matrix:

$$A = \sum_{j=M}^H \Pi_j \cdot G_j \cdot \Pi_j^t; \quad (18)$$

vector of potentials of independent circuit nodes:

$$\varphi = (\varphi_1, \varphi_2, \dots, \varphi_{N_F+2}); \quad (19)$$

vector of free terms:

$$B = \sum_{j=M}^H \Pi_j^t \cdot T_j; \quad (20)$$

and Π_j, G_j, T_j, Π_j^t are the incidence matrices, coefficient matrices, free terms vectors and matrices transposed to Π_j matrices for the j -th structural element of the circuit ($j = M, K, A, D, H$).

Logical equations of the N_F -phase rectifier control system. The operation of the thyristor rectifier control system will be described by logical equations, which have the following form:

$$Z_j = Z_{U_j} \wedge Z_{\alpha_j} \wedge Z_{K_j} = \text{true } j = (1, \dots, 2 \cdot N_F), \quad (21)$$

where Z_j is the condition for opening the j -th thyristor (the j -th thyristor is opened at the true value of Z_j); Z_{U_j} is the condition of opening of thyristors on voltage (Z_{U_j} accepts true value at positive voltage on the j -th thyristor when $U_{T_j} \geq 0$); Z_{α_j} accepts true value when the current angle of the j -th thyristor is in the set range taking into account an ignition angle; Z_{K_j} accepts true value when the j -th thyristor locked, the symbol « \wedge » indicates the operation of logical multiplication (conjunction).

For a diode, the logical equation has the form

$$Z_D = Z_{D_U} \wedge Z_{D_K}, \quad (22)$$

where Z_{D_U} is the condition of opening the diode by voltage (Z_{D_U} has true value at positive voltage on the diode $Z_{D_U} \geq 0$); Z_{D_K} has true value when the diode is locked.

The state of the diode remains constant (locked) for the bridge circuit and conductive – for the circuit with a star connection, when all the thyristors of the anode valve group are locked, i.e. in the electrical circuit and the equation system the anode thyristor group remains but is out of operation (this applies to the program code, which implements the mathematical model of the AC rectification system and the algorithm for calculating electromagnetic processes).

The second-order numerical Runge-Kutta method was used to integrate the DES in the mathematical model of the EMVS, which successfully combines a sufficient level of accuracy with the optimal cost of machine time, and the Gauss method was used to solve the linear system of algebraic equations of electrical state (17).

Algorithm for calculating electromagnetic processes. The input data for the calculation of electromagnetic processes of the system (Fig. 1) is divided into three groups. E_M, L_M, R_M, f_M, N_F – amplitude of electromotive force, inductance and active resistance of phase branches of the network, frequency and number of phases of the network; L_W, R_W – inductance and active resistance for the conducting state of thyristors and diodes; L_Z, R_Z – inductance and active resistance for the closed state of thyristors and diodes; R_H, L_H – active resistance and inductance of active-inductive load; t_V – recovery time of thyristors properties for their locked state.

The second group of input data includes the initial conditions, which are combined into a vector of integrated variables V and a vector K_{Π} of the state of the valves. These vectors have the following structure:

$$V = (i_H, i_D, i_{T_1}, \dots, i_{T_{2N_F}}, i_{M_1}, \dots, i_{M_{N_F}}, t), \quad (23)$$

where t is the integration time;

$$K_{\Pi} = (K_{T_1}, K_{T_2}, K_{T_3}, \dots, K_{T_{2N_F}}, K_D). \quad (24)$$

The elements of the vector K_{Π} (24) have the values:

- 1 – for the conductive state of the valves;
- 0 – for locked state in the case of controlled valves;
- 2 – for locked and uncontrolled valves.

The third group includes the following input data that relate directly to the operation of program code: t_K – final integration time; Δt – step of DES integration in non-switching time intervals; Δt_K – step of integration within the time interval of restoration of thyristor properties for their locked state.

The calculation of electromagnetic processes occurring in the EMVS is performed in the following sequence.

1. Based on the initial conditions: (vector $V(23)$), the array of states of the valves K_{Π} (24) and the input data of the first group matrices of coefficients and vectors of free terms of the structural elements of the rectification system according to the diagram (Fig. 1) are formed: (5), (8); cathode thyristor group – (13), (15) and all other structural elements.

2. On the basis of matrices of coefficients and vectors of free terms of structural elements the matrix of coefficients and vector of free terms of system of equations (17) by (18), (20), accordingly, is formed.

3. The system of equations of electrical state (17) with respect to the vector of potentials of independent nodes φ (19) is solved and the integration vector pV is formed, which is equal to the time derivative of the vector of integrated variables V (23) and has the following structure:

$$pV = (p i_H, p i_D, p i_{T_1}, \dots, p i_{T_{2N_F}}, p i_{M_1}, \dots, p i_{M_{N_F}}, 1). \quad (25)$$

4. Logical equations (21) are solved and the state of thyristors is determined. If the state of the thyristors has changed (at least one of them has opened), then the integration vector pV (25) is redefined.

5. One of the explicit numerical methods is integrating the DES with a given integration step Δt , resulting in its solution (new value of the vector V (23)) at the current integration step.

6. A check is performed regarding the change the value to negative current of any of the open thyristors in the current integration step. If the current of an arbitrary open thyristor has changed from a positive value to a negative one, the DES is inverted, which determines the time at which the open thyristor current is zero (passes from zero from plus to minus). From this point in time, at time interval t_V , and until the time when the j -th thyristor restores its properties for the closed state, the thyristor parameters (its inverse inductance G_{T_j} and active resistance R_{T_j} from (13), (15) for the cathode and similarly for anode thyristor group) changes (the resistance increases and the inverse inductance decreases) according to a given law (linear, parabolic, exponential, or arbitrary others). During the switching time t_V , it is reasonable to reduce the integration step Δt_K by at least one or even two orders of magnitude ($\Delta t_K = \Delta t / 100$) compared to the set integration step Δt for the off-

switching period. In the first integration step after the end of the switching period, the thyristor parameters are assigned a value for the locked state, the state indicator of the thyristor K_{T_j} is set to 0 ($K_{T_j} = 0$), and the integration step returns a value that corresponds outside the switching period.

7. With a certain multiplicity of integration steps, the results of process calculations are output to information files. These results are all the coordinates included in the vector of integrated variables V (23) and the potentials of independent nodes of the diagram (Fig. 1) (19) and their difference in any combination, as well as the results of harmonic analysis of selected coordinates.

8. At each integration step, a check is performed regarding the current integration time t outside its set final value t_K . If the current value of the integration time t is equal to or exceeds the set final t_K ($t \geq t_K$) value, the DES integration procedure is terminated, and otherwise, when $t < t_K$ – continues.

Based on the above mathematical model and the corresponding algorithm, the program code was developed in the FORTRAN programming language for computer modelling of electromagnetic processes occurring in the rectification system of the N_F -phase current (Fig. 1). To test the proposed method for the correctness of its theoretical provisions and suitability for practical application, with the help of the developed software code computer simulation of electromagnetic processes occurring in EMVS is performed (Fig. 1) on several diagrams of the electrical power circuit (the bridge circuit of the rectifier and the star rectifier circuit) with the number of phases $N_F = 1, 2, 3, 6$ and 12 (of 24 possible). The following are the results of computer simulation of electromagnetic processes for a three-phase bridge EMVS.

The input data of the first group are selected with such numerical values that the main coordinates, which are rectified voltage and current i_H, u_H correlated with the values of rectified current and voltage of the valve excitation system of turbogenerators TGV series 500 and 800 MW. Therefore, the main input data of the first group have the following numerical values: for 3-phase electrical network $E_M = 800$ V, $L_M = 0.1 \cdot 10^{-6}$ H, $R_M = 0.1 \cdot 10^{-5}$ Ω , $f = 50$ Hz – amplitude of electromotive force, inductance and resistance of phase electric branches of the network, as well as the frequency of its voltage and current; for rectifier and diode: $L_W = 0.1 \cdot 10^{-3}$ H, $L_Z = 0.1 \cdot 10^3$ H – inductance of thyristor (and diode) branches in conductive and closed states, respectively; $R_W = 0.001$ Ω , $R_Z = 1000$ Ω – active resistance of thyristor (and diode) branches in the conductive and closed states, respectively; $\alpha_r = 0^\circ$ – thyristor control angle; for load: $L_H = 0.075$ H, $R_H = 1.5$ Ω – inductance and active resistance; $\Delta t = 10$ μ s – integration step; $\Delta t_K = 0.1$ μ s – integration step on the switching interval (locking) of valves; $t_K = 0.65$ s – final integration time; $t_V = 50$ μ s – full recovery time of the thyristor properties for the locked state.

The task of modelling is to study the patterns of electrical processes that occur in the thyristors of the rectifier with an emphasis on the study of switching processes that occur during the locking of thyristors, taking into account the presence of inverse (reverse) current. It is noted above that the proposed method and, accordingly, the mathematical model provide the ability to choose the law of change of thyristor parameters during their switching. In this context, at the first stage of the study we consider the linear law of change of parameters of thyristors that switch during their locking.

Figure 2 shows the calculated dependencies of the instantaneous phase currents of the cathode thyristor group.

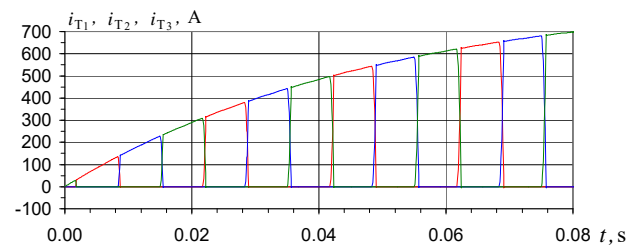


Fig. 2. $i_{T_1}, i_{T_2}, i_{T_3}$ – phase currents of the cathode group

It is obvious that the instantaneous currents of the anode thyristor group have a similar character to the currents of the cathode group, but are shifted by 180° .

An important coordinate in terms of analysis of electromagnetic processes in the EMVS is the rectified current, the curve of which is shown in Fig. 3.

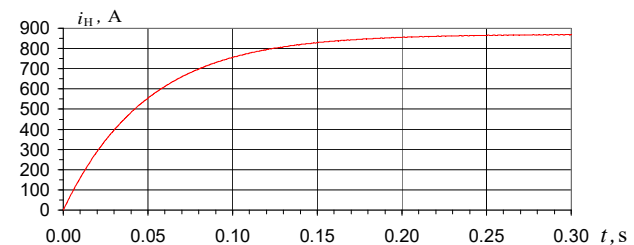


Fig. 3. i_H – rectified current

Figure 3 shows that the curve of the rectified current encircles the curves of the valve currents of the cathode thyristor group in the upper circuit, which corresponds to the physics of electromagnetic processes occurring in the EMVS. In general, the curves of the calculated dependencies of the phase currents of the cathode thyristor group and the rectified current shown in Fig. 2, 3, reflect the course of the transient in EMVS from zero initial conditions and provide information about the functioning of the mathematical model and the corresponding program code on the physics of processes occurring in this system, and, to some extent, the level of adequacy of the real physical system at the level of the nature of the curves qualitatively and at the level of their numerical values quantitatively. From Fig. 3 it is seen that the rectified current acquires a steady-state value

according to the time constant, the value of which is determined by the load parameters, i.e. their ratio L_H/R_H .

From the point of view of the method declared above, it is fundamentally important to obtain information on the presence and regularity of changes in the inverse current of thyristors that switch during their locking, as well as the nature of changes in thyristor parameters at the stage of their locking (during the restoration time of the properties of thyristors for the locked state). Such information is provided by the curves of current, inverse inductance and active resistance of the thyristor, which is locked. For thyristor No. 1 these curves are shown in Fig. 4-6.

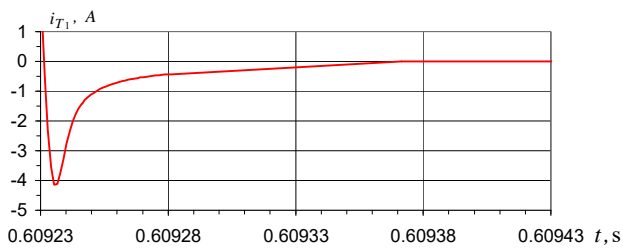


Fig. 4. i_{T_1} – inverse current of the first thyristor (linear law)

The nature of the curve in Fig. 4 clearly indicates not only the presence of the inverse current of the first thyristor (transition of thyristor current to the negative region), but also the pattern of its change, according to which it increases to a certain maximum value (here it is $i_{T_1} = -4.19$ A), and then – its decrease to the steady-state value, which is equal to $i_{T_1} = -0.2$ A.

The presence of inverse current and the regularity of its change are quite expected and are perceived as those that generally correspond to the process of restoring the properties of thyristors for the closed state during their switching. Obviously, here the maximum value of the inverse current is determined by the pattern of changes in the parameters of the switching thyristors. We remind that in this variant of calculations the linear law of change of parameters of the switching thyristors is accepted.

The nature of the curves of inverse inductance (Fig. 5) and active resistance (Fig. 6) is absolutely obvious, because the value of these coordinates varies according to the linear law within given limits according to the initial assumptions and basic provisions of the proposed method.

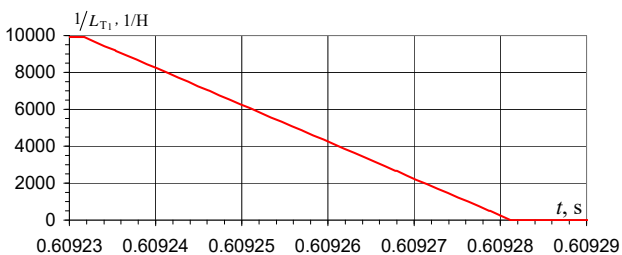


Fig. 5. $1/L_{T_1}$ – inverse inductance of the first thyristor (linear law)

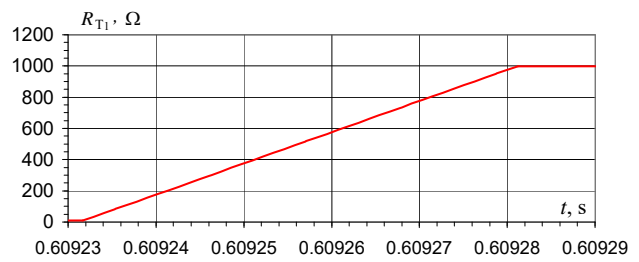


Fig. 6. R_{T_1} – active resistance of the first thyristor (linear law)

In order to determine the effect on the laws of change of the inverse current of thyristors during their locking, we consider similar calculation dependencies obtained on the basis of the parabolic law of change of parameters of thyristors that switch. As for the linear law, Fig. 7-9 show the calculated dependencies of the inverse current, inverse inductance and active resistance of the first thyristor.

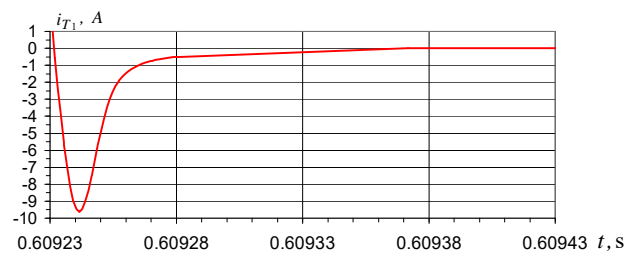


Fig. 7. i_{T_1} – inverse current of the first thyristor (parabolic law)

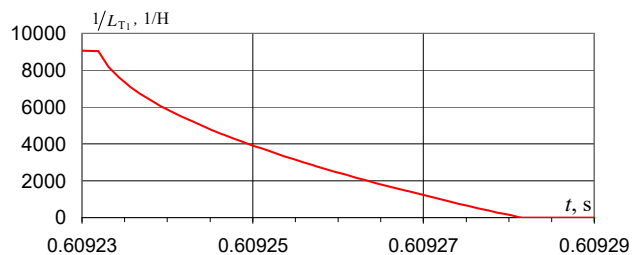


Fig. 8. $1/L_{T_1}$ – inverse inductance of the first thyristor (parabolic law)

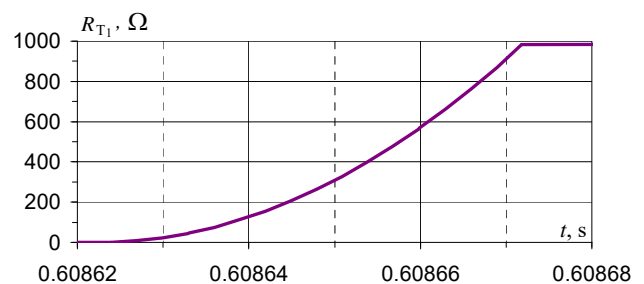


Fig. 9. R_{T_1} – active resistance of the first thyristor (parabolic law)

Figure 7 shows that in general the nature of the current of the first thyristor is similar to the nature of the current in Fig. 4, and the current curve in Fig. 7 differs from the current in Fig. 4 by larger maximum value of inverse current, which is equal to $i_{T_1} = -9.63$ A. This

difference is explained by the lower value of active resistance and inductance of the thyristor at the beginning of the recovery period of thyristor properties for the locked state, which is clearly seen in Fig. 8, 9, in which the corresponding curves have a parabolic shape at the stage of changing the parameters of thyristors.

The fact that the values of the inverse current maximum for the linear and parabolic laws of change of parameters of the thyristor which switches are different (which is a priori obvious) means the problem of choosing the law variant during computer simulation. On the one hand, the linear law on average should describe the change of parameters quite accurately, but, on the other hand, in real conditions such physical processes are almost rarely linear, so there is reason to believe that we should apply some other low – nonlinear (e.g. parabolic) law. Just as the recovery time of thyristor properties for the locked state is different depending on the size and type of thyristors and their individual structures (emitters and bases), it is logical in each case to select the law of change of thyristor parameters. At this stage of the study this is only about methods of accounting for inverse current at a fundamentally higher level of adequacy, than proposed by other currently known methods and, as a consequence, more accurate consideration of thyristor switching processes that occur during their locking.

Thus, the results of mathematical modeling of EMVS taking into account the presence of inverse current in thyristors that switch during their locking, obtained using the proposed method, give grounds to argue that in principle this approach is sufficiently substantiated in terms of accepted correct initial assumptions and consistent real processes that occur in the thyristor at the stage of its locking and restoration of properties for the locked state, at the level of concentration of electric charge carriers in real thyristors, which ultimately manifests itself in changes in thyristor resistance and its function as a semiconductor. The concentration of charges in the structures of the thyristor and its resistance are causally related, which means that if it is reasonable and rational to choose the necessary law of change of thyristor parameters for the recovery phase for the locked state, such a law will correspond to real concentrations of electric charges, which justifies their consideration.

Conclusions and prospects of research.

1. In the current large number of methods of mathematical modelling of VFCs, too little attention is paid to the consideration of inverse currents that occur during closing valves and which actually exist in closed valves and have some impact on both VFC processes and their functioning in general. Correct consideration of inverse currents of valves (especially during their locking) remains an urgent problem, the solution of which would significantly increase the level of adequacy of mathematical modelling of VFCs.

2. In some methods, inverse valve currents are not taken into account at all, for example, in key S-models [14] either obtained incorrectly due to the instantaneous switching of valves accepted in the initial assumptions

and, as a consequence, a sudden change in the first derivative of the valve current that switches during its locking, and therefore inverse currents are ignored [15-17] based on the smallness of their values.

3. It is proposed to simulate the process of locking valves, taking into account the restoration of their properties for the locked state, by changing (according to the determined law) the parameters of inverse inductance and active resistance, for a known locking time. The final locking of the valves should be performed after the time of restoration of the properties of the valves for the locked state. This method, on the one hand, provides a smooth change in the parameters of the valves during their locking and, consequently, the correct values of the inverse current, and, on the other hand, takes into account the occurrence and dynamics of changes in inverse current at the stage of closing the valves during the restoration of their properties for the closed state, which significantly increases the adequacy of mathematical modelling of VFCs and electrical systems containing VFCs.

4. The results of computer simulation of VFCs, obtained using the proposed method in the mathematical model, suggest that the presence and regularity of changes in inverse currents corresponds to the processes occurring in VFCs at the level of concentration of electric charge carriers in terms of the value and the nature of the inverse current, which, in turn, indicates an increase in the adequacy of mathematical modelling of VFCs.

5. The subject of further research is to determine the laws of change of dynamic parameters of valves in accordance with the laws of change in the concentration of charge carriers in their design and at the same time functional structures (bases and emitters).

Conflict of interest. The author declares no conflict of interest.

REFERENCES

1. Shapoval I.A., Mykhalskyi V.M., Doroshenko A.L. Speed control of the doubly-fed induction machine with controlled converters in the stator and rotor circuits. *Technical Electrodynamics*, 2017, no. 6, pp. 18-25. (Ukr). doi: <https://doi.org/10.15407/techned2017.06.018>.
2. Mazurenko L.I., Lishchenko A.I. *Asinkhronnye generatory s ventil'nym i ventil'no-emkostnym vzbuzhdeniem dlia avtonomnykh energoustanovok* [Asynchronous generators with valve and valve-capacitive excitation for autonomous power plants]. Kyiv, Naukova Dumka Publ., 2011. 272 p. (Rus).
3. Mazurenko L.I., Vasylyv K.M., Dzhura O.V., Kotsiuruba A.V. Simulation model and control algorithm for isolated hydro-wind power system. *Technical Electrodynamics*, 2020, no. 1, pp. 17-26. (Ukr). doi: <https://doi.org/10.15407/techned2020.01.017>.
4. Novikov M.A., Panfilov Zh.I., Remizevich T.V., Rashitov P.A. Analysis of the processes of simultaneous switching of thyristor bridges in converters with multi-winding transformers. *Elektrichestvo*, 2013, no. 6, pp. 29-35. (Rus).
5. Shydlovska N.A., Zakharchenko S.M. Progress of semiconductor discharge-pulse systems for processing granular conductive media. *Technical Electrodynamics*, 2020, no. 3, pp. 69-78. (Ukr). doi: <https://doi.org/10.15407/techned2020.03.069>.

6. Dzhudzi L., Pelli B. *Silovye poluprovodnikovye preobrazovateli chastoty* [Power semiconductor frequency converters]. Moscow, Energoatomizdat Publ., 1983. 400 p. (Rus).
7. Zhemerov G.G. *Tiristornye preobrazovateli chastoty s neposredstvennoi svyaz'iu* [Thyristor frequency converters with direct connection]. Moscow, Energiia Publ., 1977. 280 p. (Rus).
8. Zhemerov G.G., Krylov D.S., Mashura A.V. Energy efficiency of the subway electrical supply system with electrical energy recovery at braking. *Electrical Engineering & Electromechanics*, 2019, no. 5, pp. 25-30. doi: <https://doi.org/10.20998/2074-272X.2019.5.04>.
9. Khlopenko N.J. Calculation and design of a robust speed controller of a frequency-controlled induction electric drive. *Electrical Engineering & Electromechanics*, 2020, no. 3, pp. 31-36. doi: <https://doi.org/10.20998/2074-272X.2020.3.05>.
10. Butkevych O.F., Chyzenko O.I., Popovych O.M., Trach I.V. An influence of the facts upon an electrical network's mode during direct start-up of an asynchronous machine in the complex load's composition. *Technical Electrodynamics*, 2018, no. 6, pp. 62-68. (Ukr). doi: <https://doi.org/10.15407/techned2018.06.062>.
11. Bibik O.V., Mazurenko L.I., Shykhnenko M.O. Formation of characteristics of operating modes of switched reluctance motors with periodic load. *Electrical Engineering & Electromechanics*, 2019, no. 4, pp. 12-16. doi: <https://doi.org/10.20998/2074-272X.2019.4.02>.
12. Onikienko Y.O., Pilinsky V.V., Popovych P.V., Lazebnyi V.S., Smolenska O.I., Baran V.S. Modelling of operation modes and electromagnetic interferences of gan-transistor converters. *Electrical Engineering & Electromechanics*, 2020, no. 3, pp. 37-42. doi: <https://doi.org/10.20998/2074-272X.2020.3.06>.
13. Rymsha V.V., Radimov I.N., Gulyy M.V., Merkulov I.V. Motorsolve software package: verification of parameters and characteristics of the brushless permanent magnet motor. *Electrical Engineering & Electromechanics*, 2019, no. 5, pp. 20-24. <https://doi.org/10.20998/2074-272X.2019.5.03>.
14. Tonkal' V.E., Rudenko V.S., Zhuikov V.Ia. *Ventil'nye preobrazovateli peremennoi struktury* [Valve converters of variable structure]. Kyiv, Naukova Dumka Publ., 1989. 336 p. (Rus).
15. Plakhtyna E.G. *Matematicheskoe modelirovanie elektromashinno-ventil'nykh sistem* [Mathematical modeling of electromachine-valve systems]. Lvov, Vishcha Shkola Publ., 1986. 164 p. (Rus).
16. Dizhur D.P. Method of simulation on a digital computer of valve converter circuits. *Izvestia of the Research Institute of Direct Current*, 1970, no. 16, pp. 7-9. (Rus).
17. Fil'ts R.V. *Matematicheskie osnovy teorii elektromekhanicheskikh preobrazovatelei* [Mathematical foundations of the theory of electromechanical converters]. Kyiv, Naukova Dumka Publ., 1979. 208 p. (Rus).
18. Hutsaliuk V.Y., Yurchenko O.M., Zubkov I.S., Pazenko V.P. Serial connecting of resonant voltage inverters for high-frequency induction heating equipment. *Technical Electrodynamics*, 2018, no. 4, pp. 70-73. (Ukr). doi: <https://doi.org/10.15407/techned2018.04.070>.
19. Belov G.A., Serebriannikov A.V., Garanin S.G. Calculation and analysis of processes in reversible pulse converters with two-way differential pulse-width modulation. *Elektrichestvo*, 2013, no. 2, pp. 42-63. (Rus).
20. Goriakin D.V., Mytsyk G.S. Study of the operating modes of a three-phase bridge inverter circuit. *Elektrichestvo*, 2012, no. 5, pp. 23-31. (Rus).
21. Mazurenko L.I., Vasylyv K.M. The law of the electric magnetic processes of the security exercise systems of the autonomous asynchronized generator on the case of the cascade three-phase three-flexible voltage modulator. *Technical Electrodynamics*, 2018, no. 6, pp. 46-49. (Ukr). doi: <https://doi.org/10.15407/techned2018.06.046>.

Received 03.02.2022

Accepted 25.03.2022

Published 01.06.2022

K.M. Vasylyv¹, Doctor of Technical Science, Professor,

¹ Lviv Polytechnic National University,

12, Bandera Str., Lviv, 79013, Ukraine,

e-mail: karl.vasylyv@gmail.com (Corresponding author)

How to cite this article:

Vasylyv K.M. Method of dynamic parameters for mathematical modelling of switching processes of valves closing of semiconductor converters. *Electrical Engineering & Electromechanics*, 2022, no. 3, pp. 28-38. doi: <https://doi.org/10.20998/2074-272X.2022.3.05>

G.V. Bezprozvannykh, M.V. Grynshyna

Effective parameters of dielectric absorption of polymeric insulation with semiconductor coatings of power high voltage cables

Introduction. The presence of semiconductor shields leads to additional dielectric losses compared to polymer insulation without shields. Losses in cables in the presence of semiconductor coatings depend on the dielectric permittivity and resistivity of the composite polymeric material, which are frequency-dependent characteristics. **Purpose.** To determine in a wide range of frequencies, taking into account the variance of electrophysical characteristics and thickness of semiconductor shields effective electric capacitance and tangent of dielectric losses angle of high-voltage power cables with polymer insulation. **Methodology.** Serial-parallel nonlinear circuit replacement of semiconductor coatings and linear polymer insulation to determine in a wide range of frequency the effective parameters of the dielectric absorption of a three-layer composite system of high-voltage power cables of single core. **Practical value.** The obtained relations are the basis for the development of practical recommendations for substantiating the thickness and electrophysical parameters of semiconductor shields to reduce the impact on the effective tangent of the dielectric losses angle of a three-layer composite system of high-voltage power cables. References 23, figures 6.

Key words: semiconductor coatings, polymer insulation, high-voltage power cable, nonlinear substitution circuit, complex dielectric permittivity, active conductivity, effective electric capacitance, effective tangent of dielectric losses angle.

На підставі послідовно-паралельної нелінійної схеми заміщення напівпровідних покриттів та лінійної електричної полімерної ізоляції у широкому діапазоні частоти визначено ефективні параметри діелектричної абсорбції силових високовольтних кабелів одножильного виконання. За результатами моделювання, з урахуванням дисперсії електрофізичних характеристик напівпровідних покриттів, доведено, що ефективна електрична ємність тришарової композитної ізоляційної системи визначається ємністю полімерної ізоляції. Встановлено характер частотних залежностей та максимальні значення ефективного тангенсу кута діелектричних втрат в залежності від співвідношення між питомою електропровідністю на постійному і змінному струмі та товщиною напівпровідних екранів. Отримані співвідношення є підставою для розроблення практичних рекомендацій щодо обґрунтування товщини та електрофізичних параметрів напівпровідних покриттів для зменшення їх впливу на ефективний тангенс кута діелектричних втрат тришарової композитної електроізоляційної системи силових високовольтних кабелів. Бібл. 23, рис. 6.

Ключові слова: напівпровідні покриття, полімерна ізоляція, силовий високовольтний кабель, нелінійна схема заміщення, комплексна діелектрична проникність, активна питома провідність, ефективна електрична ємність, ефективний тангенс кута діелектричних втрат.

Introduction. Electricity supply of 15 million units of different consumer groups in Ukraine is provided by medium voltage networks the length of which is over 92 % of networks of all classes [1]. The need to replace about 140 thousand km of electrical networks causes the introduction of high-voltage power cables with polymer insulation based on cross-linked polyethylene, high-performance thermoplastic elastomers [2, 3]. With the introduction of modern high-voltage cable systems, there is, first, the possibility of widespread use of an extensive distributed cable network for data transmission of large volumes [4, 5]. Secondly, the diagnosis of insulation to identify signs of its degradation, which are most pronounced in the high frequency range [6-12].

A design feature of high-voltage power cables with polymer insulation is the presence of semiconductor shields on the conductor core and insulation to equalize the electric field on the core surface and reduce the electric field on the insulation surface [13, 14]. Semiconductor shields are applied simultaneously with the extrusion of polymer insulation. This technology provides high adhesion between the shields and insulation, reduces the likelihood of gas inclusions in the insulation and on the border with semiconductor shields.

Typically, semiconductor layers of composite polymeric material are used by adding carbon black as a filler in the polymer lattice. This material provides a gradual change in the electrical conductivity and

dielectric permittivity during the transition of the electric field from the conductor to the electrical insulation [14].

The introduction of acetylene carbon black impurities with a resistivity of particles in the range from 0.0001 to 100 $\Omega\cdot\text{m}$ leads to a symmetrical radial profile of the electric field in the power cable of coaxial design, which prevents the increase of the local field. The local electric field is the main stimulus for the formation and growth of water treeings, partial discharges and even mechanical ruptures of power cables [15].

The presence of semiconductor shields leads to additional dielectric losses compared to polymer insulation without shields. Losses in cables in the presence of semiconductor coatings depend on the dielectric permittivity and resistivity of the composite polymer material, which are frequency-dependent parameters [16, 17].

The paper uses the concept of dielectric absorption, which is associated with energy losses in polyethylene insulation, which in turn are determined by the electrical capacitance and the tangent of the angle of dielectric losses. In the general case, the term «dielectric absorption» is explained, for example, in [18, 19] and is used in the study of physical mechanisms of electromagnetic energy absorption, residual charge generation, etc., as well as in the theory of electromagnetic waves [20]. Also, in [19] dielectric absorption and losses are separated.

© G.V. Bezprozvannykh, M.V. Grynshyna

Analysis of literature sources. Electrophysical characteristics of semiconductor coatings significantly affect the distribution of the electric field and losses in cables at operating frequency of 50 Hz [13]. In [21], the authors obtained an effective tangent of the dielectric losses angle of three-layer composite insulation without taking into account the dependence on the frequency of conductivity and dielectric permittivity and the thickness of semiconductor coatings.

The influence of semiconductor coatings taking into account the polarization losses in the frequency range 200 Hz – 20 kHz is taken into account in [16] on the basis of a parallel substitution circuit in the form of electric capacitance and resistance of each component of the three-layer composite system connected in series.

Using the substitution circuit of polyethylene cross-linked insulation with three relaxation RC-circuits in [22] the emergence of relaxation maxima on the frequency dependence of the dielectric losses angle tangent in polymer insulation with semiconductor shields of medium voltage power cables was proved.

In [17], it was experimentally shown that dielectric losses in semiconductor shields become dominant in high-voltage power cables with polymer insulation at frequency of more than 10 MHz.

The issues of determining the influence of the thickness and electrophysical characteristics of semiconductor coatings on the effective electric capacitance and the tangent of the dielectric losses angle of high-voltage power cables in a wide frequency range remain unresolved and extremely relevant.

The goal of the paper is to determine the effective electric capacitance and tangent of the dielectric losses angle of high-voltage polymer-insulated power cables in a wide frequency range, taking into account the dispersion of electrophysical characteristics and the thickness of semiconductor shields.

Dispersion of electrophysical characteristics of semiconductor coating materials. Polymer non-polar insulation of power cables (cross-linked polyethylene, thermoplastic elastomers) is characterized by high dielectric properties in a wide frequency range. Thus, for cross-linked polyethylene insulation, the specific volume conductivity γ is equal to $(10^{-13} - 10^{-14})$ S/m; dielectric permittivity – at the level of 2.5 (static value) and, practically, weakly dependent on the frequency in the region of weak electric fields, which causes insignificant value of the dielectric losses coefficient $\varepsilon''(\omega)$ and, accordingly, the dielectric losses tangent $\text{tg}\delta$ of polymer insulation. The dispersion of dielectric permittivity for cross-linked polyethylene is $2.5 - 2.38 = 0.12$ in the frequency spectrum up to 100 MHz [3].

Semiconductor coatings are characterized by high values of specific volume conductivity, dielectric permittivity and dielectric losses coefficient, due to the morphological and structural features of the polymer material.

Conditionally composite polymer material with soot impurities consists of three phases: insulating (Fig. 1, region I), percolation (Fig. 1, region II) and conductive (Fig. 1, region III) [23].

In the low-frequency region, the tunneling effect between soot (carbon) particles is considered to be the main mechanism, which causes a weak dependence of the specific electrical conductivity of the semiconductor on the frequency.

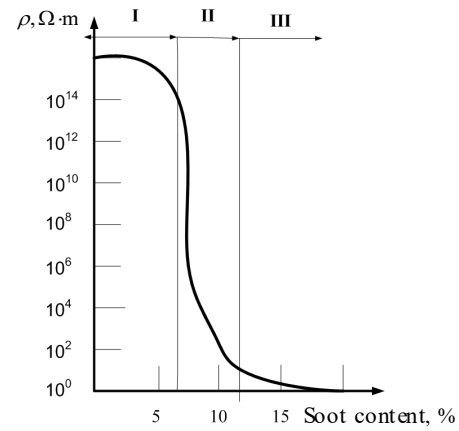


Fig. 1. Influence of soot content on the specific conductivity of semiconductor coating of power cables

In this case, the specific volumetric conductivity γ differs little from the specific volumetric conductivity γ_{dc} at DC. The tangent of the dielectric losses angle $\text{tg}\delta_e$ due to electrical conductivity decreases inversely proportional to the circular frequency ω and the real part $\varepsilon'(\omega)$ of the complex dielectric permittivity ε^* of the semiconductor coating material (Fig. 2,a) [21]

$$\text{tg}\delta_e = \frac{\gamma_{dc}}{\omega \cdot \varepsilon_0 \cdot \varepsilon'(\omega)}, \quad (1)$$

where $\varepsilon_0 = 8.85 \cdot 10^{-12}$ F/m is the dielectric constant.

The total tangent of the dielectric losses angle $\text{tg}\delta_{semi}$ of the semiconductor coating takes into account the losses on the electrical conductivity $\text{tg}\delta_e$ and polarization $\text{tg}\delta_{pol}$ [16, 21]

$$\text{tg}\delta_{semi} = \text{tg}\delta_e + \text{tg}\delta_{pol} = \frac{\gamma_{dc}}{\omega \cdot \varepsilon_0 \cdot \varepsilon'(\omega)} + \frac{\varepsilon''(\omega)}{\varepsilon'(\omega)}, \quad (2)$$

where $\varepsilon''(\omega)$ is the frequency-dependent imaginary part of the complex dielectric permittivity (Fig. 2,b).

Taking into account that the active specific volume conductivity $\gamma_{ac}(\omega)$ at the alternating voltage of the circular frequency ω is determined by the imaginary part $\varepsilon''(\omega)$ of the complex dielectric permittivity (Fig. 2,c)

$$\gamma_{ac}(\omega) = \omega \cdot \varepsilon_0 \cdot \varepsilon''(\omega), \quad (3)$$

the frequency dependence of the tangent of the dielectric losses angle of semiconductor coatings is defined as

$$\text{tg}\delta_{semi}(\omega) = \frac{\gamma_{semi}(\omega)}{\omega \cdot \varepsilon_0 \cdot \varepsilon'(\omega)}, \quad (4)$$

where $\gamma_{semi}(\omega) = \gamma_{dc} + \gamma_{ac}(\omega)$.

Under the condition $\gamma_{ac}(\omega) \gg \gamma_{dc}$, which is valid for modern compositions of semiconductor shields of high-voltage power cables, the tangent of the dielectric losses angle of semiconductor coatings is determined on the basis of [16]

$$\text{tg}\delta_{semi}(\omega) = \frac{\gamma_{ac}(\omega)}{\omega \cdot \varepsilon_0 \cdot \varepsilon'(\omega)}. \quad (5)$$

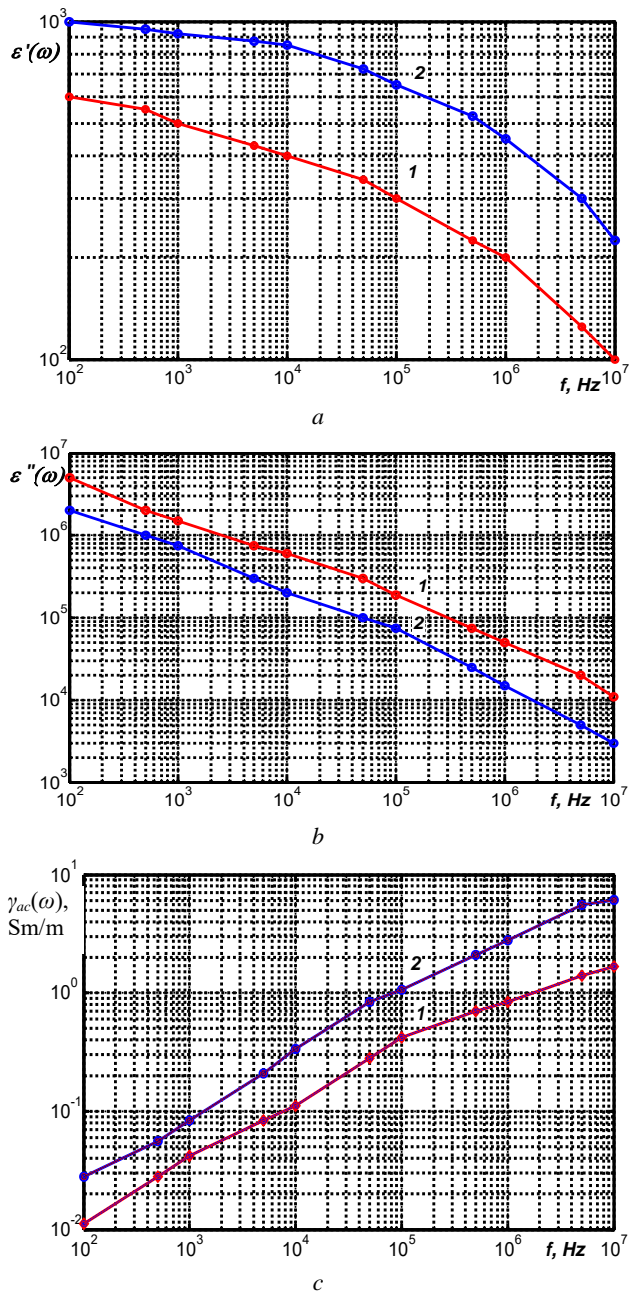


Fig. 2. Typical frequency dependencies of electrophysical characteristics of coatings on the core (curve 1) and insulation (curve 2) of high-voltage power cables under the condition of linear volt-ampere characteristics of semiconductor materials

Effective parameters of dielectric absorption of polymer insulation with semiconductor coatings. The serial-parallel substitution circuit of a three-layer composite insulation system taking into account the dispersion of electrophysical characteristics of semiconductor coatings of power high-voltage cables is presented in Fig. 3.a.

In Fig. 3.a the following marked: C_{ins} , $C_1(\omega)$, $C_2(\omega)$ – capacitances and G_{ins} , $G_1(\omega)$, $G_2(\omega)$ – active conductivities of layers of polymer insulation and semiconductor coatings on the conductive core and insulation according to the parallel substitution circuit, respectively

$$C_1(\omega) = \frac{\varepsilon'_1(\omega) \cdot \varepsilon_0 \cdot S_1}{\Delta_1}; \quad C_{ins} = \frac{\varepsilon'_{ins} \cdot \varepsilon_0 \cdot S_{ins}}{\Delta_{ins}}; \quad (6)$$

$$C_2(\omega) = \frac{\varepsilon'_2(\omega) \cdot \varepsilon_0 \cdot S_2}{\Delta_2};$$

$$G_1(\omega) = \gamma_{semi1}(\omega) \cdot \frac{S_1}{\Delta_1}; \quad G_{ins} = \gamma_{ins} \cdot \frac{S_{ins}}{\Delta_{ins}}; \quad (7)$$

$$G_2(\omega) = \gamma_{semi2}(\omega) \cdot \frac{S_2}{\Delta_2};$$

where ε'_{ins} , $\varepsilon'_1(\omega)$, $\varepsilon'_2(\omega)$ are the real parts of the complex dielectric permittivities of insulation, semiconductor coatings on the core and insulation; γ_{ins} is the volumetric specific conductivity of insulation; γ_{semi1} , γ_{semi2} are the total volumetric specific conductivities taking into account the frequency dependence of the active conductivity of semiconductor coatings on the core and insulation; S_{ins} , S_1 , S_2 are the cross sections and Δ_{ins} , Δ_1 , Δ_2 are the thicknesses of insulation and semiconductor coatings on the core and insulation, respectively.

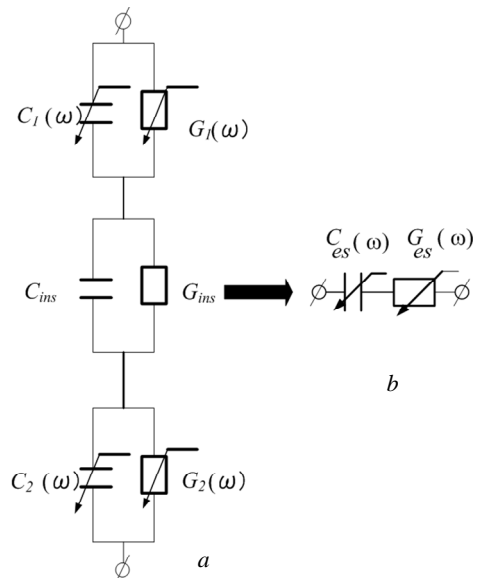


Fig. 3. Serial-parallel (a) and equivalent serial (b) nonlinear substitution circuit of electrical insulation and semiconductor coatings of high-voltage power cables

The transition from parallel to sequential substitution circuit allows to determine the tangent of the dielectric losses angle, electrical capacitance and active conductivity of each of the components, taking into account (5) – (7):

– for semiconductor coating on the core:

$$\text{tg} \delta_1(\omega) = \frac{G_1(\omega)}{\omega \cdot C_1(\omega)};$$

$$C_{1s}(\omega) = C_1(\omega) \cdot (1 + \text{tg} \delta_1^2(\omega)); \quad (8)$$

$$G_{1s}(\omega) = \frac{\omega \cdot C_{1s}(\omega)}{\text{tg} \delta_1(\omega)};$$

– for cable insulation:

$$C_{inss} = C_{ins} \cdot (1 + \text{tg} \delta_{ins}^2);$$

$$G_{inss} = \frac{\omega \cdot C_{inss}}{\text{tg} \delta_{ins}}; \quad (9)$$

– for semiconductor coating on insulation:

$$\begin{aligned} \operatorname{tg} \delta_2(\omega) &= \frac{G_2(\omega)}{\omega \cdot C_2(\omega)}; \\ C_{2s}(\omega) &= C_2(\omega) \cdot (1 + \operatorname{tg} \delta_2^2(\omega)); \\ G_{2s}(\omega) &= \frac{\omega \cdot C_{2s}(\omega)}{\operatorname{tg} \delta_2(\omega)}; \end{aligned} \quad (10)$$

and determine the effective electrical parameters (Fig. 3,b) of the three-layer composite system under the given frequency electrophysical characteristics and thickness of semiconductor coatings and insulation:

– electrical capacitance $C_{es}(\omega)$:

$$\begin{aligned} C_{es}(\omega) &= \frac{C_{1s} \cdot C_{inss} \cdot C_{2s}}{C_{1s} \cdot C_{inss} + C_{1s} \cdot C_{2s} + C_{inss} \cdot C_{2s}} = \\ &= \frac{2 \cdot \pi \cdot A_1 \cdot A_{ins} \cdot A_2 \cdot D_1 \cdot D_{ins} \cdot D_2}{\omega^2 \cdot \varepsilon_0 \cdot [A_1 \cdot A_{ins} \cdot \varepsilon_2'(\omega) \cdot \Delta_2 \cdot D_1 \cdot D_{ins} + A_1 \cdot A_2 \cdot \varepsilon_{ins}' \cdot \Delta_{ins} \cdot D_1 \cdot D_2 + A_{ins} \cdot A_2 \cdot \varepsilon_1'(\omega) \cdot \Delta_1 \cdot D_{ins} \cdot D_2]}; \end{aligned} \quad (11)$$

and the tangent of the angle of the dielectric losses $\operatorname{tg} \delta_{es}(\omega)$

$$\begin{aligned} \operatorname{tg} \delta_{es}(\omega) &= \frac{\omega \cdot C_{es}(\omega)}{G_{es}(\omega)} = \frac{\omega \cdot C_{es}(\omega) \cdot (G_{1s}(\omega) \cdot G_{inss} + G_{1s}(\omega) \cdot G_{2s}(\omega) + G_{inss} \cdot G_{2s}(\omega))}{G_{1s}(\omega) \cdot G_{inss} \cdot G_{2s}(\omega)} = \\ &= \frac{\omega \cdot \varepsilon_0 \cdot D_1 \cdot D_{ins} \cdot D_2 \cdot \left[A_1 \cdot A_{ins} \cdot \frac{\varepsilon_2''(\omega)}{\gamma_{semi2}(\omega)} \cdot \frac{\Delta_2}{D_2} + A_1 \cdot A_2 \cdot \frac{\varepsilon_{ins}''}{\gamma_{ins}} \cdot \frac{\Delta_{ins}}{D_{ins}} + A_{ins} \cdot A_2 \cdot \frac{\varepsilon_1''(\omega)}{\gamma_{semi1}(\omega)} \cdot \frac{\Delta_1}{D_1} \right]}{\omega^2 \cdot \varepsilon_0 \cdot [A_1 \cdot A_{ins} \cdot \varepsilon_2'(\omega) \cdot \Delta_2 \cdot D_1 \cdot D_{ins} + A_1 \cdot A_2 \cdot \varepsilon_{ins}' \cdot \Delta_{ins} \cdot D_1 \cdot D_2 + A_{ins} \cdot A_2 \cdot \varepsilon_1'(\omega) \cdot \Delta_1 \cdot D_{ins} \cdot D_2]}; \end{aligned} \quad (12)$$

where

$$\begin{aligned} A_1 &= (\omega^2 \cdot \varepsilon_0^2 \cdot \varepsilon_1'(\omega) + \gamma_{semi1}^2(\omega)), \\ A_{ins} &= (\omega^2 \cdot \varepsilon_0^2 \cdot \varepsilon_{ins}' + \gamma_{ins}^2), \\ A_2 &= (\omega^2 \cdot \varepsilon_0^2 \cdot \varepsilon_2'(\omega) + \gamma_{semi2}^2(\omega)) \end{aligned}$$

are the dimensional coefficients (S^2/m^2), which take into account the frequency dependencies of the electrophysical characteristics of semiconductor shields and polymer insulation;

$$\begin{aligned} D_1 &= (r_g + \Delta_1 / 2), \\ D_{ins} &= (r_g + \Delta_1 + \Delta_{ins} / 2), \\ D_2 &= (r_g + \Delta_1 + \Delta_{ins} + \Delta_2 / 2) \end{aligned}$$

are the geometric factors depending on the radius of the core r_g , the thickness of the semiconductor coating on the core Δ_1 , the insulation thickness Δ_{ins} and the thickness of the semiconductor coating on the insulation Δ_2 , respectively.

Frequency dependencies of effective parameters of dielectric absorption of three-layer composite system of power cables. Figure 4 shows the model frequency dependencies of the effective capacitance (Fig. 4,a) and the effective tangent of the dielectric losses angle (Fig. 4,b) determined on the basis of (11), (12) of the single-core power cable with conducting core cross section of 95 mm^2 of voltage of 35 kV. The thickness of the cross-linked polyethylene insulation is 7 mm. The value of the tangent of the dielectric losses angle of polyethylene insulation is $\operatorname{tg} \delta_{ins} = 1 \cdot 10^{-4}$ at frequency of 50 Hz and varies inversely proportional to the frequency in accordance with (1): the determinant is the losses on electrical conductivity.

Curves 1, 1' and 2 correspond to the components of the electrical capacitance: 1 and 1' – semiconductor shield on the conductive core, the thickness of which is 0.8 and 1.6 mm, respectively; curve 2 – semiconductor shield on

cross-linked polyethylene insulation with thickness of 0.6 mm, curve 3 – actual effective capacitance of the three-layer composite system (Fig. 4,a). The volume specific conductivities on the DC of semiconductor coatings on the core and insulation are equal to $\gamma_{dc1} = 10^{-2} \text{ S/m}$, $\gamma_{dc2} = 1 \text{ S/m}$, respectively. For polyethylene insulation – $\gamma_{ins} = 10^{-13} \text{ S/m}$. The active specific volume conductivities of semiconductor screens $\gamma_{ac}(\omega)$ at AC voltage were determined on the basis of (3) taking into account the frequency dependence of the components presented in Fig. 2,c.

Curve 4 is the value of the insulation capacitance determined by (13) [15]

$$C_{ins} = \frac{2 \cdot \pi \cdot \varepsilon_{ins}' \cdot \varepsilon_0}{\log(D_2 / D_1)}, \text{ F/m.} \quad (13)$$

The simulation results prove that the values of the effective capacitance of the three-layer insulation (curve 3, Fig. 4,a), determined on the basis of (11), practically do not differ from the values obtained on the basis of (13) (curve 4, Fig. 4,a). The effective capacitance of a cable with semiconductor shields is determined by the dielectric permittivity of the insulation itself and the thickness of the components: the effect of semiconductor shields is insignificant in the high frequency range (see Fig. 4,a).

The effective tangent of the dielectric losses angle of a three-layer composition significantly depends on both the electrophysical properties of semiconductor shields materials and their thickness, even with the same electrophysical characteristics (compare curves 1 and 1', Fig. 4,b). Increasing the thickness of the semiconductor shield along the conductive core by 2 times leads to an increase in the effective tangent of the dielectric losses angle by 2 times with the manifestation of the characteristic dipole maximum at frequency of 50 kHz.

Variation of electrophysical properties and thickness of semiconductor shields along the core and cross-linked

polyethylene insulation of 35 kV power cable leads to different nature of frequency dependencies of the effective tangent of the dielectric losses angle (curves 1–5, Fig. 5,a). The effective tangent of the dielectric losses angle of the three-layer composite system is (1–7) times higher than the dielectric losses tangent of the actual polymer insulation $\text{tg}\delta_{\text{ins}}$ for frequency of 50 Hz (compare curves 1–5, Fig. 5,b) in a wide frequency range due to the active specific conductivity of semiconductor coatings (see Fig. 2,c).

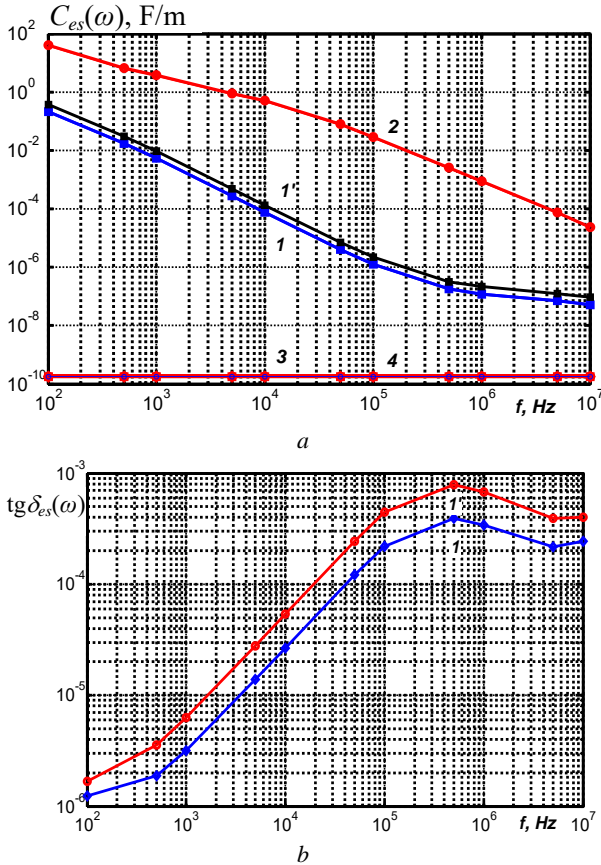


Fig. 4. Frequency dependencies of equivalent parameters dielectric absorption of high-voltage power cable taking into account the dispersion of electrophysical characteristics of semiconductor shields

In Fig. 5a,b curves 1–5 correspond to the model dependencies, curve 6 (Fig. 5,a) – to the experimental one for a sample of power single-core cable with polyethylene insulation (insulation thickness 7 mm) at voltage of 35 kV, which has long been unprotected from moisture – natural humidity (there are no water-blocking tapes in the cable construction). Dielectric parameters are measured by a digital meter of the capacitance and the tangent of the dielectric losses angle RLC Meter DE-5000 in the frequency range 100 Hz – 100 kHz.

Curve 1 – the thickness of semiconductor shields on the conductor and insulation is 1.2 and 0.6 mm, curve 2 – $\Delta_1 = 0.6$ mm and $\Delta_2 = 1.2$ mm with specific conductivity at DC $\gamma_{dc1} = 10^{-4}$ S/m, $\gamma_{dc2} = 10^{-2}$ S/m, respectively; curves 3, 4 – $\Delta_1 = 0.6$ mm and $\Delta_2 = 1.2$ mm with $\gamma_{dc1} = 10^{-4}$ S/m, $\gamma_{dc2} = 10^{-4}$ S/m (curve 3) and $\gamma_{dc1} = 10^{-2}$ S/m, $\gamma_{dc2} = 10^{-4}$ S/m (curve 4); curve 5 – $\Delta_1 = 1.2$ mm and $\Delta_2 = 0.6$ mm with $\gamma_{dc1} = 10^{-2}$ S/m, $\gamma_{dc2} = 1$ S/m.

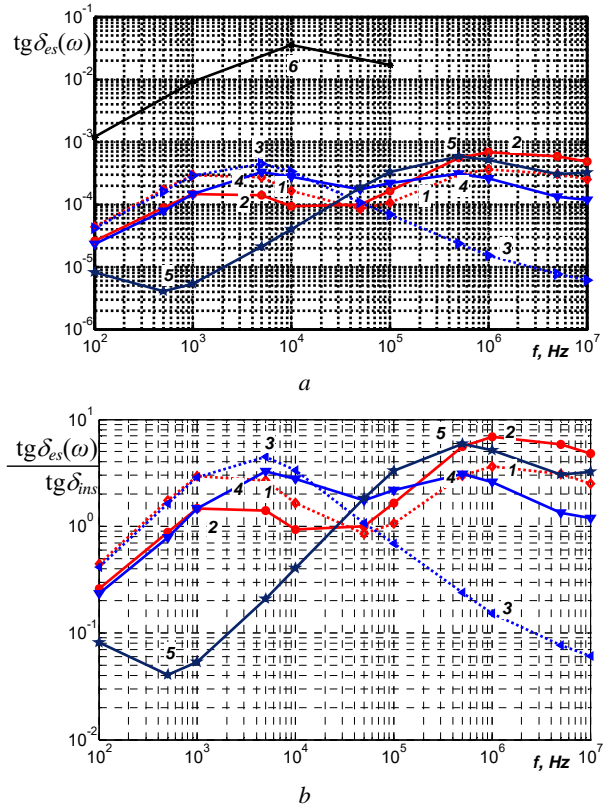


Fig. 5. Frequency dependencies of the tangent of the dielectric losses angle at different electrical properties and thickness semiconductor shield of the power cable for voltage of 35 kV

Thus, provided:

- 1) $\Delta_1 > \Delta_2$ and $\gamma_{ac1} > \gamma_{dc1}$, $\gamma_{ac2} \approx \gamma_{dc2}$ (curve 1) there are two characteristic maxima of the effective tangent of the dielectric losses angle near the frequency of 1 kHz and 1 MHz with values of $\text{tg}\delta_{\text{es}}$ 3–3.3 times higher than $\text{tg}\delta_{\text{ins}}$;
- 2) $\Delta_1 < \Delta_2$ and $\gamma_{ac1} > \gamma_{dc1}$, $\gamma_{ac2} > \gamma_{dc2}$ (curve 3) there is one maximum of $\text{tg}\delta_{\text{es}}$ at frequency of 5 kHz with a value exceeding 4.5 times;
- 3) $\Delta_1 > \Delta_2$ and $\gamma_{ac1} \approx \gamma_{dc1}$, $\gamma_{ac2} \approx \gamma_{dc2}$ (curve 5) there is one maximum of $\text{tg}\delta_{\text{es}}$ near the frequency of 50 MHz with values of $\text{tg}\delta_{\text{es}}$ 6 times higher than $\text{tg}\delta_{\text{ins}}$.

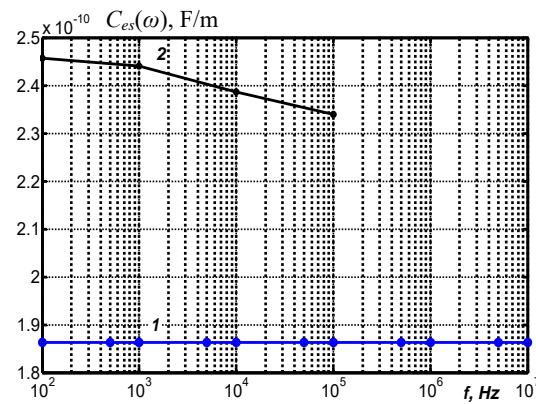


Fig. 6. Model (curve 1) and experimental (curve 2) dependencies of equivalent capacitance of single-core cable for voltage of 35 kV

The nature of the change in the frequency model dependence of the effective tangent of the dielectric losses

angle for curve 3 is more consistent with the experimental curve 6 of the sample of power cable with moistened polyethylene insulation. Confirmation of humidity and diffusion of acetylene carbon black (carbon) according to the theory of percolation is the manifestation of the frequency dependence of the capacitance of the sample of 35 kV power cable with insulation thickness of 7 mm (Fig. 6, curve 2).

Conclusions.

For the first time in a wide frequency range the influence of electrophysical characteristics, taking into account the dispersion of complex dielectric permittivity and active specific conductivity, as well as the thickness of semiconductor shields on the effective dielectric absorption parameters of three-layer composite electrical insulation system of high voltage cables has been determined.

The effective electrical capacitance of a three-layer composite system is determined by the electrical capacitance of the polymer insulation and depends on the dielectric permittivity and insulation thickness, which is confirmed by experimental data.

The considered algorithm for determining the effective tangent of the dielectric losses angle in a wide frequency range is the basis for creating a methodology for substantiating the electrophysical characteristics and thickness of semiconductor shields to reduce their impact on effective dielectric absorption parameters of high-voltage polymer-insulated power cables.

Conflict of interest. The authors declare no conflict of interest.

REFERENCES

1. SOU-N EE 20.302: 2007 Standards for testing electrical equipment (new version 2020). – K., 262 p. (Ukr). Available at: <http://www.elec.ru/articles/innovacionnyc-proryv-na-rynke-silovyh-transformatorov> (Accessed 28 March 2021).
2. Wire and Cable Market (Type - Wire, and Cable; Voltage Type - Low Voltage, Medium Voltage, and High and Extra High Voltage; Applications - Power Transmission and Distribution, Transport, Data Transmission, Infrastructure): Global Industry Analysis, Trends, Size, Share and Forecasts to 2024. *Infinium Global Research*, 2020. Available at: <https://www.infiniumglobalresearch.com/ict-semiconductor/global-wire-and-cable-market> (Accessed 28 March 2021).
3. Huang X., Zhang J., Jiang P. Thermoplastic insulation materials for power cables: History and progress. *Gaodianya Jishu/High Voltage Engineering*, 2018, vol. 44, no. 5, pp. 1377-1398. doi: <https://doi.org/10.13336/j.1003-6520.hve.20180430001>.
4. Cataliotti A., Daidone A., Tine G. Power Line Communication in Medium Voltage Systems: Characterization of MV Cables. *IEEE Transactions on Power Delivery*, 2008, vol. 23, no. 4, pp. 1896-1902. doi: <https://doi.org/10.1109/TPWRD.2008.919048>.
5. Zhao H., Zhang W., Wang Y. Characteristic Impedance Analysis of Medium-Voltage Underground Cables with Grounded Shields and Armors for Power Line Communication. *Electronics*, 2019, vol. 8, no. 5, p. 571. doi: <https://doi.org/10.3390/electronics8050571>.
6. Linde E., Verardi L., Fabiani D., Gedde U.W. Dielectric spectroscopy as a condition monitoring technique for cable insulation based on crosslinked polyethylene. *Polymer Testing*, 2015, vol. 44, pp. 135-142. doi: <https://doi.org/10.1016/j.polymertesting.2015.04.004>.
7. Bezprozvannykh G.V., Kostjukov I.A. A calculation model for determination of impedance of power high voltage single-core cables with polymer insulation. *Electrical Engineering & Electromechanics*, 2021, no. 3, pp. 47-51. doi: <https://doi.org/10.20998/2074-272X.2021.3.08>.
8. Araneo R., Celozzi S., Faria J.A.B. Frequency-domain analysis of the characteristic impedance matrix of high-voltage transmission lines. *2017 International Symposium on Electromagnetic Compatibility – EMC EUROPE*, 2017, pp. 1-6. doi: <https://doi.org/10.1109/EMCEurope.2017.8094662>.
9. Papazyan R. Concepts for market-based MV cable operations and maintenance using insulation parameters measurements. *2020 12th Electrical Engineering Faculty Conference (BulEF)*, 2020, pp. 1-5. doi: <https://doi.org/10.1109/BulEF51036.2020.9326055>.
10. Heider M.Z., Rahman M.M., Al-Arainy A.A. Study of frequency variant tan delta diagnosis for MV cables insulation status assessment. *2019 5th International Conference on Advances in Electrical Engineering (ICAEE)*, 2019, pp. 260-264. doi: <https://doi.org/10.1109/ICAEE48663.2019.8975616>.
11. Sun B., Makram E., Xu X. Impacts of Water-Tree Fault on Ferroresonance in Underground Cables. *Journal of Power and Energy Engineering*, 2017, vol. 05, no. 12, pp. 75-86. doi: <https://doi.org/10.4236/jpee.2017.512010>.
12. Burkes K.W., Makram E.B., Hadidi R. Water Tree Detection in Underground Cables Using Time Domain Reflectometry. *IEEE Power and Energy Technology Systems Journal*, 2015, vol. 2, no. 2, pp. 53-62. doi: <https://doi.org/10.1109/IPETS.2015.2420791>.
13. Kucheriava I.M. Power cable defects and their influence on electric field distribution in polyethylene insulation. *Technical Electrodynamics*, 2017, no. 2, pp. 19-24. doi: <http://doi.org/10.15407/teched2017.02.019>.
14. Wei Y., Liu M., Han W., Li G., Hao C., Lei Q. Charge Injection Characteristics of Semi-Conductive Composites with Carbon Black-Polymer for HVDC Cable. *Polymers*, 2019, vol. 11, no. 7, p. 1134. doi: <https://doi.org/10.3390/polym11071134>.
15. Bezprozvannykh G.V., Kyessayev A.G. The technological and exploitative factors of local increase of electric field strength in the power cable of coaxial design. *Electrical Engineering & Electromechanics*, 2016, no. 6, pp. 54-59. doi: <https://doi.org/10.20998/2074-272X.2016.6.09>.
16. Liu T., Fothergill J., Dodd S., Nilsson U. Influence of semicon shields on the dielectric loss of XLPE cables. *2009 IEEE Conference on Electrical Insulation and Dielectric Phenomena*, 2009, pp. 246-249. doi: <https://doi.org/10.1109/CEIDP.2009.5377792>.
17. Chunchuan Xu, Boggs S.A. High frequency properties of shielded power cable. Part 2: sources of error in measuring shield dielectric properties. *IEEE Electrical Insulation Magazine*, 2006, vol. 22, no. 1, pp. 7-13. doi: <https://doi.org/10.1109/MEL.2006.1618966>.
18. Fröhlich H. *Theory of dielectrics. Dielectric constant and dielectric loss*. Oxford, Clarendon Press, 1949. 180 p.
19. Murphy E.J., Lowry H.H. The Complex Nature of Dielectric Absorption and Dielectric Loss. *The Journal of Physical Chemistry*, 1930, vol. 34, no. 3, pp. 598-620. doi: <https://doi.org/10.1021/j150309a014>.
20. Von Hippel A.R. *Dielectrics and waves*. New York, London, John Wiley and Sons, Chapman and Hall, 1959. 284 p.
21. Zolotarev V.M., Zolotarev V.V., Buzko S.V., Antonets T.Yu., Naumenko A.A. Effect of shield conductivity on

dielectric losses in cables. *Bulletin NTU «KhPI»*, 2014, no. 21, pp. 50-54. (Rus). Available at: http://repository.kpi.kharkov.ua/bitstream/KhPI-Press/9217/1/vestnik_HPI_2014_21_Zolotaryov_Vliyaniye.pdf (Accessed 15 April 2021).

22. Bezprozvannykh A.V., Kessaev A.G., Shcherba M.A. Frequency dependence of dielectric loss tangent on the degree of humidification of polyethylene cable insulation. *Technical Electrodynamics*, 2016, no. 3, pp. 18-24. doi: <https://doi.org/10.15407/techned2016.03.018>.

23. Rother R. *Fillers for Polymer Applications*. Springer International Publishing, 2017. 317 p. doi: <https://doi.org/10.1007/978-3-319-28117-9>.

Received 10.01.2022

Accepted 11.02.2022

Published 01.06.2022

G.V. Bezprozvannykh¹, Doctor of Technical Science, Professor,
M.V. Grynyshyna², Postgraduate Student, Tech. Director,

¹National Technical University «Kharkiv Polytechnic Institute»,
2, Kyrpychova Str., Kharkiv, 61002, Ukraine,

e-mail: bezprozvannykh@kpi.kharkov.ua (Corresponding author)

²TOV «Interkabel Kiev»,

5, Dachnaya Str., p. Kapitanovka,

Kiev-Svyatoshinsky district, Kiev region, 08112, Ukraine,

e-mail: m.grynyshyna@interkabel.ua

How to cite this article:

Bezprozvannykh G.V., Grynyshyna M.V. Effective parameters of dielectric absorption of polymeric insulation with semiconductor coatings of power high voltage cables. *Electrical Engineering & Electromechanics*, 2022, no. 3, pp. 39-45. doi: <https://doi.org/10.20998/2074-272X.2022.3.06>

M. Ali Moussa, A. Derrouazin, M. Latroch, M. Aillerie

A hybrid renewable energy production system using a smart controller based on fuzzy logic

Introduction. This article proposes an improved energy management and optimization system with an intelligent economic strategy based on fuzzy logic technology with multiple inputs and outputs (I/O). It is used to control hybrid electric energy sources built around photovoltaic solar panels, wind turbine and electric energy storage system assisted by the electric grid. **The novelty** in this work that solar photovoltaic, wind turbine and storage system energy sources are prioritized over the grid network which is solicited only during adverse weather conditions, in order to supply a typical household using up to 4,000 Wh per day. In addition of that, the surplus of renewable energy produced during favorable climatic condition is used to produce hydrogen suitable for household heating and cooking using electrolyzer system. **Purpose.** Development of improved energy management and optimization system with an intelligent economic strategy based on fuzzy logic technology. This system is embedded on Arduino 2560 mega microcontroller, on which the fundamental program of fuzzy logic and the distribution of events with all possible scenarios have been implemented according to a flowchart allowing the management of the hybrid system. **Methods** as well as a parametric search and a simulation to characterize the system, are carried out in order to put on the proposed techniques to ensure continuous accommodation at home. **Results.** The proposed system results confirm their effectiveness by visualizing the output control signals from the electronic switches. **Practical value** of which transmits power through a single-phase DC/AC converter to power the AC load for the accommodation. References 20, figures 9.

Key words: hybrid energy system, renewable energy, battery storage, fuzzy logic, smart management.

Вступ. У статті пропонується вдосконалена система керування та оптимізації енергоспоживання з інтелектуальною економічною стратегією, заснованою на методі нечіткої логіки з декількома входами та виходами. Вона використовується для керування гібридними джерелами електричної енергії, побудованими на основі фотоелектричних сонячних панелей, вітрових турбін та системи зберігання електричної енергії за допомогою електричної мережі. **Новизна** роботи полягає в тому, що сонячні фотоелектричні, вітряні турбіни та джерела енергії системи зберігання енергії мають пріоритет над електромережею, яка запитується лише за несприятливих погодних умов, щоб забезпечувати типове домашнє господарство до 4000 Вт·год на день. Крім того, надлишки відновлюваної енергії, що виробляється у сприятливих кліматичних умовах, використовуються для виробництва водню, придатного для опалення та приготування їжі за допомогою електролізера. **Мета.** Розробка вдосконаленої системи керування та оптимізації енергоспоживання з інтелектуальною економічною стратегією, що заснована на методі нечіткої логіки. Ця система вбудована в мегамікроконтролер Arduino 2560, на якому реалізована головна програма нечіткої логіки та розподілу подій з усіма можливими сценаріями за блок-схемою, що дозволяє керувати гібридною системою. Зазначені **методи**, а також параметричний пошук та моделювання для характеристики системи реалізуються для того, щоб застосувати запропоновані методи для забезпечення безперервного проживання у будинку. **Результати.** Результати реалізації запропонованої системи підтверджують їх ефективність візуалізацією вихідних сигналів керування від електронних перемикачів. **Практичне значення** полягає у передачі потужності через однофазний перетворювач постійного струму у змінний для живлення навантаження змінного струму для житлових приміщень. Бібл. 20, рис. 9.

Ключові слова: гібридна енергетична система, відновлювана енергія, акумуляторна батарея, нечітка логіка, інтелектуальне керування.

Introduction. To avoid the problems of pollution in the production of electricity, alternative solutions can be photovoltaic (PV), wind, or even hydroelectric sources. In addition, the distribution networks cannot be sufficient to supply electricity to the entire world population: whether they are in the mountains or on an island, in the least inhabited regions or in the middle of the desert, the sites difficult to be access or very isolated cannot always be connected to the network, for lack of technical solutions or economic viability. However, being able to be sized for domestic use, renewable energy sources lend themselves particularly well to the production of electricity called isolated sites, or micro-grids. They are then often associated with batteries, which ensure the storage of energy in the event of excess production, or to compensate for the momentary lack of power during peak consumption [1-5].

Hybrid energy systems (HES) combining several sources, such as renewable energy systems (RES), the national distribution network (the historical network), traditional energy sources and storage systems are generally considered as a solution for the future is efficient and reliable, many analyzes (planning and sizing) have been performed on single-source renewable energy sources, with the main objective being to determine the best system configuration for efficient and safe operation.

They can be developed in a substantial way for urban electrification or isolated (rural) sites. When, the cost of grid extension of rural electrification is prohibitive due to geographic isolation, low population density, or limited financial resources. In both cases, the issue of energy management, particularly in terms of resource control and efficiency, becomes essential. In this, it has become in the space of a few years, one of the eminently strategic subjects. Its implementation is both complex and exciting as the prospects are promising, especially in relation to smart grid technologies.

A different hybrid energy system has been studied in many research papers [6-18]. The authors in [19] are proposing to realize a technical-economic capacity of a hybrid renewable energy system (HRES) to occupy the energy demand of a university site in the Himalayan state of northeastern Sikkim, and also the other aspect of exploring the electrical voltage of other renewable energy resources such as biogas and syngas and hydrokinetic energy, in addition to a solar-wind hybridization mainly carried out in the resource-rich urban planning territory of the east of the Himalayas. The authors in [20] operating a hybrid off-grid renewable energy system (HRES) for an institution's huge high-rise urban development in Nigeria. The exploitation is based on a comparison of the employment of a single

criterion with a combination of factors in determining the most feasible energy system. A wind turbine, a diesel generator, a PV system, and a battery storage system are all part of the proposed HRES – Multiple Energy Resources Hybrid Optimization (HOMER).

The goal of the paper is the development of improved energy management and optimization system with an intelligent economic strategy based on fuzzy logic technology.

This paper is a continuity of previous work [17], where a complex hybrid energy system is studied, sized, optimized and a smart router system is achieved to manage electric energy flow based on fuzzy logic techniques. The added value in this contribution is the implementation of artificial intelligence in hardware based on Arduino type microcontroller which built on multi analog/digital inputs/outputs and PWM (pulse width modulation technique), from where electronic switches command' signals are highlighted and discussed.

Hybrid energy system design. The proposed hybrid energy system HES is a combination of solar energy conversion system comprising solar panels with integrated a MPPT (maximum power point tracker) converter, wind energy conversion system built on direct current outcome converter permanent magnet synchronous wind turbine and then a storage system with acid-plumb batteries.

The equipment of the dwelling operates at 220V 50 Hz with an optimal use of the energy thanks to economic LED lighting lamps and zenithal daylight. The standard equipment used in this house consumes total amount energy about 4 kWh per day with a peak of 660 W when using the entire electric component at the same time. The system energy flow is managed by a smart energy router system based on artificial intelligence using fuzzy logic algorithm [8].

Figure 1 shows the global hybrid system with the combination of solar PV, wind turbine and storage within all the regulators.

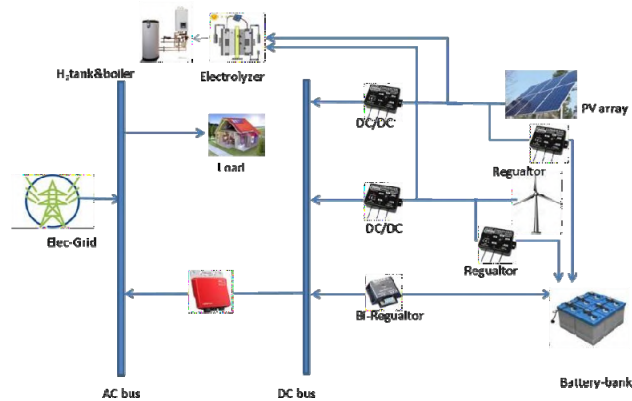


Fig. 1. Synoptic of the proposed HPS (Hybrid Power System)

Components of the hybrid energy system. As part of our work, solar energy has been favored as a primary renewable energy source because of the chosen site at north of Algeria. The selected PV panels are polycrystalline type delivering, each of them, an output summer voltage amount of 30.7 V and developing 250 W nominal power. The panels are equipped with MPPT regulators [9] and connected in parallel to obtain an

overall power of 2 kW. This choice was pointed due to their quality/price [9, 10]. The connection of the solar panels in parallel mode to multiply the output current and maintain a standardized output voltage at 24 V DC which is fed directly into the common DC bus of the system

Considering the case study, the instantaneous power cannot exceed, according to the established dimensioning and for the case of maximum of energy demand, the value of 660W. For this reason and taking into account the wind potential in the study area, our choice was oriented towards small, inexpensive EO-24-1000R-UGS-Silent three- bladed wind turbine with 2.9 m rotor diameter, developing nominal power up to 1 kW.

Because of their availability on the market in different capacities, as well as their proven effectiveness, especially in the automotive field, our choice was pointed to an electrochemical lead-acid storage type, although the cycling behavior of the latter is not important compared to other technologies such as lithium. But they have the advantage of an affordable investment, much simpler maintenance and their resistance to high electrical capacity demands. What joins our goal to develop at low cost the use and generalization of the renewable energy in our country.

Given the uncertain nature of renewable resources, particularly solar and wind, deficits and excess energy production can be observed. For the second situation, the excess of energy is often harmful for the stability of the system. For that, several works proposed an evacuation of this surplus produced electric energy in a specific load which one calls dump load [17]. Previous work in reference [18], proposed to recover this surplus of energy production, from only renewable sources especially during favorable climatic conditions, and to exploit it to produce hydrogen with the help of an electrolyze device in order to be useful for household heating and cooking

Fuzzy logic controller. The intelligent controller, as shown in Fig. 2, with its multiple image entries of the available power profiles as well as the outputs such as grid to load (G2L), PV to load (PV2L), wind turbine to load (W2L), battery storage to load (B2L), PV to battery storage (PV2B), wind turbine to battery storage (W2B), electric grid to battery storage (G2B), PV to electrolyzer (PV2E) and wind turbine to electrolyzer (W2E), represents the routes pointed by the intelligent controller allowing renewable and conventional energies transfer to the load, to the electrolyze and the storage. The Fuzzy Logic System Controller (FLSC) is designed according to well-defined basic conditions allowing the best functioning of the overall system for all its scenarios and possible operating points by considering the logical constraints initially fixed by an expert [19] as:

- the principal sources of load feeding are PV and wind energy, followed by battery storage and finally the electrical grid;
- batteries are replenished by the grid only when solar and wind energy levels are low;
- when all other sources of energy are off, the power grid powers the load.

Only PV solar energy and a wind turbine are used to power the hydrogen production system. These instructions and recommendations initially dictated for suitable operation of the intelligent controller are shown

in the simplified diagram below in Fig. 3, which generate a set of 81 rules. The formulation and implementation of these constraints are established using fuzzy logic tools and performing dozens of combinations with the three levels – H (high) 3, M (medium) 2 and L (low) 1. On the other hand, the logical results of the FLSC are imposed for each combination at the entrance of the four energetic states (charge, solar, wind, storage).

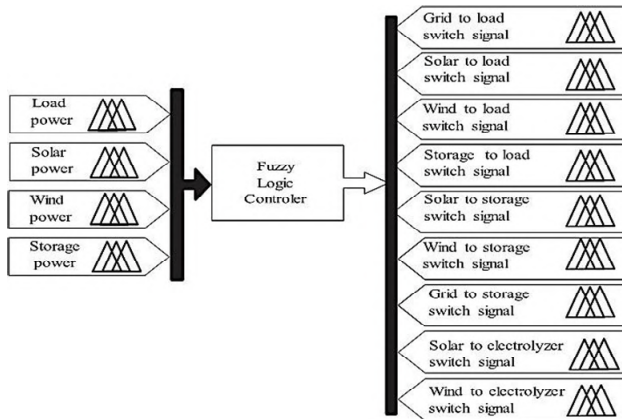


Fig. 2. FLSC intelligent controller diagram (fuzzy logic smart controller)

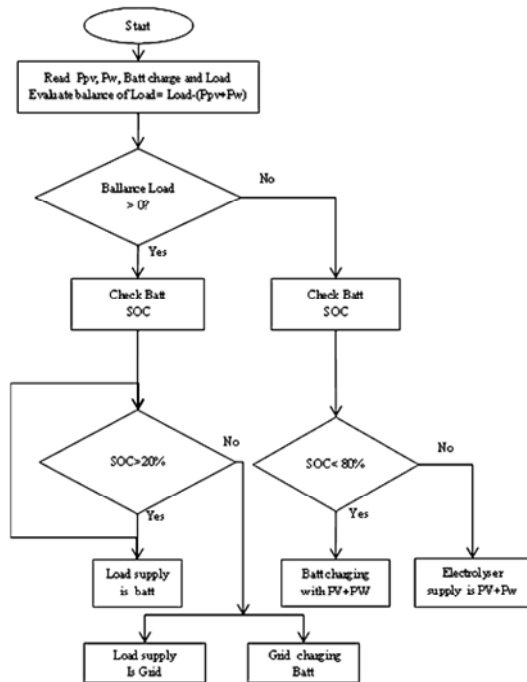


Fig. 3. Operational flowchart of the HPS-FLSC (hybrid power system – fuzzy logic system controller). Here SOC is the state of charge

FLSC hardware implementation. In the last section on a previous work [17], we presented a simulation work on MATLAB fuzzy logic, the results obtained are detailed, where the outputs of the FLSC manage the PWM blocks in order to control the command signals duty cycle of electronic switches.

In the goal to move from simulation to emulation, we successfully implemented the topology of smart controller under Arduino mega 2560 microcontroller, which is built on more eeprom memory capacity, over than fifty analog and digital I/O and thirteen ready pulse width modulation PWM outputs. That why we pointed this type of hardware.

It corresponds wildly to the presented FLSC controller, which needs to control nine electronic switches. The work consists to convert the MATLAB fuzzy logic FLSC program to the open-source Arduino Software (IDE) sketch. The entries are images depicted of the inputs energy profiles like the load demand, the PV, the wind turbine and the capacity of the batteries.

Figure 4 presents the electrical scheme of the controller using Proteus electronic software where all connections with the microcontroller are shown. The outgoing are connected to LEDs displaying the level of the output PWM signal depending on the four inputs power profiles' states exactly as illuminated in precedent section.

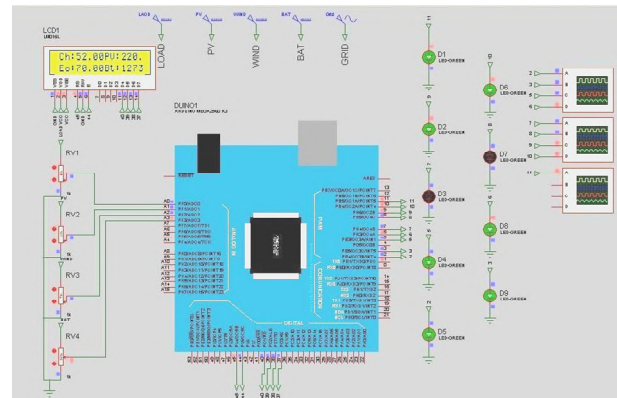


Fig. 4. Electrical scheme of the Arduino-FLSC controller

Using MATLAB tools for simulation, data power profiles for solar and wind energy, as well as battery storage, were imposed on the system during a typical day in May to ensure the reliability of the intended FLSC controller [20]. The load supplies vary from month to month. Summer is the hottest season in the northern hemisphere. As a result, the load demand for those months would be reduced, and for the other three seasons, more gloomy days with lower temperatures are projected. As a result, due to the possibility of heating and additional lights, these months would have a higher electricity demand. Figure 5 depicts the power profile inputs as they change during the course of a typical day.

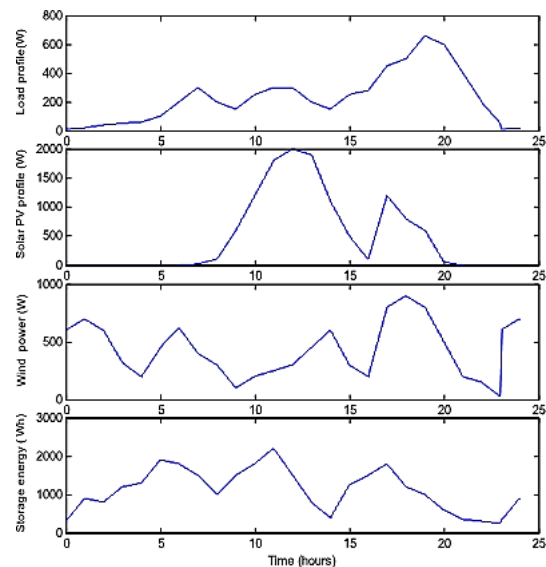


Fig. 5. Power profiles versus time of the hybrid power system (HPS) during 24 hours

Results and discussion. Figure 6 shows the FLSC defuzzification findings utilizing the corresponding membership functions in MATLAB Fuzzy tools. The resulting analog signals oscillate between 0 and 1, and PWM techniques are used to convert each FLSC output to a square signal with a variable duty cycle and fixed frequency. Each command signal is injected into a matching electronic switch, and all of the switches' selected quantities of available energy sources are added together and converted to AC current via the DC/AC converter to fulfill habitation appliances. Excess DC-produced renewable energy is used directly to make hydrogen. Based on these results [18, 20], the implementation of the hardware consists to conversion and adaptation of the validated MATLAB program in the IDE platform where command lines are processed and compiled in IDE-Arduino microcontroller software.

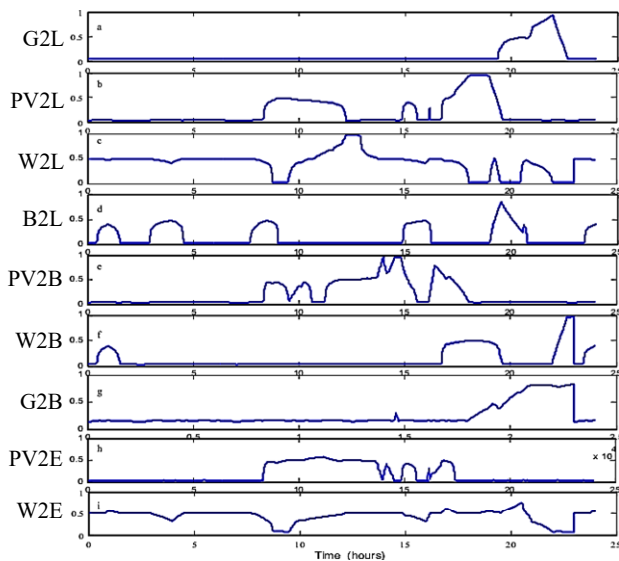


Fig. 6. FLSC outcome switches command signals

In order to validate the operative FLSC program after many steps from MATLAB to Ide-Arduino, a simulation in Proteus software is scheduled and rule no. 2 is tested, where the input sand the outputs of the FLSC-Arduino obey to a series of codes as mentioned in the framed line [1.1.1.2, 1.1.1.2.1.1.1.1.1] shown in the Fig. 7 below. The settings of the input levels are assumed by potentiometers which are visualized on LCD display in Fig. 4 as:

- load (Ch): 52 W of 660 W → Low L → level 1,
- PV: 220 W of 2000 W → Low L → level 1,
- wind turbine: 70 W of 1000 W → Low L → level 1,
- battery: 1273 W-h of 2400 W-h → Medium M → level 2.

With the same reasoning, the FLSC-Arduino outcomes are shown in the Fig. 8 under PWM command signals, which are ready to excite the electronics switches. The width (duty-cycle) of the 9 outputs from the top to the bottom correspond widely to the suite of the series line [1.1.1.2; 1.1.1.2.1.1.1.1.1]→[L.L.L.M; L.L.L.M.L.L.L.L.L]

The top to the bottom correspond widely to the suite of the series line: [1.1.1.2; 1.1.1.2.1.1.1.1.1]→[L.L.L.M; L.L.L.M.L.L.L.L.L]

Figure 9 presents a screenshot of the real cabling and running hardware.

```
[System]
Name='FLSC49-15mars'
Type='mamdani'
Version=2.0
NumInputs=4
NumOutputs=9
NumRules=80
AndMethod='min'
OrMethod='max'
ImpMethod='min'
AggMethod='max'
DefuzzMethod='centroid'
```

```
[Rules]
1 1 1 1, 2 1 1 1 1 1 3 1 1 (1) : 1
1 1 1 2, 1 1 1 2 1 1 1 1 1 (1) : 1
1 1 1 3, 1 1 1 2 1 1 1 1 1 (1) : 1
1 1 2 1, 1 1 2 1 1 2 1 1 1 (1) : 1
```

Fig. 7. FLSC Fuzzy Inference System file screenshot (codification of rule no. 2)

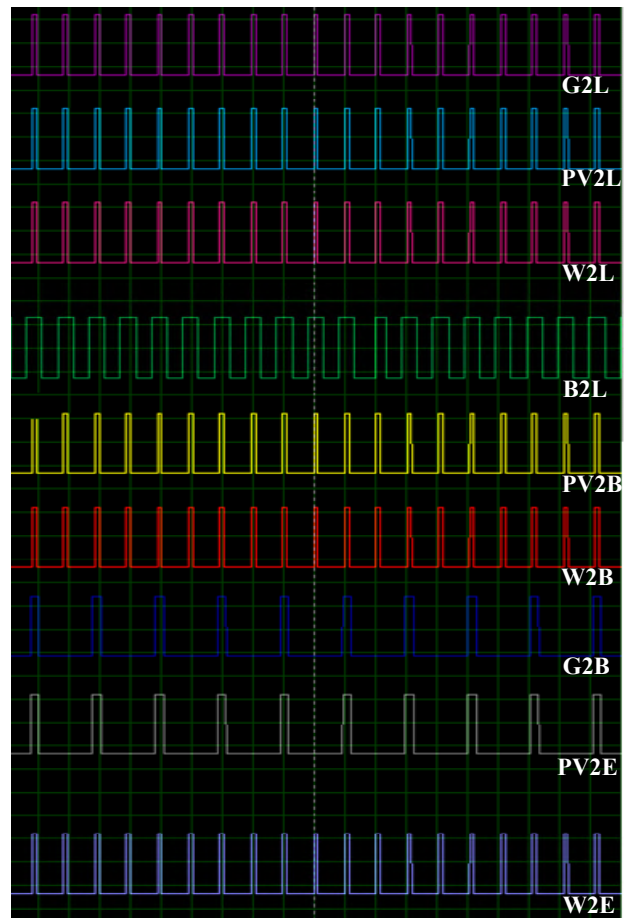


Fig. 8. PWM signals from FLSC-Arduino. From Top to Bottom: the multiple outputs are G2L, PV2L, W2L, BAT2L, PV2B, W2B, G2B, PV2E, W2E

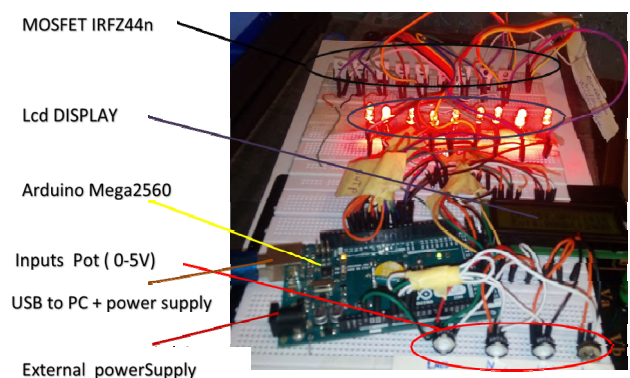


Fig. 9. Image of the FLSC-Arduino on a test plate

Conclusion.

A household hybrid energy system with solar-wind sources and storage was constructed and simulated using fuzzy logic smart controllers. 81 operating rules were designed and applied in the system for backup and energy requests as part of the management plan. The fuzzy logic program processed on MATLAB has been adapted and converted to IDE-Arduino program which is implemented in microcontroller type Arduino mega 2560. The validation of the operating FLSC under the hardware was successful and outcomes correspond likely to the rules and constraints imposed by the expert. The FLSC-Arduino output PWM signals can excite directly the electronic switches in order to convey simultaneously the available energy from the sources to the user.

Conflict of interest. The authors declare that they have no conflicts of interest.

REFERENCES

1. Assahout S., Elaissaoui H., El Ougli A., Tidhaf B., Zrouri H. A Neural Network and Fuzzy Logic based MPPT Algorithm for Photovoltaic Pumping System. *International Journal of Power Electronics and Drive Systems*, 2018, vol. 9, no. 4, pp. 1823-1833. doi: <https://doi.org/10.11591/ijpeds.v9.i4.pp1823-1833>.
2. Abdouraziq M.A., Maaroufi M. Experimental Verification of the main MPPT techniques for photovoltaic system. *International Journal of Power Electronics and Drive Systems*, 2017, vol. 8, no. 1, pp. 384-391. doi: <https://doi.org/10.11591/ijpeds.v8.i1.pp384-391>.
3. Chalok K.H., Tajuddin M.F.N., Sudhakar Babu T., Md Ayob S., Sutikno T. Optimal extraction of photovoltaic energy using fuzzy logic control for maximum power point tracking technique. *International Journal of Power Electronics and Drive Systems*, 2020, vol. 11, no. 3, pp. 1628-1639. doi: <https://doi.org/10.11591/ijpeds.v11.i3.pp1628-1639>.
4. Al-Majidi S.D., Abbod M.F., Al-Raweshidy H.S. A novel maximum power point tracking technique based on fuzzy logic for photovoltaic systems. *International Journal of Hydrogen Energy*, 2018, vol. 43, no. 31, pp. 14158-14171. doi: <https://doi.org/10.1016/j.ijhydene.2018.06.002>.
5. Sahraoui H., Chrifi-Alaoui L., Drid S., Bussy P. Second order sliding mode control of DC-DC converter used in the photovoltaic system according an adaptive MPPT. *International Journal of Renewable Energy Research*, 2016, vol. 6, no. 2, pp. 375-383. doi: <https://doi.org/10.20508/ijrer.v6i2.3369.g6797>.
6. Sahraoui H., Mellah H., Drid S., Chrifi-Alaoui L. Adaptive maximum power point tracking using neural networks for a photovoltaic systems according grid. *Electrical Engineering & Electromechanics*, 2021, no. 5, pp. 57-66. doi: <https://doi.org/10.20998/2074-272X.2021.5.08>.
7. Naik K.A., Gupta C.P. Fuzzy logic based pitch angle controller/or SCIG based wind energy system. *2017 Recent Developments in Control, Automation & Power Engineering (RDCAPE)*, 2017, pp. 60-65. doi: <https://doi.org/10.1109/RDCAPE.2017.8358240>.
8. Ngo Q.-V., Yi C., Nguyen T.-T. The fuzzy-PID based-pitch angle controller for small-scale wind turbine. *International Journal of Power Electronics and Drive Systems*, 2020, vol. 11, no. 1, pp. 135-142. doi: <https://doi.org/10.11591/ijpeds.v11.i1.pp135-142>.
9. Yasmine A., Rafik B., Rachid B., Adel M. Grid connected photovoltaic system efficiency and quality improvement using fuzzy-incond MPPT. *International Journal of Power Electronics and Drive Systems*, 2020, vol. 11, no. 3, pp. 1536-1546. doi: <https://doi.org/10.11591/ijpeds.v11.i3.pp1536-1546>.
10. Baniyounes A.M., Ghadi Y.Y., Zahia M.M.A., Adwan E., Oliemat K. Energy, economic and environmental analysis of fuzzy logic controllers used in smart buildings. *International Journal of Power Electronics and Drive Systems*, 2021, vol. 12, no. 2, pp. 1283-1292. doi: <https://doi.org/10.11591/ijpeds.v12.i2.pp1283-1292>.
11. Derrouazin A., Aillerie M., Mekakia-Maaza N., Charles J.-P. Multi input-output fuzzy logic smart controller for a residential hybrid solar-wind-storage energy system. *Energy Conversion and Management*, 2017, vol. 148, pp. 238-250. doi: <https://doi.org/10.1016/j.enconman.2017.05.046>.
12. Farah L., Haddouche A., Haddouche A. Comparison between proposed fuzzy logic and ANFIS for MPPT control for photovoltaic system. *International Journal of Power Electronics and Drive Systems*, 2020, vol. 11, no. 2, pp. 1065-1073. doi: <https://doi.org/10.11591/ijpeds.v11.i2.pp1065-1073>.
13. Birane M., Larbes C., Chekneane A. Comparative study and performance evaluation of central and distributed topologies of photovoltaic system. *International Journal of Hydrogen Energy*, 2017, vol. 42, no. 13, pp. 8703-8711. doi: <https://doi.org/10.1016/j.ijhydene.2016.09.192>.
14. Derrouazin A., Mekakia-Maaza N., Taleb R., Nacef M., Aillerie M. Low Cost Hybrid Energy Smart Management System Applied for Micro-grids. *Energy Procedia*, 2014, vol. 50, pp. 729-737. doi: <https://doi.org/10.1016/j.egypro.2014.06.090>.
15. Tahri G., Foitih Z.A., Tahri A. Fuzzy logic control of active and reactive power for a grid-connected photovoltaic system using a three-level neutral-point-clamped inverter. *International Journal of Power Electronics and Drive Systems*, 2021, vol. 12, no. 1, pp. 453-462. doi: <https://doi.org/10.11591/ijpeds.v12.i1.pp453-462>.
16. Solaris-store. Available at: <https://www.solaris-store.com/1307-panneau-solaire-ibc-polysol-260w.html> (Accessed 22 May 2019).
17. Derrouazin A. *Contribution à l'optimisation d'un système intelligent de routage des sources d'énergie hybrides pour application à l'habitat*. PhD Thesis, University of Science and Technology of Oran, Algeria, 2017. (Fra).
18. Ravi Sankar R.S., Kumar S.V.J., Rao G.M. Adaptive Fuzzy PI Current Control of Grid Interact PV Inverter. *International Journal of Electrical and Computer Engineering*, 2018, vol. 8, no. 1, pp. 472-482. doi: <https://doi.org/10.11591/ijece.v8i1.pp472-482>.
19. Baruah A., Basu M., Amuley D. Modeling of an autonomous hybrid renewable energy system for electrification of a township: A case study for Sikkim, India. *Renewable and Sustainable Energy Reviews*, 2021, vol. 135, pp. 110158. doi: <https://doi.org/10.1016/j.rser.2020.110158>.
20. Babatunde O., Denwigwe I., Oyebode O., Ighravwe D., Ohiaeri A., Babatunde D. Assessing the use of hybrid renewable energy system with battery storage for power generation in a University in Nigeria. *Environmental Science and Pollution Research*, 2022, vol. 29, no. 3, pp. 4291-4310. doi: <https://doi.org/10.1007/s11356-021-15151-3>.

Received 22.01.2022

Accepted 20.04.2022

Published 01.06.2022

Mohamed Ali Moussa¹, Doctor of Engineering,
Ahmed Derrouazin¹, Doctor of Engineering,
Maamar Latroch¹, Doctor of Engineering,
Michel Aillerie², full Professor of Engineering,
¹Laboratory LGEER, Department of Electrotechnic,
University of Hassiba BenBouali, Chlef, Algeria,
e-mail: m.alimoussa@univ-chlef.dz (Corresponding author),
derrsid@gmail.com, maamar.latroch@gmail.com,
²Optical Materials, Photonics and Systems Laboratory,
University of Loraine, Paris-Saclay, F-57070, Metz, France,
e-mail: aillerie@metz.supelec.fr

How to cite this article:

Ali Moussa M., Derrouazin A., Latroch M., Aillerie M. A hybrid renewable energy production system using a smart controller based on fuzzy logic. *Electrical Engineering & Electromechanics*, 2022, no. 3, pp. 46-50. doi: <https://doi.org/10.20998/2074-272X.2022.3.07>

B. Babes, N. Hamouda, S. Kahla, H. Amar, S.S.M. Ghoneim

Fuzzy model based multivariable predictive control design for rapid and efficient speed-sensorless maximum power extraction of renewable wind generators

Introduction. A wind energy conversion system needs a maximum power point tracking algorithm. In the literature, several works have interested in the search for a maximum power point wind energy conversion system. Generally, their goals are to optimize the mechanical rotation or the generator torque and the direct current or the duty cycle switchers. The power output of a wind energy conversion system depends on the accuracy of the maximum power tracking controller, as wind speed changes constantly throughout the day. Maximum power point tracking systems that do not require mechanical sensors to measure the wind speed offer several advantages over systems using mechanical sensors. **The novelty.** The proposed work introduces an intelligent maximum power point tracking technique based on a fuzzy model and multivariable predictive controller to extract the maximum energy for a small-scale wind energy conversion system coupled to the electrical network. The suggested algorithm does not need the measurement of the wind velocity or the knowledge of turbine parameters. **Purpose.** Building an intelligent maximum power point tracking algorithm that does not use mechanical sensors to measure the wind speed and extracts the maximum possible power from the wind generator, and is simple and easy to implement. **Methods.** In this control approach, a fuzzy system is mainly utilized to generate the reference DC-current corresponding to the maximum power point based on the changes in the DC-power and the rectified DC-voltage. In contrast, the fuzzy model-based multivariable predictive regulator follows the resultant reference current with minimum steady-state error. The significant issues of the suggested maximum power point tracking method, such as the detailed design process and implementation of the two controllers, have been thoroughly investigated and presented. The considered maximum power point tracking approach has been applied to a wind system driving a 5 kW permanent magnet synchronous generator in variable speed mode through the simulation tests. **Practical value.** A practical implementation has been executed on a 5 kW test bench consisting of a dSPACEs1104 controller board, permanent magnet synchronous generator, and DC-motor drives to confirm the simulation results. Comparative experimental results under varying wind speed have confirmed the achievable significant performance enhancements on the maximum wind energy generation and overall system response by using the suggested control method compared with a traditional proportional integral maximum power point tracking controller. References 24, tables 3, figures 15. **Key words:** small-scale wind generator, maximum power point tracking, fuzzy system, fuzzy model based multivariable predictive control, linear matrix inequalities approach.

Вступ. Система перетворення енергії вітру потребує алгоритму відстеження точки максимальної потужності. У літературі є кілька робіт, присвячених пошуку системи перетворення енергії вітру із точкою максимальної потужності. Як правило, їх метою є оптимізація механічного обертання або моменту, що крутить, генератора і перемикачів постійного струму або робочого циклу. Вихідна потужність системи перетворення енергії вітру залежить від точності контролера стеження за максимальною потужністю, оскільки швидкість вітру постійно змінюється протягом дня. Системи стеження за точками з максимальною потужністю, яким не потрібні механічні датчики для вимірювання швидкості вітру, мають ряд переваг у порівнянні з системами, що використовують механічні датчики. **Новизна.** Пропонована робота представляє інтелектуальний метод відстеження точки максимальної потужності, заснований на нечіткій моделі та багатопараметричному прогнозуючому контролері, для отримання максимальної енергії для маломасштабної системи перетворення енергії вітру, підключеної до електричної мережі. Пропонований алгоритм не вимагає вимірювання швидкості вітру або знання параметрів турбіни. **Мета.** Побудова інтелектуального алгоритму відстеження точки максимальної потужності, який не використовує механічні датчики для вимірювання швидкості вітру та витягує максимально можливу потужність з вітрогенератора, а також простий та зручний у реалізації. **Методи.** У цьому підході до управління нечітка система в основному використовується для генерування еталонного постійного струму, що відповідає точці максимальної потужності, на основі змін потужності постійного струму та постійної випрямленої напруги. Навпаки, багатопараметричний прогнозуючий регулятор на основі нечіткої моделі слідує за результируючим еталонним струмом з мінімальною помилкою, що встановилася. Істотні проблеми запропонованого методу відстеження точки максимальної потужності, такі як процес детального проектування та реалізація двох контролерів, були ретельно досліджені та представлені. Розглянутий підхід до відстеження точки максимальної потужності був застосований до вітрової системи, що приводить у дію синхронний генератор з постійними магнітами потужністю 5 кВт у режимі змінної швидкості за допомогою моделювання. **Практична цінність.** Для підтвердження результатів моделювання було виконано практичну реалізацію на випробувальному стенді потужністю 5 кВт, що складається з плати контролера dSPACEs1104, синхронного генератора з постійними магнітами та електроприводів з двигунами постійного струму. Порівняльні експериментальні результати при різній швидкості вітру підтвердили значні поліпшення продуктивності з максимального вироблення енергії вітру і загального відгуку системи при використанні запропонованого методу управління в порівнянні з традиційним пропорційно-інтегральним контролером спостереження за точкою максимальної потужності. Бібл. 24, табл. 3, рис. 15. **Ключові слова:** малогабаритний вітрогенератор, відстеження точки максимальної потужності, нечітка система, багатопараметричне прогностичне управління на основі нечіткої моделі, метод лінійних матричних нерівностей.

Introduction. Over the past decades, wind power has grown faster than any other source of renewable energy, national policymakers' concerns about global warming, energy diversification, safety supplies, and other factors have contributed to this enormous growth. Various types of converter topologies have been introduced to generate electricity from wind generators and manage distributed energy towards electrical

networks. Each of them requires a suitable type of generator (e.g., permanent magnet synchronous generators (PMSGs), induction generators (IGs), doubly fed induction generators (DFIGs) [1, 2]. Permanent magnet synchronous wind generators with a six diodes bridge rectifier, followed by a DC-DC boost chopper and a grid inverter seem to be a very good solution for small-

© B. Babes, N. Hamouda, S. Kahla, H. Amar, S.S.M. Ghoneim

scale wind turbines to achieve low cost and complexity, high reliability, and good performance by controlling the electromechanical energy conversion with minimal influence on the electrical network [3, 4], notably if the converter control is exploited with the appropriate maximum power point tracking (MPPT) algorithm. As for the MPPT algorithms, there are many MPPT approaches have been mentioned in the literature.

In most cases, these approaches rely on wind velocity measurement or wind speed-sensorless method, such as duty cycle control method, look-up table for optimum rotor speed control method, and optimum tip-speed ratio (TSR) control method. However, these schemes require precise knowledge of the wind power system parameters either before or during execution.

Moreover, the wind turbine components tend to modify their characteristics over time. Therefore, a control strategy independent of the wind generator parameters does not necessitate any prior information of the wind speed, such as the perturbation and observation (P&O) method, which is very flexible and accurate [5-7]. Moreover, this strategy is straightforward, simple, and suitable for wind generators with low inertia. Recently, there have been many articles on the MPPT methodology, especially the simplified and advanced P&O methods [8], adaptive MPPT method [9], two-stage MPPT algorithm [10], hill-climb searching algorithm [11], and modifiable step size-based P&O algorithm [12]. Despite being simple and adaptable, these MPPT techniques suffer from the problems of high steady-state errors and huge frequency variations. Other MPPT algorithms, such as fuzzy reasoning-based MPPT technique [13], neural network technique [14], and advanced vector technique [15], have also been proposed in the literature. Nevertheless, these

control strategies necessitate extensive calculations and are not always effective. Moreover, these control techniques need extra control efforts as well as costly sensors [16].

The goal of the paper is to introduce a new intelligent maximum power point tracking method for a small-scale wind generator connected to the electrical network.

The suggested MPPT technique is mainly based on a fuzzy system for deriving the reference DC-current. An innovative fuzzy model-based multivariable predictive algorithm is used to follow the reference DC-current accurately and then implement the intelligent MPPT algorithm. The suggested MPPT method can capture the maximum amount of energy from a wind generator while retaining excellent performance and quality.

Subject of investigations. This article explains how to properly manage important challenges in the design and implementation of the two regulators. Experimental results demonstrate the significant performance enhancements that can be achieved in the maximum power generation and overall system response using the suggested intelligent MPPT method. The two regulators are simple and easy to operate in modern wind power generators equipped with a six diode rectifier and boost circuit.

System description. The synoptic schematic of the considered wind power system is illustrated in Fig. 1. The conversion circuit comprises of a wind turbine with three blades, a multi-pole three-phase PMSG, a six-diode bridge rectifier, a DC-DC boost chopper, and a source voltage inverter (VSI), which is coupled to the grid. The harvested wind energy is sent immediately to the PMSG, which is transformed into electrical power by this generator.

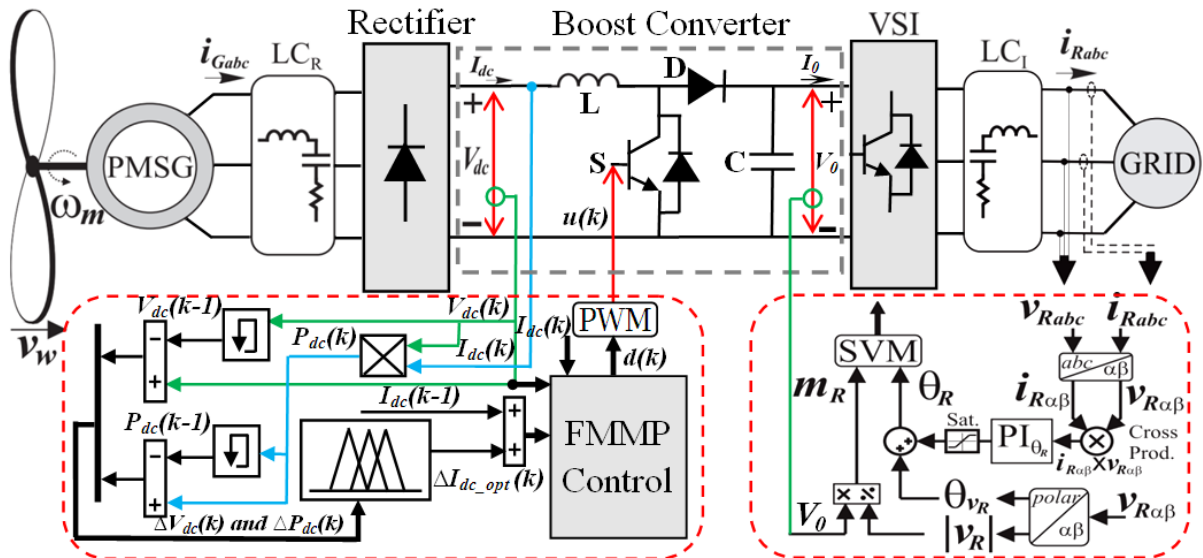


Fig. 1. Synoptic schematic of the considered wind system

The resulting electrical power can then be converted using a conventional rectifier. The boost chopper boosts the rectified DC-voltage (V_{dc}), then supplied into the electrical network through the VSI. Because the traditional rectifier is uncontrollable, a boost chopper is employed to guarantee the maximum power capture of electrical energy from the wind generator. Only one

electronic switch is required, which minimizes the system's cost and simplifies its control, consequently maintaining high system reliability and stability [17].

The VSI adjusts the power flow between the DC-bus voltage (V_0) and the electrical grid as a result independent grid-side. The mechanical power produced by the wind generator can be expressed as in [18]:

$$P_m = \frac{1}{2} \rho A C_p (\lambda, \beta) v_w^3, \quad (1)$$

where ρ represents the air mass density; C_p indicates the performance coefficient of the wind generator; A denotes the swept surface of the three blades, v_w denotes the wind velocity; λ is the tip speed ratio (TSR); β is the inclination angle of the blade (in this study set to zero).

A general form is utilized for modeling C_p . The equation is derived from the characteristics of the wind turbines [19]:

$$C_p = 0.5176 \left(\frac{116}{\lambda_i} - 0.4\beta - 5 \right) e^{-\frac{21}{\lambda_i}} + 0.0068\lambda_i; \quad (2)$$

$$\frac{1}{\lambda_i} = \frac{1}{\lambda + 0.08\beta} - \frac{0.055}{\beta^3 + 1}, \quad (3)$$

where λ is the ratio of the linear turbine rotation to the wind velocity, which is stated as:

$$\lambda = \frac{\omega_m R}{v_w}, \quad (4)$$

where ω_m and R are the turbine rotational speed and radius, respectively.

Figure 2 displays the C_p against λ graph obtained by (2). It's worth noting, that there is a unique optimum value of the λ_{opt} at which the C_p is at its highest value C_p^{\max} [20].

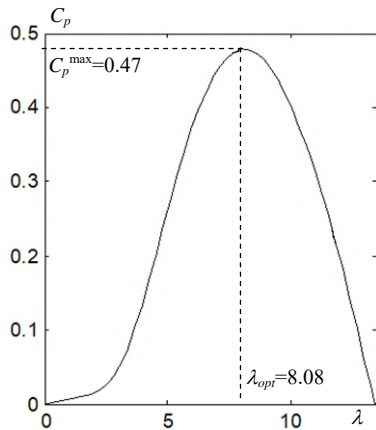


Fig. 2. $C_p = f(\lambda)$ of the considered wind generator

Thus, the mechanical energy collected from the wind generator is likewise at its peak if the wind generator works at the MPP $(\lambda_{opt}, C_p^{\max}) = (8.08, 0.47)$. The optimum mechanical power (P_{\max}) can be established by replacing (4) into (1), as shown in:

$$P_{\max} = k_p \omega_{m_opt}^3, \quad (5)$$

where ω_{m_opt} represents the optimum mechanical angular speed of the wind generator for a given wind velocity; k_p is the power control coefficient calculated as follows:

$$k_p = \frac{\rho \pi R^5 C_p^{\max}}{2 \lambda_{opt}^3}. \quad (6)$$

From (1), (5) the approximate relationship is obtained:

$$P_{\max} \propto v_w^3 \propto \omega_{m_opt}^3, \quad (7)$$

where symbol \propto indicates that the relationship is an approximation between the two variables.

The back-EMF of the PMSG is proportional to rotational velocity, and can be calculated as:

$$E = k_e \omega_m, \quad (8)$$

where k_e is the back-EMF coefficient of the wind generator.

The phase terminal AC voltage V_{ac} in the root-mean square (RMS) for a three-phase PMSG is defined as:

$$V_{ac} = E - I_{ac}(R_s + j\omega_e L_s), \quad (9)$$

with:

$$\omega_e = p \omega_m, \quad (10)$$

where I_{ac} , R_s , L_s are the line-current in RMS, the line-resistor, and the line inductance, respectively; ω_e is the electrical angular speed of the PMSG; p is the number of pole pairs.

Using a six-diode bridge rectifier, the rectified DC-voltage (V_{dc}) is related to the phase-voltage of the PMSG, therefore can be calculated as:

$$V_{dc} = \frac{3\sqrt{6}}{\pi} V_{ac}. \quad (11)$$

Assuming no power losses, the electrical DC-power (P_{dc}) can be expressed as:

$$P_{dc} = 3V_{ac} I_{ac} = V_{dc} I_{dc}, \quad (12)$$

where I_{dc} represents the rectified DC-current, which can be determined by replacing (11) in (12):

$$I_{dc} = \frac{\pi}{\sqrt{6}} I_{ac}. \quad (13)$$

Equations (8)–(10) can then be used to get the following equation:

$$\begin{cases} V_{dc} = \frac{3\sqrt{6}}{\pi} \left(k_e - \frac{\sqrt{6}}{6} p L_s I_{ac} \right) \omega_m; \\ V_{dc}^{opt} = \frac{3\sqrt{6}}{\pi} \left(k_e - \frac{\sqrt{6}}{6} p L_s I_{ac} \right) \omega_m^{opt}, \end{cases} \quad (14)$$

where V_{dc}^{opt} is the optimum rectified DC-voltage at the MPP.

Substituting (5) into (14) gives:

$$V_{dc} \propto \omega_m \text{ and } V_{dc}^{opt} \propto \omega_m^{opt}. \quad (15)$$

From (5), (14) at the MPP, the following relationship is valid:

$$V_{dc} \propto \omega_m \text{ and } P_{\max} \propto (V_{dc}^{opt})^3. \quad (16)$$

Meanwhile, the optimum DC-power can be described as:

$$P_{dc}^{opt} = \eta P_{\max} = V_{dc}^{opt} I_{dc}^{opt}, \quad (17)$$

where η is the conversion coefficient from the PMSG to the DC-side, which is considered constant; I_{dc}^{opt} is the optimum DC-current or the reference DC-current (I_{dc}^*).

Mixing (16), (17) gives:

$$I_{dc}^{opt} \propto (V_{dc}^{opt})^2. \quad (18)$$

Substituting (18) into (17) yields:

$$I_{dc}^{opt} \propto (P_{dc}^{opt})^{\frac{2}{3}}. \quad (19)$$

As indicated in (18), (19), I_{dc}^{opt} is proportional to the square of V_{dc}^{opt} , and is directly related to P_{dc}^{opt} . As a result, when I_{dc} is kept close to its optimal (reference I_{dc}^*) value I_{dc}^{opt} , the wind generator may produce the maximum amount of electrical power P_{dc}^{\max} .

Fuzzy-based MPPT controller for wind power generator. The main objective of this section is to

construct a MPP current-reference generator by using a fuzzy logic controller that meets the actual MPP. In particular, this generator is designed to compute on-line the optimal DC-current value I_{dc}^{opt} . So that, if the DC-current I_{dc} is being equal to I_{dc}^{opt} then, the maximal power is captured. The key benefit of this MPPT system is that it doesn't necessitate the use of either wind velocity sensors or rotor velocity sensors. Generally, the fuzzy system can be divided into three steps: 1) fuzzification; 2) aggregation, and 3) defuzzification. As shown in Fig. 1, the P_{dc} and V_{dc} variations are selected as the two input parameters for the fuzzy MPPT system. At the k^{th} sampling period, both variables are calibrated by the scaling gains K_1 , K_2 , and updated using the following equations:

$$\Delta P_{dc}[k] = K_1(\Delta P_{dc}[k] - \Delta P_{dc}[k-1]); \quad (20)$$

$$\Delta V_{dc}[k] = K_2(\Delta V_{dc}[k] - \Delta V_{dc}[k-1]), \quad (21)$$

where $\Delta P_{dc}[k]$ and $\Delta V_{dc}[k]$ are the DC-power and the DC-voltage variations, respectively; $P_{dc}[k]$, $V_{dc}[k]$, $P_{dc}[k-1]$ and $V_{dc}[k-1]$ represent the DC-power and the DC-voltage at the time interval $[k]$ and $[k-1]$.

The DC-power can be determined as:

$$P_{dc}[k] = V_{dc}[k] \cdot I_{dc}[k], \quad (22)$$

where $I_{dc}[k]$ and $V_{dc}[k]$ are the DC-current and the DC-voltage at the time interval k .

The change in the optimum DC-current $\Delta I_{dc}[k]$ is used as an output of the proposed fuzzy MPPT generator. To create the fuzzy sets of inputs and output variables, the triangular symmetrical membership functions (MFs) with the overlap are utilized to make the fuzzy MPPT system more sensitive to small signals, illustrated in Fig. 3.

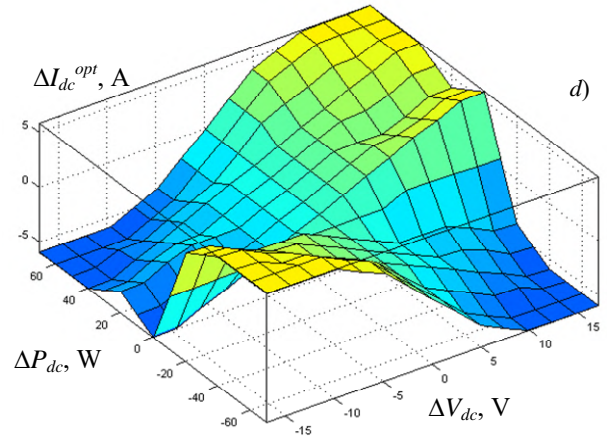
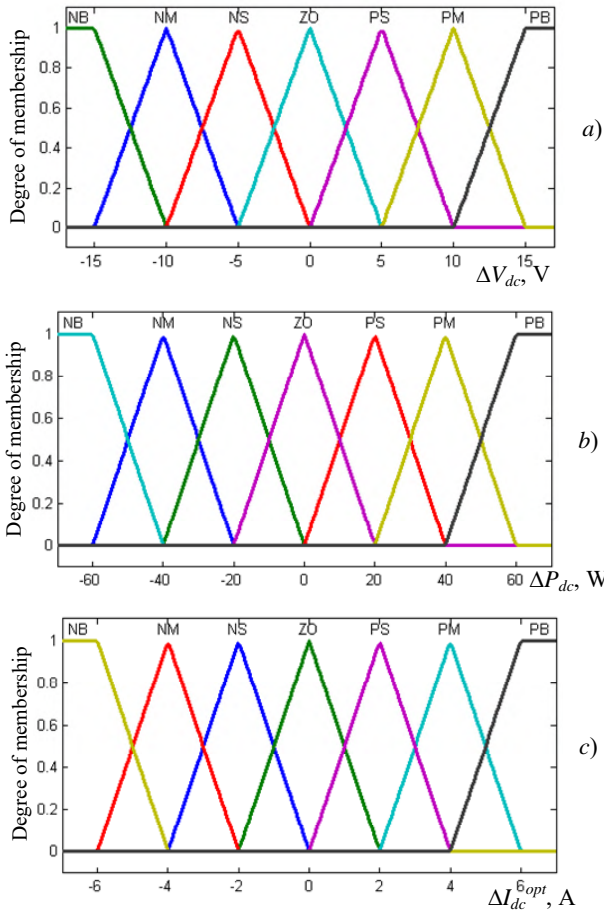


Fig. 3. Normalized membership functions (MFs) and corresponding surface view

The input/output parameters, i.e. $\Delta P_{dc}[k]$, $\Delta V_{dc}[k]$ and $\Delta I_{dc}^{opt}[k]$ are represented by linguistic terms, such as Positive-Big (PB), Positive-Medium (PM), Positive-Small (PS), Zero (ZE), Negative-Big (NB), Negative-Medium (NM), and Negative-Small (NS).

The following IF-THEN rules define the desired relationships between inputs and outputs:

R_i : **IF** $\Delta P_{dc}[k]$ is A_i and $\Delta V_{dc}[k]$ is B_j , **THEN** $\Delta I_{dc}^{opt}[k]$ is C_k , where $i, j = 1, 2, \dots, 7$; $k = 1, 2, 3, \dots, 49$, where A_i and B_j indicate the antecedents and C_k indicate the consequent parts, respectively.

The IF-THEN rules are summarized in Table 1. This article uses a fuzzy system with Mamdani method for the inference process [21].

Table 1

		Fuzzy control rules						
		ΔV_{dc}						
ΔP_{dc}	ΔI_{dc}^{opt}	NB	NM	NS	ZE	PS	PM	PB
	NB	PB	PB	PB	ZE	NM	NB	NB
	NM	PM	PM	PM	ZE	NS	NM	NM
	NS	PM	PS	PS	ZE	NS	NS	NM
	ZE	NM	NM	NS	ZE	PS	PM	PB
	PS	NM	NS	NS	ZE	PS	PS	PM
	PM	NM	NM	NM	ZE	PS	PM	PM
	PB	NB	NB	NB	ZE	PM	PB	PB

The output level $\Delta I_{dc}^{opt}[k]$ of each fuzzy rule is normalized by a factor related to the firing strength w_i , which is calculated from the minimum operation such as:

$$w_i = \min(\mu_{\Delta P_{dc}}(\Delta P_{dc}[k]), \mu_{\Delta V_{dc}}(\Delta V_{dc}[k])), \quad (23)$$

The defuzzification is realized using the centroid method (COA) of a last combined fuzzy set. The last combined fuzzy set is determined by the sum of all rule output fuzzy sets using the maximum aggregation approach [22]. Therefore, the variation in the optimum DC-current $\Delta I_{dc}^{opt}[k]$ is calculated according to the following relationship:

$$\Delta I_{dc}^{pot}[k] = \frac{\sum_{j=1}^n \mu(\Delta I_{dc}^{opt}(j)) \times (\Delta I_{dc}^{opt}(j))}{\sum_{j=1}^n \mu(\Delta I_{dc}^{opt}(j))}. \quad (24)$$

The output of the fuzzy MPPT system is $\Delta I_{dc}^{opt}[k]$, which is converted to the optimum DC-current, $I_{dc}^{opt}[k]$ by:

$$I_{dc}^{pot}[k] = I_{dc}^{pot}[k-1] + \Delta I_{dc}^{pot}[k]. \quad (25)$$

Fuzzy model based multivariable predictive (FMMP) regulator. In this part, a FMMP regulator is developed for a DC-DC boost chopper in order to follow the optimum DC-current (I_{dc}^*). The FMMP regulator is effective for DC-DC boost chopper because this control strategy is a sort of control technique that was primarily introduced to regulate constrained linear and nonlinear systems. In addition, the FMMP regulator has a quick dynamic behavior, excellent stability, and robustness against parameter variation in a variety of working conditions.

Control system design. Since the PMSG can provide the rectified DC-current (I_{dc}), it can be used as a current source. Therefore, only the dynamic of the boost chopper is studied and described in this paper. In the next part, the T-S fuzzy model of the boost chopper is utilized to represent the original nonlinear behavior for the control design goal using the sector nonlinearity method.

T-S fuzzy model of the DC-DC boost chopper. As can be seen from Fig. 1, the global nonlinear dynamical behavior of the DC-DC boost chopper in regular state-variable representation can be expressed as follows:

$$\begin{bmatrix} \frac{dI_{dc}}{dt} \\ \frac{dV_o}{dt} \end{bmatrix} = \begin{bmatrix} 0 & -(1-u) \\ -\frac{(1-u)}{C} & -\frac{L}{R_L C} \end{bmatrix} \begin{bmatrix} I_{dc} \\ V_o \end{bmatrix} + \begin{bmatrix} \frac{1}{L} \\ 0 \end{bmatrix} V_{dc}, \quad (26)$$

where I_{dc} is the input inductor current or DC-current; u is the equivalent control signal that takes values in the domain $\{0, 1\}$; $R_L = V_o/I_o$ is the total equivalent resistance; V_o is the output DC-voltage; I_o is the output DC-current; C and L are the capacitance and inductance values respectively.

Finally, a DC-DC boost chopper's discrete-time state space representation is used to derive (26), considering the sampling period T_s , and replacing the control signal u by its respective duty ratio $D(k)$. The result of this discretization can be expressed as:

$$\begin{bmatrix} I_{dc}(k+1) \\ V_o(k+1) \end{bmatrix} = \begin{bmatrix} 1 & -\frac{T_s}{L} \\ \frac{T_s}{C} & -\left(\frac{T_s}{R_L C}\right) \end{bmatrix} \begin{bmatrix} I_{dc}(k) \\ V_o(k) \end{bmatrix} + \begin{bmatrix} \frac{(V_{dc}(k) - V_o(k))}{L} \\ -\frac{I_{dc}(k)T_s}{C} \end{bmatrix} D(k). \quad (27)$$

According to the expressions (26), (27) and the T-S fuzzy model [23], the boost chopper can be described by a second-order r_i -rule fuzzy system. The i^{th} rule of the discrete T-S fuzzy model is written as follows:

Fuzzy rules r_i :

IF $w_1(t)$ is F_{i1} and ... and $w_g(t)$ is F_{ig} , **THEN** $x(k+1) = A_i x(k) + B_i u(k)$; where $i = 1, 2, \dots, k$; $A_i \in R^{n \times n}$, $B_i \in R^{n \times m}$; k values denote the number of fuzzy rules; w_1, w_2, \dots, w_g are the premise variables; $F_{ij}(j = 1, 2, \dots, g)$ are the fuzzy sets; $x(k) \in R^n$ are the system variables; $u(k)$ are the control input signal; A_i, B_i are the state vectors of the local sub-system inadequate sizes.

Using the singleton fuzzification, product inference rule, and weighted average defuzzification, the above fuzzy rules base is deduced as follows:

$$x(k+1) = \sum_{i=1}^k \mu_i(w(k)) \{A_i x(k) + B_i u(k)\}, \quad (28)$$

where:

$$\mu_i(w(k)) = \frac{\prod_{j=1}^g F_{ij}(w_j(k))}{\sum_{i=1}^k \prod_{j=1}^g F_{ij}(w_j(k))}. \quad (29)$$

The term $F_{ij}(w_j(k))$ is the grad of membership of $w_j(t)$ in F_{ij} . Note that, where for $i = 1, 2, \dots, k$. For deriving the T-S model of the DC-DC boost chopper, let the fuzzy premises variable vector $w(k)$ be selected as:

$$w_1(k) = I_{dc}(k), \quad w_2(k) = V_o(k).$$

Since, the system states of the boost chopper are bounded; the premise variables will also be bounded. In this paper, the fuzzy premise variables vary in the range defined as:

$$\max(I_{dc}(k)) = D_1, \quad \min(I_{dc}(k)) = d_1;$$

$$\max(V_o(k)) = D_2, \quad \min(V_o(k)) = d_2.$$

From the above, the corresponding MFs of the T-S system can be written as:

$$F_{11} = \frac{I_{dc}(k) - d_1}{D_1 - d_1}, \quad F_{12} = 1 - F_{11};$$

$$F_{21} = \frac{V_o(k) - d_2}{D_2 - d_2}, \quad F_{22} = 1 - F_{21}.$$

These membership functions are considered triangular shape as demonstrated in Fig. 4.

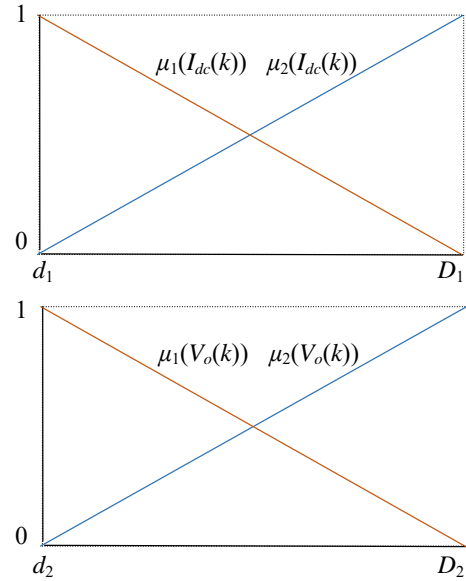


Fig. 4. Picture MFs of the T-S fuzzy model

Based on the sector nonlinearity notion, we have the following relationships:

$$I_{dc}(k) = F_{11}D_1 + F_{21}d_1, \quad V_o(k) = F_{21}D_2 + F_{22}d_2.$$

As a result, the complete fuzzy boost chopper model is equivalent to:

$$x(k+1) = A_i(k) + \left(\sum_{i=1}^4 \mu_i(I_{dc}(k), V_o(k)) B_i \right) d(k), \quad (30)$$

where A_i and B_i are the local sub-models matrices given by (for $i = 1, 2, \dots, 4$):

$$A_1 = A_2 = A_3 = A_4 = A = \begin{bmatrix} 1 & -\frac{T_s}{L} \\ \frac{T_s}{C} & 1 - \left(\frac{T_s}{R_L C}\right) \end{bmatrix}$$

and:

$$B_1 = \begin{bmatrix} \frac{(V_{dc} - d_2)I_s}{L} \\ \frac{d_1 I_s}{C} \end{bmatrix}, B_2 = \begin{bmatrix} \frac{(V_{dc} - d_2)I_s}{L} \\ -\frac{D_1 I_s}{C} \end{bmatrix}$$

It can be seen that (30) corresponds with the system (27) inside the polytope area $[d_1, D_1] \times [d_2, D_2]$. This operating space is shown in Fig. 5.

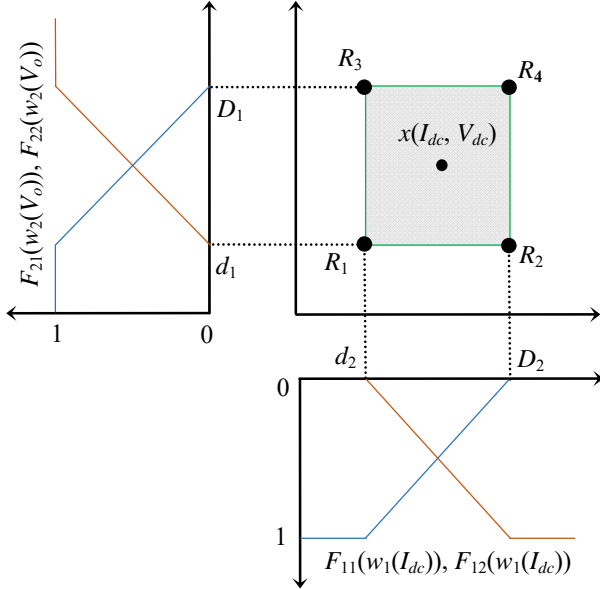


Fig. 5. T-S Fuzzy representation of the boost chopper

Multivariable predictive current control. A multivariable predictive current control method based on the T-S fuzzy model is introduced to obtain an accurate tracking control of the optimum DC-current (I_{dc}^{opt}) for the DC-DC boost chopper. In this work, the boost chopper's state variables are restricted by physical limits required by the wind generator users due to the technical specifications of the power converters. Therefore, constraints must be set while designing the boost chopper regulator. The primary function of the multivariable predictive control (MPC) is to compute a series of future operating signals in such a way that it reduces a specified objective function calculated over a prediction horizon [24]. The quadratic objective function to be minimized by the MPC controller is given by:

$$\min J = \sum_{j=H_w}^{H_p} (r(k+j) - \hat{y}(k+j|k))^T Q (r(k+j) - \hat{y}(k+j|k)) + \sum_{j=1}^{H_u} (u(k+j-1))^T + \Delta u(k+j-1)^T S \Delta u(k+j-1) \quad (31)$$

Subject to the following constraints:

$$x_{\min} \leq \hat{x}(k+j|k) \leq x_{\max}; \quad y_{\min} \leq \hat{y}(k+j|k) \leq y_{\max};$$

$$u_{\min} \leq \hat{u}(k+j|k) \leq u_{\max}; \quad \Delta u_{\min} \leq \Delta u(k+j|k) \leq \Delta u_{\max},$$

where k is the current sampling instant; H_u indicates the control cost horizon; H_w denotes the start point of the prediction horizon; H_p signifies the end point of the prediction horizon; $H_u < H_p$, and $\Delta u(k+j-1)$ represents the control increments vector, $r(k+j)$ is the future reference trajectory, $y(k+j|k)$ is the j step-ahead prediction of the system; Q is the weighting matrix of the tracking error; R and S are the weighting matrices.

Thus, two parts determine the objective function (32): the first part is concerned with reducing the difference between predicted output and reference trajectory. The second part is a penalty for exerting control effort. Further, the above-mentioned objective function can be defined in a more comprehensive matrix form [25]:

$$J(\Delta U_n) = J_{\min} + 2[\Gamma + \Theta \bar{U}_{k-1} - Y_{ref}^n]^T Q \Lambda \Delta U_n + \Delta U_n^T [\Delta^T Q \Lambda + R + S] \Delta U_n, \quad (32)$$

where

$$J_{\min} = Y_{ref}^T Q Y_{ref} + \Gamma^T Q \Gamma - 2Y_{ref}^T Q \Gamma + \bar{U}_{k-1}^T S \bar{U}_{k-1} + \bar{U}_{k-1}^T R \bar{U}_{k-1}, \quad (33)$$

where J_{\min} represents the minimal cost due to the reference and the unconstrained output response.

The fuzzy model (30) is utilized to predict the output of the system, subject to amplitude and rate saturation on the system states and control inputs:

$$\begin{bmatrix} I \\ -I \\ L \\ -L \\ \Lambda \\ -\Lambda \end{bmatrix} \Delta U_n \leq \begin{bmatrix} \tilde{U}_{\max} \\ -\tilde{U}_{\min} \\ U_{\max} \\ -U_{\min} \\ Y_{\max} - \Gamma \\ -Y_{\max} + \Gamma \end{bmatrix} \quad (34)$$

and

$$I = \begin{bmatrix} 1 & 0 & \dots & 0 \\ 0 & 1 & \dots & 0 \\ \vdots & \vdots & \ddots & \vdots \\ 0 & 0 & \dots & 1 \end{bmatrix} \in R^{H_u+1 \times H_u+1};$$

$$L = \begin{bmatrix} 1 & 0 & \dots & 0 \\ 1 & 1 & \dots & 0 \\ \vdots & \vdots & \ddots & \vdots \\ 1 & 1 & \dots & 1 \end{bmatrix} \in R^{H_u+1 \times H_u+1},$$

where the predicted output may be written as:

$$\hat{Y} = \Gamma + \Lambda \Delta U_n \quad (35)$$

where $Y \in R^{H_{pn0}}$, $\Gamma \in R^{H_{pn0}}$, $\Lambda \in R^{H_{pn0} \times H_{pmi}}$, and $\Delta U_n \in R^{H_{pmi}}$, n_0 and n_i are the total number of system outputs and inputs; Γ is the unconstrained output response; $\Lambda \Delta U_n$ is the constrained output response.

So, the new constrained optimization problem minimizes a convex objective function (33), on a convex set (35). This convex objective function has global minima only if the Hessian matrix of the objective function is positive-definite [26]. In the light of the above description, equation (35) can be transformed into the form:

$$\min \Delta U_n(k)^T H \Delta U_n(k) - P^T \Delta U_n(k). \quad (36)$$

The Hessian matrix H is positive-definite if it satisfies the following condition:

$$\text{rank}(\Lambda) = H_u. \quad (37)$$

Thus, the restrictions (34) can be expressed in one form that can be simply exploited later by the proposed optimization method:

$$\Lambda U_n(k) \leq B. \quad (38)$$

The Schur complement theorem is utilized to make the non-linear criterion (36) in Linear Matrix Inequalities (LMI)

format. Moreover, this theorem can minimize the linear objective function with LMI restrictions [27]. Therefore, the LMI-based problem of central importance to this paper is that of minimizing a linear subject to LMI constraints:

$$\begin{aligned} & \text{minimize } c^T x; \\ & \text{subject to: } F(x) > 0, \end{aligned}$$

where $F(x)$ is the symmetric matrix that depends affinely on the variable x , and c is the real vector. The solution then minimizes the linear term $c^T x$ [28].

LMI problem. An optimization LMI problem necessitates restructuring the main problem to include a linear objective function and strict inequality constraints. Generally, the minimization of a convex quadratic objective $J(\Delta U_n)$ can be achieved by the following equivalent minimization algorithm:

$$\begin{aligned} & \text{Minimize } \gamma \text{ and finding an acceptable } \Delta U_n \text{ that} \\ & \text{satisfies the following condition:} \\ & J(\Delta U_n) < \gamma. \end{aligned} \quad (39)$$

The relationship (32) can be converted to LMI form using Schur complement [27].

Given: $Q(x) = Q(x)^T$, $R(x) = R(x)^T$, and $S(x)$ depend affinely on x . Then LMI (41) is equivalent to the inequalities (39):

$$1) \begin{bmatrix} Q(x) & S(x) \\ S(x)^T & R(x) \end{bmatrix} < 0; \quad (40)$$

$$2) \begin{cases} R(x) < 0; \\ Q(x) - S(x)R(x)^{-1}S(x)^T < 0. \end{cases} \quad (41)$$

Although the inequality (39) is strict but not in linear form. Thus, it must be converted by Schur complement theorem into LMI conditions:

$$\begin{aligned} & \min \gamma \in \mathbb{R}^+ \\ & \text{subject to} \end{aligned} \quad (42)$$

$$\begin{bmatrix} 2\left[\Gamma + \Theta \bar{U}_{k-1} - Y_{ref}^n\right]^T Q \Lambda \Delta U_n + J_{\min} - \gamma & \Delta U_n^T \\ \Delta U_n & -\left[\Lambda^T Q \Lambda + R + S\right]^{-1} \end{bmatrix} < 0.$$

The aforementioned constraints (34) must be written in a diagonal form defining thus a convex matrix space and symmetric. Hence, the final form of the original optimization problem can be presented as LMI terms. Therefore, the objective function can be reformulated as follows:

$$\begin{aligned} & \min \gamma \in \mathbb{R}^+ \\ & \text{subject to:} \end{aligned} \quad (43)$$

$$\begin{bmatrix} 2\left[\Gamma + \Theta \bar{U}_{k-1} - Y_{ref}^n\right]^T Q \Lambda \Delta U_n + J_{\min} - \gamma & \Delta U_n^T \\ \Delta U_n & -\left[\Lambda^T Q \Lambda + R + S\right]^{-1} \end{bmatrix} < 0.$$

$$\begin{bmatrix} I \\ -I \\ L \\ -L \\ \Lambda \\ -\Lambda \end{bmatrix} \Delta U_n \leq \begin{bmatrix} \tilde{U}_{\max} \\ -\tilde{U}_{\min} \\ U_{\max} \\ -U_{\min} \\ Y_{\max} - \Gamma \\ -Y_{\max} + \Gamma \end{bmatrix}; \quad (44)$$

$$\text{diag}(I \Delta U_n - U_{\max}) \leq 0;$$

$$\text{diag}(-I \Delta U_n + \tilde{U}_{\min}) \leq 0;$$

$$\text{diag}(L \Delta U_n - \tilde{U}_{\max}) \leq 0;$$

$$\text{diag}(-L \Delta U_n + \tilde{U}_{\min}) \leq 0;$$

$$\text{diag}(\Lambda \Delta U_n - Y_{\max} + \Gamma) \leq 0;$$

$$\text{diag}(\Lambda \Delta U_n + Y_{\min} - \Gamma) \leq 0.$$

Simulation and experimental verifications. At first, the performance of the suggested control method incorporating fuzzy based MPPT algorithm is thoroughly examined in simulation using MATLAB/Simulink software. Then experimental tests are performed in laboratory to validate the proposed control strategy.

Simulation investigation of wind energy conversion system (WECS) control system based FMMP current controller. This part shows the advantages of implementing the derived predictive algorithm and the fuzzy MPPT control scheme. First, the off-line calculations which are necessary for the calculation of the control signal are stated. Second, the system is simulated based on the small-sized wind turbine model, the key parameters utilized in numerical simulations are listed in Table 2. Finally, simulation results that demonstrate the prevalence of the suggested control algorithm are presented. The control problem is to keep the wind generator at the maximum output power while controlling the DC-current of the boost chopper without oscillations, since these oscillations can cause a variety of issues for consumers for example, and the power outage. The discrete time T-S fuzzy system (30) of the boost chopper can be created using a sampling interval of 0.001 ms, the FMMP scheme is developed with the following conditions: the control horizon is $H_u = 2$, and the prediction horizon is $H_p = 20$. The limitations are selected as:

$$0 \leq I_{dc} \leq 10 \text{ A} \quad \text{and} \quad 0 \leq V_o \leq 600 \text{ V}.$$

An additional restriction on the boost duty cycle is imposed as follow:

$$0 \leq d(k) \leq 0.98.$$

The values of the weighting matrices in (31) are:

$$Q = \text{eye}(H_p),$$

$$S = 0.5 \cdot \text{eye}((H_u + 1)n_i), \quad R = 0.1 \cdot \text{eye}((H_u + 1)n_i).$$

where eye returns an $(n \times m)$ matrix with ones on the main diagonal and zeros elsewhere.

Table 2

System parameters	
Parameters of the PMSG utilized in simulation	Values
Nominal power	5 kW
Nominal voltage	380 V
Pole pairs	4
Nominal torque	9.5 N·m
Nominal speed	3000 rpm
Nominal current	8 A
Back-EMF coefficient	150 V/K·rpm
Stator resistor	0.245 Ω
d -axis inductor	5 mH
q -axis inductor	5 mH
Inertia	5 kg·m ²

Simulation results. The simulation plots of each state variable are shown in Fig. 6,a-h. The outcomes were obtained based on a 50 s variable wind profile. Figure 6,a shows the wind input used in the computer simulations. The variation in the wind velocity comprises high wind velocity ranges from 11 to 13 m/s.

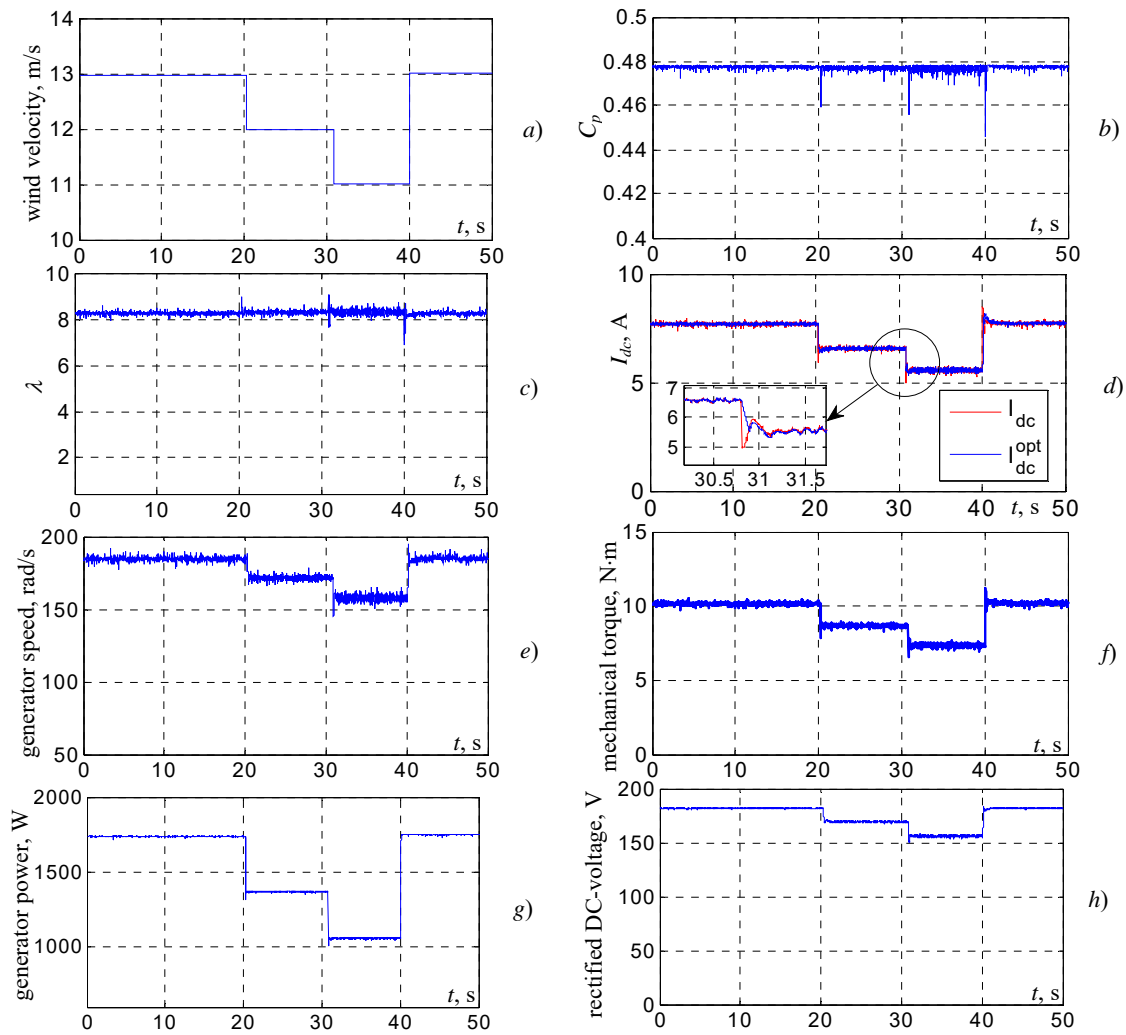


Fig. 6. Simulation results of the fuzzy MPPT algorithm

Figure 6,*b* exhibits the simulated waveform of the C_p , which is maintained at the optimum value of 0.478, and it is not influenced by the variations in the wind speed, which shows the good performances of the developed fuzzy based MPPT scheme. The resulting TSR is shown in Fig. 6,*c*. It shows that the TSR of the blade remains approximately constant and changes only at limited values around the best TSR of 8.08. It can be observed from Fig. 6,*d*, that the DC-current tracks the optimum current accurately by using the suggested control method, which adjusts the torque generator to obtain the maximum electrical power from the wind turbine with a fast response time. As depicted in Fig. 6,*e*, the rotational speed of the generator is constantly adapted to the wind velocity, so that the maximum energy is captured from the wind generator.

The mechanical torque waveform is illustrated in Fig. 6,*f*, as can be observed from Fig. 6,*f* the torque generator changes according to the variation in wind velocity to accommodate the variations in the DC-current of the boost chopper. Figure 6,*g* displays the generator output power, which is well correlated to changes in wind speed. It can also be noted that using the recommended control technique, the generator output power quickly recovers to its maximum value according to changes in wind velocity. The DC-DC boost chopper can also be used to increase the rectified DC-voltage.

As shown in Fig. 6,*h*, the optimal DC-current is proportional to the rectified DC-voltage, their relationship is in line with (14). Therefore, it can be better controlled to obtain the optimal rectified DC-voltage by using the suggested control approach. The simulation results demonstrate that the designed control method can generate the maximum wind power under different wind speeds by adjusting the DC-current of the boost chopper.

Experimental verification of WECS control system based on FMMP current controller. The 5 kW semi-controlled WECS scheme is built in laboratory to prove the effectiveness of the suggested MPPT algorithm. In the experimental WECS, the PMSG is attached to the shaft of a 5 kW DC-motor to emulate the dynamic and static behaviors of the real wind generator. A conventional boost chopper is utilized to drive the DC-motor. The design parameters of the developed WECS prototype are summarized in Table 3.

The boost chopper is built with SEMIKRON IGBT modules, and the driver circuit for the IGBTs modules is SEMIKRON SKHI61. The rectified DC-voltage and DC-current are measured using a voltage sensor and a Hall-effect current sensor, respectively. The proposed intelligent MPPT regulator is implemented using a dSPACEDS1104 controller board installed in a host PC computer, the sampling time is set as 20 kHz, and the

switching frequency of the IGBTs is also kept at 20 kHz. A portable power meter and a digital oscilloscope are utilized to record the experimental results.

The schematic circuit of the complete hardware-setup is depicted in Fig. 7, and the experimental elements of the developed WECS prototype are shown in Fig. 8.

Table 3

System parameters			
Parameters of the WECS for experiments			
PMSG parameters	Values	PMSG parameters	Values
Rated power	5 kW	Torque constant	2.39 N·m/A
Rated voltage	380 V	Mechanical time constant	2.3 ms
Pole pairs	4	DC-motor parameters	
Rated torque	22.5 N·m	Rated current	15 A
Rated speed	2000 rpm	Rated voltage	220 V
Rated current	12 A	Grid-connected converter parameters	
Permanent magnet flux	0.39 Wb	DC-bus capacitance	2200 μ F
Stator resistor	0.65 Ω	Filter inductor	10 mH
d-axis inductor	8 mH	Filter resistor	0.2 Ω
q-axis inductor	8 mH	Grid voltage	220 V

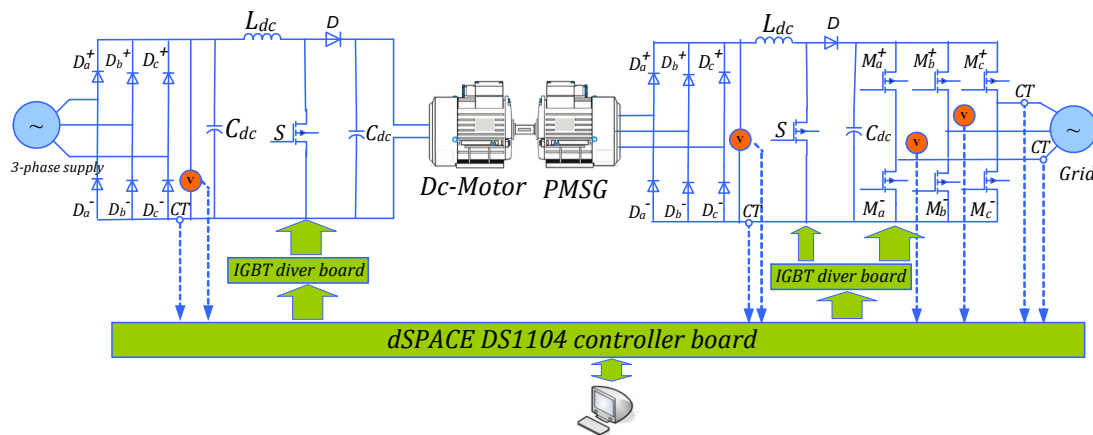


Fig. 7. Arrangement of laboratory system

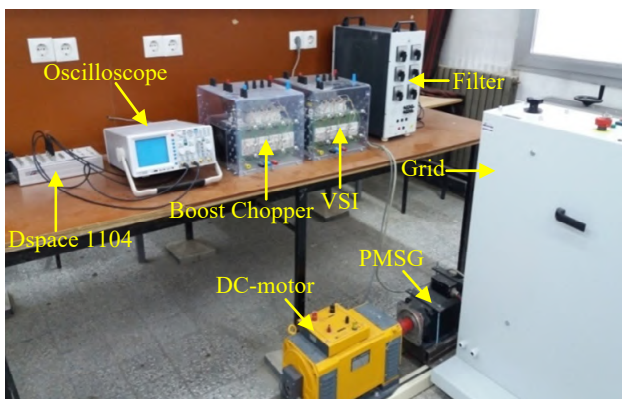


Fig. 8. Laboratory test rig

Experimental results. In this part, the performance of the suggested intelligent MPPT algorithm is verified for different wind velocities and compared with that of a traditional PID regulator. In the first test, the wind velocity is step-function or ramp-function changed arbitrarily from 6-8 m/s as illustrated in Fig. 9,a.

The C_p of the emulated wind turbine and the rectified DC-voltage, the output power of the PMSG (DC-power), and the duty ratio of the boost chopper are illustrated in Fig. 9,b. The obtained results show that a rapid MPP tracking is realized with the proposed intelligent MPPT algorithm.

Despite the change in wind velocity, the real value of C_p closely matches its optimal value (0.478). Besides

the rapid change in the wind velocity, the rectified DC-voltage and the DC-power are smoothed because of the system inertia.

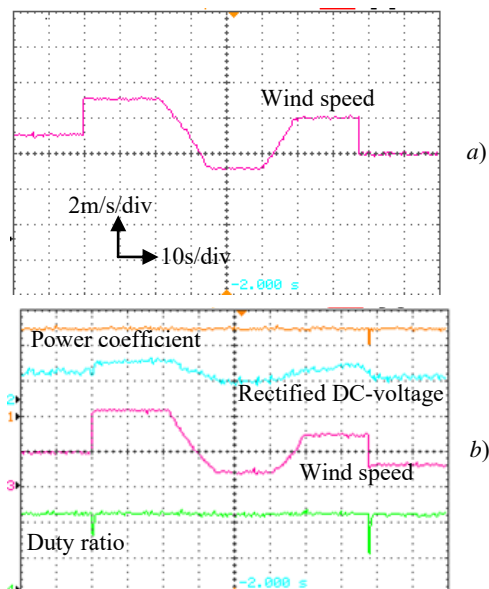


Fig. 9. Experimental results with step-variations in wind velocity

Experiments have also been carried out with time-varying wind speeds. All the waveforms are given in Fig. 10,a,b. It can be observed, that the suggested intelligent MPPT regulator is constantly looking for new MPP.

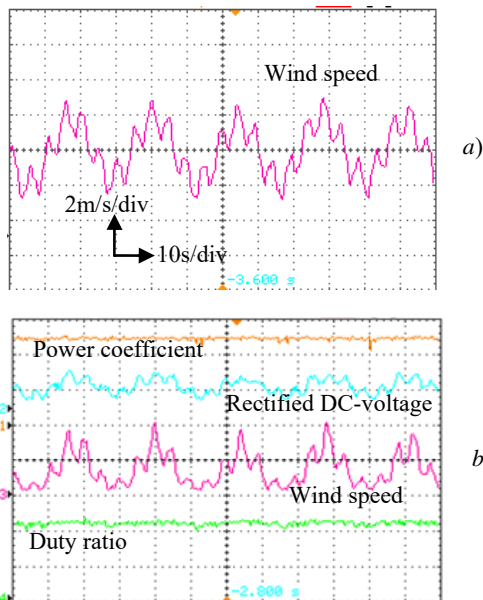


Fig. 10. Experimental results with turbulent wind changes

The functionality of the proposed FMMP current controller was also experimentally verified and compared with the typical PI regulator. The comparison has been done by observing the C_p , the rectified DC-voltage, the DC-power, and the boost duty cycle waveforms. The test results in Fig. 11 display the programmed switching between the proposed FMMP and PI current control methods. During the last testing scenario, the C_p and the optimal output power followed their peak values well by utilizing the suggested fuzzy MPPT control method.

The maximum divergence of the C_p from its peak value is 0.02 with the suggested MPPT method. We can also note that there is no deviation between the real and optimal output powers. On the other hand, when utilizing the traditional PI regulator, the C_p values oscillate in a larger range, and deviations of electrical power from its peak values are also observed from moment to moment.

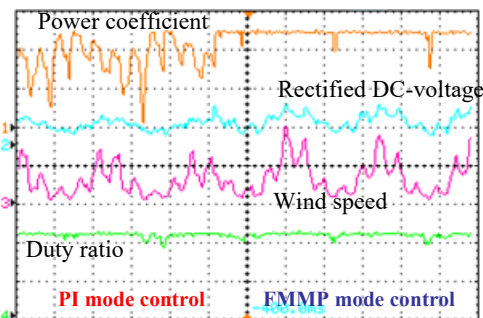


Fig. 11. Comparison of proposed FMMP current controller to conventional PI control method

We can see in Fig. 12, that the electrical energy produced by the wind generator using the suggested intelligent MPPT controller (E_{FMMP}) is greater than that produced by the traditional PI control method (E_{PI}). Therefore, it proves the effectiveness of the suggested intelligent MPPT controller.

Figure 13 depicts the experimental results of the output three-phase voltage (a) and current (b) of the PMSG for a wind speed of 10 m/s.

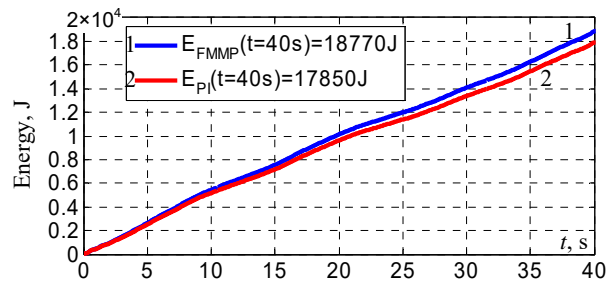


Fig. 12. Total generated electrical energy

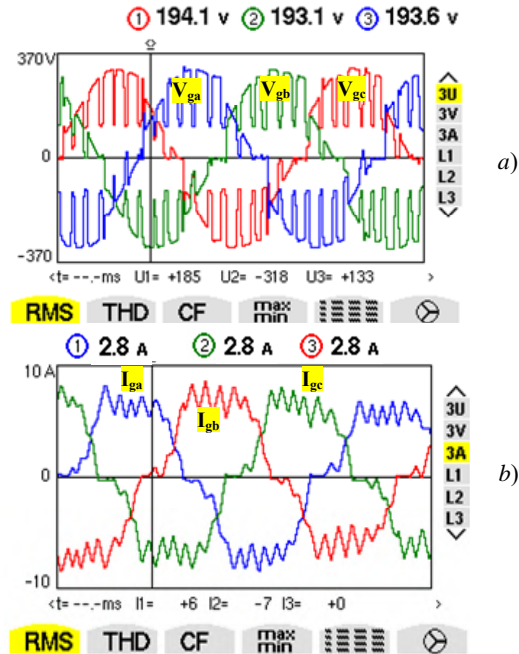


Fig. 13. Experimental waveforms of the WECS with the designed grid-side regulator

Figure 14 illustrates the system performances on the grid-side converter. From Fig. 14,a, it can be seen that all the injected grid currents (I_{ga} , I_{gb} , I_{gc}) and grid voltages (V_{ga} , V_{gb} , V_{gc}) have a sinusoidal shape of 50 Hz. Figure 14,b illustrates Fresnel diagram of the main current and voltage using the classical control of the grid-side converter.

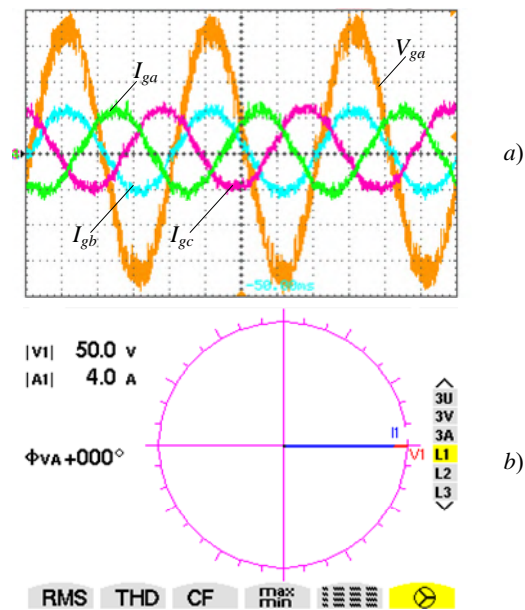


Fig. 14. Experimental results of the WECS with the designed grid-side control algorithm

Finally, Fig. 15,a displays that the total harmonic distortion (THD) of the injected grid current and voltage is 2.5 %, which is below the threshold limit of 5 %. In addition, it meets the requirement of a power factor with a value of 0.996, as depicted in Fig. 15,b.

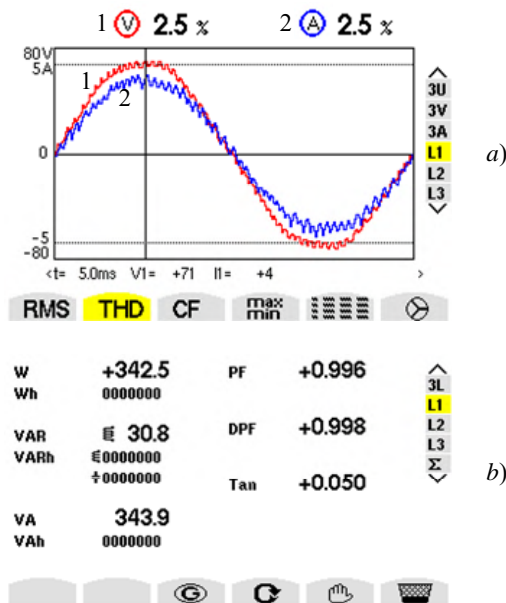


Fig. 15. Experimental results of the WECS with the grid-side control algorithm

Conclusions.

In this article, an extension of fuzzy model based multivariable predictive current control strategy has been applied to the DC-DC boost chopper of wind energy conversion system to enhance the capability of capturing the maximum output energy based on an intelligent fuzzy maximum power point tracking controller. The considered control algorithm synthesis of the fuzzy model based multivariable predictive controller is based on the fuzzy system, optimization technique, and linear matrix inequalities formulation. In this approach, at every sampling period, a quadratic cost function with a specific prediction horizon and control horizon is minimized such that constraints on the control input are satisfied.

Furthermore, the designed intelligent maximum power point tracking regulator has also been employed to derive the optimum DC-current corresponding to the maximum power point of the wind generator based on the changes in the DC-power and rectified DC-voltage. While the fuzzy model based multivariable predictive current regulator has been designed to follow the derived optimum DC-current with minimum steady-state tracking error, this allows the wind generator to produce the maximum electrical energy.

Simulation and experimental results have affirmed the significant improvements in maximum electrical energy harvesting and mechanical stresses minimization. In addition, compared to the traditional proportional integral controller, the suggested control approach has greater overall control efficiency and can be utilized to harvest maximum wind power more efficiently.

Conflict of interest. The authors declare that they have no conflicts of interest.

Acknowledgment. The authors express their gratitude to Taif University Researchers Supporting Project Number TURSP-2020/34), Taif, Saudi Arabia.

REFERENCES

- Babes B., Rahmani L., Chaoui A., Hamouda N. Design and Experimental Validation of a Digital Predictive Controller for Variable-Speed Wind Turbine Systems. *Journal of Power Electronics*, 2017, vol. 17, no. 1, pp. 232-241. doi: <https://doi.org/10.6113/JPE.2017.17.1.232>.
- Amrane F., Chaiba A., Francois B., Babes B. Experimental design of stand-alone field oriented control for WECS in variable speed DFIG-based on hysteresis current controller. *2017 15th International Conference on Electrical Machines, Drives and Power Systems (ELMA)*, 2017, pp. 304-308. doi: <https://doi.org/10.1109/ELMA.2017.7955453>.
- Lee J., Kim Y. Sensorless fuzzy-logic-based maximum power point tracking control for a small-scale wind power generation systems with a switched-mode rectifier. *IET Renewable Power Generation*, 2016, vol. 10, no. 2, pp. 194-202. doi: <https://doi.org/10.1049/iet-rpg.2015.0250>.
- Hamouda N., Babes B., Kahla S., Soufi Y. Real time implementation of grid connected wind energy systems: predictive current controller. *2019 1st International Conference on Sustainable Renewable Energy Systems and Applications (ICSRESA)*, 2019, pp. 1-6. doi: <https://doi.org/10.1109/ICSRESA49121.2019.9182526>.
- Kesraoui M., Korichi N., Belkadi A. Maximum power point tracker of wind energy conversion system. *Renewable Energy*, 2011, vol. 36, no. 10, pp. 2655-2662. doi: <https://doi.org/10.1016/j.renene.2010.04.028>.
- Zhu Y., Cheng M., Hua W., Wang W. A novel maximum power point tracking control for permanent magnet direct drive wind energy conversion systems. *Energies*, 2012, vol. 5, no. 5, pp. 1398-1412. doi: <https://doi.org/10.3390/en5051398>.
- Kazmi S.M.R., Goto H., Guo H., Ichinokura O. A Novel Algorithm for Fast and Efficient Speed-Sensorless Maximum Power Point Tracking in Wind Energy Conversion Systems. *IEEE Transactions on Industrial Electronics*, 2011, vol. 58, no. 1, pp. 29-36. doi: <https://doi.org/10.1109/TIE.2010.2044732>.
- Xia Y., Ahmed K.H., Williams B.W. A New Maximum Power Point Tracking Technique for Permanent Magnet Synchronous Generator Based Wind Energy Conversion System. *IEEE Transactions on Power Electronics*, 2011, vol. 26, no. 12, pp. 3609-3620. doi: <https://doi.org/10.1109/TPEL.2011.2162251>.
- Ching-Tsai Pan, Yu-Ling Juan. A Novel Sensorless MPPT Controller for a High-Efficiency Microscale Wind Power Generation System. *IEEE Transactions on Energy Conversion*, 2010, vol. 25, no. 1, pp. 207-216. doi: <https://doi.org/10.1109/TEC.2009.2032604>.
- Agarwal V., Aggarwal R.K., Patidar P., Patki C. A Novel Scheme for Rapid Tracking of Maximum Power Point in Wind Energy Generation Systems. *IEEE Transactions on Energy Conversion*, 2010, vol. 25, no. 1, pp. 228-236. doi: <https://doi.org/10.1109/TEC.2009.2032613>.
- Lin W.-M., Hong C.-M. Intelligent approach to maximum power point tracking control strategy for variable-speed wind turbine generation system. *Energy*, 2010, vol. 35, no. 6, pp. 2440-2447. doi: <https://doi.org/10.1016/j.energy.2010.02.033>.
- Kazmi S.M.R., Goto H., Guo H.-J., Ichinokura O. A Novel Algorithm for Fast and Efficient Speed-Sensorless Maximum Power Point Tracking in Wind Energy Conversion Systems. *IEEE Transactions on Industrial Electronics*, 2011, vol. 58, no. 1, pp. 29-36. doi: <https://doi.org/10.1109/TIE.2010.2044732>.
- Galdi V., Piccolo A., Siano P. Designing an Adaptive Fuzzy Controller for Maximum Wind Energy Extraction. *IEEE Transactions on Energy Conversion*, 2008, vol. 23, no. 2, pp. 559-569. doi: <https://doi.org/10.1109/TEC.2007.914164>.

14. Pucci M., Cirrincione M. Neural MPPT Control of Wind Generators With Induction Machines Without Speed Sensors. *IEEE Transactions on Industrial Electronics*, 2011, vol. 58, no. 1, pp. 37-47. doi: <https://doi.org/10.1109/TIE.2010.2043043>.
15. Cardenas R., Pena R. Sensorless Vector Control of Induction Machines for Variable-Speed Wind Energy Applications. *IEEE Transactions on Energy Conversion*, 2004, vol. 19, no. 1, pp. 196-205. doi: <https://doi.org/10.1109/TEC.2003.821863>.
16. Chedid R., Mrad F., Basma M. Intelligent control of a class of wind energy conversion systems. *IEEE Transactions on Energy Conversion*, 1999, vol. 14, no. 4, pp. 1597-1604. doi: <https://doi.org/10.1109/60.815111>.
17. Chiang H., Tsai H. Design and implementation of a grid-tied wind power micro-inverter. *IET Renewable Power Generation*, 2013, vol. 7, no. 5, pp. 493-503. doi: <https://doi.org/10.1049/iet-rpg.2012.0342>.
18. Hamouda N., Benalla H., Hemsas K., Babes B., Petzoldt J., Ellinger T., Hamouda C. Type-2 Fuzzy Logic Predictive Control of a Grid Connected Wind Power Systems with Integrated Active Power Filter Capabilities. *Journal of Power Electronics*, 2017, vol. 17, no. 6, pp. 1587-1599. doi: <https://doi.org/10.6113/JPE.2017.17.6.1587>.
19. Beddar A., Bouzekri H., Babes B., Afghoul H. Real time implementation of improved fractional order proportional-integral controller for grid connected wind energy conversion system. *Revue Roumaine Des Sciences Techniques Serie Electrotechnique et Energetique*, 2016, vol. 61, no. 4, pp. 402-407. Available at: http://revue.elth.pub.ro/upload/89285817_ABeddar_RRST_4_2_016_pp_402-407.pdf (Accessed 12 June March 2021).
20. Kahla S., Bechouat M., Amieur T., Sedraoui M., Babes B., Hamouda N. Maximum power extraction framework using robust fractional-order feedback linearization control and GM-CPSO for PMSG-based WECS. *Wind Engineering*, 2021, vol. 45, no. 4, pp. 1040-1054. doi: <https://doi.org/10.1177/0309524X20948263>.
21. Bose B.K. Expert system, fuzzy logic, and neural network applications in power electronics and motion control. *Proceedings of the IEEE*, 1994, vol. 82, no. 8, pp. 1303-1323. doi: <https://doi.org/10.1109/5.301690>.
22. Mamdani E.H., Assilian S. An Experiment in Linguistic Synthesis with a Fuzzy Logic Controller. *International Journal of Human-Computer Studies*, 1999, vol. 51, no. 2, pp. 135-147. doi: <https://doi.org/10.1006/ijhc.1973.0303>.
23. Takagi T., Sugeno M. Fuzzy identification of systems and its applications to modeling and control. *IEEE Transactions on Systems, Man, and Cybernetics*, 1985, vol. SMC-15, no. 1, pp. 116-132. doi: <https://doi.org/10.1109/TSMC.1985.6313399>.
24. Wang L. *Model predictive control system design and implementation using MATLAB*. Springer London, 2009. doi: <https://doi.org/10.1007/978-1-84882-331-0>.

Received 08.02.2022

Accepted 23.03.2022

Published 01.06.2022

Badreddine Babes¹, Senior Researcher A,
 Nouredine Hamouda¹, Senior Researcher A,
 Sami Kahla¹, Senior Researcher A,
 Hichem Amar¹, Senior Researcher B,
 Sherif S.M. Ghoneim², PhD, Associate Professor,
¹Research Center in Industrial Technologies CRTI,
 P.O. Box 64, Cheraga 16014 Algiers, Algeria,
 e-mail: elect_babes@yahoo.fr (Corresponding author),
 n.hamouda@crti.dz, s.kahla@crti.dz, h.amar@crti.dz,
²Department of Electrical Engineering,
 College of Engineering, Taif University,
 Taif 21944, Saudi Arabia,
 e-mail: s.ghoneim@tu.edu.sa

How to cite this article:

Babes B., Hamouda N., Kahla S., Amar H., Ghoneim S.S.M. Fuzzy model based multivariable predictive control design for rapid and efficient speed-sensorless maximum power extraction of renewable wind generators. *Electrical Engineering & Electromechanics*, 2022, no. 3, pp. 51-62. doi: <https://doi.org/10.20998/2074-272X.2022.3.08>

H. Chappa, T. Thakur

A novel load shedding methodology to mitigate voltage instability in power system

Aim. A novel technique for detecting imminent voltage instability is proposed in this paper, accompanied by a novel load shedding approach to protect the system from voltage instability. **Methodology.** The proposed methodology utilizes the computation of nodal reactive power loss to voltage sensitivities with load increments in the system. **Originality.** The nodal reactive power loss to voltage sensitivity is a novel computation and is explored to detect the likelihood of voltage instability in this work. **Results.** If the system is experiencing an unprecedented load growth and if all the measures reach their limits, then load shedding is the last resort to safeguard the system against instability. The sudden change in nodal reactive power loss to voltage sensitivities is utilized to devise the quantity of load to be cut in the system. **Practical value.** The time-based simulations performed in New England 39 bus test system (NE-39 bus), the simulated results show that nodal reactive power loss to voltage sensitivities can be used as a trusted indicator for early diagnosing of menacing voltage instability and the timely implementation of load shedding developed from nodal reactive power loss to voltage sensitivities on the system ensures voltage stability. References 29, tables 1, figures 9.

Key words: voltage stability, sensitivity analysis, nodal reactive power losses, load shedding.

Мета. У статті пропонується новий метод виявлення навислої нестабільності напруги, що супроводжується новим підходом до скидання навантаження для захисту системи від нестабільності напруги. **Методологія.** У запропонованій методиці використовується розрахунок вузлових втрат реактивної потужності залежно від чутливості до напруги при збільшенні навантаження у системі. **Оригінальність.** У цій роботі вузлові втрати реактивної потужності залежно від чутливості до напруги являють собою новий розрахунок і досліджуються визначення ймовірності нестабільності напруги. **Результати.** Якщо система відчуває безпрецедентне зростання навантаження і всі заходи досягають меж своїх можливостей, скидання навантаження є останнім засобом захисту від нестабільності. Раптова зміна вузлових втрат реактивної потужності, залежно від чутливості до напруги, використовується для визначення величини навантаження, яка повинна бути відсічена в системі. **Практична цінність.** Моделювання, засноване на часі, виконане в тестовій системі шини New England 39 (шина NE-39), та результати моделювання показують, що залежність вузлових втрат реактивної потужності від чутливості до напруги може використовуватися як надійний індикатор для ранньої діагностики загрозової нестабільності напруги та своєчасного впровадження скидання навантаження, що виникає внаслідок втрати реактивної потужності у вузлах, до чутливості системи до напруги, а забезпечує стабільність напруги. Бібл. 29, табл. 1, рис. 9.

Ключові слова: стабільність напруги, аналіз чутливості, вузлові втрати реактивної потужності, скидання навантаження.

Introduction. Power system voltage stability maintenance is of paramount importance in practical grid. Power system is tremendously non-linear system and is continuously subjected to several disturbances. It is very strenuous for the system operators to monitor and operate such highly non-linear system stably. Early detection of voltage instability is a pressing concern for system operators. Voltage instability may lead to complete or partial blackout in the system. After detection, the immediate concern is the prevention of system from reaching unstable state. One of the proven preventive measure is load shedding. The introduction of deregulation along with renewable penetration due to high energy demand is forcing the grid to operate in a manner in which it is not designed to operate. The operating status of the systems is continuously monitored by the system operators to find the current state of the system. All the nodes in the system have to maintain acceptable voltages. Maintaining these acceptable voltages under highly stressed conditions is a major challenge for power system operators. According to [1] voltage stability is the ability of the system to maintain acceptable voltages at all the buses under all operating conditions. Voltage stability problem, in general, occurs due to [1]:

- 1) severe loading in the system especially voltage dependent load;
- 2) line or generator contingency under highly stressed;
- 3) insufficient reactive power support in the system;
- 4) reverse action of on load tap changer.

To address the voltage instability issue in the power system, a considerable amount of research has been done

so far. Many methodologies were developed based on offline study of the considered test system P-V curves and Q-V curves that are drawn based on the repetitive runs of the Newton-Raphson load flow (NR load flow) were used to analyse the system stability. However, since these methodologies were based on an offline analysis, they might not be appropriate for real-time detection. On the other hand sensitivity analysis [3] has been done to assess the voltage instability by neglecting real power variations. Such assumptions may not be valid if the system is under a highly stressed condition.

Early diagnosis of voltage instability in power system gained much attention from the past two decades, as it could trigger a complete or partial blackout in the system. Voltage instability detection in real-time can be done by utilizing synchrophasor measurements [2]. Phasor measurement units (PMU) are the main devices for synchrophasor measurements. The methodologies developed in [4, 5] utilize the concept of tracking Thevenin equivalent parameters. However, it is observed in [6], that these methodologies do not detect the accurate point of instability. Moreover, accuracy of the tracking of Thevenin parameters depends on the window size being considered. This problem has been overcome in [7]. All these methodologies come under the category of local measurements where only one bus of interest can be monitored. Even though these methodologies give sufficient picture of instability but they are not suitable to monitor many nodes at a time that are prone to voltage instability.

© H. Chappa, T. Thakur

Wider area measurements may be utilized for assessing voltage stability issues in the system at a time. However, it requires more number of PMUs to be installed. The index in [8] utilizes the rate of change of voltage for detecting voltage instability. The methodology in [9] developed a load shedding scheme to ensure both voltage and frequency stability. The methodology in [10] utilized the reduced set of measurements from PMU and computed the singular values of the Jacobian matrix in near real-time. The voltage distance collapse and the quantity of load to shed for ensuring voltage stability is proposed in [11]. Fast detection of voltage instability in real-time are proposed in [12, 13] by utilizing the nodal reactive power losses. Voltage instability for renewable integrated grid and the locations for reactive power support based on the dominant load type is presented in [14]. The sites that are suitable for renewable penetration are shown with the simulated results.

A methodology to shed the load based on eigen values is presented in [14]. The minimal eigen value of the power flow Jacobian matrix has adequate information to explore it as an indicator. The system has to be continually checked for this indicator before taking any preventive action. The main issue with this indicator is that the power flow Jacobian matrix is topology sensitive. Power system is dynamic system and topological changes in the network are recurrent. In such scenarios the computation of the singular eigenvalue of the power flow Jacobian matrix in real time would be a complex task. Under-voltage load shedding based on estimation of Thevenin parameters is proposed in [15]. Thevenin parameters are estimated by using recursive least square approximation techniques. Emergency load shedding based on minimum eigen values of power flow Jacobian matrix is formulated in [16]. Under-voltage relays are placed based on the values of applied L index [17] to the considered system. The amount of load to shed is decided based on the PQ limit curves. A combined load shedding method [18] is proposed by considering both frequency and voltage stability. For this, sensitivity analysis and center of inertia frequency is considered to determine the amount of load shedding at individual node. In the same token, another adaptive algorithm [19] is developed for both frequency and voltage stability. This algorithm works in three stages and the major building block is the drawing up of a lookup table and its update in near real-time. The lookup table encompasses optimal location and minimal load shedding along with consideration for the incidents that require post load shedding.

Frequency measurement and voltage stability index are used in [20] for adaptive load shedding. This algorithm considers the PMU measurements at the bus of interest and voltage stability index is computed from those measurements. The coupling between under-frequency and prolonged low voltage condition is exploited for developing the load shedding conditions. The sensitivity of dynamic voltage curves is explored in [21] to develop load shedding blueprint. The originality of this work is consideration of the dynamic conditions of the load and system to develop the minimal load shedding scheme. This dynamic load conditions study is very relevant in voltage stability investigations as the non-

intersection of load characteristic and system characteristic results in voltage collapse. Furthermore, the contingencies under stressed condition affect the likelihood of voltage collapse. The contingency analysis is rigorously studied here to obtain the minimal load shedding condition.

The under frequency conjoined with voltage stability assessment is considered in [22] for minimal load shedding. It is identified that load shedding to avoid only the frequency instability may have adverse effect on voltage instability. The corrective action for under frequency protection may not be sufficient for the support of voltage stability. The supplementary arrangement is made in this work to support for voltage stability. The thermal limit of the transmission lines depend on the scale of loading of the lines. If loading is beyond the thermal limits, and the non-intersection of system curve and load curve initiates the voltage instability. To this end, the load rate of transmission is monitored in [23] to prevent the cascading failure that occurs due to voltage and frequency instability. This load shedding is based on the ranking of the outage sensitivity index and voltage magnitude. The scheme in [24] considers the under-frequency precise load shedding coupled with voltage stability criteria. The synchrophasor measurements are used to develop methodology by considering the load dynamics. This two stage load shedding is very essential for real time system monitoring. This scheme protects the system from both voltage instability and under-frequency condition. The minimal load shedding is however limited to a particular node is the main limitation of this work. An optimal load shedding based on PMU measurements for practical power system is proposed in [25].

Under impedance load shedding scheme is presented in [26] by considering the motor dynamics as they play a prominent role in driving the system to instability. By considering the load demand response and using multi-period optimal power flow, smallest singular value of the Jacobian matrix is improved in [27] by shedding the load at suitable locations. PMU measurement based methodology for load shedding is proposed in. This method considers the multiport modelling equations to estimate the Thevenin parameters and an index is obtained therefrom. This index is used in load shedding algorithm to shed minimal amount of load without compromising the stability of the system. The power flow Jacobian matrix was computed using PMU data in [28]. Following that, the power flow Jacobian matrix was subjected to V-Q sensitivity analysis. Such analysis is useful for identifying the vulnerable nodes in the system from a voltage stability point of view. At the weak nodes a fixed amount of load i.e. 5 % load shedding is employed and checked for the stability condition. In this method the load shedding is done only at weak nodes corresponding to voltage instability.

The detailed literature review shown above disclose that, most of the methodologies use singularity condition of power flow Jacobian matrix or sensitivity analysis of Jacobian matrix for detecting instability. In the sensitivity analysis of the power flow Jacobian matrix, decoupling of active power variations with respect to voltage is considered. This assumption is not a valid assumption

especially when the system is under stress condition. However, reactive power loss to voltage sensitivity may provide accurate and early detection of voltage collapse in power system.

Goal. In this work nodal reactive power loss to voltage sensitivity has been used as a litmus test for detecting the voltage instability and a load shedding scheme is also derived therefrom. The main reason for considering nodal reactive power loss to voltage sensitivity is that it can be obtained in real-time. Moreover, the sensitivity analysis obtained from the reduced Jacobian matrix seems to be inaccurate especially when the system is under the stressed condition. This assumption for decoupling of active power variations and voltage is overcome by considering Nodal Reactive Power loss to Voltage Sensitivity (NRPVS). The following sections go into sensitivity analysis and bus reactive power losses calculations in greater depth.

Nodal reactive power loss calculation. The reactive power loss in the power system has correlation with the bus voltage. Usually, the reactive power loss is attributed as line reactive power loss. However, it has been identified in the literature that bus reactive power loss is proposed and that bus reactive power loss trend in the system has significant link with the voltage trend in time domain simulations. The computation of nodal reactive power loss is as follows. Figure 1 presents the bus B-1 with its interconnections and a PMU.

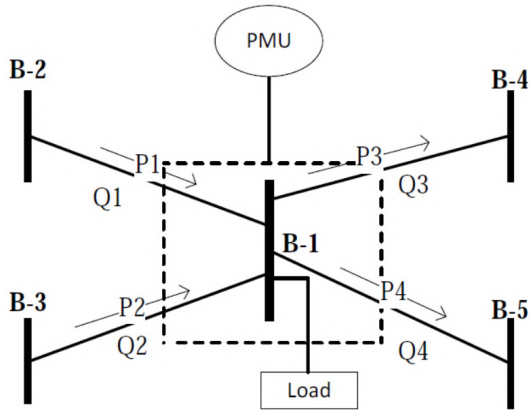


Fig. 1. Power network showing direction of real power flow and line losses [11]

This bus B-1 is the monitored bus. The direction of arrows indicates the active power flow direction in the lines. The load flow equation at any given node j is represented as:

$$S_{bus}^j = V_j \sum_{i=1}^n I_i^* \quad (1)$$

where S_{bus}^j is the apparent power at bus j ; V_j is the voltage at bus j ; I_i is the current at bus i .

PMU measurements are utilized in bus B-1 to compute all the line losses and direction of active power flows. The bus reactive power losses are evaluated at any bus j by using the following equation:

$$Q_{loss}^j = \sum_{i=1, i \neq j}^n I_{ij}^2 \cdot X_{ij}, \quad (2)$$

where I_{ij} is the current from any bus i to j ; X_{ij} is the reactance of the line placed between buses i and j .

In brief, the nodal reactive power losses are the summation of line reactive power losses feeding the bus of interest.

There are several methodologies proposed to detect the incipient voltage instability by considering the decoupling of power flow Jacobian matrix. As the name suggests, Jacobian matrix represents the sensitivities of the bus voltages and reactive power losses. The decoupling of the Jacobian matrix essentially means considering the real power load and voltage are weakly coupled and subsequently the terms belong to them will be dropped. In the same line the terms related to reactive power and frequency are also dropped. The details of the sensitivity analysis are as follows:

Sensitivity analysis. The power balance equations under steady state by assuming bus numbers $i = 1, 2 \dots n$ for a n -bus system are given as

$$P_{Gi} - P_{Di}(V_i) - \sum_{j=1}^n V_i V_j Y_{ij} \cos(\theta_i - \theta_j - \alpha_{ij}) = 0; \quad (3)$$

$$Q_{Di}(V_i) - \sum_{j=1}^n V_i V_j Y_{ij} \sin(\theta_i - \theta_j - \alpha_{ij}) = 0. \quad (4)$$

where P_{Gi} is the real power generated at bus i ; $P_{Di}(V_i)$ is the load demand at bus i and this load demand is function of voltage; $V_i, V_j, \theta_i, \theta_j$ are the voltages and the corresponding angles at buses i and j respectively; Y_{ij} is the admittance between buses i and j ; α_{ij} is the angle corresponding to Y_{ij} .

By applying NR load flow method to (3), (4) yields [1]:

$$\begin{bmatrix} \Delta P \\ \Delta Q \end{bmatrix} = \begin{bmatrix} J_{P\theta} & J_{PV} \\ J_{Q\theta} & J_{QV} \end{bmatrix} \begin{bmatrix} \Delta \theta \\ \Delta V \end{bmatrix}; \quad (5)$$

$$\begin{bmatrix} \Delta P \\ \Delta Q \end{bmatrix} = [J] \begin{bmatrix} \Delta \theta \\ \Delta V \end{bmatrix}, \quad (6)$$

where J is the Jacobian matrix and

$$J_{P\theta} = \frac{\partial P}{\partial \theta}, \quad J_{PV} = \frac{\partial P}{\partial V}, \quad J_{Q\theta} = \frac{\partial Q}{\partial \theta}, \quad J_{QV} = \frac{\partial Q}{\partial V}, \quad (7)$$

and $\Delta P, \Delta Q, \Delta \theta$ and ΔV are the incremental changes in real power, reactive power, bus voltage angle and bus voltage magnitude respectively.

If real power variations are assumed to be zero then (5) can be simplified as

$$\Delta \theta = -[J_{P\theta}]^{-1} J_{PV} \Delta V; \quad (8)$$

$$\Delta Q = [J_{QV} - [J_{P\theta}]^{-1} J_{PV} J_{Q\theta}] \Delta V; \quad (9)$$

$$\Delta Q = J_R \Delta V; \quad (10)$$

$$\Delta V = J_R^{-1} \Delta Q, \quad (11)$$

where J_R is the diminished Jacobian matrix.

The diagonal elements of J_R represent the Q-V sensitivities at any node.

Sensitivity analysis is obtained from the assumption that active power variations are decoupled from voltage variations. This is not a valid assumption if the system is under high stress. By applying Schur decomposition to the Jacobian matrix in (6), the gravity of the active power dissimilarity under stressed conditions can be deduced.

Suggested methodology. The development in synchrophasor measurements leads to the accurate measurement of voltage magnitudes, branch currents, and phasor angles. These measurements are used to compute nodal reactive power losses. It has been observed that nodal reactive power loss along with voltage magnitudes at any node has suitable information to detect imminent voltage instability. In addition to that, the critical aspect of Q-V sensitivity analysis may be overcome by considering nodal reactive power to voltage sensitivity analysis. When a system is subjected to continuous load increments, then reactive power loss in the branches also increases continuously. If the system is stressed with excessive loading, then line losses will increase, especially the reactive power losses. This has effect on voltage magnitude at the buses.

At the stroke of voltage instability branch reactive power losses increase abruptly and voltage magnitudes rapidly reduce to unacceptably low values. The power system perceives this condition as non-intersection of system characteristic with load characteristic. The type load and the magnitude of load are essentially accountable for this condition. The voltage instability condition can be identified using the reactive power losses and voltage magnitudes from the PMU measurements. It has been identified that nodal reactive power loss trajectory can detect the voltage instability accurately as opposed to voltage magnitude. In the case of overcompensated systems voltage collapse takes place at voltage magnitudes close to nominal values. So voltage magnitude alone is not a suitable criterion for voltage instability detection.

As the bus reactive power losses are obtained from line reactive powers losses, the trend of these losses along with voltage magnitudes at any node gives reliable information to detect voltage instability. It has also been discerned that the bus power losses shoots up at high load conditions but much before loadings corresponding to voltage collapse. This property of the trend of nodal power losses (reactive) has been exploited here to detect the voltage instability.

Under normal operating conditions with nominal loadings on the system NRPVS trend is smooth but if the system is sufficiently stressed then its trend varies abruptly and will progress in the direction of sharp change. At the collapse point, a large sudden change in NRPVS occurs. The point where the first sharp change in NRPVS occurs is the detection point and the time at which it occurs is known as instability detection time.

After early detection of voltage instability from NRPVS, its values are used to determine the quantity of load to cut in each bus to ensure both voltage stability and acceptable voltage magnitudes.

Load shedding at any load busy J can be computed as

$$Loadshed_j = \frac{NRPVS_j}{\sum_{J \in nl} NRPVS_j}, \quad (12)$$

where $J \in nl$ means the bus j corresponds only to the load buses; $Loadshed_j$ is the load shedding at load bus j and $NRPVS_j$ is the nodal reactive power loss to voltage sensitivity at bus j .

The flowchart of the algorithm is given Fig. 2.

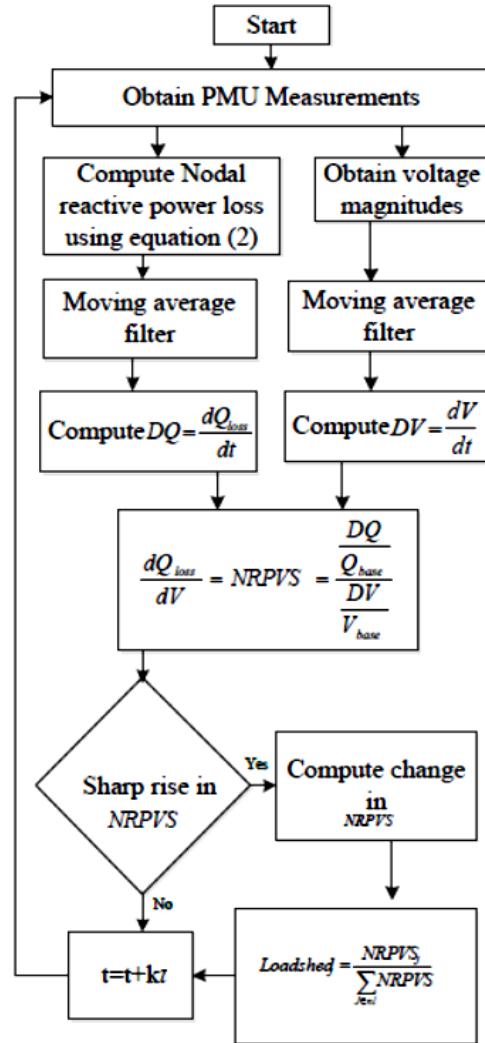


Fig. 2. Proposed methodology

The steps of the algorithm to implement in real time are as follows:

- 1) Obtain the PMU measurements at all the load buses.
- 2) With these measurements compute the bus reactive power losses by considering the direction of active power flows and branch reactive power losses.
- 3) As PMU data may contain noise signals, these are filtered by using moving average filter.

Moving average filter. It contains a sliding window of suitable size of our choice. The output of this filter at any time k is given as:

$$Y_k = \frac{1}{M} \sum_{j=k-M+1}^k Y_j, \quad (13)$$

where M is the window size.

- 4) Evaluate rate change in bus 1 reactive power losses and rate change in voltage magnitudes in all the load buses.

5) Then normalize the computed rate change in bus reactive power losses and rate change in voltage magnitudes with its base values. Base values are the values obtained under base load condition of the system. This normalization is done only for computational simplicity.

6) Divide normalized rate change of bus reactive losses with normalized rate change of voltage magnitude and name it as NRPVS.

7) Monitor NRPVS under real time and find any sudden change.

8) Compute the value of NRPVS at the instant of sudden change.

9) Compute load shedding in each node by using the values in previous step.

Simulation results. The proposed methodology has been tested in New England 39 bus test system with all the dynamic components responsible for voltage stability issues. All the synchronous generators are considered with two-axis flux decay model with enforced excitation limits. The equations governing the model are as follows:

$$\dot{\delta}_i = \Omega_b \cdot (\omega_i - 1); \quad (14)$$

$$\dot{\omega}_i = \frac{P_{mi} - P_{ei} - D_i \cdot (\omega_i - 1)}{M_i}; \quad (15)$$

$$\dot{e}'_{qi} = \frac{-f_{si}(e'_{qi}) - (x_{di} - x'_{di}) \cdot i_{di} + v_{fi}^*}{T'_{d0i}}; \quad (16)$$

$$\dot{e}'_{di} = \frac{-e'_{di} + (x_{qi} - x'_{qi}) \cdot i_{qi}}{T'_{q0i}}; \quad (17)$$

$$P_{ei} = (v_{qi} + r_{ai} \cdot i_{qi}) \cdot i_{qi} + (v_{di} + r_{ai} \cdot i_{di}) \cdot i_{di}; \quad (18)$$

$$v_{qi} + r_{ai} \cdot i_{qi} - e'_{qi} + (x'_{di} - x_{li}) \cdot i_{di} = 0; \quad (19)$$

$$v_{di} + r_{ai} \cdot i_{di} - e'_{di} + (x'_{qi} - x_{li}) \cdot i_{qi} = 0; \quad (20)$$

$$\dot{V}_{mi} = \frac{V_i - v_{mi}}{T_{ri}}; \quad (21)$$

$$\dot{V}_{ri} = \frac{K_{ai} \cdot \left(v_{refi} - v_{mi} - v_{r2i} - \frac{k_{fi}}{T_{fi}} \cdot v_{fi} \right) - v_{rli}}{T_{ai}}; \quad (22)$$

$$v_r = \begin{cases} v_{rli} & \text{if } v_{rmini} \leq v_{rli} \leq v_{rmaxi}; \\ v_{rmaxi} & \text{if } v_{rli} > v_{rmaxi}; \\ v_{rmini} & \text{if } v_{rli} < v_{rmini}; \end{cases}; \quad (23)$$

$$v_{ri} = \frac{-\left(\frac{k_{fi}}{T_{fi}} \right) \cdot v_{fi} + v_{r2i}}{T_{fi}}; \quad (24)$$

$$\dot{v}_{fi} = \frac{-v_{fi} \cdot (1 + s_e(v_{fi})) - v_{ri}}{T_{ei}}; \quad (25)$$

where all parameters are described in Table 1.

The load is considered as the composite ZIP load with 20 % constant impedance load, 20 % constant current load, and 60 % constant power load. The ZIP load model mimics the practical load and therefore such model is being considered. The simulations are performed in PSAT [29] toolbox in MATLAB environment. The data obtained from PSAT simulations were treated as the data from PMU measurements. All of the load buses are loaded with (0.001+j0.001) pu/s. This load increment is applied simultaneously to all the load nodes. Such load increment is known as stress in the system. The authors believe that any index should detect the unforeseen event with accuracy for the concomitant load variations in the

system. This work proposed for long term voltage stability and therefore such a pattern of load increment is chosen for simulations. This pattern of load increment plunge the system from a stable operating state to an unstable state.

Table 1

Description of parameters		
No.	Parameters	Description
1	δ	Rotor angle
2	Ω_b	Base speed
3	ω	Rotor speed in p.u.
4	P_{mi}	Mechanical power input
5	P_{ei}	Electrical power input
6	D	Damping coefficient
7	M	Mechanical starting time
8	e_{qi}	q-axis transient voltage
9	e'_{di}	d-axis transient voltage
10	x_{qi}	Synchronous reactance in q-axis
11	x'_{qi}	Transient reactance in q-axis
12	x_{di}	Synchronous reactance in d-axis
13	x'_{di}	Transient reactance in d-axis
14	i_a	Quadrature axis current
15	i_d	Direct axis current
16	T'_{d0}	Open circuit transient time constant in d-axis
17	T'_{q0}	Open circuit transient time constant in q-axis
18	v_{qi}	q-axis voltage
19	v_{di}	d-axis voltage
20	r_a	Armature resistance
21	x_{li}	Leakage reactance
22	v_f	Field voltage
23	v_{mi}	Transducer
24	T_r	Transducer time constant
25	K_f	Stabilizer gain
26	T_f	Stabilizer time constant
27	K_a	Amplifier gain
28	v_r	Regulator voltage
29	v_{ref}	Reference voltage
30	v_{rmaxi}	Regulator maximum voltage
31	v_{rmini}	Regulator minimum voltage
32	v_{r1}	Saturation voltage point 1
33	v_{r2}	Saturation voltage point 2
34	$s_e(v_f)$	Saturation function
35	T_{ei}	Field circuit time constant
36	V	Terminal voltage

The proposed methodology detects the early occurrence of voltage instability. The voltage magnitude plot is shown in Fig. 3 delineate that voltage magnitude drops as load increases. This is due to the fact that the transmission line acting drain to reactive power. This causes insufficient reactive power support at load buses. The insufficient reactive power support is reflected as drop in voltage magnitude. The incessant drop in voltage against time is regarded as voltage instability problem. The voltage plot depicts that voltage instability occurred at 182 s.

The plot of nodal reactive losses at the cogitated buses is shown in Fig. 4. This figure depicts reactive losses in the nodes with time-based load increments. As mentioned earlier and from the reactive power loss equations the nodal reactive power losses trend has something noteworthy. If the load variations are less and continual, the nodal reactive power loss trend shows a small variation. The line reactive power loss seems to be

linear till a particular load increment and any load increment beyond that limit causes the reactive power loss to shoot up. As the nodal reactive power loss is the summation of all the incoming line reactive power losses and therefore nodal reactive power losses also increase abruptly. The point at which such abrupt change occurs has some information to report the stability status of the system. However, if the stress on the system is continuous and reaches the point instability, the nodal reactive power losses increase abruptly. It has been observed that voltage magnitude and nodal reactive power loss has a direct relationship and this is explored in this work.

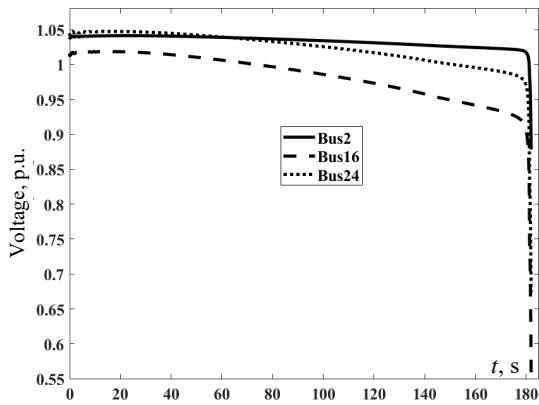


Fig. 3. Plot of voltages in p.u.

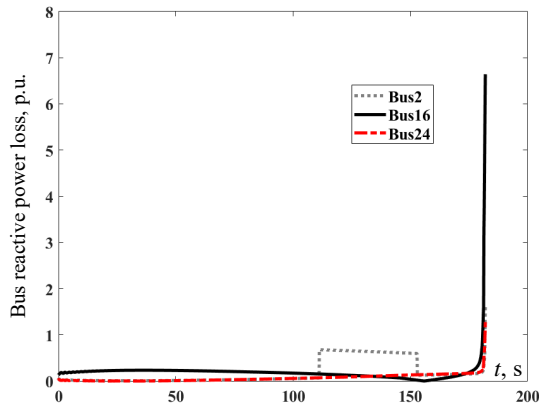


Fig. 4. Bus reactive power losses in p.u.

The reactive power loss to voltage sensitivity plot is evinced in Fig. 5. It has been noticed from Fig. 5 that, sudden change in reactive power loss to voltage occurs at 147 s. At this instant NRPVS is computed at all the nodes and the values are shown in Fig. 6. From this figure, it is observed that buses 2, 16 and 24 have the maximum change and therefore the plots of these buses are shown in this paper.

The quantity of load to cut at the load buses are computed using the above computed NRPVS. The plot in Fig. 7 shows the quantity of load to cut in the load buses to safeguard the system from the occurrence of voltage instability. The above-computed amount of load for load shedding has been applied on all the load buses at 148 s and it is observed that voltage magnitudes of all the nodes improved and the system is stable. The improved voltages after application of load shedding strategy are shown in Fig. 8. The comparison of voltages before and after the application of load shedding strategy is shown in Fig. 9. For this plot only 16 bus has been considered. However, it is obvious that at other nodes also voltage magnitudes will improve and system reaches stable state.

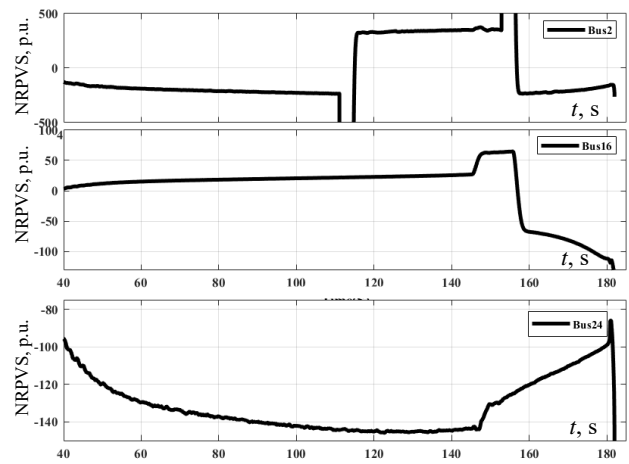


Fig. 5. Curves of NRPVS for buses 2, 16 and 24

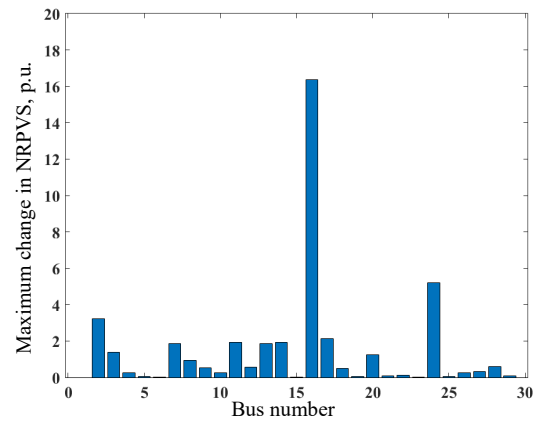


Fig. 6. NRPVS of load buses at 146 s

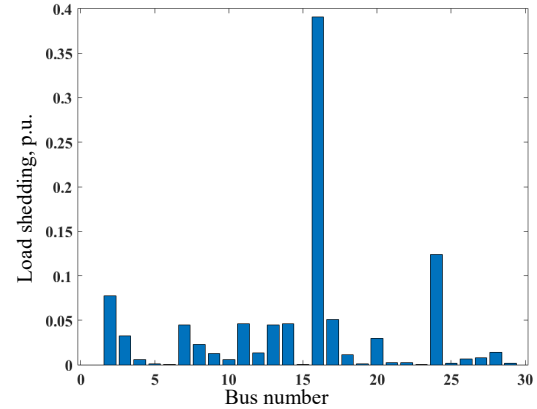


Fig. 7. Load to be shed in all nodes

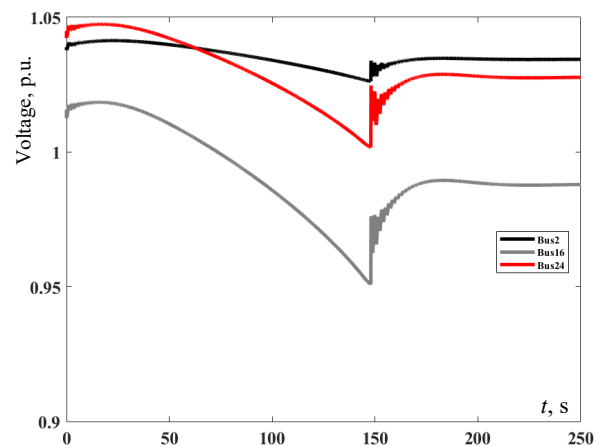


Fig. 8. Voltages plot after load shedding

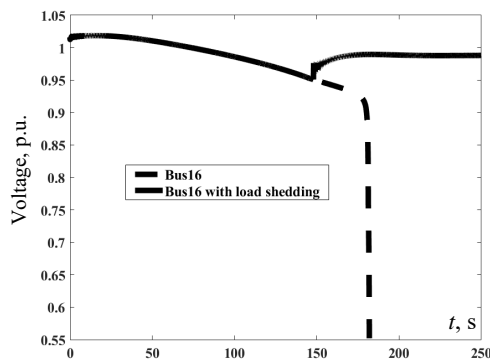


Fig. 9. Comparison of voltages with and without load shedding

Conclusions.

In this work, a novel methodology for voltage instability detection and its prevention through load shedding has been proposed. Nodal reactive power loss to voltage sensitivity has been developed and the trend of it is used for voltage instability detection. The value of the sudden change in nodal reactive power loss to voltage sensitivity is used to devise the load shedding scheme. The nodes at which this sudden change occurs are considered here to show the simulation results. This methodology while applied to New England 39 bus test system, detected voltage instability at time close to 150 s where the actual voltage instability occurred at 182 s. This is leaving a margin of 32 s for the system operator to respond. Load shedding, which is a means for preserving the voltage instability, when applied at 150 s, the system reached to stable state. The simulated results show that this methodology could detect the voltage instability in good time and the load shedding can bring back the voltages to acceptable values.

Conflict of interest. The authors declare that they have no conflicts of interest.

REFERENCES

- Kundur P. *Power System Stability and Control*. New York, McGraw Hill Publ., 1994. 1200 p. Available at: <http://powerunit-ju.com/wp-content/uploads/2018/01/Power-System-Stability-and-Control-by-Prabha-Kundur.pdf> (Accessed 12 May 2021).
- Chappa H., Thakur T. Voltage instability detection using synchrophasor measurements: A review. *International Transactions on Electrical Energy Systems*, 2020, vol. 30, no. 6, art. no. e12343. doi: <https://doi.org/10.1002/2050-7038.12343>.
- Gao B., Morison G.K., Kundur P. Voltage stability evaluation using modal analysis. *IEEE Transactions on Power Systems*, 1992, vol. 7, no. 4, pp. 1529-1542. doi: <https://doi.org/10.1109/59.207377>.
- Wang Y., Li W., Lu J. A new node voltage stability index based on local voltage phasors. *Electric Power Systems Research*, 2009, vol. 79, no. 1, pp. 265-271. doi: <https://doi.org/10.1016/j.epsr.2008.06.010>.
- Vourmas C.D., Van Cutsem T. Local Identification of Voltage Emergency Situations. *IEEE Transactions on Power Systems*, 2008, vol. 23, no. 3, pp. 1239-1248. doi: <https://doi.org/10.1109/TPWRS.2008.926425>.
- Wang Y., Pordanjani I.R., Li W., Xu W., Chen T., Vaahedi E., Gurney J. Voltage Stability Monitoring Based on the Concept of Coupled Single-Port Circuit. *IEEE Transactions on Power Systems*, 2011, vol. 26, no. 4, pp. 2154-2163. doi: <https://doi.org/10.1109/TPWRS.2011.2154366>.
- Cui B., Wang Z. Voltage stability assessment based on improved coupled single-port method. *IET Generation, Transmission & Distribution*, 2017, vol. 11, no. 10, pp. 2703-2711. doi: <https://doi.org/10.1049/iet-gtd.2016.2067>.
- Sodhi R., Srivastava S.C., Singh S.N. A Simple Scheme for Wide Area Detection of Impending Voltage Instability. *IEEE Transactions on Smart Grid*, 2012, vol. 3, no. 2, pp. 818-827. doi: <https://doi.org/10.1109/TSG.2011.2180936>.
- Seethalekshmi K., Singh S.N., Srivastava S.C. A Synchrophasor Assisted Frequency and Voltage Stability Based Load Shedding Scheme for Self-Healing of Power System. *IEEE Transactions on Smart Grid*, 2011, vol. 2, no. 2, pp. 221-230. doi: <https://doi.org/10.1109/TSG.2011.2113361>.
- Lim J.M., DeMarco C.L. SVD-Based Voltage Stability Assessment From Phasor Measurement Unit Data. *IEEE Transactions on Power Systems*, 2016, vol. 31, no. 4, pp. 2557-2565. doi: <https://doi.org/10.1109/TPWRS.2015.2487996>.
- Kamel M., Karrar A.A., Eltom A.H. Development and Application of a New Voltage Stability Index for On-Line Monitoring and Shedding. *IEEE Transactions on Power Systems*, 2018, vol. 33, no. 2, pp. 1231-1241. doi: <https://doi.org/10.1109/TPWRS.2017.2722984>.
- Chappa H.K., Thakur T., Srivastava S.C. Reactive power loss based voltage instability detection using synchrophasor technology. *2015 IEEE PES Asia-Pacific Power and Energy Engineering Conference (APPEEC)*, 2015, pp. 1-5. doi: <https://doi.org/10.1109/APPEEC.2015.7381029>.
- Chappa H., Thakur T. A Fast Online Voltage Instability Detection in Power Transmission System Using Wide-Area Measurements. *Iranian Journal of Science and Technology, Transactions of Electrical Engineering*, 2019, vol. 43, no. S1, pp. 427-438. doi: <https://doi.org/10.1007/s40998-018-0120-2>.
- Chappa H.K., Thakur T., Suresh Kumar L.V., Kumar Y.V.P., Pradeep D.J., Reddy C.P., Ariwa E. Real Time Voltage Instability Detection in DFIG Based Wind Integrated Grid with Dynamic Components. *International Journal of Computing and Digital Systems*, 2021, vol. 10, no. 1, pp. 795-804. doi: <https://doi.org/10.12785/ijcds/100173>.
- Tsai S.-J. S., Wong K.-H. Adaptive undervoltage load shedding relay design using Thevenin equivalent estimation. *2008 IEEE Power and Energy Society General Meeting - Conversion and Delivery of Electrical Energy in the 21st Century*, 2008, pp. 1-8. doi: <https://doi.org/10.1109/PES.2008.4596370>.
- Arya L., Pande V., Kothari D. A technique for load-shedding based on voltage stability consideration. *International Journal of Electrical Power & Energy Systems*, 2005, vol. 27, no. 7, pp. 506-517. doi: <https://doi.org/10.1016/j.ijepes.2005.05.001>.
- Kessel P., Glavitsch H. Estimating the Voltage Stability of a Power System. *IEEE Transactions on Power Delivery*, 1986, vol. 1, no. 3, pp. 346-354. doi: <https://doi.org/10.1109/TPWRD.1986.4308013>.
- Jianjun Z., Dongyu S., Dong Z., Yang G. Load Shedding Control Strategy for Power System Based on the System Frequency and Voltage Stability. *2018 China International Conference on Electricity Distribution (CICED)*, 2018, pp. 1352-1355. doi: <https://doi.org/10.1109/CICED.2018.8592262>.
- Shekari T., Gholami A., Aminifar F., Sanaye-Pasand M. An Adaptive Wide-Area Load Shedding Scheme Incorporating Power System Real-Time Limitations. *IEEE Systems Journal*, 2018, vol. 12, no. 1, pp. 759-767. doi: <https://doi.org/10.1109/JSYST.2016.2535170>.
- Saffarian A., Sanaye-Pasand M. Enhancement of Power System Stability Using Adaptive Combinational Load Shedding Methods. *IEEE Transactions on Power Systems*, 2011, vol. 26, no. 3, pp. 1010-1020. doi: <https://doi.org/10.1109/TPWRS.2010.2078525>.
- Arief A., Nappu M.B., Dong Z.Y. Dynamic under-voltage load shedding scheme considering composite load modeling. *Electric Power Systems Research*, 2022, vol. 202, p. 107598. doi: <https://doi.org/10.1016/j.epsr.2021.107598>.

22. Horri R., Mahdinia Roudsari H. Adaptive Under-Frequency Load-Shedding Considering Load Dynamics and Post Corrective Actions to Prevent Voltage Instability. *Electric Power Systems Research*, 2020, vol. 185, p. 106366. doi: <https://doi.org/10.1016/j.epsr.2020.106366>.
23. Hoseinzadeh B., Leth Bak C. Centralized coordination of load shedding and protection system of transmission lines. *International Transactions on Electrical Energy Systems*, 2019, vol. 29, no. 1, p. e2674. doi: <https://doi.org/10.1002/etep.2674>.
24. Yao M., Molzahn D.K., Mathieu J.L. An Optimal Power-Flow Approach to Improve Power System Voltage Stability Using Demand Response. *IEEE Transactions on Control of Network Systems*, 2019, vol. 6, no. 3, pp. 1015-1025. doi: <https://doi.org/10.1109/TCNS.2019.2910455>.
25. Mahari A., Seyedi H. A wide area synchrophasor-based load shedding scheme to prevent voltage collapse. *International Journal of Electrical Power & Energy Systems*, 2016, vol. 78, pp. 248-257. doi: <https://doi.org/10.1016/j.ijepes.2015.11.070>.
26. Modarresi J., Gholipour E., Khodabakhshian A. A New adaptive and centralised under-voltage load shedding to prevent short-term voltage instability. *IET Generation, Transmission & Distribution*, 2018, vol. 12, no. 11, pp. 2530-2538. doi: <https://doi.org/10.1049/iet-gtd.2017.0783>.
27. Gadiraju K.V.R., Kolwalkar A., Gurralla G. *Systems and methods for predicting power system instability*. US Patent no. 20130154614, Jun. 2013. Available at: <http://www.freepatentsonline.com/y2013/0154614.html> (Accessed 12 May 2021).
28. Jamroen C., Piriyanont B., Dechanupaprittha S. Load shedding scheme based on voltage instability index using synchrophasor data. *2017 International Electrical Engineering Congress (IEECON)*, 2017, pp. 1-4. doi: <https://doi.org/10.1109/IEECON.2017.8075776>.
29. Milano F. An Open Source Power System Analysis Toolbox. *IEEE Transactions on Power Systems*, 2005, vol. 20, no. 3, pp. 1199-1206. doi: <https://doi.org/10.1109/TPWRS.2005.851911>.

Received 10.02.2022

Accepted 26.03.2022

Published 01.06.2022

Hemanthakumar Chappa¹, PhD, Assistant Professor,
Tripta Thakur², PhD, Director General,

¹ Department of Electrical & Electronics Engineering,
GMR Institute of Technology,

Rajam-532 127, Srikakulam Dist., Andhra Pradesh, India,

e-mail: hemanthkumar.ch@gmrit.edu.in (Corresponding author);

² National Power Training Institute,

NPTI Complex, Sector-33, Faridabad, 121003, Haryana, India,

e-mail: tripta_thakur@yahoo.co.in

How to cite this article:

Chappa H., Thakur T. A novel load shedding methodology to mitigate voltage instability in power system. *Electrical Engineering & Electromechanics*, 2022, no. 3, pp. 63-70. doi: <https://doi.org/10.20998/2074-272X.2022.3.09>

H. Sekhane, D. Labeled, M.A. Labeled

Modelling and performance testing of a digital over-current relay enhanced designed model

Introduction. The over-current relay is widely used to protect distribution and transmission electrical systems against excessive currents occurring due to short circuit or overload conditions. Many works have been carried out in the field of models simulation design of digital over-current relays in the literature, but unfortunately many of them are more complex design models, have very slow execution time and only work in simple faults cases. **Purpose.** The purpose of this work is to present the performance of a modified and improved model of a digital over-current relay designed in Simulink/MATLAB environment with more simplified design, faster execution time, and able to operate under more complex fault conditions. **Methodology.** Before starting tests, modelling of over-current relay is presented in details, of which the basic logics of the proposed model to implement inverse and instantaneous characteristics are well explained. Afterwards, various tests are carried out for the performance analysis of the enhanced designed relay model in terms of: operating speed for eliminating faults that has arisen, ability to distinguish between a fault current and load starting current, capacity distinguish between real and temporary fault currents, the way to manage variable faults over time, and the degree of harmony between primary protection relay and back-up protection relay. **Originality.** The originality of our proposed work consists in the development and improvement of a digital over-current relay model designed in Simulink/MATLAB environment in such way that it becomes able to operate under new harsh test conditions. This developed designed model is implemented and applied in a 400V radial distribution power system with a load that causes a starting current. **Results.** The obtained values of simulation are compared with the theoretically calculated values and known existing models. The obtained results after various tests validate the good performance of our enhanced designed model. References 18, tables 3, figures 18.

Key words: digital over-current relay, inverse and instantaneous characteristics, load starting current, primary protection, back-up protection.

Вступ. Реле надструму широко використовується для захисту електричних систем розподілу та передачі від надмірних струмів, що виникають внаслідок короткого замикання або перевантаження. У літературі було виконано багато робіт у галузі моделювання цифрового реле надструму, але, на жаль, багато з них є більш складними моделями конструкції, з дуже повільним часом виконання, і вони працюють лише у випадках простих несправностей. **Метою** даної роботи є представлення продуктивності модифікованої та вдосконаленої моделі цифрового реле надструму, розробленої в середовищі Simulink/MATLAB, з більш спрощеною конструкцією, швидшим часом виконання та здатністю працювати в більш складних умовах несправностей. **Методологія.** Перед початком випробувань детально представлено моделювання реле надструму, з якої добре пояснено основні логіки запропонованої моделі для реалізації зворотних і миттєвих характеристик. Після цього проводяться різноманітні випробування для аналізу продуктивності вдосконаленої розробленої моделі реле з точки зору: швидкості роботи для усунення виниклих несправностей, здатності розрізняти струм несправності та пусковий струм навантаження, можливості розрізняти реальні та тимчасові струми несправності, спосіб управління змінними несправностями в часі та ступінь відповідності реле первинного захисту та реле резервного захисту. **Оригінальність** запропонованої нами роботи полягає в розробці та вдосконаленні моделі цифрового реле надструму, розробленої в середовищі Simulink/MATLAB таким чином, щоб вона стала здатною працювати в нових жорстких умовах випробувань. Ця розроблена модель реалізована та застосована у радіальної розподільчої енергосистемі 400 В з навантаженням, що викликає пусковий струм. **Результати.** Отримані результати моделювання порівнюються з теоретично розрахованими значеннями. Результати, отримані після різноманітних випробувань, підтверджують хорошу продуктивність нашої покращеної розробленої моделі. Бібл. 18, табл. 3, рис. 18.

Ключові слова: цифрове реле надструму, зворотні та миттєві характеристики, пусковий струм навантаження, первинний захист, резервний захист.

Introduction. According to the International Electrotechnical Commission (IEC), the protection of electrical networks is the set of monitoring devices intended for the detection of faults and abnormal situations such as short-circuits, variation in voltage, machine faults, etc. and ensuring the stability of an electrical network with the aim of ensuring an uninterrupted power supply and avoids the destruction of expensive equipment. Generally, this protection is provided by relays which are devices that continuously compare electrical variables such as: current, voltage, frequency, etc. with predetermined values, and when the monitored value exceeds the threshold they automatically give opening orders to its associated circuit breakers [1]. Many types of relays have been employed by electric power utilities such as over- and under-voltage, over- and under-frequency and over-current relays (OCR), etc. However, this latter is the most commonly used, and they can be applied in any zone in the power system for both primary and back-up protection [2, 3].

Currently, in view of growing demand for precise, selective and reliable OCR due to the increasing complexity and capacity of power systems on the one hand, and the development of logic, communication, information storage and processing capacities of modern microprocessors on the other hand, traditional electromechanical and solid state relays are replaced by digital relays which are faster, more compact, more reliable in operation, ensuring minimal power outage in case of fault and has advantages in terms of data logging and adaptive functionality, etc. [2, 4, 5].

The goal of the paper is to present the performance of a modified and improved model of a digital over-current relay designed in Simulink/MATLAB environment for some new cases.

The performance of the proposed digital OCR is sought and tested on a line between two buses of a 400 V radial distribution power system where the objectives of

this work are summarized in testing the following characteristics: operating speed, ability to distinguish between a fault current and load pickup current, capacity distinguish between real and temporary fault currents, the way to manage variable faults, degree of harmony between primary protection and back-up protection.

The remainder of the paper is organized as follows. First, the current-time characteristic of an OCR is explained. Then, the OCR modelling is presented on details. Next, the enhanced designed digital OCR is implemented in a 400 V radial network to carry out a different test. Finally, we conclude our paper with some remarks, and a prospect.

Current-time characteristic of an OCR. OCR has the function of detecting single-phase, two-phase or three-phase over-currents. The protection can be time-delayed and will only be activated if one, two or three phases of the monitored current exceed the specified setting threshold for a period at least equal to the selected time delay also called «operating time», and is calculated based on the protection algorithm incorporated in the relay microprocessor [1, 6]. According to this delay the current-time characteristic of a typical OCR shown in Fig. 1 can be one of two as follows.

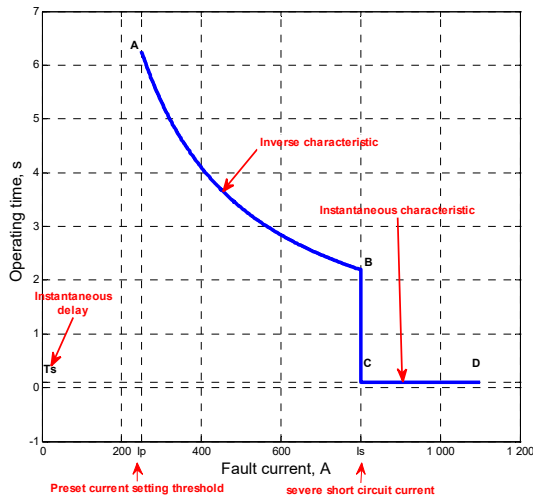


Fig. 1. Current-time characteristic of an OCR

Inverse characteristic. This characteristic means that the operating time of the relay is inversely proportional to the fault current i.e. the higher the current, the shorter the operating time (see curve AB in Fig. 1). This characteristic is used for the protection of electrical installations against excessive fault currents below severe fault levels but able enough that they will damage such installations if maintained for a certain period [2, 6, 7].

On the other hand, inverse characteristic of a relay may have to be modified depending on the characteristics and the required operating time of other protection devices used in the electrical network. This is why IEC defines several types of inverse delay protection which are distinguished by the gradient of their curves: Standard Inverse (SI), Very Inverse (VI), Extremely Inverse (EI) and Long Inverse (LI) [7, 8].

The operating time in inverse characteristic of OCR (noted T) is depicted as per IEEE standard by the following general expression [3]:

$$T = \frac{K}{\left(I_f / I_p\right)^n - 1}, \quad (1)$$

where K is the constant for relay characteristic; I_f is the actual fault current; I_p is the pre-set current setting threshold; n is the constant representing inverse-time type.

By selecting suitable values of n and K any desired relay curve can be obtained. Equation (1) can be modified in terms of actual faults as:

$$T = \frac{K}{I_f^n}, \quad (2)$$

with $I_p < I_f < I_s$, where I_s is the short circuit current.

It is important to note that the fault current I_f detected by the relay is implicitly assumed constant. Otherwise, during a transient or a variable fault current this will lead to an inaccurate operating time by the relay.

Instantaneous characteristic. This characteristic (shown in curve BCD of Fig. 1) means that the relay operates in the fastest possible time i.e. as soon as the fault current becomes greater than the value of the short circuit current I_s . In this case the operating time is only of the order of a few milliseconds:

$$T = T_s, \quad (3)$$

with $I_f > I_s$, where T_s is the instantaneous operating time.

Relays with instantaneous characteristic are graded by a time interval of Definite Time (DT sec) between them, e.g. the relay R_3 imposed at the end of the network of Fig. 2 is set to operate as fast as possible with an instantaneous operating time T_{s3} , while its upstream relay R_2 is set to a higher independent operating time ($T_{s2} = T_{s3} + DT$). The instantaneous operating times of the remaining relays increase sequentially at DT sec on each section, moving back up to the source [9].

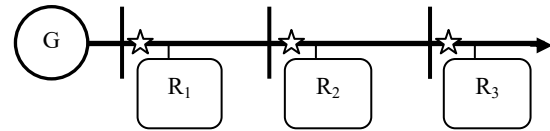


Fig. 2. Graded relays in radial network [9]

Modelling of OCR. Digital relays also called «programmable relays» based on microprocessors are of great importance in the protection field, especially in industry in view of their ability to protect against various faults (over-currents, over-voltages, thermal overloads, etc.) [10, 11]. The general functional diagram of a microprocessor-based OCR implemented in a power system is shown in Fig. 3.

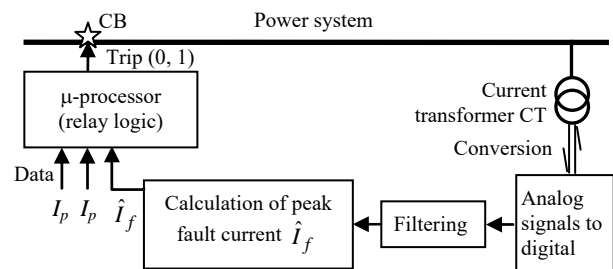


Fig. 3. General block diagram of a microprocessor-based OCR implemented in a power system

The digital relay operation is based on continuous data sampling [10]. Firstly, it takes the signal during run

time via an analog-to-digital converter. Then, the digital signal is filtered from any harmonics which can cause the relay to malfunction as well as to avoid the operating time reduction of the relay which causes coordination problems [12]. After that, the relay calculates the peak value of the measured fault current (\hat{I}_f) (also noted I_f), then the data (I_f , I_p , I_s) entered into the relay logic (μ -processor) which finally gives the opening (0) or closing (1) order to its associated circuit breaker (CB).

The global output of the digital OCR is the logical multiplication (AND) of the outputs of inverse and instantaneous characteristics elements [13].

Modelling of inverse characteristic. The basic logic for implementing the inverse characteristic is summarized as follows.

Measuring fault current peak value I_f . To detect the fault current, it must firstly compare the alternating current value (I) of frequency (f) entering the OCR with the pre-set current constant value of the latter. For this, it is mandatory to convert the fundamental sinusoidal filtered signal of the current into DC form [14, 15], and by measuring its slope (S) at zero crossing we obtain its peak value (I_f) as follows.

The instantaneous equation of the sinusoidal current is:

$$I(t) = I_f \cdot \sin(2 \cdot \pi \cdot f \cdot t). \quad (4)$$

The derivative of (I) as a function of time is:

$$\frac{dI(t)}{dt} = I_f \cdot 2 \cdot \pi \cdot f \cdot \cos(2 \cdot \pi \cdot f \cdot t). \quad (5)$$

The slope « S » at zero crossing is taken from (5) such that $t = 0$:

$$S = \frac{dI(0)}{dt} = I_f \cdot 2 \cdot \pi \cdot f. \quad (6)$$

From (6) we extract:

$$I_f = \frac{S}{2 \cdot \pi \cdot f}. \quad (7)$$

The designed block diagram of the peak current measurement I_f calculated by (7) in Simulink is shown in Fig. 4 in which the peak obtained at each zero crossing is held constant by the sample and hold the block until the next zero crossing.

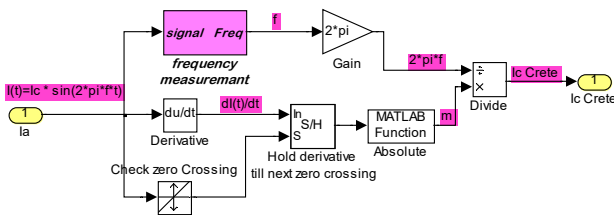


Fig. 4. Designed block diagram of peak current measurement

Frequency measurement and block design. The fundamental signal frequency entering the relay is determined by measuring the time between two consecutive zero crossings (T_1 and T_2), which gives half the time period (T) [2]:

$$T/2 = T_2 - T_1. \quad (8)$$

From (8), frequency is determined by:

$$f = \frac{1}{T} = \frac{1}{2 \cdot (T_2 - T_1)}. \quad (9)$$

Figure 5 depicts the frequency measurement block designed in Simulink. Firstly, the signal enters the «Hit Crossing» block which transmits it only at its zero crossings to the «If» block, and the latter sends the value of the ramp signal at that instant to the output. The duration of the generated ramp can be calculated and saved in a variable « A ». By temporarily storing « A » in another variable « B » using the «Transport Delay» block, « B » is therefore can be subtracted from the instant of the next zero crossing « A » at any time and this will give half of the period of time whose value is retained by the «Sample and Hold» block, until the next zero crossing. After having carried out the calculations according to (9), on the value retained, we obtain the instantaneous frequency [2].

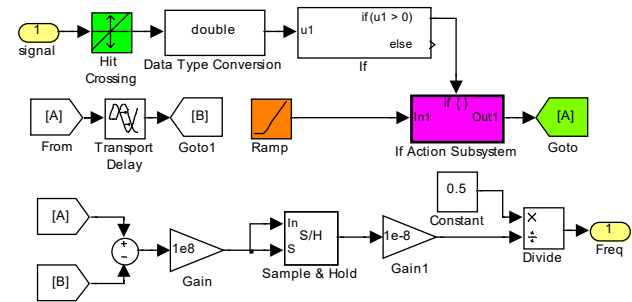


Fig. 5. Designed block diagram of frequency measurement

Measuring and design of the remainder basic logic of the inverse characteristic. After measuring the frequency and peak value of current I_f , the latter must be compared with the constant preset value of pickup current I_p of the relay using the comparator block «Relational Operator». If $I_f > I_p$, the value of I_f is raised to an appropriate power n to reach the desired relay curve, then integrated in the «Integrator» block [2].

As long as $I_f > I_p$, the integrator output continues to increase until it becomes equal to the pre-set value of constant K , causing the relay to send a trip signal («0»). If the excess current is temporary (due to load starting, or any switching action, etc.) and when it dies out to below I_p before reaching K , the rising integrator output is reset by the feedback reset logic to prevent any relay malfunction [2].

If the fault current is permanent and has a constant level, the value of I_f^n will also remain constant and therefore the output of the integrator will be:

$$C_{st} = \int_0^t I_f^n dt = I_f^n \cdot t. \quad (10)$$

Equation (10) is the equation of a straight line with slope I_f^n . On the other hand, the greater the fault current magnitude, the greater the rate of rise of integrator output and therefore a shorter time to reach the value of the constant K .

Modelling of instantaneous characteristic. As mentioned previously, when I_f is greater than short-circuit current I_s , OCR operates in instantaneous characteristic mode and sends a «0» trip signal to its associated circuit breaker after a shorter fixed delay of « T_s » seconds. The logic for implementing the instantaneous characteristic is shown in Fig. 6 below.

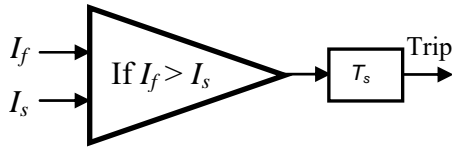


Fig. 6. Block diagram for implementing instantaneous characteristics of a digital OCR

Simulation and performance testing. In order to test the performances of the enhanced digital OCR model, the considered power system is a radial distribution network (see Fig. 7), with a load causing a starting current. It is worth to mention that the considered network is supposed without losses. Further, the electrical network parameters are summarized in Table 1, where U is the network voltage; P is the active power; Q is the reactive power; P_F is the power factor; T_{acc} is the accelerating period of the load; I_{isc} is the initial starting current; I_r is the nominal (rated) current.

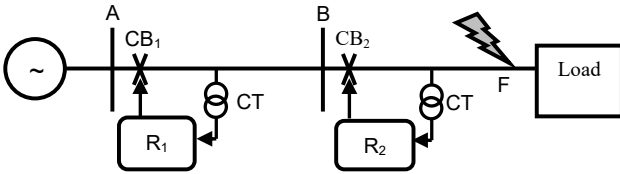


Fig. 7. Single line diagram of the proposed radial power network with coordination of relays (primary and backup protection)

Table 1

Electrical network parameters						
U, V	P, kW	$Q, kVAr$	P_F	f_s, Hz	T_{acc}, s	I_{isc}, A
400	100	61.97	0.85	60	2	$3 \cdot I_r$

Parameters calculation and relays settings choice.

In this sub-section, before starting to carry out the tests, it is firstly essential to calculate some necessary parameters and to make an adequate choice for relay setting of primary protection as well as for relay of backup protection. This choice is based on the parameters given in previous Table 1 and those calculated.

Calculation of the rated current at full load and the initial starting current. The rated current I_r at full load is calculated as follows:

$$I_r(rms) = \frac{P}{\sqrt{3} \cdot U \cdot \cos\varphi} = \frac{100 \cdot 10^3}{\sqrt{3} \cdot 400 \cdot 0.85} \cong 169.81 A. \quad (11)$$

From (11), the peak value of I_r is:

$$\hat{I}_r = \sqrt{2} \cdot I_r \cong 240.15 A. \quad (12)$$

From Table 1 the initial starting current is I_{isc} :

$$I_{isc}(rms) = 3 \cdot I_r \cong 509.43 A. \quad (13)$$

The peak value of I_{isc} is:

$$\hat{I}_{isc} = \sqrt{2} \cdot I_{isc} \cong 720.44 A. \quad (14)$$

Relays settings choice. The pickup current I_p (peak value) must be set to a value greater than the rated current I_r . We therefore choose a value somewhat close ($I_p = 250 A$) and similar for both primary (R_2) and emergency (R_1) protection relays. On the other hand, severe fault current setting I_s (as a peak value) must be greater than the initial starting current ($\hat{I}_{isc} \cong 720.44 A$). Consequently, a relatively close value ($I_s = 800 A$) is chosen for the relay R_2 . In addition, the instantaneous operating time is chosen as $T_{SR2} = 0.1 s$, and the constant K is selected such that it does not cause false tripping during start-up and transient conditions ($K_{R2} = 900$).

Furthermore, for a good relays coordination, R_1 must have a higher setting of I_s , K and T_s than that of R_2 . Therefore, the setting of these parameters is maintained as: $I_{SR1} = 1000 A$, $K_{R1} = 1000$ and $T_{SR1} = 0.2 s$. The parameters settings of R_1 and R_2 relays chosen in this subsection are collected and tabulated in Table 2.

Moreover, in this work the constant representing inverse-time type is chosen as $n = 0.9$, the total simulation time is $t = 10 s$ and the contact operating time of circuit breakers is assumed to be zero.

Table 2

Selected parameters settings of R1 and R2 relays				
	I_p, A (peak)	I_s, A (peak)	K	T_s, s
R_2	250	800	900	0.1
R_1	250	1000	1000	0.2

Test 1: Start-up, temporary fault and permanent fault test.

To see and verify the enhanced designed relay behavior, it is considered three different situations: starting period [0-2 s], temporary fault period [3-4 s] and permanent fault period [5-end] whose fault current value is $I_f = 400 A$. The models of [2], [16], [17] and [18] were invested so that the inverse characteristic was added to the last three models and the first model was developed and improved and then the four models were combined to obtain a final modified and improved model that illustrated in Fig. 8 to be able to operate under hard conditions tests.

Start-up period. From Fig. 9 below, during the acceleration period, the initial starting current I_{isc} (peak value) is greater than the pickup current I_p of R_2 , which increases the output of its integrator. At $t = 2 s$, when $I_{isc} < I_p$, the integrator output being less than K setting and drops to zero, and R_2 is reset.

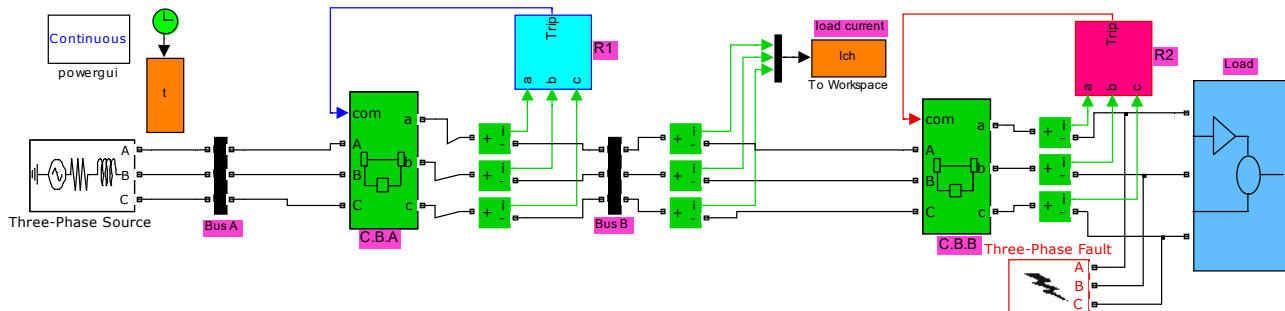


Fig. 8. Overall developed simulation model of the two OCRs implemented in the power system

The R_2 's K value is deliberately set above its maximum integrator output during the acceleration period to avoid any false tripping of relays R_1 and R_2 .

On the other hand, it can be seen also that the line representing R_2 integrator output in the load acceleration period is not straight seeing that the starting current is nonlinear (decreasing current). It is noted that if we drawing slopes in some points of this line (see Fig. 9) we notice that a large amplitude of the starting current (beginning of the current) results in a higher rate of rise of the integrator output and therefore a shorter time to reach the value of the constant K . Consequently, this remark applies to all other fault currents.

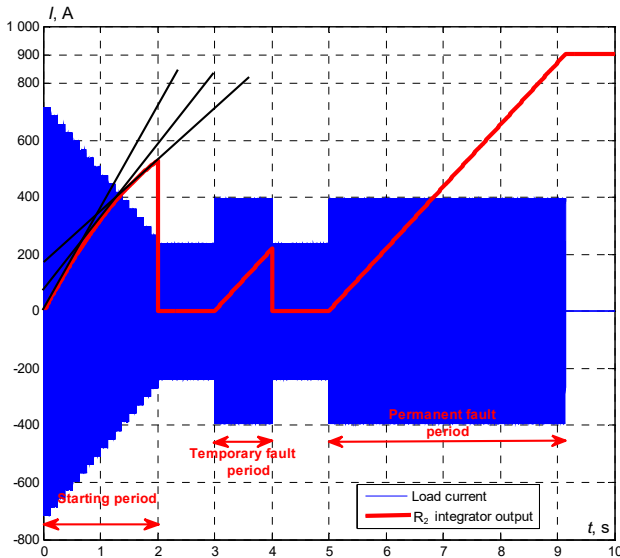


Fig. 9. Relay performance for test 1

Temporary fault period. In this case, it is clear from Fig. 9 above, that the R_2 integrator output is straight-shaped seeing that the fault current in this case is constant during this period.

As the fault is of a short duration (1 s in the interval [3-4 s]), this can't allow the output of the rising integrator of R_2 to reach the value of $K = 900$; so it goes back to zero. Relay R_2 stops counting its inverse characteristic operating time:

$$T = \frac{K}{I_f^n} = \frac{900}{400^{0.9}} \cong 4.1 \text{ s} . \quad (15)$$

As the fault time (1 s) is less than R_2 relay operating time (4.1 s), the latter therefore does not send any trip signal to its associated CB and ensures continuity of service at rated current I_r .

Permanent fault period. Contrary to the previous case, R_2 relay integrator output in this situation has sufficient time to reach the value of $K = 900$ after the same operating time of inverse characteristic calculated in (15) ($T = 4.1$ s) counted from instant $t = 5$ s.

Relay R_2 therefore sends its trip signal to its associated CB at the instant: $t = 5 \text{ s} + 4.1 \text{ s} = 9.1 \text{ s}$, while the backup protection relay R_1 remains inactive, as shown in Fig. 10, 11.

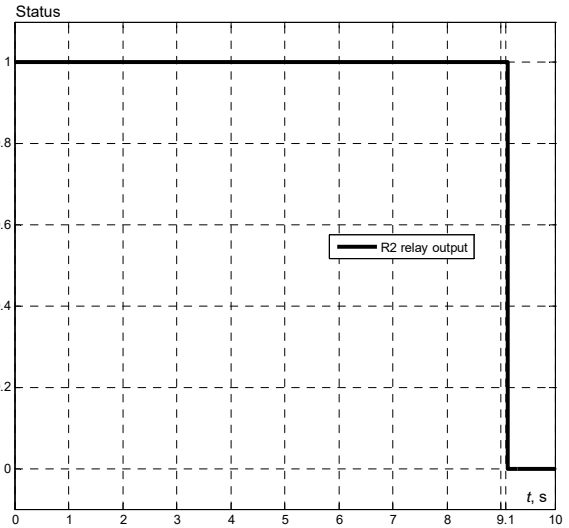


Fig. 10. R_2 status for test 1

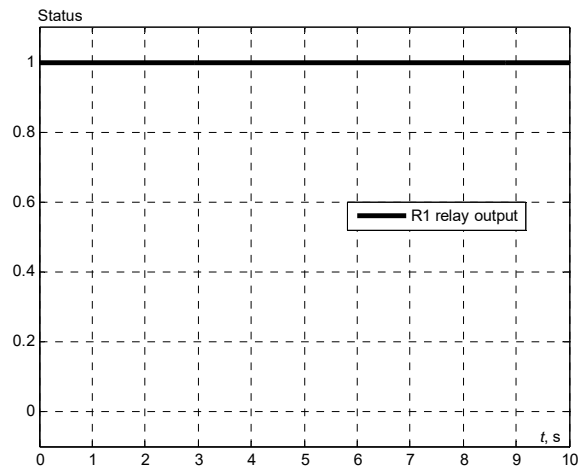


Fig. 11. R_1 status for test 1, 2, and 3

Test 2: Variable fault test. In this 2nd test, we will create a variable fault current for a relatively long duration of 3 s in the interval [3-6 s]. The considered variable fault current starts from $I_f = 270$ A at $t = 3$ s until $I_f = 960$ A at $t = 6$ s. From Fig. 12, it can be seen that unlike the falling starting current whose rising integrator output has the convex parabola shape, the rising variable fault current is also having a rising integrator output but in a concave parabola form. In addition, it is clear from the Figure that before the R_2 relay integrator output reaches the predefined value $K = 900$ (fixed only at 694.4 at $t = 5.35$ s) so that R_2 gives its tripping order in order to eliminate the fault current which is located in its inverse operating zone, the fault current reaches the severe current level ($I_f = 810.5 \text{ A} > I_s = 800 \text{ A}$) despite the long fault duration and enter in the instantaneous operating zone at $t = 5.25$ s. Therefore, R_2 relay switches from inverse mode to instantaneous mode and interrupts the fault current after the pre-set instantaneous delay $T_s = 0.1$ s, i.e. at $t = 5.35$ s (see Fig. 13). On the other hand, R_1 backup protection relay remains inactive because there is no reason to make it work (the same of Fig. 11).

The conclusion of this test is that the relay R_2 has eliminated the variable fault in instantaneous operating mode ($T_s = 0.1$ s, [5.25-5.35 s]), but after a certain period of inverse operating time ($T_{inv} = 2.25$ s [3-5.25 s]), so after a total time of $T = 2.35$ s.

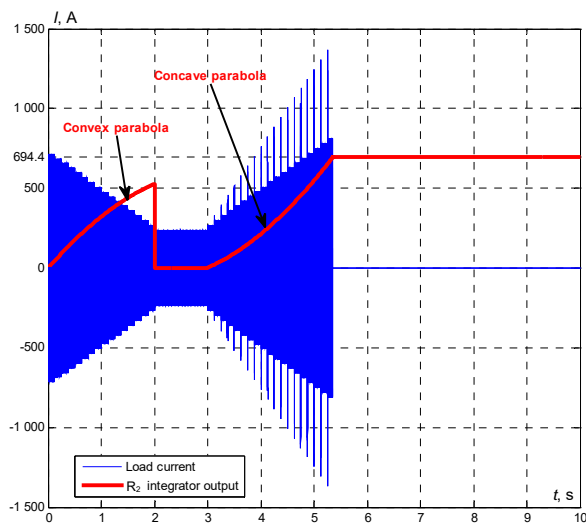


Fig. 12. Relay performance for test 2

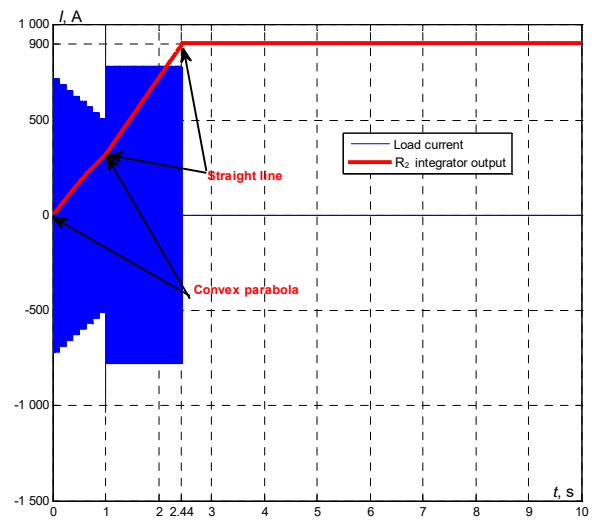


Fig. 14. Relay performance for test 3

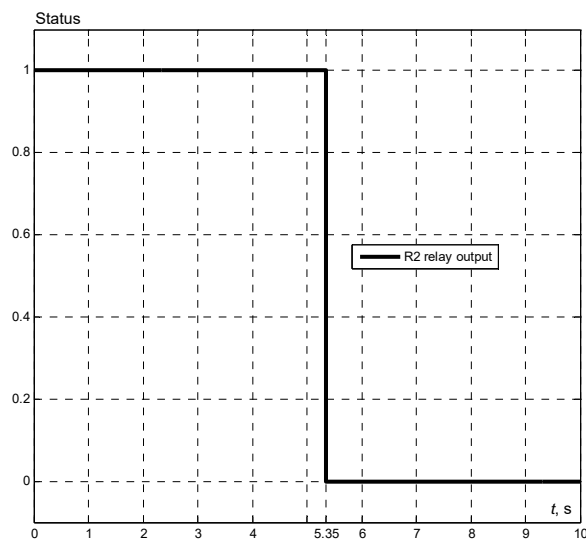


Fig. 13. R₂ status for test 2

Test 3: Testing of a fault during the acceleration period. In this 3rd test, a permanent fault current of constant value $I_f = 780$ A is considered, appeared at the instant $t = 1$ s during the acceleration period [0-2 s]. In the normal state, theoretical operating time of R₂ in inverse characteristic is:

$$T = \frac{K}{I_f^n} = \frac{900}{780^{0.9}} \cong 2.25 \text{ s.} \quad (16)$$

Hence, the fault theoretical interruption instant counting from their appearance instant ($t = 1$ s) is: $1 \text{ s} + 2.25 \text{ s} = 3.25 \text{ s}$ whereas according to Fig. 14 it can be seen that the fault is eliminated in advance at $t = 2.44$ s. i.e. 0.81 s ahead. This is explained by the fact that R₂ integrator output began to rise from the initial start-up instant ($t = 0$ s), and at the fault appearance instant ($t = 1$ s) it has reached the value 319.25; therefore, it needs only a little time to reach the pre-set value $K = 900$. It should be noted that R₂ integrator output in this case is a line composed of two parts of which the first is a convex parabola in the interval [0-1 s] due to the starting current, and the second is a straight line in the interval [1-2.44 s] due to the constant value of the fault current.

The status of R₁ and R₂ are shown respectively in Fig. 11 (the same status of previous cases) and Fig. 15. The performance presented by the relay according of this test resides in that it has the ability to distinguish between starting current which must let it to pass and fault current which must eliminate it.

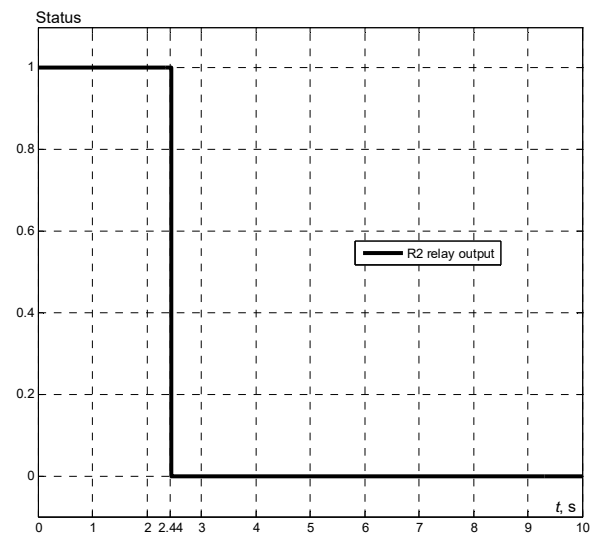


Fig. 15. R₂ status for test 3

Test 4: Fault test with broken down primary protection. In this test, it is assumed that R₂ relay of primary protection is broken down (cannot give its tripping order to its associated CB). At $t = 3$ s, a fault current which exceeds the severe current threshold of R₂ ($I_f = 840 \text{ A} > I_{sR2} = 800 \text{ A}$) is appeared. Thus, it was supposed that R₂ must eliminate this fault after an instantaneous operating time ($T_s = 0.1$ s), but in view of it is in break-down, the fault current still remains present. Consequently, the back-up protection is activated to operate through the R₁ relay; and since ($I_p < I_f < I_{sR2}$) the fault current is therefore in the inverse operating zone of R₁, whose the operating time is:

$$T = \frac{K}{I_f^n} = \frac{1000}{840^{0.9}} \cong 2.33 \text{ s.} \quad (17)$$

According to Fig. 16-18, it appears that R₁ relay gives its tripping order at $t = 5.33$ s counted from the fault

appearance instant ($t = 3$ s) i.e. after 2.33 s; it is exactly the theoretically calculated value in (17).

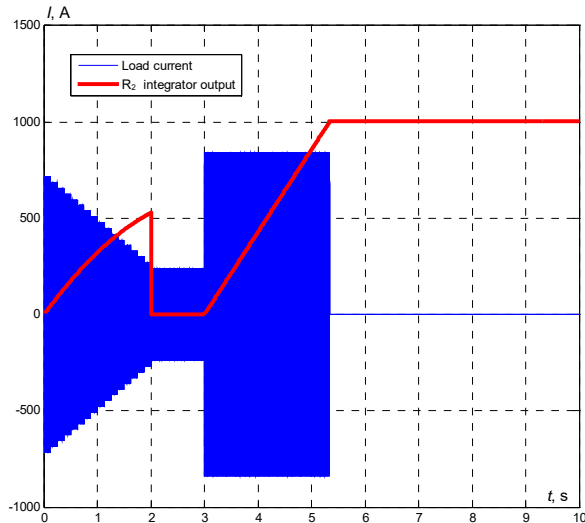


Fig. 16. Relay performance for test 4

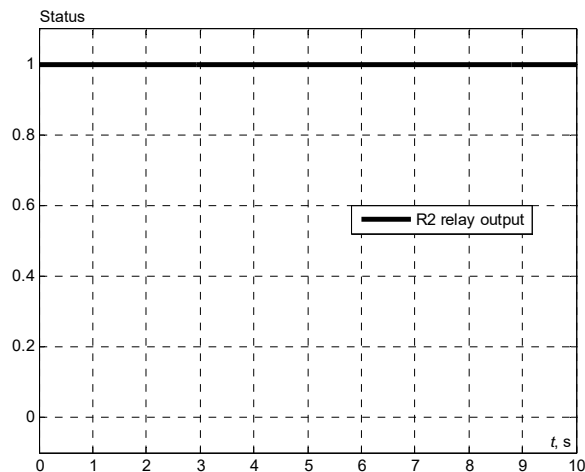


Fig. 17. R_2 status for test 4

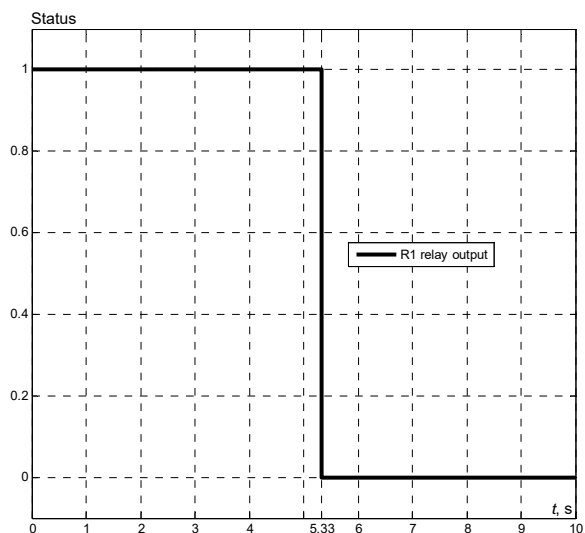


Fig. 18. R_1 status for test 4

From this test, it appears the service continuity performance guaranteed by both relays: R_2 of primary protection at the receiving end of the network, and R_1 of backup protection at the sending end to avoid any break-down problem and ensure a good protection of the power system.

On the other hand, some numerical data on improving operating speed (operating time T) of inverse characteristic of OCRs used for eliminating faults that has arisen are provided in the Table3.

Through the comparison table above, it is clear that the operating time value obtained in our test 4 is exactly the theoretically calculated value, as well as the higher accuracy of the inverse characteristic of our modified model compared to the results of other models.

Table 3

Operating time comparison with known existing models

Source	Simulation value T , s	Theoretically calculated value
[2] (case 1)	0.8	$\begin{cases} K = 3600; \\ n = 1; \\ I_f = \frac{6540}{\sqrt{2}}; \end{cases} \Rightarrow T = \frac{3600}{6540/\sqrt{2}} = 0.77$
[13] (case 3)	1.25	$\begin{cases} K = 3600; \\ n = 1; \\ I_f = \frac{4580}{\sqrt{2}}; \end{cases} \Rightarrow T = \frac{3600}{4580/\sqrt{2}} = 1.11$
Our result (test 4)	2.33	$\begin{cases} K = 1000; \\ n = 0.9; \\ I_f = 840; \end{cases} \Rightarrow T = \frac{1000}{840^{0.9}} = 2.33$

*as a reminder: K is the constant for relay characteristic; I_f is the actual fault current; n is the constant representing inverse-time type.

Conclusions.

In this paper, an enhanced designed model in Simulink/MATLAB of a digital over-current relay used as a primary protection and backup protection is presented on details. The proposed model is tested in a radial 400 V distribution network to carry out a various tests under new harsh test conditions. The simulation results proves the good and the high performance of the improved designed over-current relay on terms of: operating speed (time) for eliminating faults that has arisen, ability to distinguish between a fault current and load starting current, capacity distinguish between a real (permanent) and a temporary fault currents, the way to manage variable faults over time, and the degree of harmony (coordination) between primary relay and back-up relay. Finally, the enhanced designed digital over-current relay can be extended to design a directional over-current relay for a possible work in the future.

Conflict of interest. The authors declare that they have no conflicts of interest.

REFERENCES

1. Prévé C. *Protection of Electrical Networks*. ISTE Publ., 2006. 508 p. doi: <https://doi.org/10.1002/9780470612224>.
2. Aman M.M., Khan M.Q.A., Qazi S.A., Digital Directional and Non-Directional Over-Current Relays (Modeling and Performance Analysis), *NED University Journal of Research*, 2011, vol. VIII, no. 2, pp. 70-85. Available at: https://www.neduet.edu.pk/NED-Journal/previous_vol/pdf/11vol2paper7.pdf (Accessed 12 March 2021).

3. Jhanwar V., Pradhan A.K. Accurate Overcurrent Relay Algorithm using Fundamental Component. 2008 *Joint International Conference on Power System Technology and IEEE Power India Conference*, 2008 pp. 1-4. doi: <https://doi.org/10.1109/ICPST.2008.4745367>.
4. Sidhu T.S., Sachdev M.S., Wood H.C. Design of a microprocessor-based overcurrent relay. [*Proceedings*] WESCANEX '91, 1991, pp. 41-46, doi: <https://doi.org/10.1109/WESCAN.1991.160517>.
5. Shah K.R., Detjen E.D., Phadke A.G. Feasibility of adaptive distribution protection system using computer overcurrent relaying concept. *IEEE Transactions on Industry Applications*, 1988, vol. 24, no. 5, pp. 792-797. doi: <https://doi.org/10.1109/28.8981>.
6. Almas M.S., Leclaruji R., Vanfretti L. Over-current relay model implementation for real time simulation & Hardware-in-the-Loop (HIL) validation. *IECON 2012 - 38th Annual Conference on IEEE Industrial Electronics Society*, 2012, pp. 4789-4796. doi: <https://doi.org/10.1109/IECON.2012.6389585>.
7. Yacine A.A., Noureddine A.A., Hamid B., Farid H. Implementation of a Numerical Over-current Relay Using LabVIEW and Acquisition Card. *2018 International Conference on Electrical Sciences and Technologies in Maghreb (CISTEM)*, 2018, pp. 1-5, doi: <https://doi.org/10.1109/CISTEM.2018.8613455>.
8. Alstom Grid. *Network Protection & Automation Guide*. May 2011. 508 p. Available at: <https://rpa.energy.mn/wp-content/uploads/2016/07/network-protection-and-automation-guide-book.pdf> (Accessed 12 March 2021).
9. Atwa O.S.E. *Practical Power System and Protective Relays Commissioning*. Elsevier, Academic Press, 2019. 398 p. doi: <https://doi.org/10.1016/C2018-0-00911-1>.
10. Saleem A., Iqbal A., Mehmood K., Samad M.A., Hayat M.A., Manzoor U. Modelling and Implementation of Microprocessor Based Numerical Relay for Protection Against Over/Under Current, Over/Under Voltage. *Journal of Computational and Theoretical Nanoscience*, 2020, vol. 17, no. 2, pp. 1332-1338. doi: <https://doi.org/10.1166/jctn.2020.8809>.
11. Verzosa Q., Lee W.A. Testing Microprocessor-Based Numerical Transformer Differential Protection. *IEEE Transactions on Industry Applications*, 2017, vol. 53, no. 1, pp. 56-64. doi: <https://doi.org/10.1109/TIA.2016.2609402>.
12. Donohue P.M., Islam S. The Effect of Non-Sinusoidal Current Waveforms on Electro-Mechanical & Solid State Overcurrent Relay Operation. *2009 IEEE Industry Applications Society Annual Meeting*, 2009, pp. 1-6. doi: <https://doi.org/10.1109/IAS.2009.5324811>.
13. Naga Sujatha K., DurgaRao R., Shalini V.B. Performance analysis of digital over current relays under different fault conditions in radial and parallel feeders. *International Journal of Science and Technology*, 2017, vol. 3, no. 1, pp. 146-158. doi: <https://doi.org/10.20319/Mijst.2017.s3.1.146158>.
14. Suliman M.Y., Ghazal M. Design and Implementation of Overcurrent Protection Relay. *Journal of Electrical Engineering & Technology*, 2020, vol. 15, no. 4, pp. 1595-1605. doi: <https://doi.org/10.1007/s42835-020-00447-0>.
15. Pan Y., Steurer M., Baldwin T.L., McLaren P.G. Impact of Waveform Distorting Fault Current Limiters on Previously Installed Overcurrent Relays. *IEEE Transactions on Power Delivery*, 2008, vol. 23, no. 3, pp. 1310-1318. doi: <https://doi.org/10.1109/TPWRD.2008.919170>.
16. Maji P., Ghosh G. Designing Over-Current Relay Logic in MATLAB. *International Journal of Scientific & Engineering Research*, 2017, vol. 8, no. 3, pp. 40-43. Available at: <https://www.ijser.org/researchpaper/Designing-Over-Current-Relay-Logic-in-MATLAB.pdf> (Accessed 12 March 2021).
17. Idris M.H., Adzman M.R., Tajuddin M.F.N., Amirruddin M., Ismail M.A. Auto-reclose Relay Simulation for Research and Education. *2018 4th International Conference on Electrical, Electronics and System Engineering (ICEESE)*, 2018, pp. 29-33. doi: <https://doi.org/10.1109/ICEESE.2018.8703542>.
18. Ibrahim M.A., Ibrahim W.K., Hamoodi A.N. Design and Implementation of Overcurrent Relay to Protect the Transmission Line. *International Journal of Engineering Research and Technology*, 2020, vol. 13, no. 11, pp. 3783-3789. doi: <https://doi.org/10.37624/IJERT/13.11.2020.3783-3789>.

Received 01.02.2022
 Accepted 27.03.2022
 Published 01.06.2022

Hocine Sekhane^{1,3}, Doctor of Electrical Engineering,
 Djamel Labeled^{2,3}, Doctor of Electrical Engineering, Professor,
 Mohamed Amir Labeled^{2,3}, PhD Student,
¹Electrical Engineering Department,
 20 August 1955 University of Skikda,
 B.P.26 route d'El-Hadaiek, Skikda, 21000, Algeria.
²Electrical Engineering Department,
 Constantine 1 University,
 p.o. box, 325 Ain El Bey Way, Constantine, 25017, Algeria.
³Laboratory of Electrical Engineering of Constantine (LGEC),
 Constantine 1 University,
 p.o. box, 325 Ain El Bey Way, Constantine, 25000, Algeria.
 e-mail: docsekhoc@gmail.com (Corresponding author);
 Djamel_labeled@yahoo.fr;
 mohamedamir.labeled@student.umc.edu.dz

How to cite this article:

Sekhane H., Labeled D., Labeled M.A. Modelling and performance testing of a digital over-current relay enhanced designed model. *Electrical Engineering & Electromechanics*, 2022, no. 3, pp. 71-78. doi: <https://doi.org/10.20998/2074-272X.2022.3.10>

Матеріали приймаються за адресою:

Кафедра "Електричні апарати", НТУ "ХПІ", вул. Кирпичева, 2, м. Харків, 61002, Україна

Електронні варіанти матеріалів по e-mail: a.m.grechko@gmail.com

Довідки за телефонами: +38 067 359 46 96 Гречко Олександр Михайлович

Передплатний індекс: 01216